Numerical investigation for cracks of rib-to-deck welded connection at the crossbeam junction in OSD using XFEM

A Crack Propagation Study Based on Linear Elastic Fracture Mechanics

Akram EL Kazaz

TU Delft Delft University of Technology

Cover Picture: Erasmus Bridge ©.
https://en.wikipedia.org/wiki/File:Erasmus_bridge_Rotterdam_2018_2.jpg.

Numerical investigation for cracks of rib-to-deck welded connection at the crossbeam junction in OSD using XFEM

A Crack Propagation Study Based on Linear Elastic Fracture Mechanics

by

Akram EL Kazaz

to obtain the degree of
Master of Science
in Structural Engineering
at the Delft University of Technology
to be defended publicly on Friday, July 30th, 2021 at 03:00 PM

Student number:	4343786
Committee Chairman:	Prof. Dr. M. Veljkovic
Thesis Committee:	Dr.Ir. F.P. Van der Meer
	Dr. Junlin Heng
	Ir. Weijian Wu

An electronic version of this thesis is available at https://repository.tudelft.nl/

TU Delft Delft University of Technology

Contents

Acknowledgement

In the Name of God, Most Gracious, Most Merciful

Before everything, I have to thank God for making me believe I can start this step and complete it while facing all kinds of challenges through all the studying years within my academic career as well as my life itself. Thank you, Allah, for granting me persistence and tranquility throughout my life.

This report marks the end of my academic career at the Delft University of Technology after a long journey. Through this journey, I cannot describe how much I have learned, not only on the technical or academic side but also personally. One of the most important lessons is to have more patience when dealing with any kind of problem and think in a different way to solve them; this reflected positively on all my life aspects and gave me more strength.

First, I would like to express my appreciation for Prof. Dr. M. Veljkovic for giving me the time to discuss my research desires and suggesting an interesting topic for me. Moreover, I would like to thank him for his continuous support during my progress and his splendid words when describing my work.

In addition, I would like to deeply thank my daily supervisor Ir. Weijian Wu for his help whenever I faced challenging problems. He was always available when I contacted him and answered me instantly. I acknowledge that this great work would not have been possible without him. Once again, I would like to express my greatest thanks.

I would also like to convey many thanks to Dr.Ir. F.P. Van der Meer for his concise feedback and comments throughout all meetings as well as his excellent advice. This advice helped me greatly to present my work in a better way. I also cannot thank Dr. Junlin Heng enough for his support during the meetings as well as his praise of my research findings, giving me more confidence and optimism to complete my thesis work.

Finally, I want to thank all my family, especially my parents for raising me and encouraging me to take this challenge and become a structural engineer with an MSc degree from TU Delft. As for my fiancée, she is the one who is always there for me at any time whenever I needed her during the whole journey. She always listened carefully to me and motivated me during the bad times and the good times as well. Thank you from the bottom of my heart for your unconditional love and support. Last but not least, many thanks to all my friends, specifically my old friends for their unlimited support not only in the time of my academic career but throughout my whole life.

Akram EL Kazaz

Amsterdam, July 2021

Abstract

The orthotropic steel deck (OSD) is nowadays commonly used due to its advantages, such as its lightweight, short construction time, and high capacity to bear the loads. However, fatigue cracks occur in different welded connections in the OSD. In this study, the rib to-deck-plate connection at the crossbeam conjunction has been analysed. This connection has been considered as a very critical connection due to the high-stress concentration under local wheel loading. In addition, the crack initiating at the weld root and propagating through the deck plate thickness cannot be visually inspected until surface cracks appear when the overlay is removed for the investigation. In the Netherlands, deck plate cracks at rib-to-deck plate connections at the crossbeam constitute a significant proportion of investigated cracks. In this thesis, a numerical investigation of the aforementioned cracks is carried out.

First, XFEM is applied to study fatigue crack propagation using compact tension (CT) specimens. Commercial FE software package Abaqus® is used to build 2D and 3D CT models. The corresponding fatigue crack propagation is calculated in the direct cyclic step with strain energy release rate calculated using the virtual crack closure technique (VCCT). A good match is found between analytical calculation and 2D XFEM modeling. For 3D fatigue crack propagation, the number of cycles calculated from the automated crack propagation approach, using the low cycle fatigue step provided by Abaqus®, shows high sensitivity to element sizes, specifically the used element sizes through the thickness of the CT.

Second, 3D crack propagation is applied to OSD with a *20 mm* deck plate. For this detail, the fatigue crack initiation under compressive stress states is caused by the local loading on the deck plate. A hypothesis of changing the loading sign from compression to tension to subject the initial crack zone to tension is proposed so that this type of crack can propagate using automated XFEM. This assumption is made because high residual stresses normally exist in the welded connections and fatigue crack can propagate even under compressive stresses induced by loading. Before carrying out crack propagation calculation using VCCT, the stationary crack states were analysed using FEM and XFEM for cracks inserted with different angles. The SIFs obtained from FEM and XFEM are the same; in addition, that the SIF obtained when the detail is loaded in tension or compression has the same absolute value. Subsequently, the propagating crack analysis is carried out as a small initial crack with a depth of *0.5 mm* is inserted and Paris' law parameters C and m of $1 \cdot 10^{-13}$ and *3.0* were selected respectively. The obtained results of strain evolution as a function of loading history came close to that from the experiment with a difference of *7.75%* for the initial strain value and *10.95 %* for the maximum one. Moreover, the predicted crack shape, angle, and rate were all validated with similar crack shapes obtained from experiments in various literature. As for the crack propagation behaviour in the thickness direction, the crack arresting took place at around *75%* of the deck thickness and an angle with the vertical axis of around 30^{o}.

Finally, the deck thicknesses of *16 mm* and *10 mm* were considered. Their results converged in terms of the crack propagation behaviour with real test specimens from the literature. It is also found that the *16 mm* and *20 mm* cases had a common crack propagation behaviour in the thickness direction as the crack arrest occurred at around *75%* of the deck thicknesses, while for the *10 mm* deck case the crack developed more dangerously by penetrating through the deck plate leading to a through-thickness crack. The approach proposed by this thesis proved to be valid for predicting the crack behaviour for the considered OSD deck plate thicknesses. Thus, the structural integrity of the detail can be assessed. This proved that for the *16 mm* and *20 mm* deck plates, the structural integrity is acceptable, while the *10 mm* deck safety is not confirmed.

List of Abbreviations

OSD	Orthotropic Steel Deck
FEM	Finite Element Method
XFEM	Extended Finite Element Method
FEA	Finite Element Analysis
XFEA	Extended Finite Element Analysis
TOFD	Time of Flight Diffraction
SCF	Stress Concentration Factor
SHSS	Structural Hot Spot Stress
IIW	International Institute of Welding
FM	Fracture Mechanics
LEFM	Linear Elastic Fracture Mechanics
EPFM	Elastic-Plastic Fracture Mechanics
SIF	Stress Intensity Factor
VCCT	Virtual Crack Closure Technique
MTS	Maximum Tangential Stress
CT	Compact Tension (Specimen)
BC	Boundary Condition
RP	Reference Point
DOF	Degree of Freedom

List of Symbols

a	Actual crack depth
a_o	Initial crack size
a_f	Final crack size
a_i	Nodal enriched degree of freedom vector
Δa	Crack increment
b_i^{α}	Associated nodal enriched degree of freedom vector
c	Semi crack length
c_3, c_4	Paris law parameters that link K to $\mathcal{G}$
C	Constant in Paris equation
d	Vertical crack depth
dW_e	Work exerted for crack increment
dU^{el}	Elastic strain energy change
da/dN	Crack growth rate
E	Young's modulus of elasticity
$F_{\alpha}(x)$	The asymptotic crack tip function
G	Shear modulus
G_{th}	Strain energy release rate threshold value
ΔG	Strain energy release rate change $= G_{max} - G_{min}$
G_{max}	Strain energy release rate due to maximum loading
$\mathcal{G}$	Strain energy release rate
$\mathcal{G}_c$	Critical strain energy release rate
$H(x)$	Heaviside step function
J	J-integral
K	Stress intensity factor
K_c	Fracture toughness
ΔK	Stress intensity factor range $= K_{max} - K_{min}$
ΔK_{eff}	Effective stress intensity factor range

ΔK_{eq}	Equivalent stress intensity factor range
ΔK_{th}	Threshold value of stress intensity factor range
M_L	Bending moment at the fixed end support
$N_i(x)$	The usual nodal shape function
N	Fatigue life until failure
N_j	Number of cycles equating to the j^{th} element fracture
ΔP	Applied load range
r, θ	Polar coordinates
σ_s	Structural stress
σ_m	Membrane/mean stress
σ_b	Bending stress
σ_{nlp}	Non-linear peak stress
σ_{hs}	Hot spot stress
$\Delta\varepsilon_i$	Initial strain value difference
$\Delta\varepsilon_{max}$	Maximum strain value difference
$\Delta\varepsilon_{min}$	Minimum strain value difference
θ_i	Crack propagation direction
ν	Poisson's ratio

List of Figures

List of Tables

1 Introduction

1.1 Background knowledge

The orthotropic steel decks are commonly used nowadays due to their numerous advantages. These consist mainly of the system's high strength, short installation time, slenderness in addition to its lightweight which makes it eligible to be used in fixed as well as movable bridges. The bridge deck consists of a deck plate that is supported by closed trapezoidal steel stiffeners supported at each specific distance by a transverse cross beam which transfers its load to the main girders which are constructed in the longitudinal direction of the OSD. Figure 1.1 shows two views of the OSD with its different components.

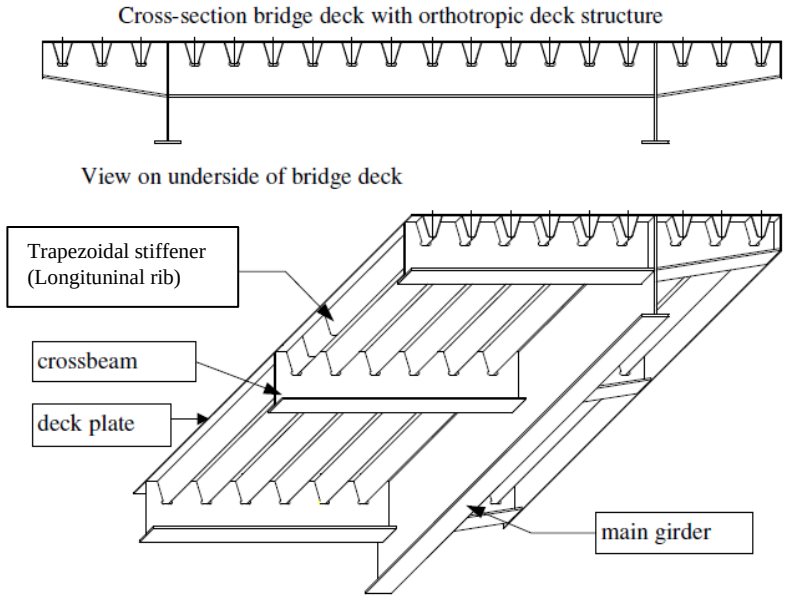

Figure 1.1: Cross-section and 3D view of the OSD [1].

1.2 Research motivation

Nowadays there is an increasing traffic intensity on both national and international levels. This leads to the increase of cyclic loads that the OSD is subjected to. Due to the latter, fatigue cracks in the OSD details are currently a very common problem. This problem occurs in the weakest parts of the bridge deck, which are the welded connections. Although there has been a lot of developments and improvements in design, manufacturing, inspections, and maintenance, fatigue remains the dominant problem in the OSD. The focus of this MSc thesis will be on one of the most critical welded details in the OSD. The stiffener to the deck plate at the connection with the cross beam is the detail that will be studied here. Within this detail, the deck plate weld root crack which cannot be visually inspected and noticed before propagating through the deck plate is the most critical. This is because this crack grows through the deck plate thickness to the road pavement. So, it can affect the traffic's safety which causes a large hazard for people's lives.

1.3 Problem definition

Figure 1.2 shows the deformed shape of the OSD cross-section due to transverse wheel loading, in addition to the internal forces acting on the stiffener-deck-crossbeam detail shown in Figure 1.2b. It is known that this connection is critical and a crack may propagate through the deck for a certain deck thickness. From Figure 1.2 (b), one can see the crack that will be studied in this thesis. This crack grows further in the deck plate thickness and length direction and has a semi-elliptical shape.

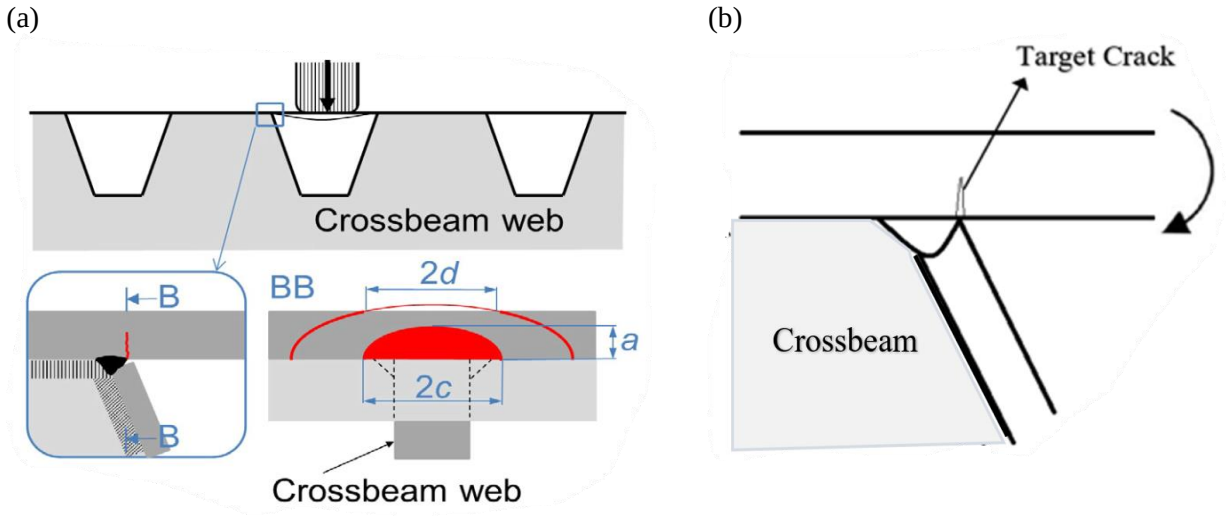

Figure 1.2: OSD deformation due to wheel load. (a) Transverse wheel load positions and OSD cross-section deformation shape. (b) Internal forces due to loading with the targeted crack.

Normally fatigue cracks occur under cyclic loads and the crack tip opens due to tensile stress. However, here the crack initiation point is subjected to nominal compressive stresses as can be seen from Figure 1.2 (b). Although a lot of studies and researchers have investigated this welded detail of the OSD by experimental work, there is still a gap in predicting the behavior of the fatigue crack initiating at this specific location under nominal compressive cyclic stresses. Moreover, experimental research only is not the optimal solution in terms of time and cost. Thus, predicting and accurately simulating this crack behavior using numerical methods such as FEM and XFEM is of big importance and is studied in this thesis carefully.

1.4 Research question

The research objective will mainly focus on the crack propagation behaviour using numerical methods to investigate this crack. Hence, the main research question will be:

How is the structural integrity affected by the propagation of fatigue cracks at the rib-to-deck plate welded connection at the crossbeam junction?

To answer this question, the following sub-questions should be answered first.

- What approach using XFEM can be used to simulate crack propagation? Are there any limitations of such an approach?
- How can the stationary crack be simulated with XFEM and conventional FEM support using this approach?
- What is the crack propagation behaviour for the detail with different deck plate thicknesses?

1.5 Thesis Outline

The thesis is divided into six chapters to keep the work done structured and the findings well ordered. The order of the chapters is based on the progressive significance, effect, and consequences of the points studied within these chapters.

Chapter 2 reviews and explains the most relevant and important findings in the literature. First, general information is given about orthotropic steel decks, fatigue cracks, fatigue assessment approaches, and the fracture mechanics approach is introduced in detail. Hence, more illustration is given for the LEFM principles and XFEM based VCCT.

Chapter 3 applies XFEM for the crack propagation study in Abaqus® for a compact tension specimen subjected to cyclic tensile load. The objective of the chapter is to simulate through-thickness crack propagation in both 2D and 3D XFE models for the CT.

Chapter 4 presents the FE models of OSDs for a 20 mm thick deck plate. These models are validated for their initial stress state with the experimental measures. The XFEM and conventional FEM are used to simulate a stationary crack using the contour integral evaluation. Then XFEM is used to simulate a propagating crack due to cyclic loading. Finally, the obtained crack shape is studied and discussed as well as the strain evolution due to the crack growth.

Chapter 5 considers a parametric analysis and how its variation affects the crack propagation shape and strain evolution. Two different deck plate thicknesses, 10 mm and 16 mm, are considered in the FE models by keeping the SHSS in the same with the OSD analysed in chapter 4.

Chapter 6 gives the conclusions based on the findings of the aforementioned chapters and answers the research questions. In addition, recommendations for further studies are given.

2 Literature Review

In this section the available literature concerning the research topic, targeted detail, targeted crack, and fatigue life prediction methods used have been reviewed hence, background knowledge and findings will be explained. The fatigue life assessment approaches will be shortly described in steps with an overview of the method history and its applicability. There will be made clear which method(s) will be used for this research and why it will be then highlighted and more elaboration on it will be provided.

2.1 Orthotropic bridge deck

Orthotropic bridge decks were firstly innovated in Germany after WWII. The new bridge system's main advantages were its lightweight, high strength short installation time, and little presence of joints in the bridge deck. The structural system of the OSD evolved over the years, as the supporting longitudinal stiffeners were previously open stiffeners as in Figure 2.1 (a). Since 1965 closed cold-formed trapezoidal stiffeners as shown in Figure 2.1(b) are used [2] because open stiffeners contribute to a heavier OSD and require more welding making the system more expensive. The crossbeam spacing now can be up to 4 m. However, fatigue problems are more frequent in OSD with closed stiffeners as they constrain the transverse deformation of the deck plate due to higher flexural stiffness [3,4] in addition to the presence of welded connection leading to stress concentration at it. Moreover, due to the increased traffic intensity on a national and international scale, fatigue problems occurred in OSD over the years in several welded details of the OSD. The most critical detail affected by fatigue in OSD which is also the detail of interest for this MSc thesis is the stiffener-to-deck plate welded connection.

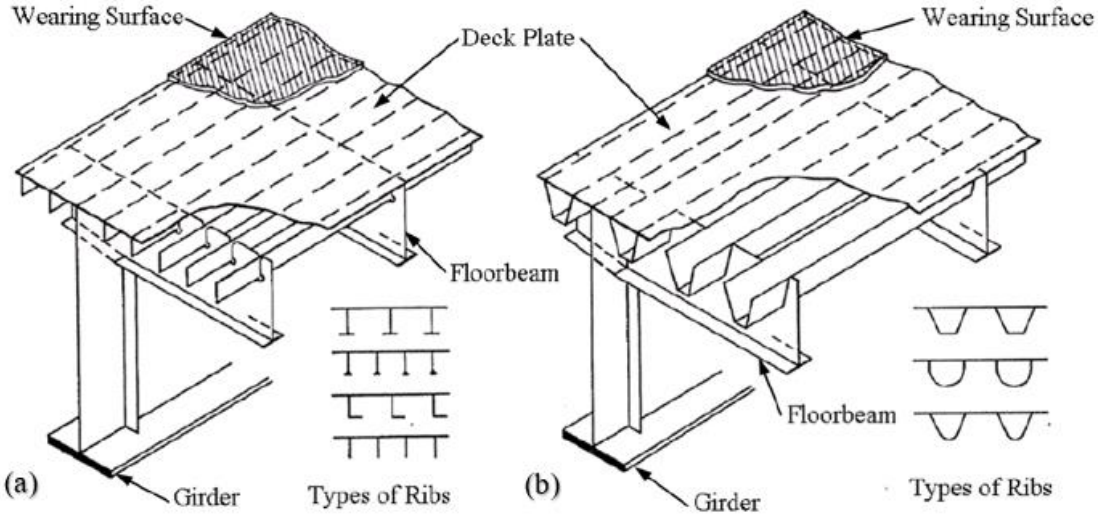

Figure 2.1: Orthotropic bridge deck with its components [5]. *(a) Deck with open stiffeners (b) Deck with closed stiffene.*

2.2 Targeted detail

The OSD local deformation shape and magnitude are significantly dependent on the transverse vehicle wheel location. As mentioned before in section 1, this leads to the internal forces shown in Figure 2.2. The rib to the deck-plate connection at the crossbeam junction is more susceptible to cracks than between the cross beams. This is because that the rib webs are welded to the deck plate and to the cross beam which

gives the connection a fixation property as the schematization in Figure 2.3. When heavy vehicle wheel loads are positioned above the stiffener centered between the rib webs, the clamping moment is high. This means that there are high-stress concentrations at that welded connection causing the strain to exceed the yield strain making it crack easily under heavy cyclic loads. Hence, the principal stress there is higher than that of the joint in between the cross beam. It has also been concluded by Wu et al [6] that the stress concentration near the weld root is higher at the connection with the cross beam leading to faster crack initiation than in the span between cross beams.

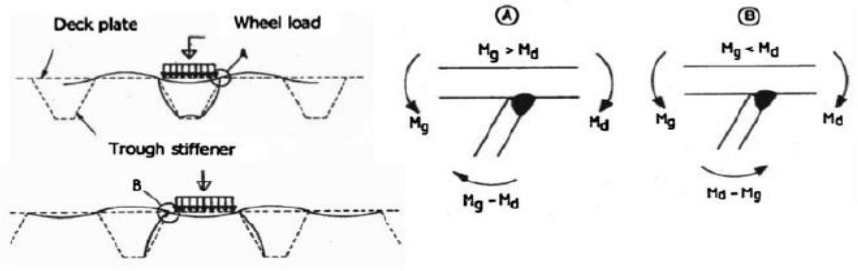

Figure 2.2: OSD deformed shape and internal forces & wheel load transverse positions[5].

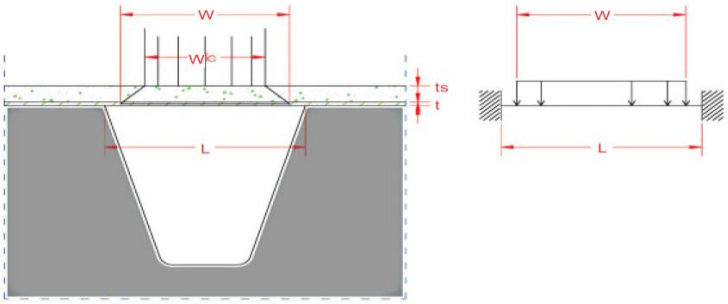

Figure 2.3: Vehicle wheel load on the rib-to-deck plate welded connection at crossbeam junction [2].

2.3 Fatigue cracks

Fatigue is a progressive localized structural damage (crack) that is permanent and happens due to the material being subjected to cyclic loading. In the rib to deck plate detail, four types of cracks can be observed as shown in Figure 2.4. According to studies [6] cracks (a) and (c) will initiate at the weld toe when the wheel position is between the closed ribs. Furthermore, crack (b) and (d) will initiate both at the weld root and grow in the deck- plate and weld joint, respectively. The crack growing through the deck plate most likely occurs at the connection with the crossbeam while the crack growing through the weld bead occurs within the span between cross beams. The most critical crack and the one affecting the traffic's safety is crack (b). Since this crack cannot be observed during visual inspections as it grows through the deck plate at the inner side of the trapezoidal rib, so it gets only visible after it has penetrated the deck plate and the asphalt or epoxy layer and grown to a certain length as shown in Figure 2.5. The crack grows further in the longitudinal direction and has a semi-elliptical shape as in Figure 2.6, where a, 2c, and 2d are the crack depth, crack top, and bottom length respectively. However, there are some methods to discover this

kind of crack and measure its length. One of these methods is time-of-flight diffraction (TOFD). It requires removal of the asphalt layer which makes it labor-intensive and quite expensive.

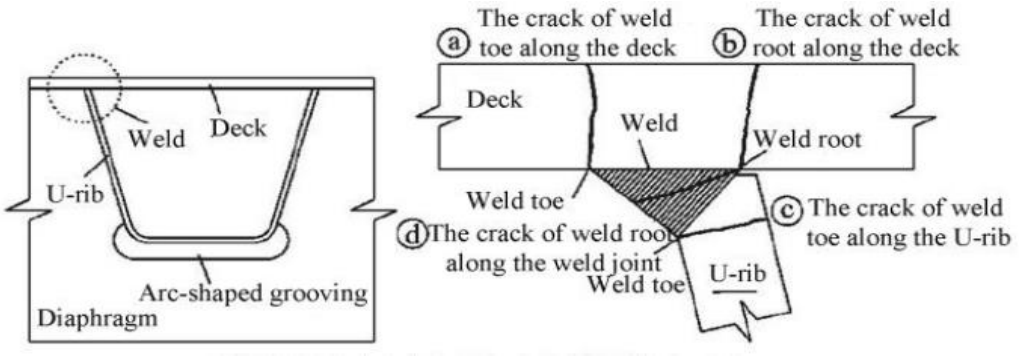

Figure 2.4: Stiffener to deck plate welded connection with the crack types occurring in this connection [6].

Figure 2.5: Visual observation of deck plate root crack [7].

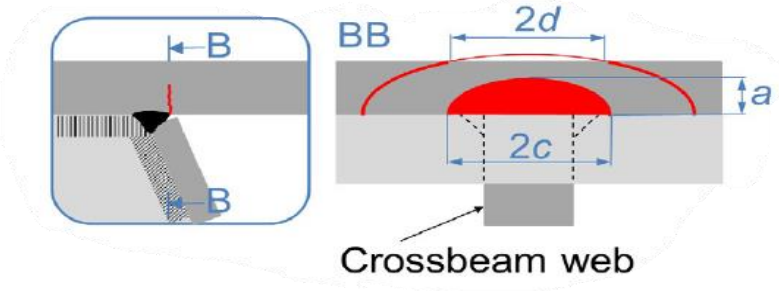

Figure 2.6: semi-elliptical crack shape [8].

Fatigue cracks introduced can be categorized according to the stress state in the detail to three fracture modes as indicated in the following figure. Opening fracture mode, sliding fracture mode and tearing fracture mode which is mode I, mode II and mode III as shown in Figure 2.7, respectively. Mode I is the most common crack mode occurring, but when dealing with OSD there will be a mixed fracture mode due to the complex stress situation in OSD welded details.

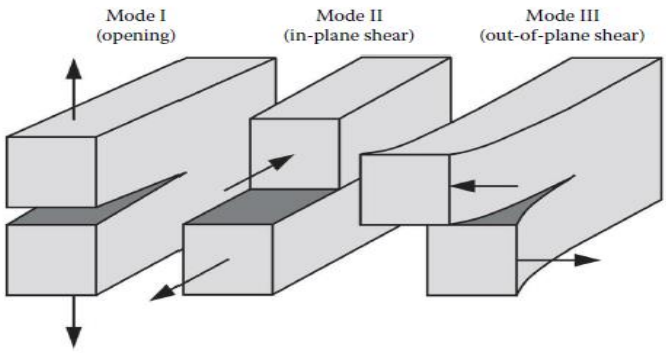

Figure 2.7: The three fracture modes that can characterize a crack [9]

2.4 Fatigue life prediction approach

The most common methods used for evaluating the fatigue life in guidelines and literature are (1) nominal stress approach, (2) hot spot stress approach, (3) effective notch stress approach, and (4) fracture mechanics' approach. The fatigue life of structures consists of two stages as can be seen from Figure 2.8. The first three assessment approaches consider the initiation period which is the initial stage and directly links it to the end of fatigue life which is the final fracture. So, it does not investigate the propagation period of the fatigue crack. As for the fracture mechanics approach, it looks more carefully at when the crack is initiated and starts to propagate till the structure completely fails due to unstable crack propagation.

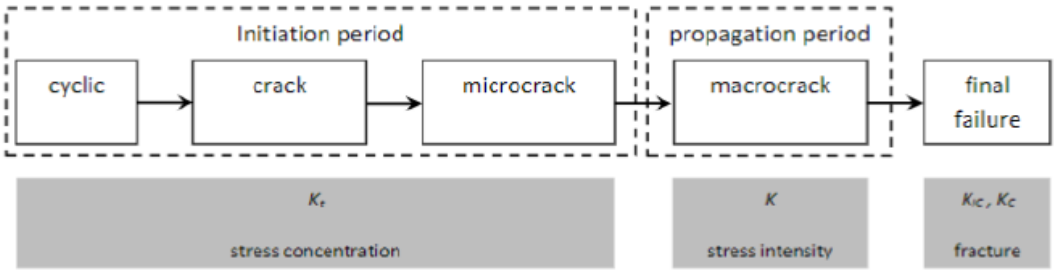

Figure 2.8: Fatigue life phases of structures [10]

2.4.1 Nominal stress approach

The nominal stress approach is a global approach for evaluating the fatigue life of a detail. It does not consider any special effects so it takes only the macro geometric shape of the detail into account at the joint [11] In other words nominal stress disregards the local stress-raising effects of the welded joint [12]. Nominal stress is based on linear elastic material behavior and can be determined simply for regular geometries as the average stress at the weld throat or the weld toe in the plate.

In NEN-EN-1993-1-9 the classified fatigue detail categories with its given S-N (Wohler) curves (based on linear damage calculation by the "Palmgren-Miner" rule) of OSD welded details are based on nominal stresses (see Figure 2.9). Note that the stress concentrations due to weld geometry presence and are weld notch effect dismissed here.

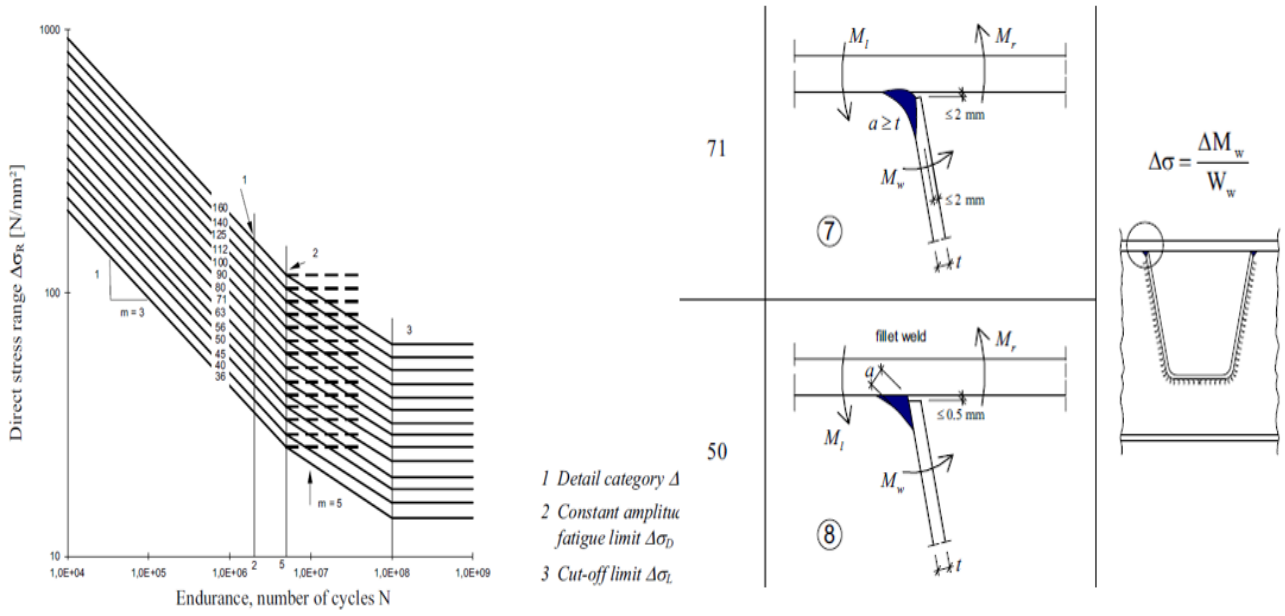

Figure 2.9: Fatigue detail class of OSD with closed stringer [13]

2.4.2 Structural hot spot stress approach

The structural hot spot stress (SHSS) approach goes one step further as it looks at the hot spots which are the locations in the structure with possible fatigue crack initiation as a result of a combination of structural stress (which is the sum of membrane stress σ_m and the bending stress σ_b as in Figure 2.10) and the weld geometry. It is a local approach that is more accurate than the nominal stress approach as the HSS includes the stress raising (concentrating) effects due to the weld but does not include the non-linear stress peak due to the effect of the presence of a notch at the weld toe which results in a non-linear stress peak so the discontinuity due to weld geometry is not considered in this method as the designer cannot know the actual local weld toe geometry beforehand [11]. Note that the notch effect is implicitly included in the experimentally determined S-N curves.

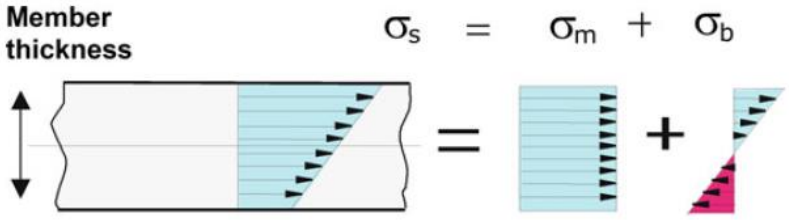

Figure 2.10: The structural stress components [11]

There are mainly two types of hot spots in plated structures: type (a) and (b) as seen in Figure 2.11. In type (a) the weld toe is located on the plate surface, while type (b) is when the weld toe is at the plate edge. In rib to deck plate connection, mostly type (a) is considered so the considered welded detail in this thesis will be of type (a) hot spot, while type (b) is mainly considered at the weld on the cross-beam edge connecting it to the longitudinal rib which is not the focus of this thesis.

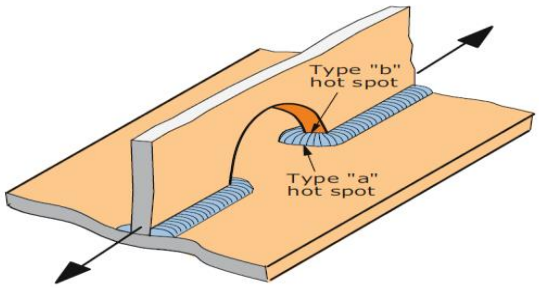

Figure 2.11: Types of hot spots in a welded detail [11]

One main problem of the hot spot stress is how to determine the stress amplitude at the crack locations accurately when evaluating the fatigue life. Another problem is that the SHSS approach is mainly applicable for fatigue strength evaluation of cracks initiating at the weld toe. However, some scholars managed to use it to evaluate the fatigue strength at the weld root [2,8]. Moreover, the SHSS approach is meshing sensitive in finite element analysis (FEA). To overcome these problems when using finite element analysis and make reliable FE-models in design practice, the international institute of welding (IIW) gives some recommendations which should be followed.

The fatigue life can be predicted using modified nominal stress by multiplying a stress concentration factor (SCF) with the nominal stress according to the Dutch national annex [14] and making use of a 2D beam model as in figure 3 or by the given or 3D FEA data of the stress ranges at the weld root. Note that when using shell elements in the 3D FE model, it will be difficult to implement the weld geometry compared to 3D solid elements.

After following the IIW recommendations for the choice of the FE, the mesh size, meshing options, identifying and analyzing the hot-spots (see reference [11]), the stresses can be extrapolated using Table 2.1 (where *it* is the deck plate thickness) to be used further to calculate the hot spot stress σ_{HSS} which will be compared to the detail category in the Dutch national annex [14] to calculate the remaining fatigue life.

Table 2.1: IIW hot spot stress extrapolation guidelines

		Relative coarse mesh		**Relative fine mesh**	
		Shell	Solid	Shell	Solid
Type a	Element size	t	t x t	≤ 0.4t	≤ 0.4t x t
	Reference points	0.5t and 1.5t		0.4t and 1.0t	
	Hot spot stress	$\sigma_{hs} = 1.5\sigma_{0.5t} - 0.5\sigma_{1.5t}$		$\sigma_{hs} = 1.67\sigma_{0.4t} - 0.67\sigma_{1.0t}$	
Type b	Element size	10mm	10mm x 10mm	4mm	4mm x 4mm
	Reference points	5mm and 15mm		4mm, 8mm and 12mm	
	Hot spot stress	$\sigma_{hs} = 1.5\sigma_{5mm} - 0.5\sigma_{1.5mm}$		$\sigma_{hs} = 3\sigma_{4mm} - 3\sigma_{8mm} + \sigma 12mm$	

2.4.3 Effective notch stress approach

The effective notch stress is the total stress at the notch root. As can be seen from figure 11 the total notch stress consists of three stress components where the nonlinear stress peak is included. The notch stress is applicable at the weld root as well as the weld toe. If the material has linear-elastic behavior the stress peak because of the presence of a notch at the weld toe or root is included in the total stress.

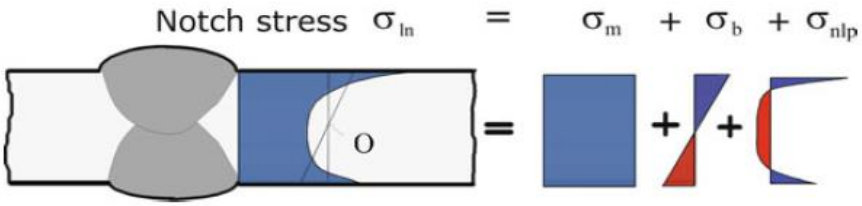

Figure 11: non-linear notch stress distribution across plate thickness [11]

The method simulates the actual notch at the weld root or toe which leads to non-linear peak stress by replacing the actual notch with an effective one. An effective notch with a 1 mm radius as indicated in Figure 2.12 is used for structural steels and aluminum alloys as it gives consistent results. An element size equal to 1/6 the radius of the effective notch is recommended by IIW when using linear finite elements. Unlike the nominal stress approach and SHSS approach, the effective notch stress has only one corresponding detail category according to the IIW. The effective notch method consumes more time than the hot spot stress method as well as not considering crack initiation or propagation phases. Thus, the notch stress will not be considered in this study.

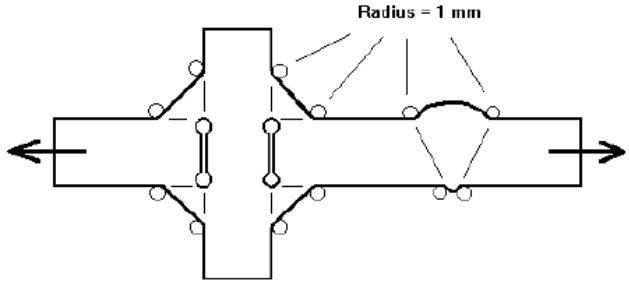

Figure 2.12: Fictitious rounding's of weld toe and roots

2.4.4 Fracture mechanics approach

The fracture mechanics (FM) approach is different from the previous approaches as previous ones use the linear cumulative damage criterion and neglect initial material defects. Here the crack propagation phase from the crack initiation till the final fracture is considered. The crack behavior is studied by fracture mechanics as the initial crack size a_i to the final crack size (a_f) can be calculated in addition to the crack propagation direction (θ_i). The number of cycles that accompany each crack increment in the crack propagation phase can also be calculated which will lead to the prediction of residual fatigue life for the structural detail.

As has been mentioned before that the first three methods study the initial stage of fatigue crack and directly link it to the final stage which is the end of fatigue life. These methods are used for structural design and check purposes as they look directly to the end of fatigue life without investigating the current crack stage or parameters and how will it grow when loading increases or changes. Under high load levels, the initiation period is less dominant, and the propagation period is more dominating. The crack propagation period can only be simulated and studied using fracture mechanics principles.

2.5 Linear Elastic Fracture Mechanics (LEFM):

One type of fracture mechanics is LEFM, which assumes that at the crack tip there is small deformation and minimally yielding. A brief overview will be mentioned about the history of the LEFM with its main theories in addition to the research theory basis.

2.5.1 History of LEFM

Inglis was one of the first to study LEFM. According to his findings, a structure containing a sharp crack should fail when an infinitesimal load is applied due to the stress concentration effect. This motivated Griffith to develop his theory of fracture based on energy instead of stress. He explained that at a crack the stress gradient is very high locally at the tip so the stress at the crack tip should not govern the overall behavior and result in fracture for the whole structure. Griffith based his theory on the first law of thermodynamics. A fracture happens when the energy stored in the structure is higher than the surface energy of the material, so the stress at the atomic level should exceed the cohesive strength of the material but this only does not cause fracture [9]. Thus, unstable crack growth (structural failure) is only possible when the applied force work is more than the sum of the difference in elastic energy of the material and the absorbed energy at the crack tip [15]. This can be expressed as shown in equation (2.1).

$$dW_e \geq dU^{el} + \mathcal{G}_c t \Delta a \tag{2.1}$$

where (dW_e) is the work exerted for a crack increment, (dU^{el}) is the elastic strain energy change , $(\mathcal{G}_c)$ is the critical energy release rate which measures the fracture toughness of the material, (*t)* is the plate thickness, and (Δa) is the crack increment.

2.5.2 Fracture parameters and their relations

Fracture mechanics is based on the concept of similitude. This entails that there is a single loading parameter characterizing the crack tip conditions, known as the stress intensity factor [9]. When studying crack behavior one should understand the parameters that characterize the crack and the relation between them. Such parameters are the stress intensity factor (SIF) and the fracture energy release rate (G). The former parameter describes the stresses, strains, and displacements in the vicinity of the crack tip; the latter quantifies the net change in potential energy that follows an increment of a propagating crack. Note that the stress intensity factor describes a local behavior, while the energy release rate is a global parameter. Anderson and Rice [9,16] introduced to use of a line integral around the crack tip, known as the J-integral. The quantity characterizes the strain energy release rate for elastic-plastic fracture mechanics (EPFM) considering the presence of large deformations. However, in linear elasticity theory, the J-integral was related to SIF for homogenous isotropic material by Shih and Asaro [17] as given in equation (2.2). Where K_I, K_{II} and K_{III} are the corresponding stress intensity factors for fracture modes I, II and III shown above in Figure 2.2.

$$J = \mathcal{G} = \frac{K_I^2}{E'} + \frac{K_{II}^2}{E'} + \frac{K_{III}^2}{2G} \tag{2.2}$$

The modulus of elasticity is then defined as in equation (2.3) for plane stress and plane strain conditions.

$$E' = \begin{cases} E & , \ plane\ stress \\ \dfrac{E}{1-\nu^2} & , \ Plane\ strain \end{cases} \tag{2.3}$$

In the out-of-plane shear mode the shear modulus G is then considered, this leads to the following equation.

$$G = \frac{E}{(1+\nu)} \tag{2.4}$$

Substituting equations (2.3) and (2.4) into equation (2.2) will yield the following relations in equations (2.5) and (2.6) for plane stress and plane strain respectively.

$$\mathcal{G} = \frac{1}{E}(K_I^2 + K_{II}^2) + \frac{1+\nu}{E}K_{III}^2 \tag{2.5}$$

$$\mathcal{G} = \frac{1-\nu^2}{E}(K_I^2 + K_{II}^2) + \frac{1+\nu}{E}K_{III}^2 \tag{2.6}$$

One model for predicting the crack propagation direction was derived by Erdogan and Sih [18] based on the concept of maximum tangential stress (MTS). This means that the crack will extend in a radial direction from the crack tip and perpendicular to the maximum tensile load applied. This is valid when the tangential stress is maximum and the shear stress is zero. The crack extension angle is given in equation (2.7).

$$\theta = \cos^{-1}\left(\frac{3K_{II}^2 + \sqrt{K_I^4 + 8K_I^2K_{II}^2}}{K_I^2 + 9K_{II}^2}\right) \tag{2.7}$$

2.5.3 Crack growth behaviour

The crack initiation phase in welded connection is relatively short compared to the crack propagation phase. The crack growth behavior was studied by Paris and Erdogan in 1961 and a relation between the crack growth rate *da/dN* and the stress intensity factor range ΔK was established. This is known as "Paris' law" [19]. The developing crack behaviour has been divided into three generalized regions as can be seen in Figure 2.13. There are two asymptotes when the relation is plotted in the log-log scale. The first asymptote indicates the threshold value for the stress intensity factor ΔK_{th} below which the fatigue crack will not grow. The crack growth rate increases as K_{max} approaches K_c which is the fracture toughness. When the K_{max} = K_c the crack length reaches the critical value, which will lead to accelerated unstable crack growth and complete failure of the structural detail. The figure is divided into three regions showing region I where the crack initiates and starts to propagate. Region II shows a linear crack growth which is called the Paris regime described by equation (2.8).

$$\frac{da}{dN} = C\,\Delta K^m \tag{2.8}$$

where C and m are material-dependent parameters from experiments that have been determined by different scholars as shown in Table 2.2. LEFM mainly studies the crack propagation in region II, considering there is an initial predefined crack that will then grow linearly. Furthermore, this research will mainly focus on the linear crack growth in region II. As for region III, it indicates the unstable crack growth when the stress intensity range approaches the fracture toughness which will then lead to failure of the structural detail [20].

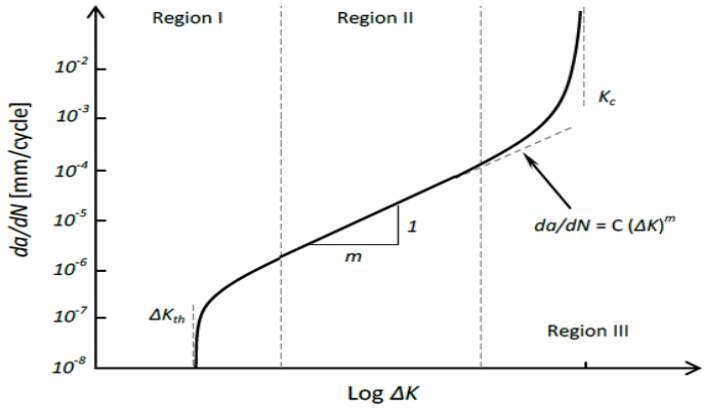

Figure 2.13: Fatigue crack growth behavior in metals [10]

2.5.4 Crack closure effects

There was a shortcoming in the Paris equation as it could not consider the mean stress effect, as the compliance of fatigue specimens did not agree with the formulae for low loads which compliance was close to an un-cracked specimen [21]. This was discovered by Elber in 1970 which led to research into a phenomenon called crack closure.

Table 2.2: Paris constants for structural steel [22]

Source	$C^{(*)}$ [-]	m [-]	ΔK_{th} $[MPa\sqrt{mm}]$	R [-]
British Standards (2007)	$5.21 \cdot 10^{-13}$	3	63	0
Hobbacher (2015) (base metal)	$3.00 \cdot 10^{-13}$	3	63	0
Hobbacher (2015) (weld metal)	$5.21 \cdot 10^{-13}$	3	63	0
Kühn *et al.* (2008)	$4.00 \cdot 10^{-13}$	3	170	0
Bignonnet *et al.* (1991)	$4.25 \cdot 10^{-13}$	3	50–71	-1
Maljaars *et al.* (2012)	$3.00 \cdot 10^{-13}$	3	80	0

Figure 2.14 shows the effect of crack closure effect on the displacement and the driving force for fatigue when a specimen is subjected to cyclic loading between K_{max} and K_{min}. K_{op} is the stress intensity factor at which the crack opens.

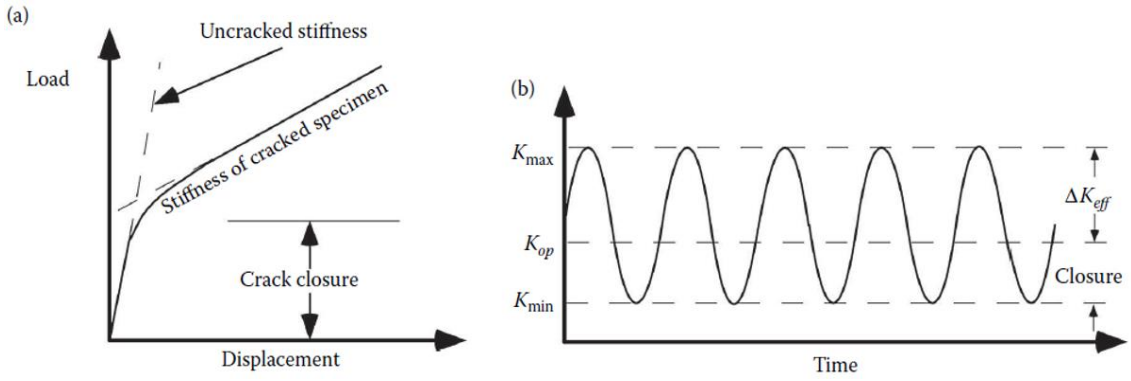

Figure 2.14: Fatigue crack closure [9]. *(a) Load-displacement behaviour for a positive load. (b) The reduced driving force for fatigue leading to the effective stress intensity range (ΔK_{eff})*

Due to the fact that during the cyclic loading the crack tip strain does not change for a closed crack, Elber assumed that there is no contribution to the fatigue crack growth from the portion of the cycle which is below K_{op}. This led to the following definition of the effective stress intensity range expressed by equation (2.9). Thus, a modified Paris equation has been proposed by Elber given in equation (2.10).

$$\Delta K_{eff} = K_{max} - K_{op} \tag{2.9}$$

$$\frac{da}{dN} = C\Delta K_{eff}^{m} \tag{2.10}$$

The latter equation showed reasonably successful results when correlating fatigue crack growth data at different cyclic load ratios. This all led to a decrease in the fatigue crack growth rate by decreasing the effective stress intensity range for different low load ranges [23].

2.6 Extended Finite Element Method (XFEM)

To numerically simulate the crack propagation in the OSD targeted detail based on the LEFM theory the commercial finite element software Abaqus® will be made use of.

2.6.1 XFEM formulation

The numerical method used therefore is the Extended Finite Element Method. XFEM was first proposed by Belytschko and Black in 1999 [24]. The method is an extension of the polynomial function space of the conventional finite element method based on the concept of partition of unity. It was developed to address discontinuity problems. Furthermore, it extends the displacement vector of the FEM by adding two enrichment degrees of freedom with the accompanying special displacement functions to include the displacement discontinuity into the conventional FEM displacement vector. The displacement vector using the XFEM is expressed in equation (2.11).

$$u(x) = \sum_{i=1}^{n} N_i(x)[\boldsymbol{u_i} + H(x) \cdot \boldsymbol{a_i} + \sum_{\alpha=1}^{m} F_\alpha(x) \cdot \boldsymbol{b_i^\alpha}] \tag{2.11}$$

Where $N_i(x)$ is the usual nodal shape function; $\boldsymbol{u_i}$ is the continuous nodal displacement vector; $H(x)$ is the Heaviside step function (for the displacement field of the elements penetrated by cracks) associated with the nodal enriched degree of freedom vector, $\boldsymbol{a_i}$; and the third term of equation (2.11) is the product of the asymptotic crack tip function, $F_\alpha(x)$, and the associated nodal enriched degree of freedom vector, $\boldsymbol{b_i^\alpha}$. Thus, the third term is used only for the elements which are cut by the crack tip.

This all can be more obvious when looking at Figure 2.15 where the normal FE is indicated and the discontinuous element consisting of crack penetration and crack tip element can be seen.

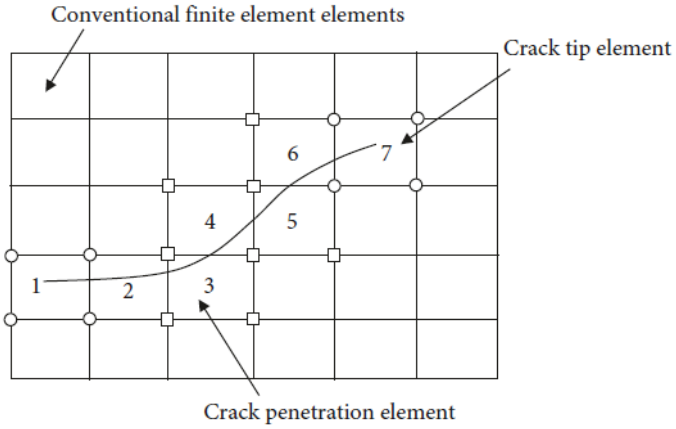

Figure 2.15: XFEM elements indication [25]

The discontinuous jump function which addresses the displacement field of the cracked elements, $H(x)$, is expressed in equation (2.12), while the asymptotic crack tip function, $F_\alpha(x)$, for an isotropic elastic material is given in equation (2.13).

$$H(x) = \begin{cases} 1 & if \ \ (x - x^*) \cdot \boldsymbol{n} \\ -1 & otherwise \end{cases} \tag{2.12}$$

$$F_\alpha(x) = [\sqrt{r}\sin\frac{\theta}{2}, \sqrt{r}\cos\frac{\theta}{2}, \sqrt{r}\sin\theta\sin\frac{\theta}{2}, \sqrt{r}\sin\theta\cos\frac{\theta}{2}] \tag{2.13}$$

Where in equation (2.12) x is a Gauss point, x^* is the point on the crack closest to x and $\boldsymbol{n}$ is the unit outward normal to the crack at x^*, and in equation (2.13) the (r, θ) form a polar coordinate system with its origin at the crack tip as indicated in Figure 2.16.

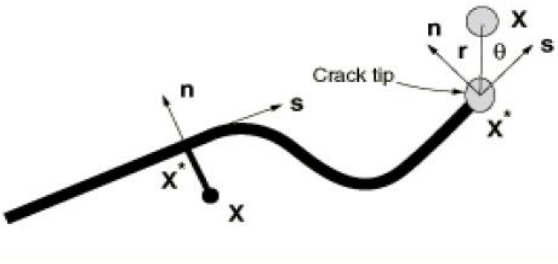

Figure 2.16: Indication of the normal and tangential coordinates for a smooth crack [26]

Like conventional FEM the XFEM solves the unknown displacement vector by using the overall stiffness matrix and load vector. Then nodal displacements are obtained and the stresses in the integration points can be calculated and extrapolated at the nodes. Moreover, the numerical integration scheme used for XFEM is also the Gaussian integral. Note that the crack penetrated elements and the crack tip elements have a discontinuous displacement field, so the stiffness matrices are also discontinuous. This leads to the element division into sub-elements, subsequently, the stiffness matrix of the element is obtained by numerically integrating the stiffness matrix of the sub-elements using a Gaussian integration scheme and then summing up the stiffness matrices of the sub-elements.

2.6.2 XFEM for propagating crack

Resulting from the fact that modeling the crack tip singularity is an arduous task as it requires continuously tracking where the crack propagates, the asymptotic singularity function is only considered in the XFEM stationary crack modeling in Abaqus®. Hence, the displacement vector when using the XFEM to model propagating cracks reduces to the expression given in equation (2.14).

$$u(x) = \sum_{i=1}^{n} N_i(x)[\boldsymbol{u_i} + H(x) \cdot \boldsymbol{a_i}] \tag{2.14}$$

The propagating cracks that will be modelled in this research will be based on the principles of LEFM and phantom nodes [26]. This method is more convenient in modeling brittle crack moving in a bulk material. The phantom nodes are shown in Figure 2.17. These nodes symbolize the discontinuity of the cracked elements. Each phantom node is fully constrained to its corresponding real node when the element is uncracked.

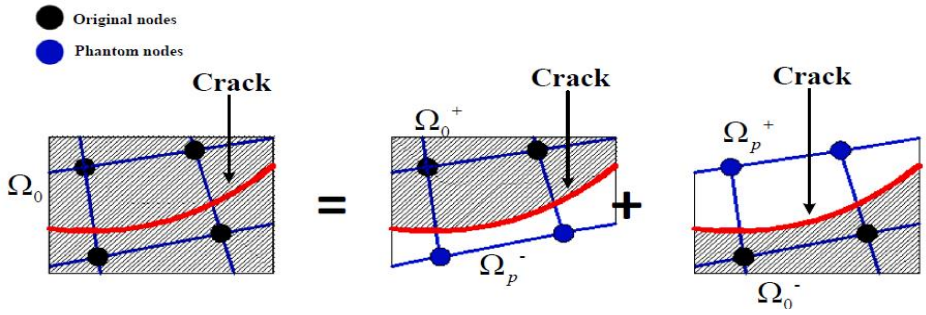

Figure 2.17: Schematic representation of the phantom nodes[27]

Since only the displacement jump function is considered in the XFEM for modeling moving crack (2.14), the crack must propagate across the entire element at a time to consider the element cracked and to avoid the necessity of modeling the stress singularity at the crack tip. Moreover, the element cracks once the fracture criterion has been met. Within the enriched element, this criterion will be met when the equivalent strain energy release rate exceeds the critical one at the crack tip as shown in expression (2.15). Thus, the crack extends after an equilibrium increment when the fracture criterion is met within a specific tolerance. The strain energy release rate is calculated at the crack tip based on the modified virtual crack closure technique (VCCT). VCCT relies on the assumption that the released strain energy when a crack is extended by an amount is the same as the required energy for the crack closing by the same amount.

$$f = \frac{\mathcal{G}_{equiv}}{\mathcal{G}_{equivC}} \geq 1.0 \tag{2.15}$$

The critical equivalent fracture energy release rate is computed in Abaqus® based on three mixed fracture modes. These modes include the BK law [28], the power-law [29], and the Reeder law [30] given in equations (2.16), (2.17), and (2.18) respectively.

$$\mathcal{G}_{equivC} = \mathcal{G}_{IC} + (\mathcal{G}_{IIC} - \mathcal{G}_{IC}) \left(\frac{\mathcal{G}_{II} + \mathcal{G}_{III}}{\mathcal{G}_I + \mathcal{G}_{II} + \mathcal{G}_{III}}\right) \tag{2.16}$$

$$\frac{\mathcal{G}_{equiv}}{\mathcal{G}_{equivC}} = \left(\frac{\mathcal{G}_I}{\mathcal{G}_{IC}}\right)^{a_m} + \left(\frac{\mathcal{G}_{II}}{\mathcal{G}_{IIC}}\right)^{a_n} + \left(\frac{\mathcal{G}_{III}}{\mathcal{G}_{IIIC}}\right)^{a_o} \tag{2.17}$$

$$\begin{aligned} \mathcal{G}_{equivC} = \mathcal{G}_{IC} &+ (\mathcal{G}_{IIC} - \mathcal{G}_{IC}) \left(\frac{\mathcal{G}_{II} + \mathcal{G}_{III}}{\mathcal{G}_I + \mathcal{G}_{II} + \mathcal{G}_{III}}\right)^{\eta} \\ &+ (\mathcal{G}_{IIIC} - \mathcal{G}_{IIC}) \left(\frac{\mathcal{G}_{III}}{\mathcal{G}_{II} + \mathcal{G}_{III}}\right) \left(\frac{\mathcal{G}_{II} + \mathcal{G}_{III}}{\mathcal{G}_I + \mathcal{G}_{II} + \mathcal{G}_{III}}\right)^{\eta} \end{aligned} \tag{2.18}$$

One of the main advantages of the extended finite element method is that it does not require that the mesh matches or conforms to the discontinuity of crack geometry. This is possible by the implementation of the level set function which is a numerical technique for the computation and analysis of the interface motion [31]. In Figure 2.18 two orthogonal signed distance functions define the crack geometry. The first defines the crack surface, while the second constructs an orthogonal surface so the intersection of the two surfaces defines the crack front.

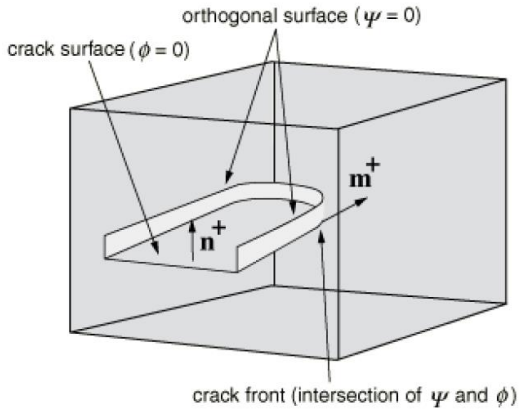

Figure 2.18: Indication of the 3D nonplanar crack by two signed distance functions [26]

2.6.3 XFEM based on LEFM using VCCT

As has been illustrated in section 2.5.3 about the growing crack behavior and regions in fracture mechanics (FM). Since the fracture energy release rate is a global crack parameter, the fracture criterion (based on VCCT), as well as the Paris formula, have been implemented in Abaqus® in terms of relative fracture energy release rate (ΔG). Where c_3 and c_4 are material constants calculated based on C and m, in addition to $G = \mathcal{G}$. Unlike Figure 2.13, the crack growth response is described in terms of the fracture energy release rate as in Figure 2.19. However, the crack growth rate relation with the relative energy release rate has the same pattern as the relation between the former and the SIF.

The Paris law has been given in expression (2.19) in terms of ΔG. The expression holds when condition (2.20) is satisfied, and G_{max} is the energy release rate when the structure is subjected to the maximum loading. As a deduction from Figure 2.19, the Paris regime is bounded at its beginning by the energy release rate threshold, G_{thresh}, below which there will be no fatigue crack initiation and growth. At the end of the Paris regime the energy release rate approaches its upper limit, G_{pl}, above which the crack will grow rapidly at an unstable rate. The critical equivalent strain energy release rate, G_C is calculated based on the mixed-mode criterion (explained in section 2.6.2) and fracture strength specified by the user in Abaqus®. Some default values are given in (2.21).

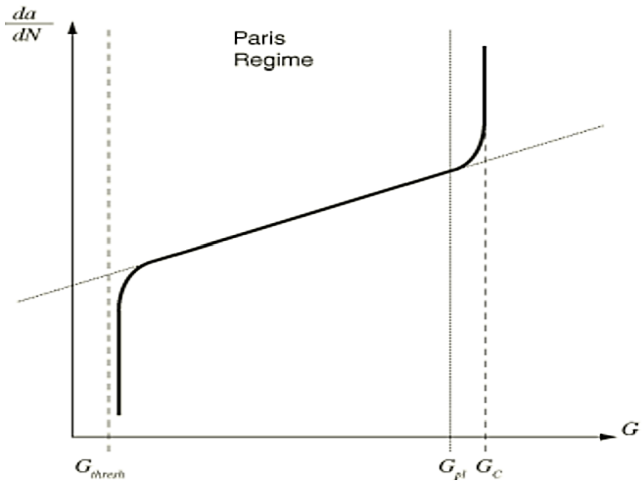

Figure 2.19:Fatigue crack growth in terms of energy release rate

$$\frac{da}{dN} = c_3\,\Delta \mathrm{G}^{\,c_4} \tag{2.19}$$

$$G_{thresh} < G_{max} < G_{pl} \tag{2.20}$$

$$\frac{G_{thresh}}{G_C} = 0.01, \qquad \frac{G_{pl}}{G_C} = 0.85 \tag{2.21}$$

So that the enriched elements in front of the crack tip fracture and the crack initiates growing, the criterion in the following expression should be met. Where N is the cycle number and $c_1,\ c_2$ are material constants.

$$f = \frac{N}{c_1 \Delta G^{c_2}} \tag{2.22}$$

In order to simulate crack growth in Abaqus® using XFEM, a cyclic loading must be inserted using the direct cyclic approach which considers a quasi-static analysis. This will introduce cyclic loading on the structure. The crack length a_N corresponds to the cycle number N. As mentioned before, the crack will only start to grow when the relative energy release rate exceeds the threshold value, ΔG_{th}. Shown in Figure 2.20

(where $\Delta a_k = \Delta a_{Nj}$, $\Delta N_k = \Delta N_j$), the crack length then increases by a certain value, $a_{N+\Delta N}$, due to the corresponding incremental number of cycles, ΔN. Given that the FE element length, the crack propagation direction (from the enriched region), and the material constants c_3 and c_4 are all known, the number of cycles needed for the crack of each enriched element in front of the crack tip can be calculated based on the Paris formula (2.19) as ΔN_j. Where j indicates the enriched element in front of the j^{th} crack tip. The XFEA leads to a crack in at least one enriched element as the analysis runs. The element that corresponds to the least cycles cracks, leading to the minimum change in cycle number as well as in the crack increment as indicated in (2.24) and (2.25). The critical element is then fractured after the loading cycle stabilizes. The element then has zero stiffness. Thus, a load redistribution is expected, and the new relative fracture energy will be calculated for the next enriched elements ahead of the crack tip under the influence of the next load cycle. This process then keeps repeating itself till the stop criterion has been met or the analysis has been manually stopped. This analysis leads to the complete fracture of at least one enriched element ahead of the crack tip after a stabilized load cycle. Consequently, the number of cycles needed to cause a certain fatigue crack length can be determined.

$$\Delta a_{Nj} = a_{N+\Delta N} - a_N \tag{2.23}$$

$$\Delta N_{min} = \min(\Delta N_j) \tag{2.24}$$

$$\Delta a_{\mathrm{N}\,min} = \min(\Delta a_{Nj}) \tag{2.25}$$

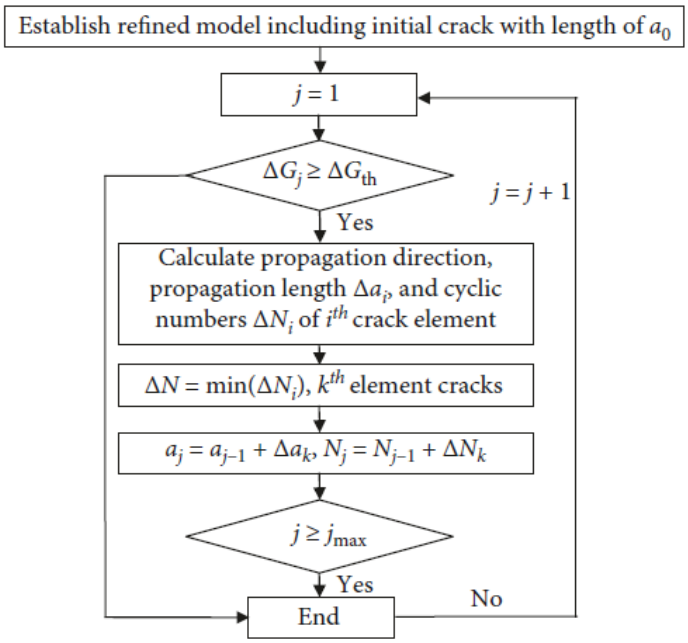

Figure 2.20: Fatigue crack propagation in XFEA [25]

3 Fatigue Crack Propagation In CT

In this chapter, a compact tension specimen with specific geometry is modelled using FEM and XFEM to simulate the fatigue crack propagation in this specimen under cyclic tensile load. Throughout this chapter the models' details, properties, as well as the models' output, will be indicated and discussed, then the results will be plotted and discussed at the end of the chapter.

3.1 Introduction

The compact tension specimen is a single edge-notch specimen that is mainly used in the field of fracture mechanics. It is used in cyclic tensile loading tests for fatigue crack propagation. These tests aim to measure the material fracture parameters (C & m) and study the fatigue crack growth. However, in this research, the CT-specimen test is simulated using FEA and XFEA to study the fatigue crack growth based on LEFM. Since the CT specimen is notched, it is a good representation of practical and real imperfections and inconsistencies such as the discontinuities due to welded connections in OSD. The CT specimen is only suitable for cyclic tensile loading and not for cyclic compressive loading or tensile compressive due to uncertainties at the crack tip. Throughout this chapter, CT specimen fatigue cracks propagation simulations (in both 2D and 3D) will be carried out for a cyclic tensile load with different stress ratios. Before making a propagating crack model a stationary crack model is made using the contour integral evaluation and stationery XFEM to evaluate the accuracy of the extracted SIFs (see Appendix A).

3.2 FE Model description

3.2.1 Geometry

First of all, the used CT dimensions have to comply with the guidelines of the standard test method for measurements of fatigue crack growth rates (ASTM E647-13) [32]. The dimensions' ranges stipulated for the CT specimen in the guideline are indicated in Figure 3.1.

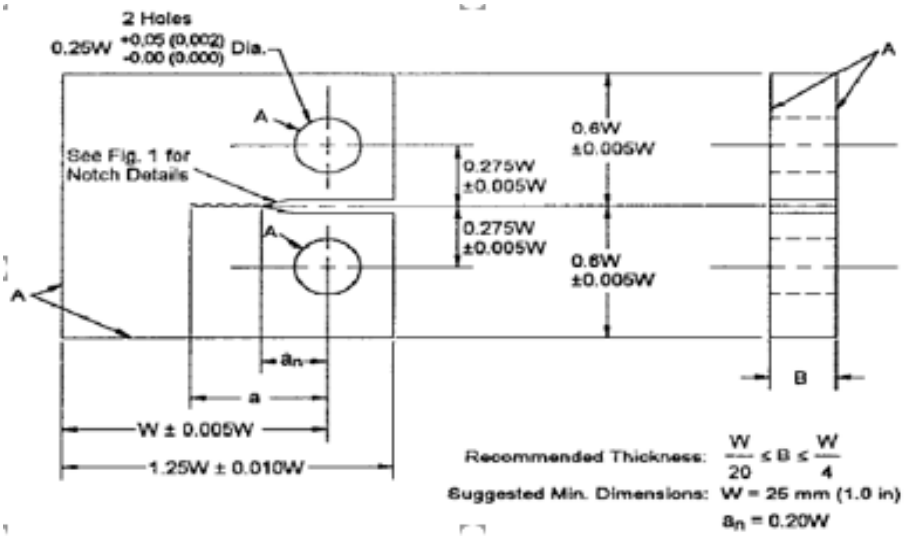

Figure 3.1: Standard CT specimen dimensions for fatigue crack growth testing [32]

2D and 3D XFEM analyses are carried out for the CT-. The dimensions of the modelled CT specimen are shown in Figure 3.2. In the model, the 'a_n' is *7.5 mm*, while 'a_0' is *12.5 mm* (*7.5 mm + 5 mm*). Thus initial

predefined crack (flaw) is 5 mm. In the 2D model, the model thickness is assigned as a plane stress/strain thickness and is equal to *6 mm*, while in 3D, the CT part geometry has a 6 mm thickness in Z-direction.

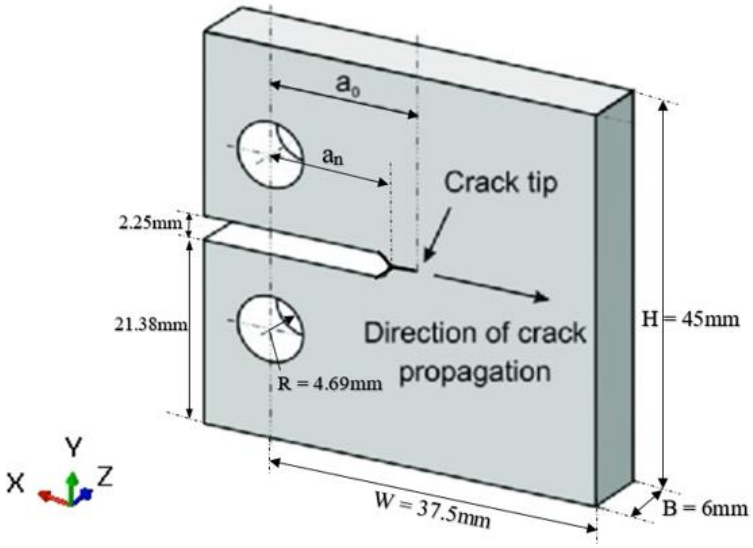

Figure 3.2: CT XFEM model dimensions [33]

3.2.2 Material properties

The considered material (steel) properties for all models are elastic material properties since fatigue crack occurs without the yield strength is reached on the global (model) level. Only a local plastic zone occurs at the crack tip when the fatigue crack is growing. Considering LEFM theory, the linear elastic material behaviour is generalized to the whole model. Hence, the material properties are indicated in Table 3.1.

Table 3.1: Elastic material properties

Young's modulus of elasticity (E)	210,000 MPa
Poisson's ratio (ν)	0.3

3.2.3 Boundary conditions

In this thesis, two different boundary conditions are investigated in the FE simulation. The aim is to study the boundary conditions' effect on the crack propagation rate in both 2D and 3D XFEA and deduct the most suitable BC which complies with the most reasonable results.

In Figure 3.3 the 2D and 3D XFE-models are shown with various boundary and loading conditions. Both single and double loading are considered for the CT model. First, in the 2D model, one tensile load is applied at the upper RP while constraining the lower RP [Figure 3.3 (a)] in the vertical direction (Y-direction). Second, double tensile loading is considered, there is no constraining for any degree of freedom (DOF) in both RPs [Figure 3.3 (b)]. Then a 3D XFE-model is made by firstly applying single tensile loading at the upper RP with the rotations around X-and Y-axis constrained to bound the out-of-plane rotations in the simulation [Figure 3.3 (c)]. The same DOFs are constrained at the lower RP in addition to the translation in Y-direction as in the 2D model. The 3D model double loading case is slightly more challenging to reach the most suitable BCs. This is basically due to the extra DOFs attributed to the 3D elements used in the 3D model. Thus, a sensitivity analysis for the BCs applied for the double loading case is considered to obtain the most appropriate BCs (see Appendix A). The most suitable BC is to fix out of plain rotations at both RPs like in the upper RP in the single-loaded 3D XFE-model.

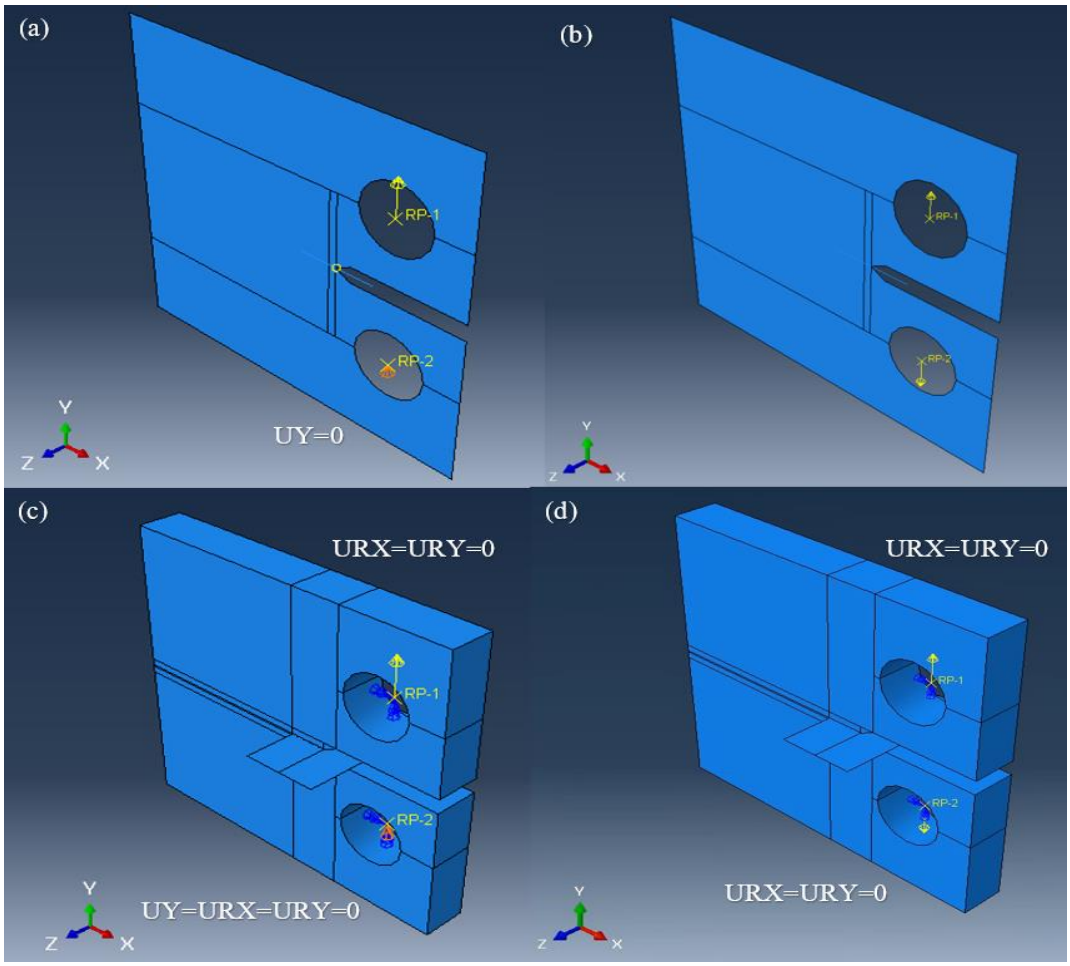

Figure 3.3: 2D & 3D CT-specimen FE-model with different BCs. (a) Single loaded 2D-model. (b) Double loaded 2D-model. (c) Single loaded 3D-model. (d) Double loaded 3D-model

3.2.4 Applied load

The loading applied on the CT model to simulate the testing conditions has a cyclic characteristic using a direct cyclic analysis (Quasi-static) for the simulation. The cyclic loading causes material strength degradation leading to fatigue crack growth along an arbitrary path [26]. The time increment specified is *0.25* with a maximum number of iterations equal to *200*. Moreover, to model the progressive damage in bulk material, the low-cycle fatigue analysis is parallelly enabled to obtain directly a stabilized cyclic response of the structure. The loading itself is a periodic type loading with amplitude to simulate the cyclic loading condition which is also the case when the CT specimen is experimentally tested. The periodic loading function follows the amplitude in Figure 3.4.

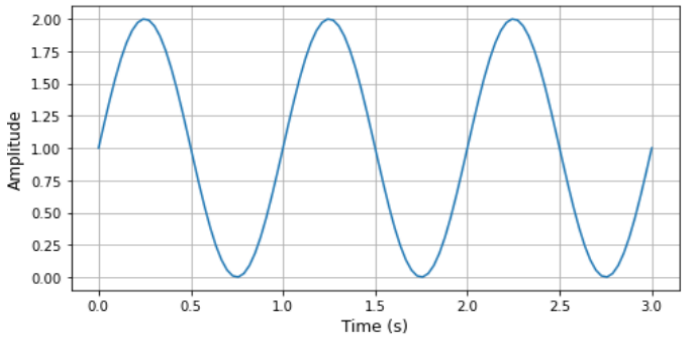

Figure 3.4: Periodic loading function

The initial load value is *1800N*, which increases to the value of *3600N* and drops to zero, leading to a stress ratio (*R*) equal to zero. The load is applied as a concentrated force at the CT-specimen perforation center points. Note that the reference points have been tied to the CT-specimen perforation lines in 2D and surfaces in 3D using kinematic coupling constraints as shown in Figure 3.5. In the 2D model, RP-1 and RP-2 have been tied to the shell edges in the upper and lower perforation, while in 3D the same reference points (RPs) are tied to the solid surface of the CT perforations. The coupling is made only to one-half of the holes as seen in the figure below.

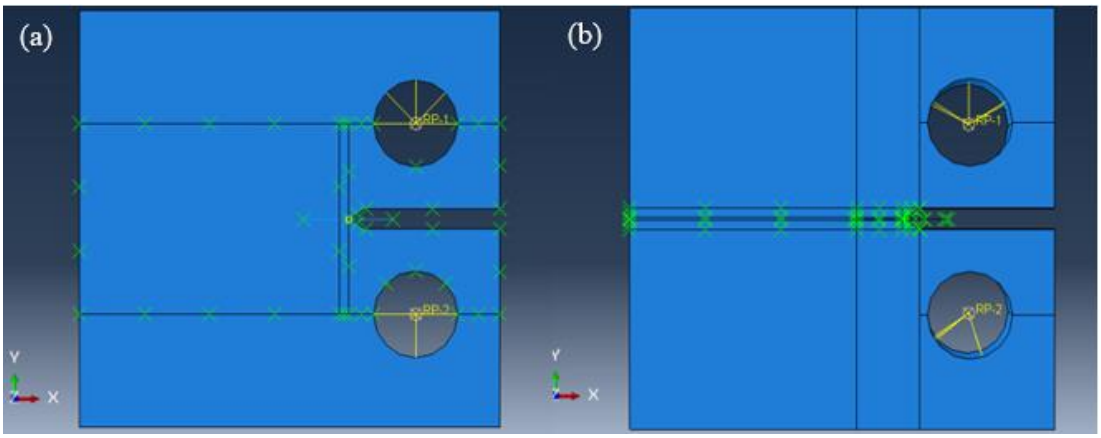

Figure 3.5: CT-specimen FE-model. (a) 2D FE-model. (b) 3D FE-model

3.2.5 Propagating crack using XFEM

To model the propagating crack in the CT specimen, the enriched feature has been used to model the discontinuity in the displacement field due to the crack propagation. In Figure 3.5 the enriched regions are shown with the initial predefined inserted crack in both 2D and 3D XFE-models. A user-defined subroutine is used to run the simulation in Abaqus®, the low cycle fatigue fracture criterion is used based on LEFM using VCCT. Paris law (2.8) is used in the subroutine with material parameters values taken same as in British Standard [34] which are also shown in Table 2.2, where $C = 5.21 \cdot 10^{-13}$ & $m = 3.0$. Moreover, the LEFM implementation of the stress intensity factors for the mixed fracture modes is carried out by considering both plane stress and plane strain conditions. This is done by using equations (2.5) and (2.6) for both 2D and 3D models. For more information about the LEFM implementation, the subroutine's Fortran code is attached in Appendix A . Note that for the 2D models K_{III} is equal to zero.

3.2.6 Finite element mesh

In the 2D XFE-model, two-element types are used depending on the situation considered (see Table 3.2). The used element types are plane stress (CPS4) and plane strain (CPE4). These element types are used in two finite element models with the LEFM equations (2.5) and (2.6) respectively. The meshing is applied in two zones, a local and a global mesh. The local mesh size is 0.25 mm and is applied in the enriched region around the crack front, while the global mesh size is 1 mm, applied at the rest of the CT geometry as shown in Figure 3.6 (a).

In the 3D XFE-model, 8-node brick elements (C3D8) are used with full numerical integration. Furthermore, a local and a global mesh are applied using structured and swept mesh controls. The local mesh size is 0.25 mm as in the 2D model and the global mesh size is 1.5 mm as mentioned in Table 3.2. From Figure 3.5 (b), the local mesh is applied at the enriched region shown in Figure 3.6 (b). The areas above and below the enriched region have a 0.25 mm width and 1.5 mm height, the latter is the global element size. First, four elements with a 1.5 mm thickness are used through the thickness. Then, only one element is used through the thickness of the 3D CT model as indicated in Figure 3.6 (b). The one element through the thickness is applied to obtain a smooth crack front and have a converged XFE solution which gives reliable results.

Table 3.2: Finite element mesh details

Model	Mesh region	Element type	Mesh Size
2D-XFEM	Local enriched shell	4-node plane stress quadrilateral (CPS4)	0.25 mm
2D-XFEM	Global non-enriched shell	4-node plane stress quadrilateral (CPS4)	1.00 mm
2D-XFEM	Local enriched shell	4-node plane strain quadrilateral (CPE4)	0.25 mm
2D-XFEM	Global non-enriched shell	4-node plane strain quadrilateral (CPE4)	1.00 mm
3D-XFEM	Local enriched solid	8-node linear brick (C3D8)	0.25 mm
3D-XFEM	Global non-enriched solid	8-node linear brick (C3D8)	1.50 mm

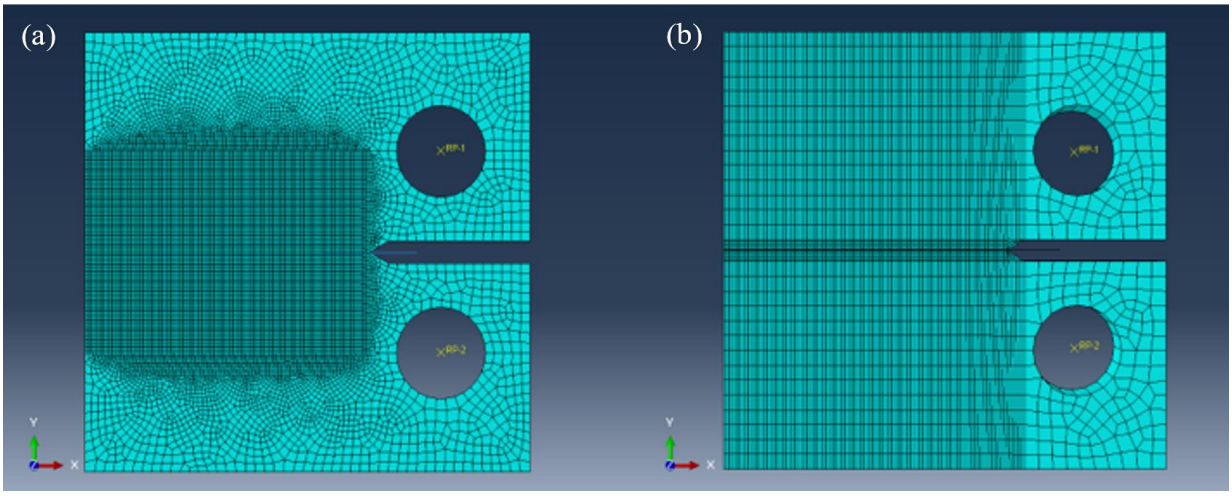

Figure 3.6: Finite element mesh. (a) 2D-model meshing. (b) 3D-model meshing.

3.3 Results and discussion

In this section, the output of the CT-specimen XFE models will be presented for both 2D and 3D models, which details have been explained in previous sections of this chapter. The output is then post-processed and results are shown and discussed.

3.3.1 2D-XFEM output

From the XFEA the provided output in the figures below has been requested in Abaqus®. To show the status of the extended finite elements (STATUSXFEM) and the crack openings. Below in Figure 3.7, a 3D-view of the deformed shapes of the CT model under cyclic tensile loading has been provided for three different crack lengths at three different numbers of cycles. The crack lengths are 5 mm, 11 mm, and 30 mm from the CT-specimen notch tip, and the corresponding number of cycles is *0*, *30226*, and *38803* cycles, respectively. These output values belong to the single-loaded XFE model with a 4-node plane strain element type and zero stress ratio ($R = 0$).

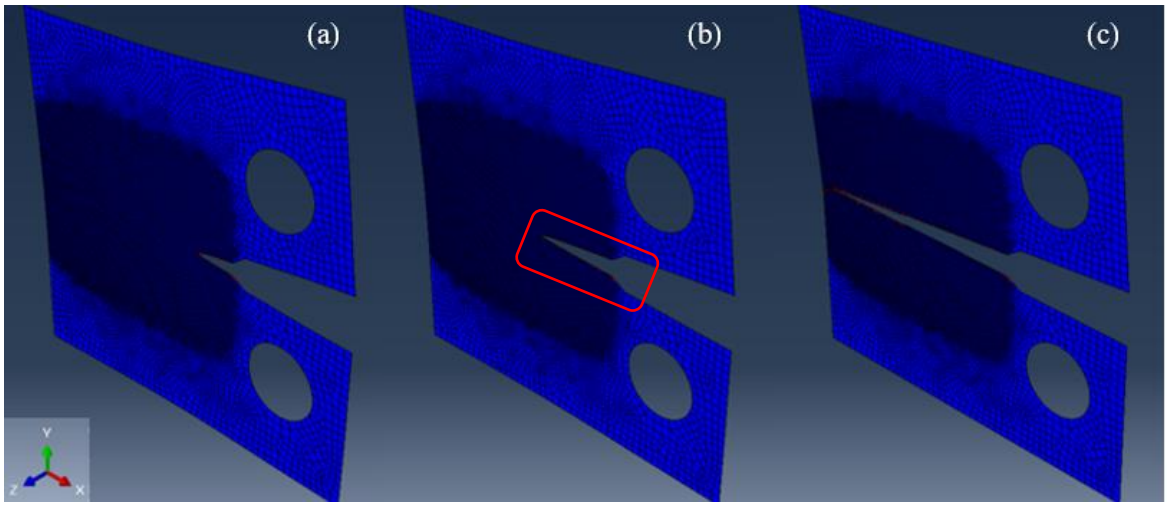

Figure 3.7: 2D-XFE model output (STATUSXFEM). (a) Deformed model at initial flaw length (5 mm). (b) Deformed shape at crack length 11 mm. (c) Deformed shape at final crack length (30 mm)

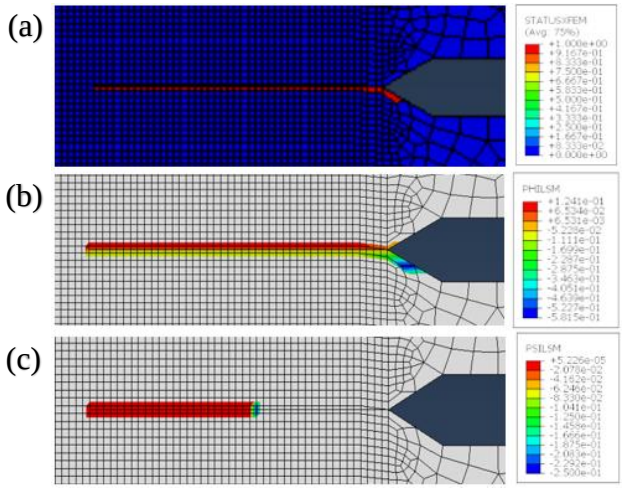

Figure 3.8: 2D-XFEM (undeformed) model output. (a) STATUSXFEM. (b) Level set value phi (PHILSM). (c) Level set value psi (PSILSM).

3.3.2 3D-XFEM output

Same as the 2D-XFEM output the 3D-XFEM model output is requested. The output of the 3D CT models where more elements are used through the thickness has been shown in Figure 3.9. The output shown in the following figures belong to the single-loaded CT model using the plane strain condition with zero stress ratio ($R = 0$). The remaining models with the assumptions mentioned before in 3.2.3 and 3.2.5 gave normatively the same output, although the results of each case are quantitively different in terms of fatigue life and crack shape.

In Figure 3.9 (a) and f (a), the deformed shape of the CT model is shown in the case of the initial predefined crack size (*5 mm*), where the corresponding number of cycles is still zero. Further, in Figure 3.9 (b) and f (b), the maximum crack size reached by the numerical simulation in Abaqus® has been shown. The crack length is equal to an average of *10.5 mm* and the number of cycles corresponding to this crack size is *139211 cycles* as shown in Figure 3.10 (b).

An important observation is that in Figure 3.10 the crack grows irregularly and unsymmetrically as it can be observed that the crack is longer at one side of the CT than on the other side. Finally, the number of cycles calculated numerically is much larger than the analytically calculated fatigue life.

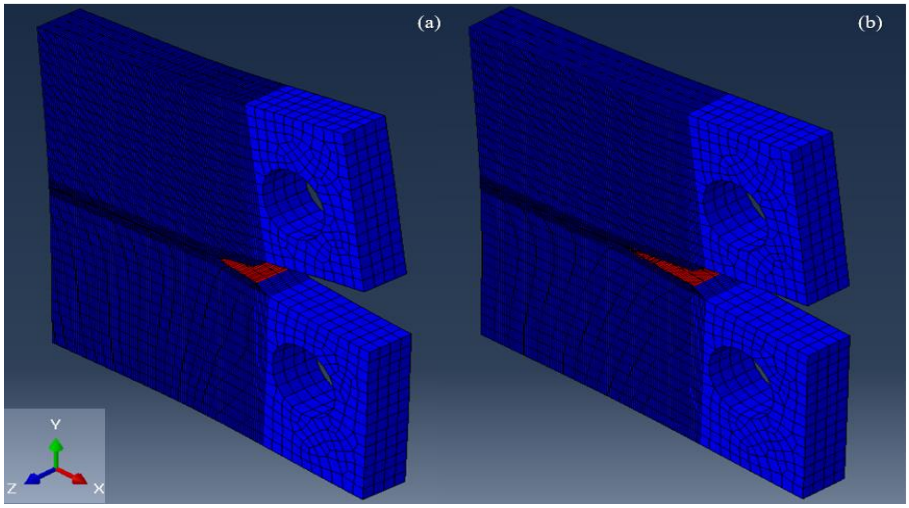

Figure 3.9: 3D XFE models with more elements through-thickness output (STATUSXFEM). (a) The deformed shape at initial crack length (5 mm). (b) The deformed shape at maximum crack length reached (11.75 mm)

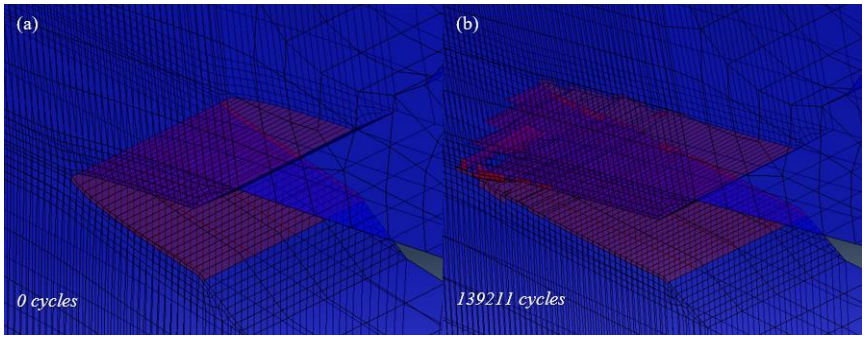

Figure 3.10: Close up propagating crack using more elements through-thickness at different crack lengths

The 3D-views of the model deformed shapes using only one element through the thickness are indicated in Figure 3.11. Note that the measurements following are for single loaded plane strain CT XFE model with

zero stress ratio ($R = 0$). It should be noted that for the 3D-models' simulations only 8-node brick elements are used and the equivalent SIF range is calculated based on both plane strain and plane stress assumptions. However, this should not be confused with that for the 2D models, plane strain and plane stress finite elements as well as plane strain and stress assumptions for calculating the ΔK_{eq} are used. For plane stain and stress constitutive assumptions, M1 and M2 are noted, respectively.

The deformed shapes correspond to different crack sizes. Figure 3.11 (a) shows the deformed shape after only the predefined flaw (*5 mm*) at a zero-corresponding number of cycles. In Figure 3.11 (b) the crack length measured from the CT notch tip is equal to *11 mm* with a corresponding number of cycles of *29435 cycles.* Finally, Figure 3.11 (c) shows the deformed shape of the final crack increment. In this phase, the crack size reached the end of the specimen model which is *30 mm* and the number of cycles corresponding to this crack size is *38363 cycles.*

The three crack stages are shown again in Figure 3.12, with their corresponding number of cycles at each crack length. The zoomed-in figures also show that there is only one element used through the CT thickness. From the figure, it can be deduced that the crack growth shape here is close to the real situation.

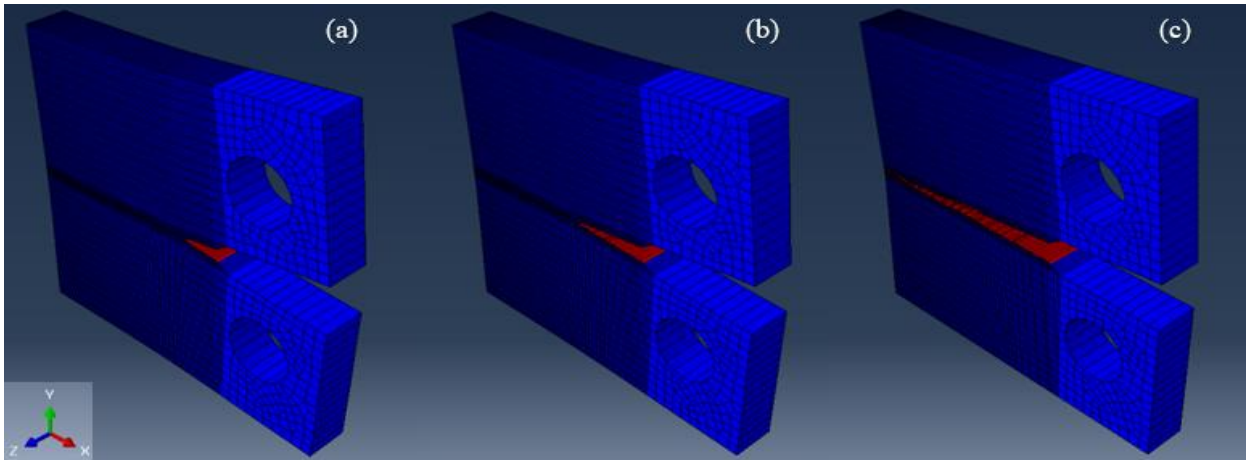

Figure 3.11: 3D XFE model with one element through-thickness output (STATUSXFEM). (a) Deformed model at initial crack length (5 mm). (b) Deformed shape at crack length 11 mm. (c) Deformed shape at final crack length (30 mm)

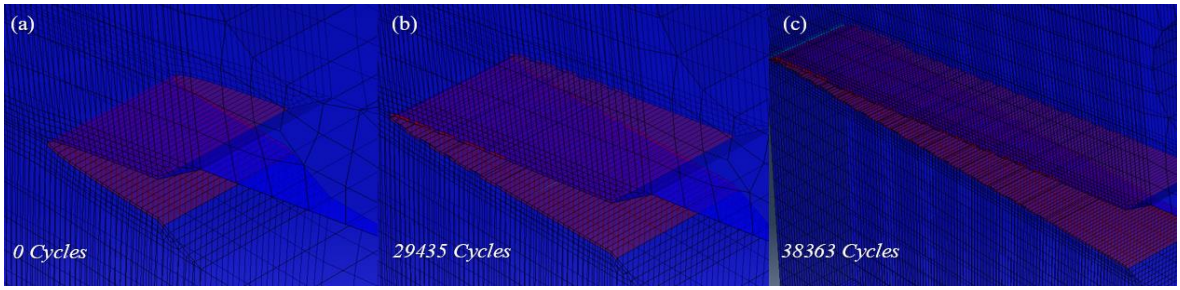

Figure 3.12: Close up on the propagating crack using one element through-thickness at different crack lengths

In Figure 3.13 some output data are presented for the 3D-XFEM model. The shown sub-figures correspond all to the CT when the crack size measured from the notch tip is equal to *11 mm*. The maximum principal stresses around the crack tip are shown in Figure 3.13 (a) showing the local plastic zone at the crack tip. The strain energy release rate (G) corresponding to a crack size *11 mm* is also shown in Figure 3.13 (b). In Figure 3.13 (c) and (d) the numerical result of the implementation of the level set functions phi and psi are shown, respectively

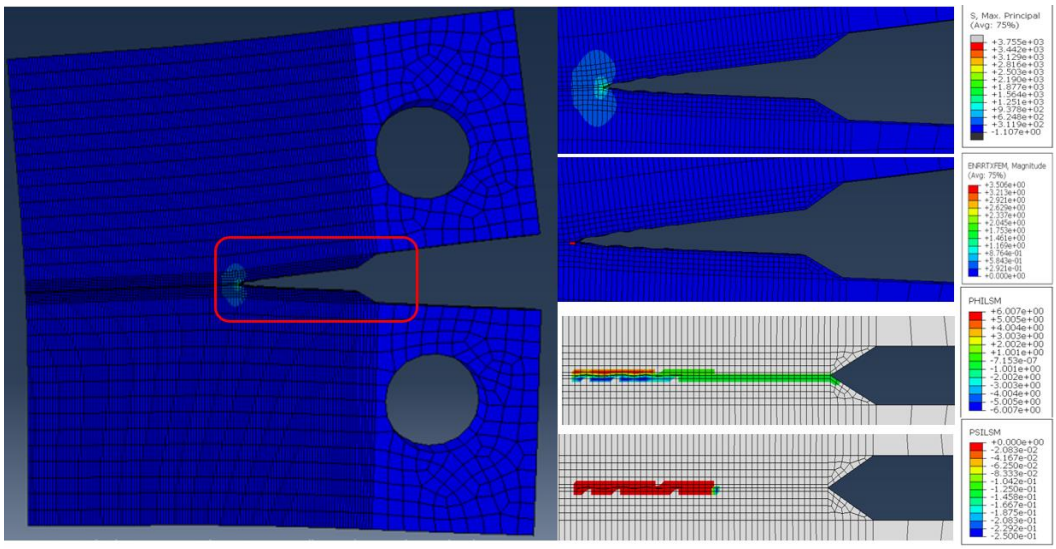

Figure 3.13: 3D-XFE model output at 11 mm crack. (a) Max. principal stress. (b) Strain energy release rate (G). (c) Level set value phi (PHILSM). (d) Level set value psi (PSILSM)

3.3.3 Validation of the numerical analysis using XFEM

The results are plotted for the 2D and 3D-XFE models. Both the single-loaded and double-loaded XFE models' results are presented in this section. The analytical results for the crack size versus the analytically calculated number of cycles for the CT using equations (2.8) and (3.1) are taken as a reference. In addition, the analytically calculated stress intensity factor range and crack growth rate are considered. The number of cycles calculated represented the fatigue life until the final fracture. A python code is scripted for the analytical fatigue life calculation and crack growth rate. The code is shown in Appendix A. Note that in the equation (3.1), $\alpha = \frac{a}{W}$. Moreover, equation (2.8) does not consider the mean stress effect. Hence, it considers a stress ratio equal to zero, thus the load ratio effect is not considered in this case.

$$\Delta K = \frac{\Delta P}{B\sqrt{W}} \frac{(2+\alpha)}{(1-\alpha)^{\frac{3}{2}}} (0.886 + 4.64\alpha - 13.32\alpha^2 + 14.72\alpha^3 - 5.6\alpha^4) \tag{3.1}$$

Analytical and numerical fatigue life

First, the 3D-XFE model using multiple elements through the thickness is considered, by plotting its fatigue life on the horizontal axis along with the corresponding crack length. This is then compared with the fatigue life calculated analytically by plotting both on the same graph as indicated in Figure 3.14.

In Figure 3.14 it is clear that the numerically calculated fatigue life does not converge with the reference at all. Note that for other CT models considering double-loading a similar crack growth behaviour is found. Considering the information given in 3.3.2 on the output of the considered models and after analyzing Figure 3.14, one can conclude that when considering multiple elements through the thickness in a crack propagation analysis using automated crack propagation in the FEM software, the fatigue life calculated by the software may not be accurate and cannot be depended on as a tool or a method to calculate fatigue life.

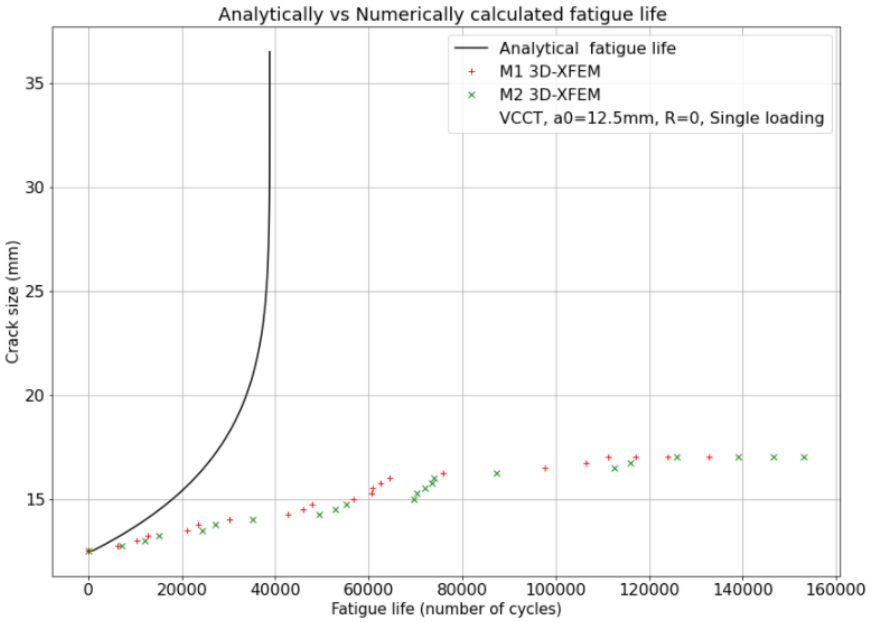

Figure 3.14: Analytically vs Numerically calculated fatigue life (Multiple elements through-thickness)

When using XFEM based on LEFM using VCCT to run an automated crack model, the software will make the crack start to grow when the relative energy release rate exceeds the threshold value, ΔG_{th}. From 2.6.3 and Figure 2.20 it is known how XFEA calculates the fatigue life of a propagating fatigue crack. Hence, when the number of elements through the thickness increases at the crack tip front the software will have to calculate ΔN_j more times because more elements have to be fractured. Thus, the total number of load cycles for a certain crack length will increase according to the following equation.

$$N_j = \min(\Delta N_{j-1} + \Delta Nj) \tag{3.2}$$

In figures Figure 3.15 and Figure 3.16 the fatigue life calculated from the analytical formulas is taken as the reference for 2D-and 3D-XFE models calibration using single and double tensile loading conditions. Figure 3.15 (a) shows the 2D-and 3D-XFE models' results for a single loaded CT as shown in Figure 3.3 (a) and (c), while Figure 3.15 (b) indicates the 2D-and 3D-XFE models' results for the double-loaded CT case which is shown in Figure 3.3 (b) and (d) for the 2D-and 3D-XFE models, respectively. Note that all the 2D and 3D numerical results have been plotted for both plane stress and plane strain situations.

Moreover, the output results are also post-processed to study the fatigue life based on the XFE modeling space (2D or 3D) as presented in Figure 3.16. All the 2D-XFE models' results in the case of single and double loaded CT have been plotted together in Figure 3.16 (a) for both plane stress and plane strain situations. Additionally, the 3D-XFE models' results are presented in Figure 3.16 (b) for the same two loading and boundary conditions mentioned before. Besides, the same two constitutive assumptions (plane strain and plane stress) are considered.

(a)

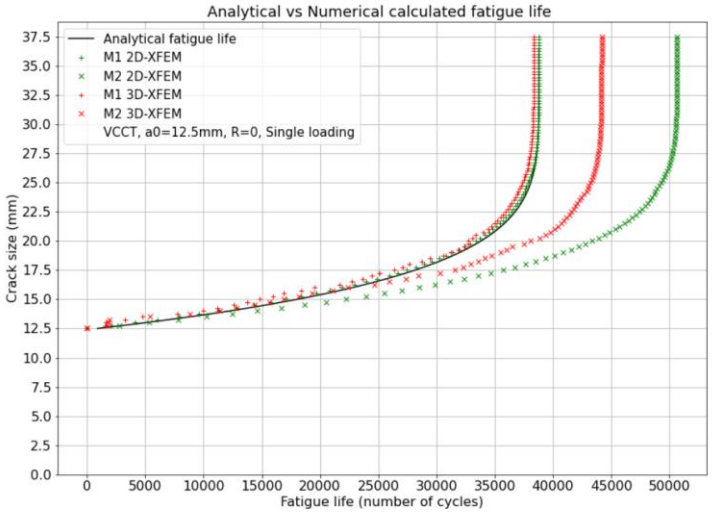

b)

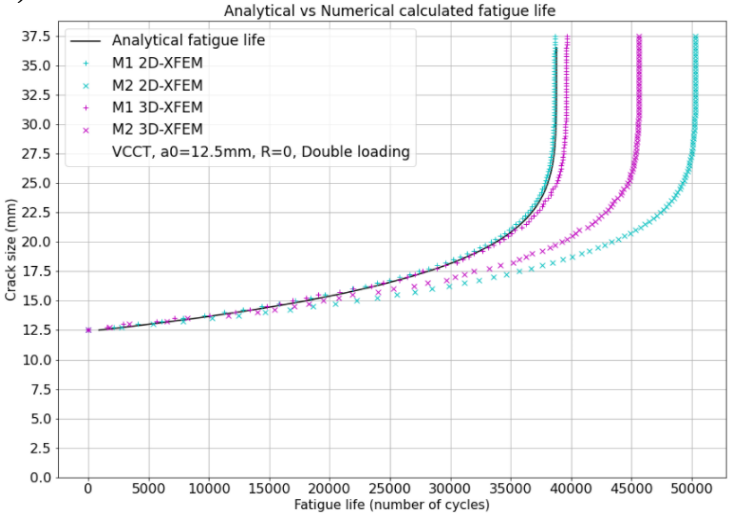

Figure 3.15 Analytically vs Numerically calculated fatigue life. (a) Single loaded XFE-model. (b) Double loaded XFE-model.

In Table 3.3 and Table 3.4 shown below, the number of cycles needed for the CT specimen to be completely cracked has been calculated and indicated. The difference percentage with the analytical (reference) solution has been also shown in the tables. The two tables are provided to give an elaboration for the above-shown figures. From Figure 3.15 (a) and Table 3.3, one can see that in the case of single loading the plane stress consideration in both 2D and 3D CT models gives a much larger estimate for the fatigue life. Not to be overlooked, that there is a difference in fatigue life between the 2D and 3D plane stress consideration.

In Figure 3.15 (b) and Table 3.4, the case of double loading shows almost similar results as in the case of the single loading. The plane stress constitutive assumption still shows higher fatigue life for the CT than that for the plane strain one. Similar to the single loading case, there is also a difference in fatigue life between the 2D and 3D plane stress constitutive hypotheses. However, the difference here differs less than in the case of single loading.

(a)

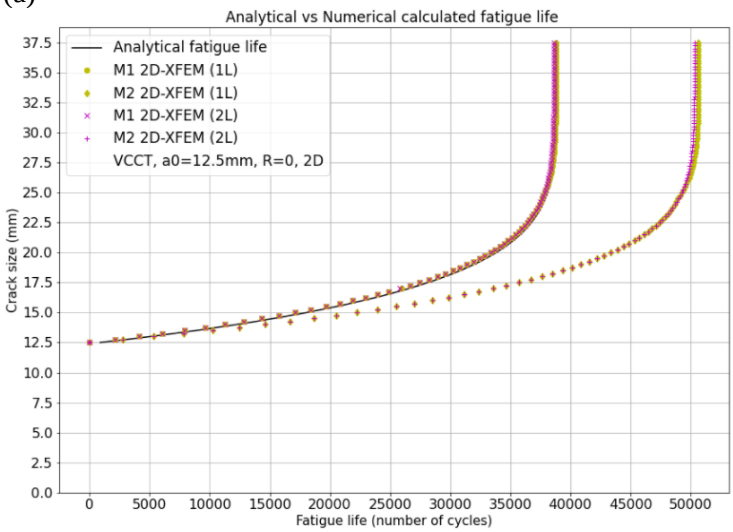

b)

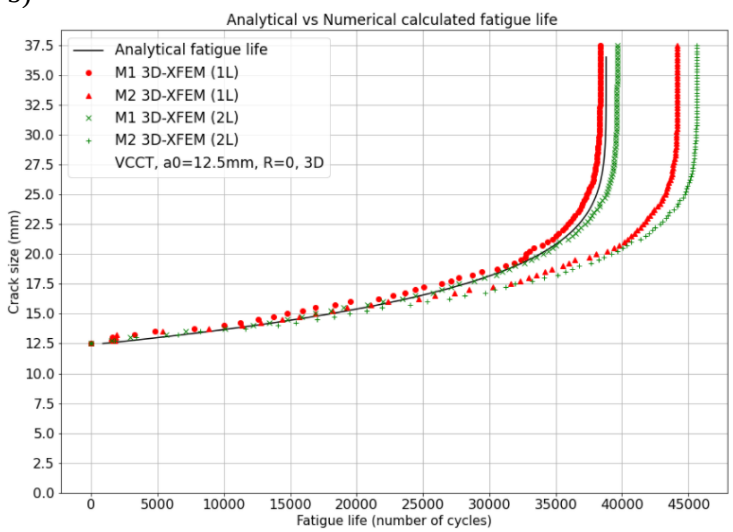

Figure 3.16: Analytical vs Numerically calculated fatigue life. (a) 2D-XFE model. (b) 3D-XFE model.

Furthermore, considering Figure 3.16 (a), (b), and Table 3.3, Table 3.4. In 2D analysis, the fatigue life resulting from both single and double loading cases are almost identical. However, in the case of 3D analysis, there are some small differences between single and double loading cases due to the 3D models DOFs definition. An important finding is that all the plane strain analyses (M1) for 2D and 3D have resulted in a similar number of cycles in comparison with the analytically calculated fatigue life till complete fracture. Nevertheless, all plane strain analyses except for the 3D single loading case slightly overestimate the fatigue resistance of the CT, while for the plane stress situation, all the analyses highly overestimate the fatigue resistance. The overestimation of the fatigue resistance makes predictions on the unsafe side in practical design applications.

Table 3.3: Difference between the analytical and numerical calculated fatigue in case of single loading

Single Loading				
Analytical calculation	2D-M1	2D-M2	3D-M1	3D-M2
38425 cycles	38803 cycles	50651 cycles	38363 cycles	44181 cycles
ΔN %	0.98 % ↑	31.82% ↑	0.99% ↓	13.03% ↑

Table 3.4: Difference between the analytical and numerical calculated fatigue in case of double loading

Double Loading				
Analytical calculation	2D-M1	2D-M2	3D-M1	3D-M2
38425 cycles	38643 cycles	50325 cycles	39637 cycles	45655 cycles
ΔN %	0.58 % ↑	30.97% ↑	3.15% ↑	18.82% ↑

The difference in fatigue life between the 2D and 3D plane stress assumptions (M2) in both single-and double-loaded CT models reflects the nature of 3D solid elements (C3D8) in numerical modeling. Though only one element is used through the thickness, the fatigue life differs from the one calculated using 2D plane stress elements (CPS4). This is attributed to the 3D solid element characteristics in explicitly including the through-thickness mechanical behaviour. As a result of this, the 3D solid elements in-plane stress analysis tends more towards the plane strain condition. This shows that due to the thickness the through-thickness straining will be less leading to higher stresses at the crack tip. Hence, a faster propagating crack takes place as shown in Figure 3.15 (a) and (b).

To elaborate more on the last paragraph, when a Mode I crack plate is loaded in uniaxial tension, the material adjacent to the crack tip which is highly stressed is constrained by the less stressed surrounding material which induces stresses in the thickness direction at the vicinity of the crack tip (see Figure 3.17). This phenomenon is referred to in fracture mechanics as plane strain. This must not be confused with the theory of elasticity definition of plane strain. Due to the practical determination of fracture toughness K_c from test results, this practical definition of plane strain is brought out, as it is found that for metallic materials there is an inverse relation between K_c and the thickness [35].

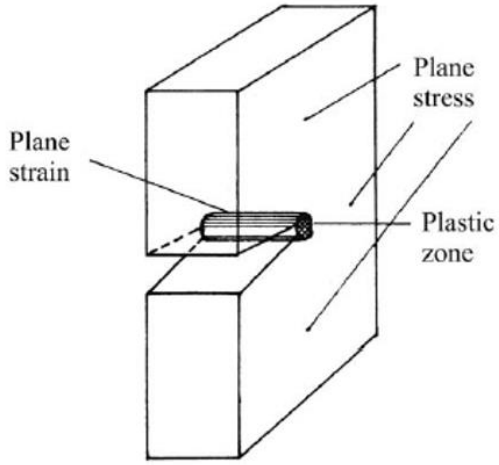

Figure 3.17: Plane strain and plastic zone in a tension specimen [36]

The limited local plasticity adjacent to the crack tip due to local material yielding will not influence the material in the interior of the plate if it is a thick plate. For instance, when considering a very thin plate, the local plastic zone at the crack tip will become very close to the plate thickness. The highly stressed area is less constrained and the material yielding will occur on *45°* planes. As a result, the stresses through the thickness will be relaxed leading to that the whole plate is in a plane stress state. Hence, in the simulations, the plane strain assumption came better along with the analytical calculation. In reality, the behaviour lies a bit between plane stress and plane strain, depending more on the plate thickness.

Analytical and numerical crack growth rate

In the figures shown below, the fatigue crack growth rate has been plotted for all considered CT-model cases versus the analytically calculated crack growth rate, which is considered as the reference crack growth rate. A log-log scale is used to plot the crack growth rate on the vertical axis with the stress intensity factor range on the horizontal axis. First, the output data is post-processed for the 2D CT models using a Python script to automatically measure the strain energy release rate at the crack tip accompanying each crack increment in the CT. After that, the stress intensity factor range is calculated using equations (2.5) and (2.6) for plane stress and strain situations, respectively, taking into account that $K_{III} = 0$ due to the 2D modelling space property. This is plotted in Figure 3.18 andFigure 3.19. Note that for all the plots, an extra plot is provided, only to highlight the region of interest which is the stable crack growth stage.

(a)

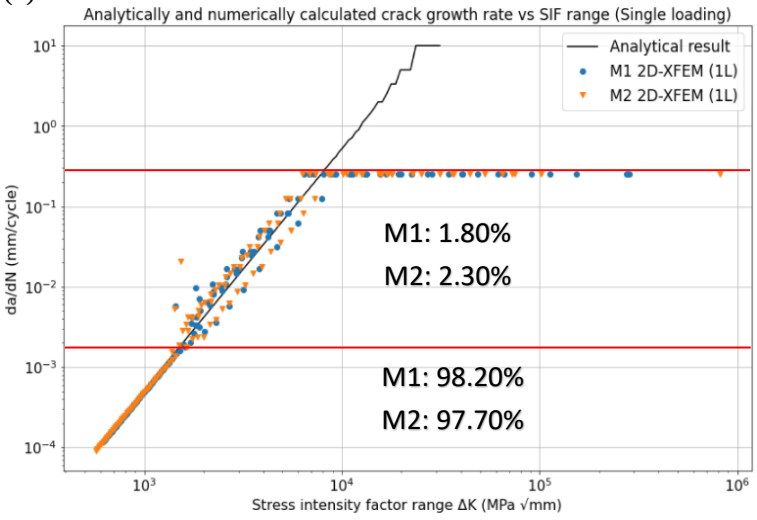

(b)

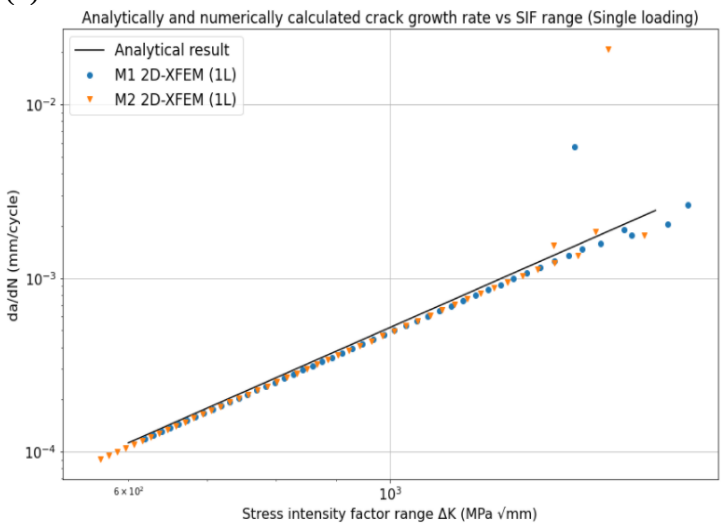

Figure 3.18: Crack growth rate vs SIF range for 2D single-loaded XFE model

(a)

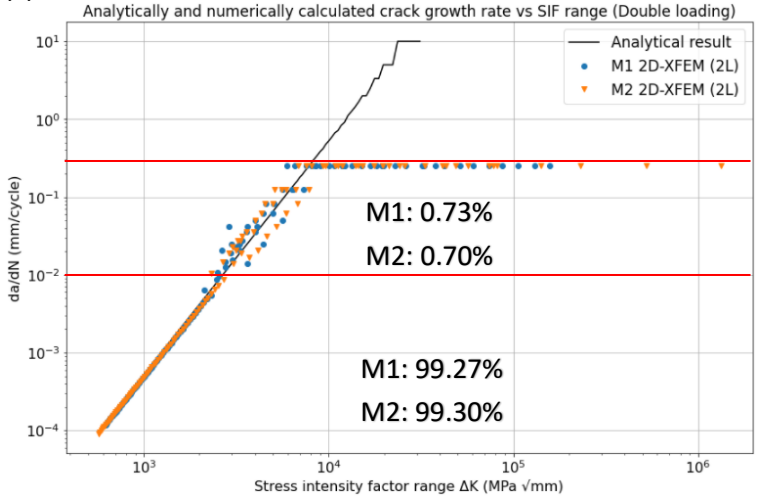

b)

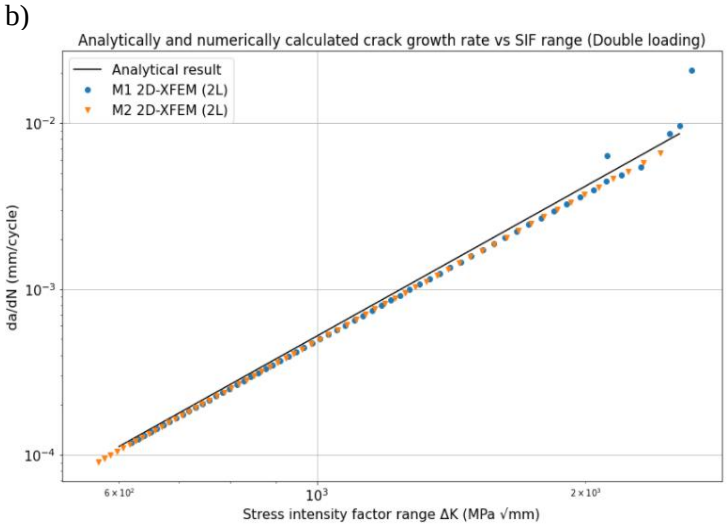

Figure 3.19: Crack growth rate vs SIF range for 2D double-loaded XFE model

As for the 3D CT models, the strain energy release rate is measured manually. Due to the complexity of the stress state in the through-thickness direction, automatically measuring the strain energy release rate is not

possible. Similar to the 2D models the stress intensity factor range is calculated using equations (2.5) and (2.6) for plane stress and strain, respectively. This is plotted in Figure 3.20 and Figure 3.21.

From Figure 3.18 and Figure 3.19, it is shown that crack growth includes two phases. The first phase is the stable crack growth stage (Paris regime) and the second one is the unstable crack growth rate. In the stable crack growth region, the crack growth rate follows the Paris law (2.8). After that, the crack growth enters an unstable region where the stress intensity factors at the crack tip approach the fracture toughness of the material. In the figures, the stable crack growth part is presented explicitly in the second plot of each figure. As can be seen from the figures, the stable stage occupies almost the whole fatigue life of the CT in all cases with a percentage of 98.20%, 97.70%, 99.27%, and 99.30%, for single-loaded plane strain, plane stress, and double-loaded plane strain, plane stress, respectively.

(a)

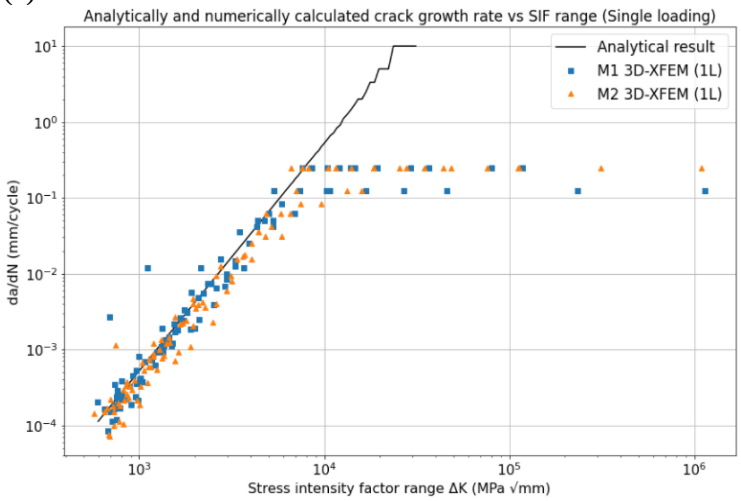

b)

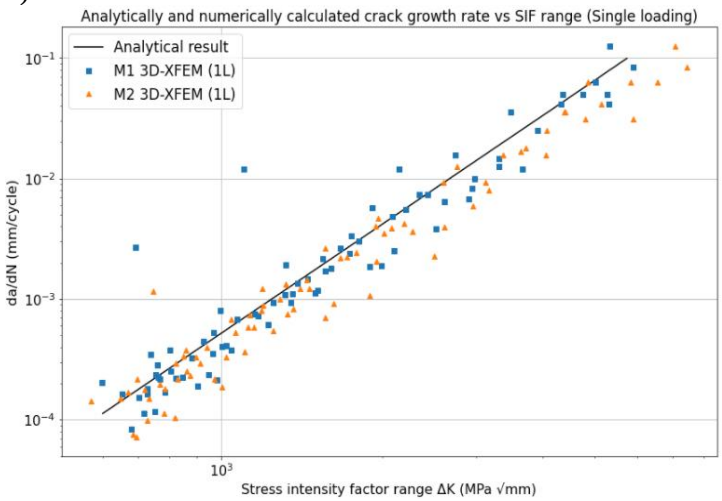

Figure 3.20: Crack growth rate vs SIF range for 3D single-loaded XFE model

(a)

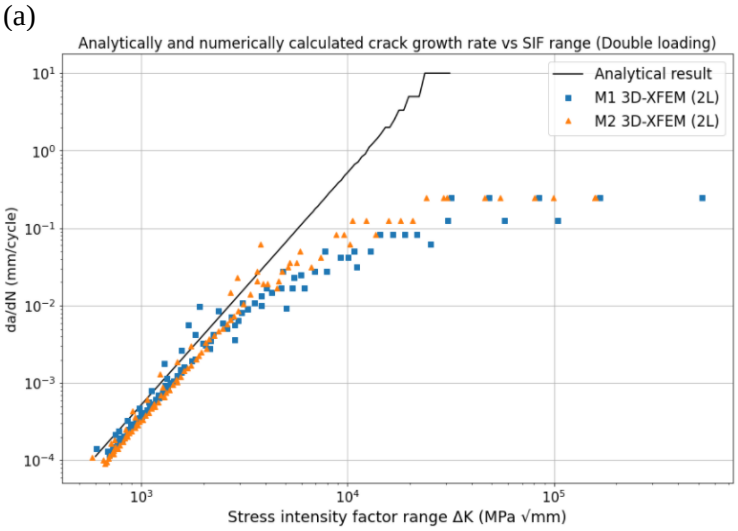

b)

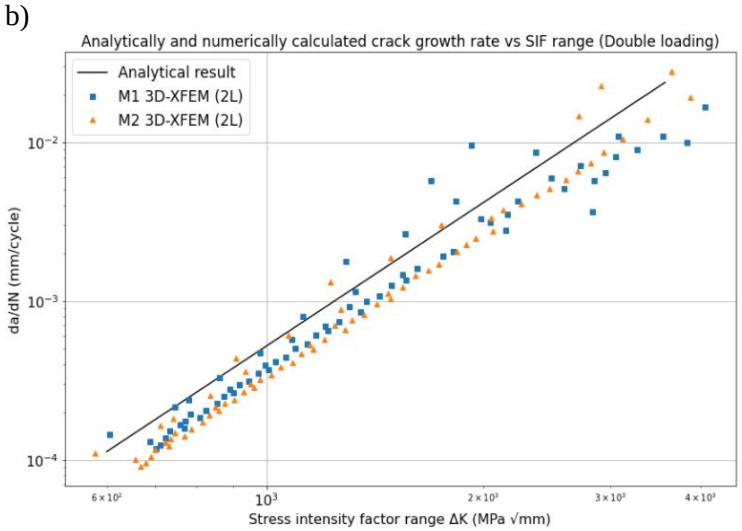

Figure 3.21: Crack growth rate vs SIF range for 3D double-loaded XFE model

In the unstable crack growth region, there are fluctuations in the measures as can be seen from the plots. This stage is not included in LEFM as the corresponding area, shows plastic behaviour in reality. In the stable region, the total crack length after each increment is relatively short and the plasticity in the CT is present in the local area at the vicinity of the crack tip. This is described by the stress intensity factor, while the rest of the CT material is behaving elastically. Hence, LEFM simulates the fatigue crack growth behaviour accurately in this region. In reality, when the crack length reaches a critical length at which the crack length is large and the remaining surrounding material is small, the remaining material part around the crack tip area then behaves plastically.

Moreover, in Figure 3.20 and Figure 3.21, almost all measured points after each crack increment from the 3D CT models show fluctuations in their crack growth rate. As mentioned before this can be due to the manual measuring of each point after each crack increment due to some load cycles. Besides, the complex stress state when using 3D 8-node solid brick elements compared to 2D elements.

Last but not least, a common behaviour in all the plots in all plots for both 2D and 3D analysis, is that at the end of fatigue life the crack growth rate reaches a constant value. Nonetheless, the stress intensity range rapidly increases. This somehow can relate to real situations where the plasticity of the material leads to very high-stress peaks at the crack tip, while the number of cycles at each increment becomes very small and the crack length increment size is constant.

3.4 Conclusion

In the CT chapter, the fatigue life and crack growth behaviour of the CT were studied. An analytical study was analysed first and is considered to be a reference for the study. After that, numerical simulations were carried out using finite element software Abaqus®. The models considered are in 2D and 3D modeling space using 2D plane strain/stress and 3D solid brick elements. Furthermore, two loading cases were considered to simulate the CT test loading conditions. Single and double-loaded CT at the reference points in the CT perforations were considered for CT loading cases. The simulations were conducted using a 0.25 mm mesh at the enriched zone and a 2 mm mesh in the rest of the CT model. For the 3D models' simulations, first, more elements were used through the thickness. After that, this was reduced to only one element through the CT thickness. Based on the FE simulations results and the comparison with the analytical solution the following conclusions are found;

- When applying 3D calculation for CT specimens, multi-element in the thickness may cause an overestimation of the fatigue life because the elements break one by one, and the corresponding fatigue life is accumulated. This is different from the 3D fatigue crack propagation observed in the experiments where crack front advances following the corresponding loading cycles. For different points at the crack front, the propagation distance depends on the driven force of the point.

- Plane strain assumption is suitable in the transition of the material properties in Pars' law from stress intensity factor-based law to strain energy release rate law as this is reflected by the accurate fatigue life calculation.

- The 2D and 3D CT simulations considering the plane strain condition in the case of single loading showed the most realistic fatigue life. The 2D simulation slightly overestimates the fatigue strength of the CT, while the 3D model underestimates it, which means that the 3D model provides a safe fatigue life estimation when taking the analytically calculated one as a reference.

- For all results, the crack growth rate in the stable region follows the Paris law. The stable crack growth is dominant in the fatigue life predictions carried out by analytical calculation and XFEM models using LEFM theory based on VCCT.

4 Crack Propagation In OSD

This chapter considers three validations and analysis aspects. First, the orthotropic steel deck (OSD) static finite element (FE) model is explained and validated for stress distribution using experimental data. After that, the proposed methodology is validated by analyzing the static FE and XFE model results. Then, the extended finite element method (XFEM) is used to make a propagating crack model and study the fatigue crack propagation. In addition to that, the strains will be carefully studied at different crack sizes. The results are then validated and discussed at the end of this chapter.

4.1 Introduction

The OSD geometry considered is the one used in experimental testing by Wu et al [37] in the Stevin II laboratory at Technical University Delft (TU Delft). The FE model is made to simulate the tested OSD specimen at Stevin II lab. The experimental work from the work done by Wu et al is compared to the FEM and XFEM modeling to study the fatigue crack [root crack (c) in Figure 2.4] propagation in the rib-to-deck plate at the connection with the cross-beam.

4.2 Methodology

To model the propagating fatigue crack in the detail of interest, FEA software Abaqus® is used. The OSD deck plate is loaded under cyclic compression due to vehicle wheel loads. This leads to a research point of the thesis, which is that how the fatigue crack initiates under cyclic compressive load as mentioned before in 1.3. In welded connections, it is believed that tensile welding residual stresses exist. However, residual stress modeling is not considered here and will not be taken into account in the numerical calculations. Alternatively, an engineering approach needs to be introduced and will be applied to enable modeling a propagating fatigue crack using automated XFEM because it does not support modeling a propagating crack under compressive load. The stress ranges in the studied detail will be tension to tension. This method will be validated first and will then be used to model the propagating crack in the OSD detail. It should be stressed here that the research focuses on the relationship between local structural integrity and crack sizes. Simulating the loading cycles is out of the scope of this thesis.

4.3 FE Model description

In this section, the FE models will be described in detail for the used modulus in the FE models. Variables in the modulus may keep constant or change with the studied cases.

4.3.1 Geometry

The FE model dimensions are the same as the experimentally tested OSD specimen. The tested OSD part consists of a 20 mm thick deck plate stiffened by eight trapezoidal longitudinal stiffeners, which are carried on three cross beams. As can be seen from Figure 4.1 (a), in four of the eight ribs “Haibach” cope holes are present at the cross-beam web connection, while the remaining four ribs are fully welded with the cross-beam. The thickness of the cross-beam webs is 16 mm and the lower flange thickness is 12 mm. Furthermore, the cross-beam lower flange width is 200 mm.

The trough dimensions themselves are as indicated in Figure 4.1 (b). The closed stiffener’s thickness is 6 mm and height is 350 mm. The trough width which is the distance between the trough webs is equal to 300 mm. In addition to that, the spacing between the ribs is 300 mm at the deck plate. Hence the center-to-

center distance of the closed stiffeners is 600 mm. Moreover, the spacing between the trough's webs at the lower flange is equal to 105 mm as shown in Figure 4.1 (b).

The welding details in this OSD segment are as follows. Butt welds are used to connect the deck plate to the rib web. In addition to that, fillet welds are used to connect the cross-beam to the deck plate as well as connecting the cross-beam to the rib webs. The weld has a 5 mm throat thickness.

The objective of this thesis is to study the crack growth at the local detail in the OSD and according to Wu et al [37] a local loading patch is applied as indicated by the red area in Figure 4.1, this leads to only a local deformation in the model with minimum or no effect on the rest of the global model. This will lead to a FE model simplification and reduction to a smaller FE model considering only the highlighted parts in Figure 4.1, which are explicitly shown in Figure 4.2. The simplified model is symmetric leading to a further reduction in the FE model size. This is pointed out in Figure 4.2 and explicitly indicated in Figure 4.3 where only half of the model in Figure 4.2 is considered. This model will be further used throughout this research for validation and crack propagation analysis using XFEM. In addition, this model will also be referred to further as the global model. The global model is divided into three parts as seen in Figure 4.4 where it consists of a global, local, and sub-local part. The last two parts are also referred to as sub 1 and 2.

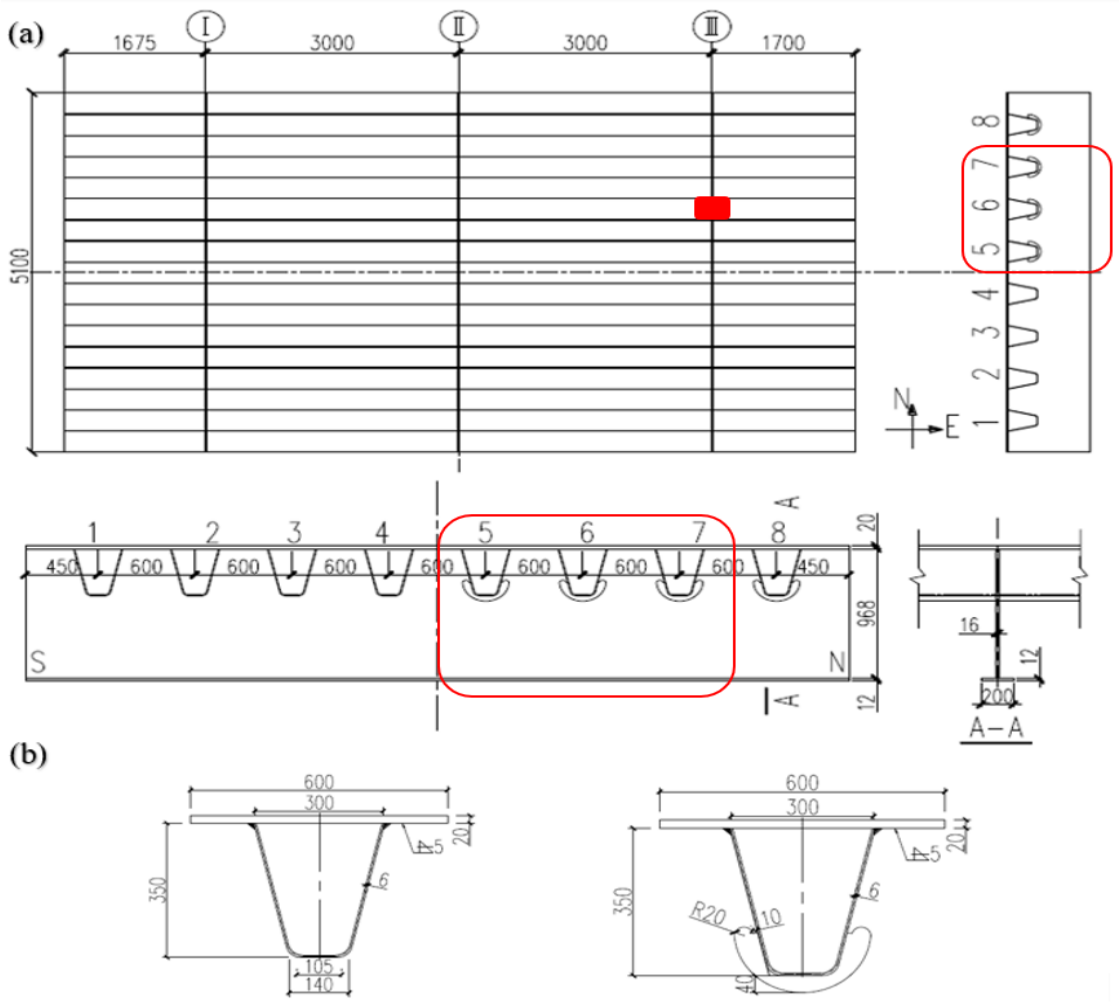

Figure 4.1: Experimentally tested OSD [37]. *(a) Full-scale OSD segment. (b) Longitudinal stiffener's details.*

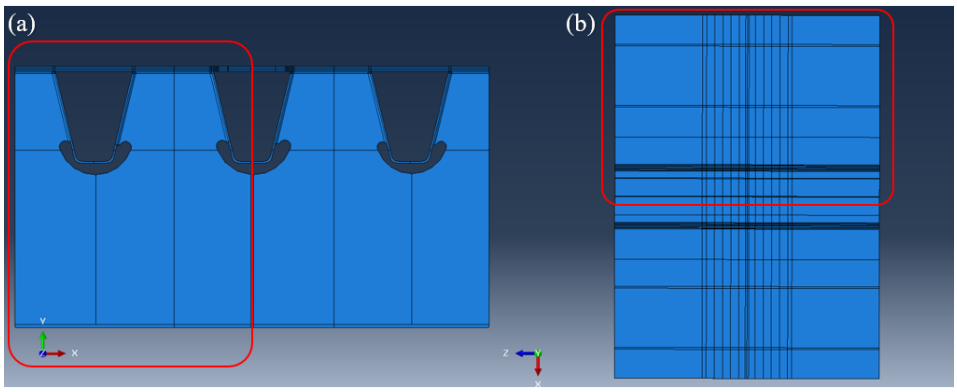

Figure 4.2: Reduced 3D FE model. (a) Side view (XY-plane). (b) Top view (XZ-plane).

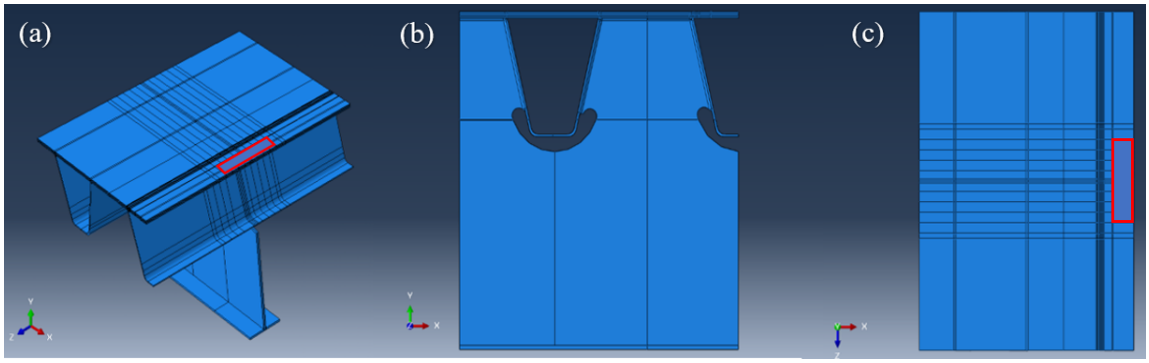

Figure 4.3: Final reduction of the 3D FE model. (a) 3D view (XYZ). (b) Side view (XY-plane). (c) Top view (XZ-plane).

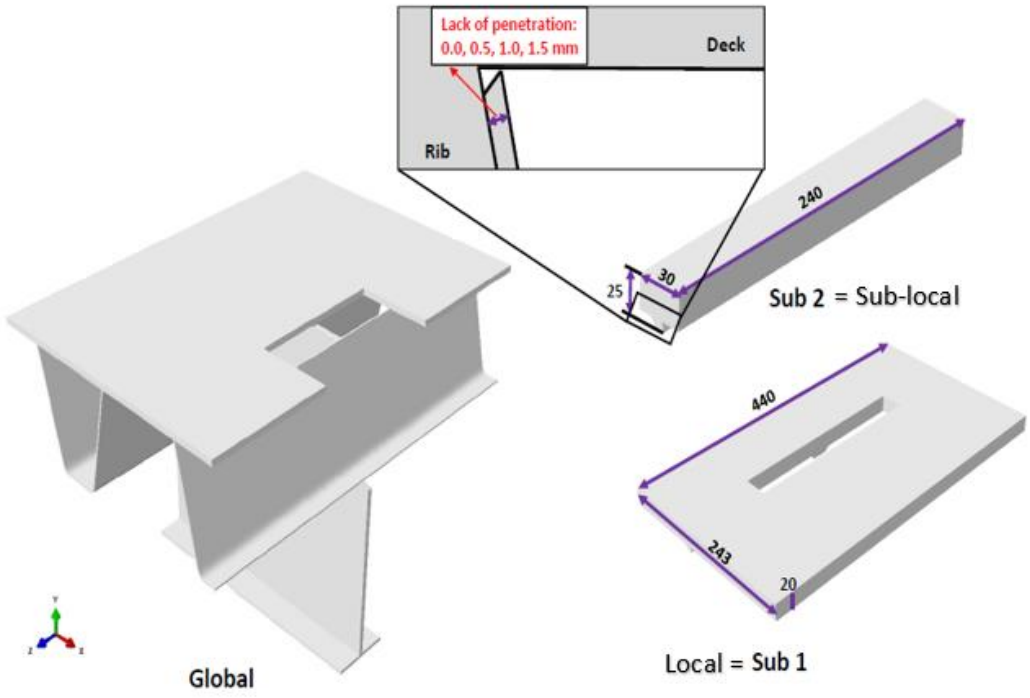

Figure 4.4: FE model sections

4.3.2 Material properties

The material used is steel and has the linear elastic property due to the same reasons explained in 3.2.2. The Young's modulus of elasticity and Poisson's ratio have the same values as given in Table 3.1.

4.3.3 Boundary conditions

The boundary conditions in the global model are applied such that the experiment is exactly simulated. Moreover, the symmetry conditions are applied because the total FE model is reduced to the global model (Figure 4.3). The boundary conditions applied are shown in Figure 4.5, where the translation in X-direction and the rotations around Y-and Z-axis are constrained for the outer longitudinal sides and the inner sides at the symmetry axis where the larger model is cut [Figure 4.5 (a)]. Additionally, the displacement in Z-direction, as well as the rotations around X-and Y-axis, are restrained for the front and back sides of the deck plate and closed ribs [see Figure 4.5 (b)]. Finally, the lower flange of the cross-beam is fully fixed in the FE model as shown in Figure 4.5 (c).

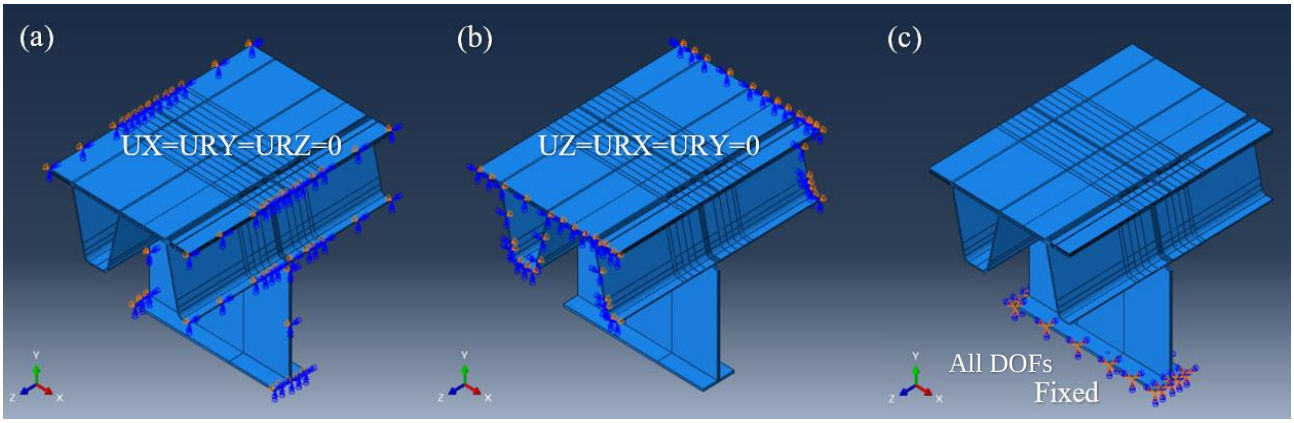

Figure 4.5: FE model boundary conditions. (a) Longitudinal & symmetry side. (b) Front & backside. (c) Crossbeam flange.

4.3.4 Applied load

The loading applied in the FE model has the same position as the experiment load and the loading patch has the same dimension as the steel deck plate contact area in the experiment. The loading area dimensions are 320 mm in Z-direction and 180 mm in the X-direction, which is reduced to 90 x 320 mm^2 in the symmetric FE model. The location of the load is on top of the deck plate, centered above the middle rib in Figure 4.2 (rib 6) at the connection with the cross beam [see Figure 4.3 (a) and (c)]. The loading resembles the local wheel load, although the contact area dimensions are smaller than the wheel dimensions from NEN-EN-1993-2 [14].

Static loading analysis

The load is applied as a pressure load on the before-mentioned surface. In the case of the static crack analysis, the load magnitude considered is similar to the experiment load magnitude since *72* kN in the model corresponding to *144* kN in the experiment for the full specimen. To compare the output values of the SIFs the load is considered as it is in the experiment without generalizing the load to the unit load.

Cyclic loading analysis

A cyclic tensile load other than the compressive load with a similar amplitude to the CT is applied on the aforementioned area using 72 kN so that a crack can propagate. This assumption will be further validated.

4.3.5 Stationary and propagating crack

In order to use XFEM to make a propagating crack model, the assumed approach should be validated first. This will be done by carrying out static analyses and after that, a propagating crack model is made using cyclic loading analyses. SIFs of the various crack shapes are calculated in both conventional finite element and extended finite element under compression and tension using the contour integral evaluation method.

Static loading analysis

The XFE models are validated by comparing their output with the FE models' output. In the XFE models, predefined cracks are inserted in the sub-local part with different inclination angles. Likewise, cracks are defined using FEM with a crack extension direction similar to the inserted cracks in the XFE models as can be seen from Figure 4.6, where a side view of the sub-local part is indicated. The crack is first inserted vertically [see Figure 4.6 (a)], then the crack is inserted inclined with angles 15°, 30°, 45° and 60° with the vertical axis (Y-axis) as indicated in Figure 4.6 (b), (c), (d) and (e), respectively.

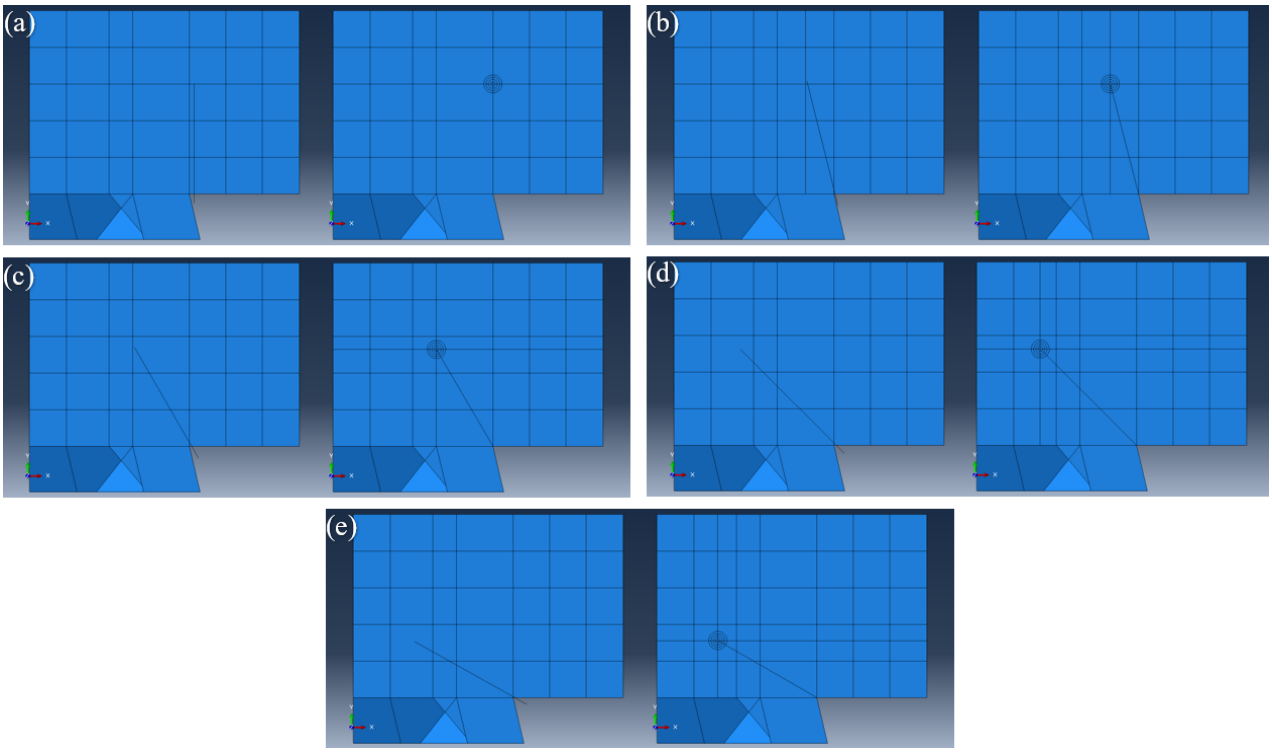

Figure 4.6: Crack definition in the sub-local part, Left XFEM, right FEM: (a) Vertical crack. (b) 15° crack. (c) 30° crack. (d) 45° crack. (e) 60° crack

Cyclic loading analysis

For the propagating crack analysis first, an initial model is considered with a large initial semi-elliptical crack. The crack angle with the vertical axis (Y-axis) is zero, meaning that a vertical crack is inserted. The initial flaw dimensions are $a_o = 5mm, c = 8.1\ mm\ and\ \frac{a_o}{c} = 0.62$ as shown in Figure 4.7. Note that the initial crack dimensions are taken ten times as large as the ones proposed by Maljaars et al [8].

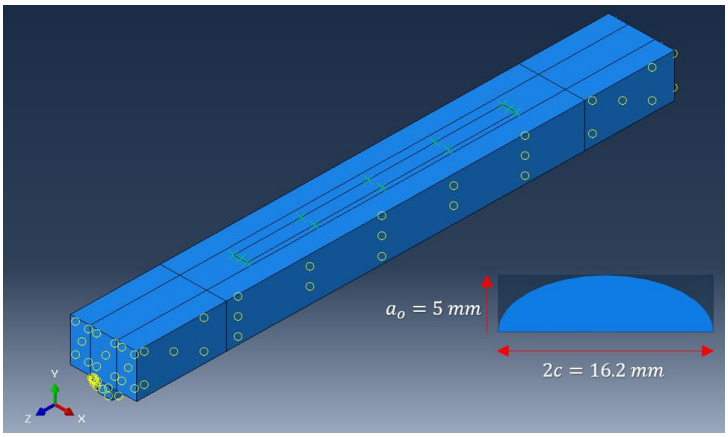

Figure 4.7: The enriched region for the propagating crack and initial crack dimensions (first model)

After that a second model has been made, this is a more accurate and more applicable model. This model is used further throughout this thesis to study fatigue crack propagation. Here a realistic initial flaw size is considered. The dimensions of this crack size are $a_o = c_o = 0.5\ mm$ as in Figure 4.8. In this model, the enriched element region is extended through the whole sub-local part as seen in the figure below. Thus, both the deck plate and part of the trapezoidal rib web are considered here for the crack propagation.

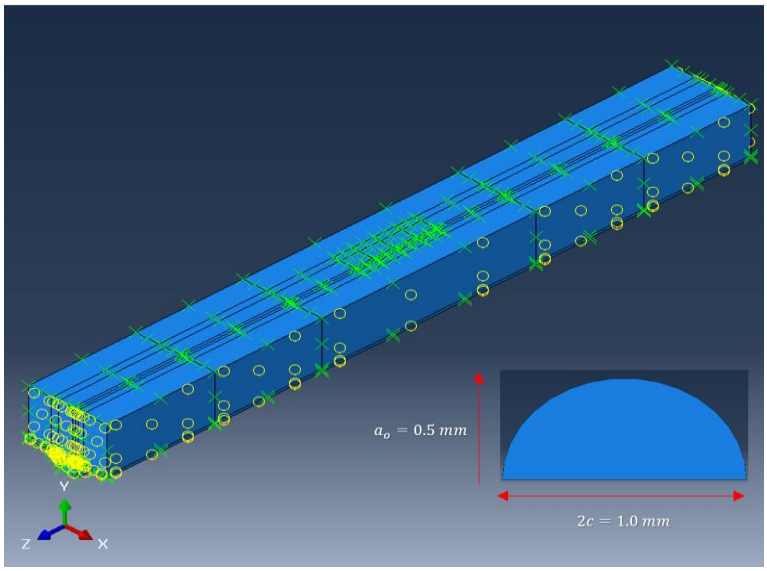

Figure 4.8: The enriched region for the propagating crack and initial crack dimensions (Improved model)

Similar to the CT propagating crack simulation (see 3.2.5) the low cycle fatigue based on the LEFM fracture criterion (using the VCCT method) is used to simulate the progressive crack growth in the OSD detail. Paris law is used with material parameters equal to the parameters used by Maljaars et al. [8] ($C = 1 \cdot 10^{-13}, m = 3.0$). This all is implemented in a user-defined sub-routine for the mixed crack mode behaviour. In this subroutine the threshold value for the stress intensity factor (K_{th}) is defined. Consequently, the crack will not propagate unless the equivalent stress intensity factor value exceeds the threshold value. The plane strain assumption is used for the improved cyclic loading model. Furthermore, the propagating crack direction is set normal to the direction of the maximum tangential stress (MTS).

4.3.6 Finite element mesh

The global model is divided into three parts, a global part where a global large mesh is applied, a local part where a relatively small mesh is used, and a sub-local part where a very fine mesh is applied [see Figure 4.9 (a), (b) and (c)]. To make local fine meshing possible in this model, the three parts are connected using tie constraints. Two refined local meshes are used at the location of the connection detail of this thesis (rib-to-deck plate at the cross-beam junction). This is done to calculate and accurately measure the high-stress peaks at the vicinity of the welded connections. As for the global mesh, it is applied at the rest of the OSD global model as seen in Figure 4.9.

Static loading analysis

The element size is *50 mm* for the global mesh [Figure 4.9 (a)]. Besides, a *2 mm* element size is used to mesh the local part as shown in Figure 4.9 (a) and (b). Moreover, an element size equal to *0.5 mm* is used for the sub-local part. This can be seen in the red highlighted area in Figure 4.9 (b). The element type used for these three meshes is an 8-node linear brick element with reduced numerical integration (C3D8R). Furthermore, the mentioned element sizes assigned to these three parts hold for the first static models used for initial stress state validation and stationary crack analysis. For more comprehension of the meshing used Table 4.1 gives a summary of all meshing strategies of the different models and analyses.

The improved static model's mesh is identical to that of the cyclic loading model for all three parts of the model. Hence, it will be completely described in the Cyclic loading analysis mesh description. Figure 4.11 as well as Table 4.1 show the different meshes for all parts.

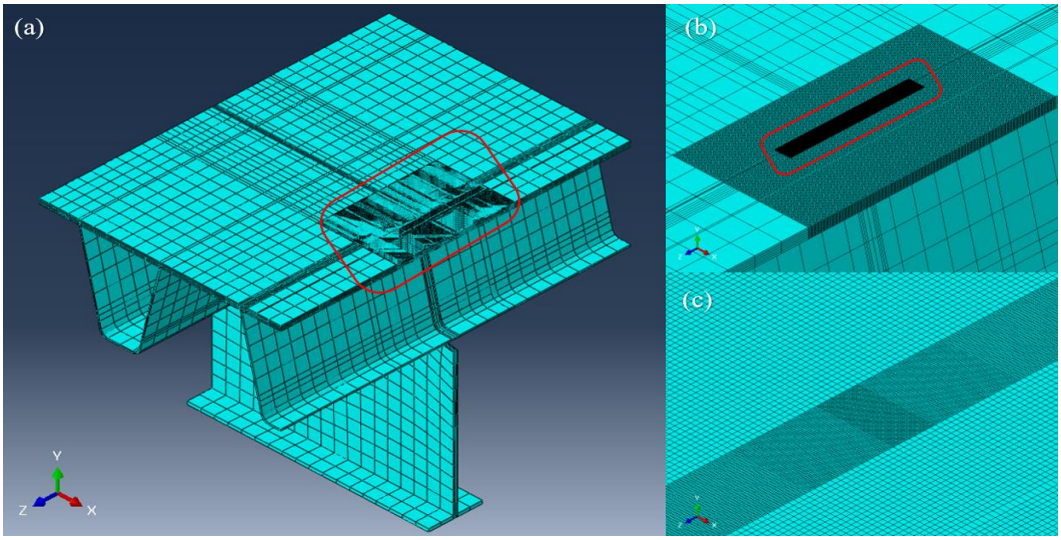

Figure 4.9: Finite element mesh. (a) Global and local mesh. (b) Local mesh zoomed 3D view. (c) Local mesh 2D view (YZ-plane)

In the stationary FE crack models, a very fine local mesh is assigned at the crack tip. The reason is to make a FE crack analysis possible and accurately calculate the stress intensity factors around the crack front. Therefore, a spiderweb shape mesh is created around the crack tip with wedge elements (C3D6) as shown in Figure 4.10 (a). A cylinder centered at the crack front with a *1 mm* radius is considered. The cylinder is partitioned into four cylinders, each with a *0.25 mm* thickness and C3D8R elements assigned, except for the inner one. While for the rest of the part C3D8R elements are assigned. For the XFE models, structured meshing is used with C3D8 elements [see Figure 4.10 (b)].

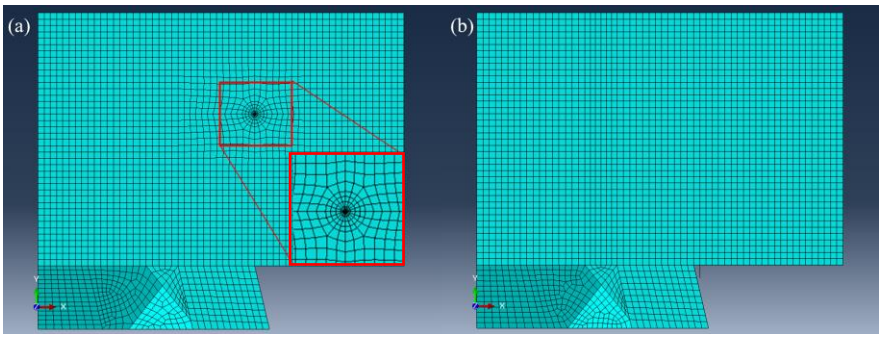

Figure 4.10: Sub-local part mesh. (a) Static FE model with a zoomed view of spider mesh. (b) Static XFE model

Cyclic loading analysis

In the beginning, a propagating crack model is made using a very fine mesh. This mesh is associated with the first model with its assigned enriched zone indicated in Figure 4.7. Both the local and sub-local parts are assigned a very fine mesh. The Local part mesh size is the same as that for the stationary crack model (*2 mm*). The sub-local mesh part mesh is different than that of the static analysis. The mesh size differs in the enriched zone. A *0.5 mm* element size with full numerical integration is used in the crack propagation zone. This element size is then increased around the enriched zone to reach a *2 mm* element size with reduced integration. All the elements have a *0.5 mm* thickness in the deck plate thickness direction.

The mesh used in this model gave good initial predictions for the crack propagation behaviour, but has a major drawback since the element size is very small. This led to a large FE model size and a much larger model output file which requires very high computational time and costs. The element sizes in the model are therefore increased to reduce the computational time as shown in Figure 4.8 for the improved models.

The mesh size is enlarged in both the local and sub-local parts. The element size in the local part is now set equal to *8 mm* and quadratic interpolation with reduced integration is used for these elements. As for the sub-local part meshing, the meshing strategy is implemented as shown in Figure 4.11 below. The principle is to reduce the model size by making the mesh at the crack initiation zone sufficiently fine and increase the element size away from that zone to reduce the model size and increase the calculation speed. This is done by making the element size equal to *0.75 mm* at the crack initiation zone, and the mesh size then varies from *0.75 mm* to *4 mm* across different regions of the sub-local part as shown in Figure 3.11. It should be also mentioned that the mesh at part of the rib web at the detail of interest is refined by making the element size in the rib web length dimension smaller in the global part of the model. This is done so that the rib web part can capture sufficient bending deformation. Table 4.1 summarizes the different element sizes used for all considered FE models of the OSD.

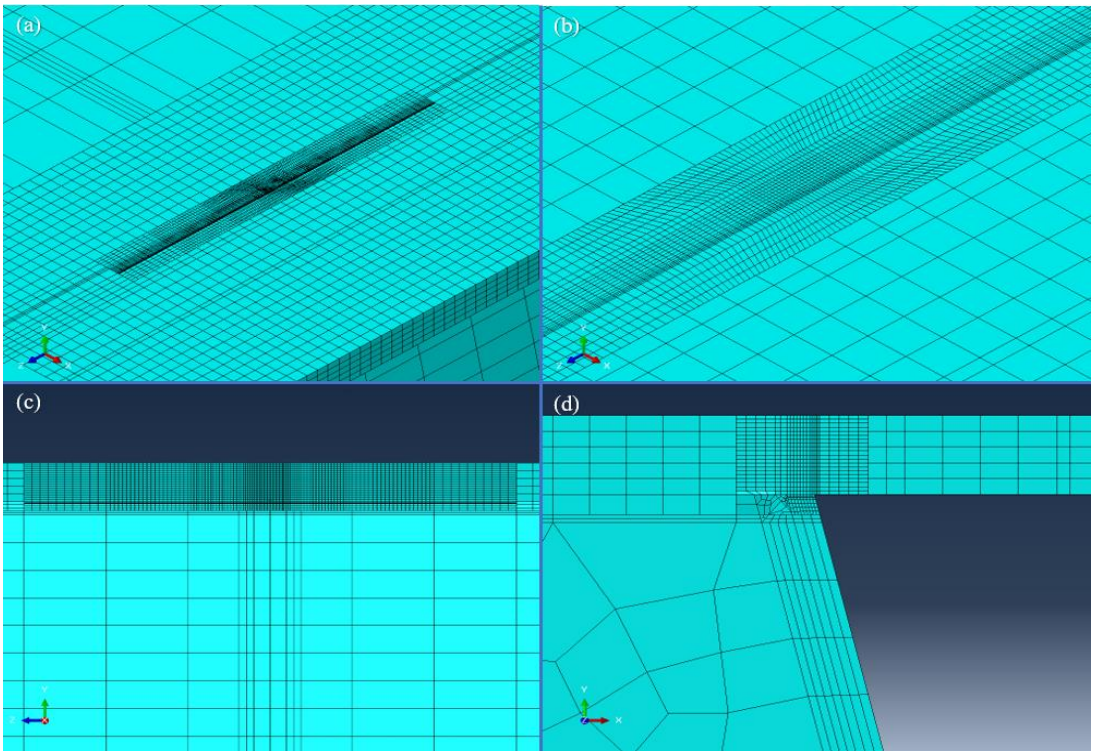

Figure 4.11: Improved finite element mesh of the sub-local model. (a) 3D view. (b) Zoomed 3D view. (c) YZ view. (d) XY view

Table 4.1: Finite element mesh details for OSD models' parts

	Global part		**Local part**		**Sub-local part**	
	Element size	Interpolation scheme	Element size	Interpolation scheme	Element size	Interpolation scheme
First static models (validation stationary crack analysis)	50 mm	Linear (C3D8R)	2 mm	Linear (C3D8R)	0.5 mm	Linear (C3D8R) (C3D8)
First cyclic loading model	50 mm	Linear (C3D8R)	2 mm	Linear (C3D8R)	0.5 mm to 2 mm	Linear (C3D8R) (C3D8)
Improved static and cyclic loading models	15 mm to 50 mm	Linear (C3D8R)	8 mm	Quadratic (C3D20R)	0.3 mm to 4 mm	Linear (C3D8R) (C3D8)

4.4 Results and discussion

Here the FEA and XFEA output and results of the 3D (X)FE models described in the previous section have been presented and explained. Based on these results the static and cyclic loading 3D FE/XFE models are validated by comparing the numerical results with the experimentally obtained results.

4.4.1 Static FE model validation

To validate the FE model in the before-mentioned section, the strains at the positions of the experimentally installed strain gauges were measured and are compared with the strains at the same positions in the FE model. The difference between both strains is then calculated and based on that difference percentage, the FE model is validated.

The strain gauges were installed at the positions shown in Figure 4.12. On both the north and south side strain gauges were installed on top of the deck plate in the longitudinal direction with a *25 mm* offset from the closed rib web center. The spacing between the gauges is *25 mm* as shown in Figure 4.12. Moreover, other strain gauges were installed in the transverse direction on top and at the bottom of the deck plate on the center plane of the cross beam as shown in the figure below. The top gauges have a *25 mm* spacing in between, starting at the rib web center. The bottom gauges started from the inward edge of the rib web with a spacing of *4mm*, *8mm*, and *8mm* between the three gauges as in Figure 4.12.

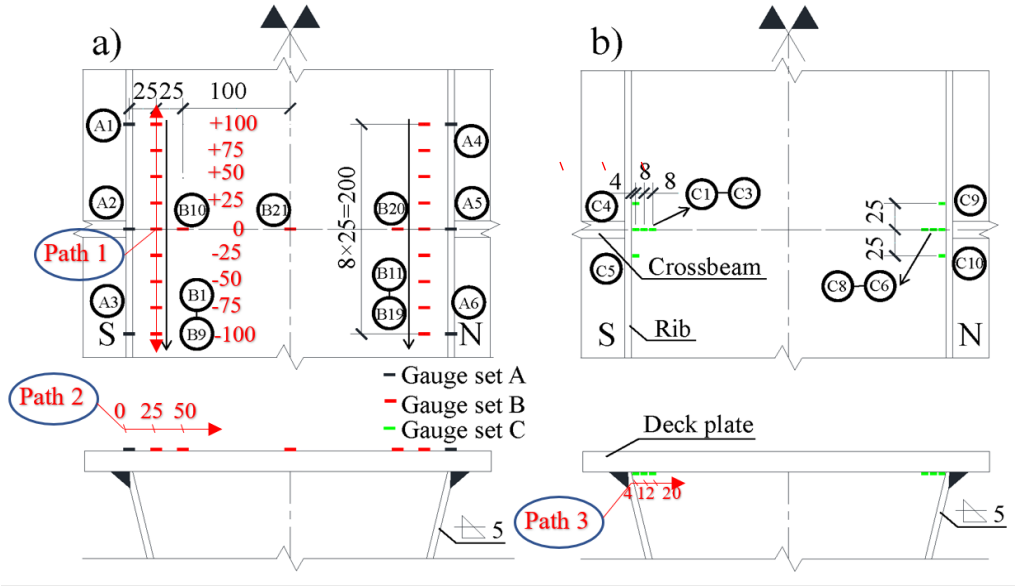

Figure 4.12: Strain gauge arrangement [37].

In the FE model, three paths are considered at the same locations of the strain gauges. Path 1 is in the longitudinal direction with a *25mm* offset from the rib web center. This path corresponds to the strain gauges installed in the longitudinal direction of the OSD as seen in Figure 4.12. Paths 2 and 3 are in the transverse direction at the deck plate top and bottom, respectively. These two paths correspond to the strain gauges in the transverse direction which are shown in Figure 4.12. The FEA output data is then read and plotted using a continuous line as shown in Figure 4.13 where the strain ($\times 10^{-6}$) is plotted on the Y-axis and strain gauge location [mm] on the X-axis. In Figure 4.13 the experimentally measured strains for the north and south side of the closed ribs (2 and 7) in the longitudinal direction are measured at specific points (see Figure 4.12 for the points' locations).

From Figure 4.13 (a), the measured strains at the south side of rib 2 are not accurate since the scatter is large. This can be due to the movement of the strain gauges during testing or the gauges are not accurately installed before the experiment. The rest of the strains have good convergence with the FE solution. When the strains from the north and south side were averaged for both ribs 2 and 7 as presented in Figure 4.13 (b), there is high convergence between the experiment results of rib 7 and the FEA results. The average accuracy of the numerical solution when compared to the mean value of the experiment's strains for rib 7, is about 98%. The accuracy for the mean value of strains measured at rib 2 is lower due to the inaccurate test results of the south side.

(a)

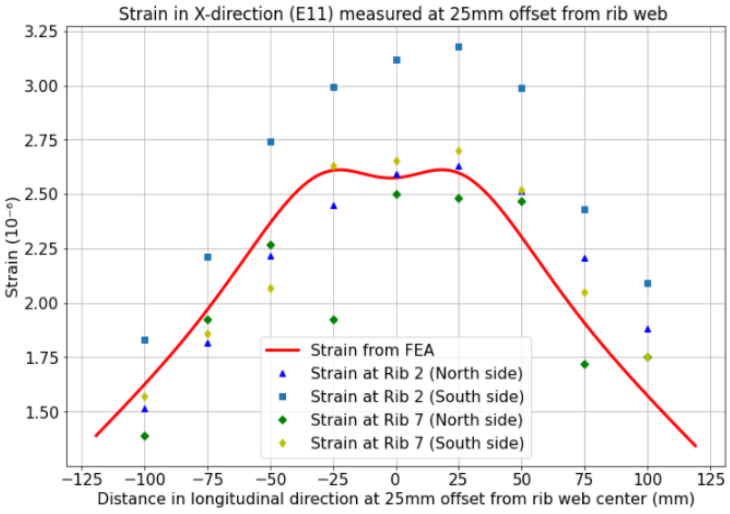

b)

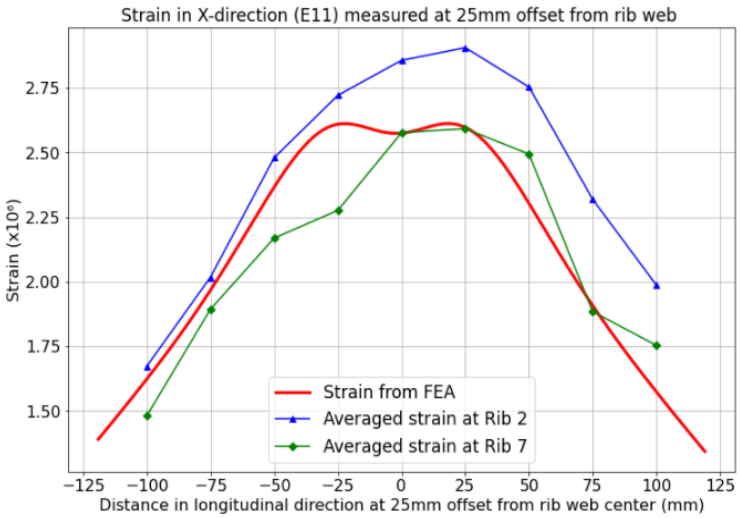

Figure 4.13: Strains in X-direction along a longitudinal path.
(a) Rib 2 & 7 (at N & S sides) measured strain vs FEA strains. (b) Averaged measured strains at rib 2 & 7 vs FEA strains

(a)

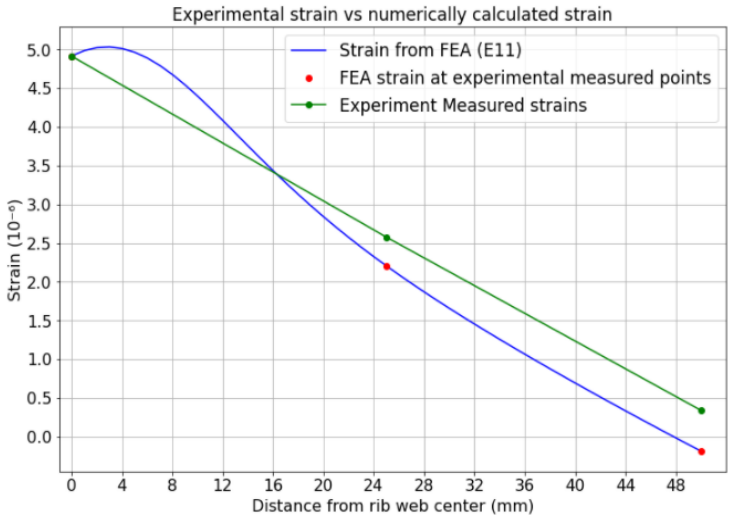

b)

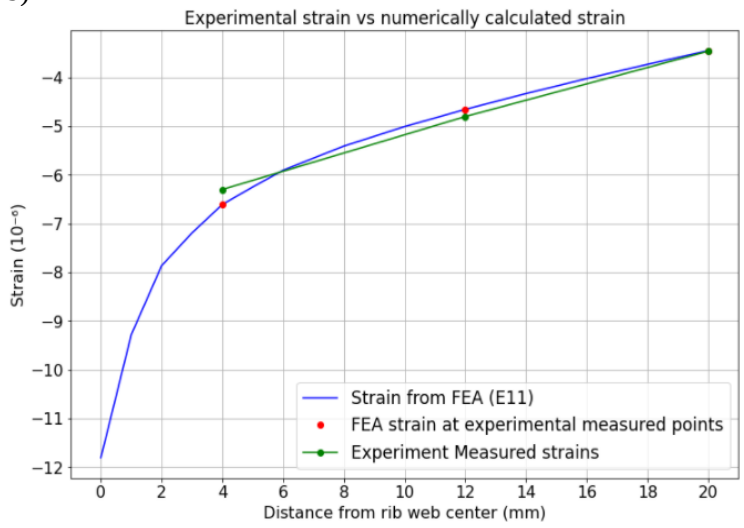

Figure 4.14: Strains in the X-direction along the transverse path. (a) Strain on deck plate top. (b) Strain at the deck plate bottom.

In the transverse direction of the OSD, the numerically calculated strains are plotted against the experimentally measured ones in Figure 4.14 for the top and bottom of the deck plate of the OSD. In Figure 4.14 (a) there is good convergence between the numerical calculated data and the experimentally measured ones. Moreover, close results are also obtained in the transverse direction at the bottom of the deck plate in

Figure 4.14 (b). The average differences between the numerically calculated results and the results measured during the experiment are 11% and 2% for Figure 4.14 (a) & (b), respectively. This all proves that the strains from the FEA are now valid as they strongly converge with the experimentally measured strains. Thus, the stress distribution is validated.

4.4.2 Stationary crack models' output

In Figure 4.15 the deformed shapes of the sub-local parts displacements (when loaded in tension and compression) in both FEA and XFEA are shown. The resultant displacements in the analyses are very alike. However, the compression case shows an identical absolute value of the displacement for the FE model, and no crack opening is seen due to the compressive load. The stationary crack is present where the crack seam and the inserted crack in the XFEM model are defined. This can also be seen for the XFE model in Figure 4.16, where different views of the STATUSXFEM output are shown.

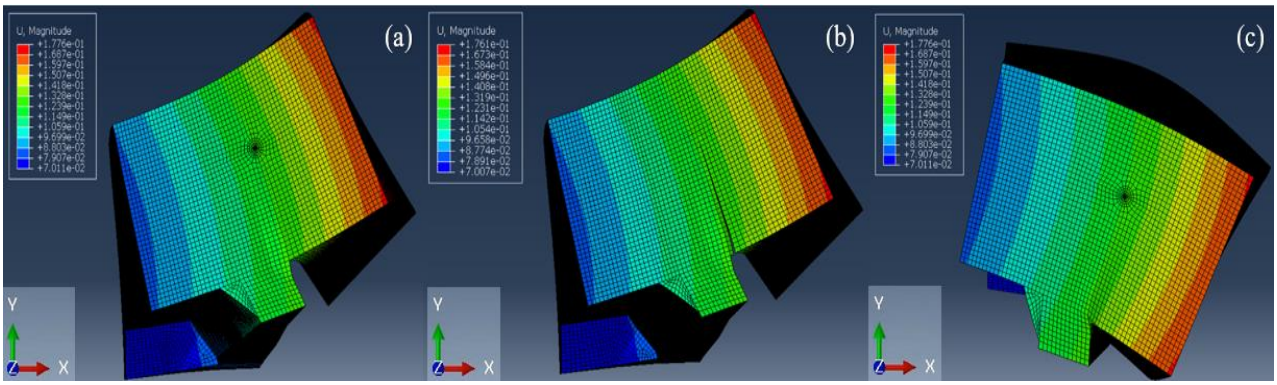

Figure 4.15:Deformed shapes of the sub-local part displacement. (a) FE model (Tension). (b) XFE model (Tension). (c) FE model (Compression).

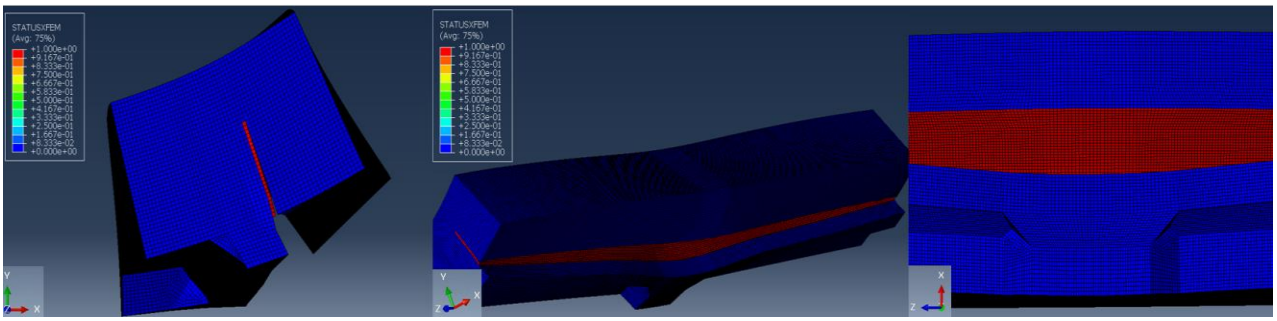

Figure 4.16: Various views of XFE model output (STATUSXFEM)

4.4.3 3D stationary crack model validation

The followed methodology is validated by first proving that the static XFE models' output is almost identical to the static FE models' one. This has been done by making a contour integral evaluation of the considered stationary cracks in tension and compression. Seven contours are evaluated around the crack front. Hence, the SIFs are calculated for seven contours at each node along the crack front. This has been done for all the inserted crack cases considered in 4.3.5 and Figure 4.6. To post-process this large amount of output data and be able to compare the results for the model validation, a Python code is scripted to plot the results for all cases in an optimized manner. Figure 8.4, Figure 8.5, and Figure 8.6 show the SIF values for all three fracture modes I, II, and III shown in Figure 2.7, respectively. The SIF values are first plotted for all seven contour integrals specified in the models' output request. However, some contour integral values have some deviations and gave unrepresentative results. Hence the most reliable contour integral

value is shown in the before-mentioned figures to obtain realistic and accurate results. The most accurate contour integral value is the last one and has been plotted and explicitly shown. The SIF values plots for all contour integral evaluations have been provided in Figure 8.4, Figure 8.5, and Figure 8.6 Appendix B.

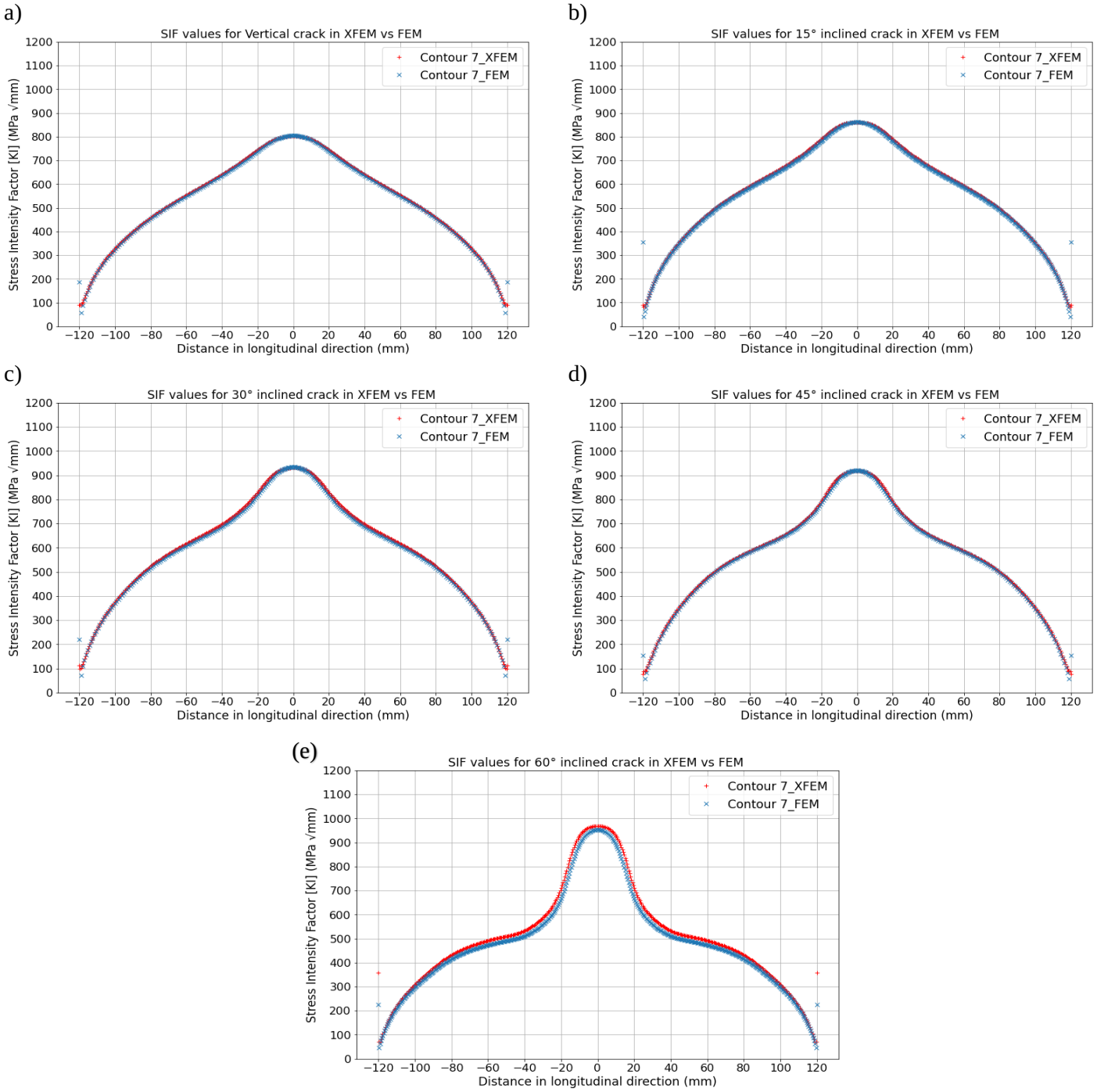

Figure 4.17: SIF values (K_I) for different crack inclinations considering only the last contour (XFEM vs FEM). (a) Vertical crack. (b) 15° crack. (c) 30° crack. (d) 45° crack. (e) 60° crack

Note that in the case of fracture modes II and III for the models with crack slope 30°, 45°, and 60°, the real SIF values for these models in the case of XFEM and FEM are the same but have opposite signs. This is

mostly due to the local coordinate system definition in the XFEM case, which differs from the local coordinate system definition in the case of the conventional FEM. Thus, for K_{II} and K_{III} the absolute values are plotted in Figure 4.18 and Figure 4.19. However, the SIF real values for modes II and III are plotted and given in Appendix B [Figure 8.7 & Figure 8.8].

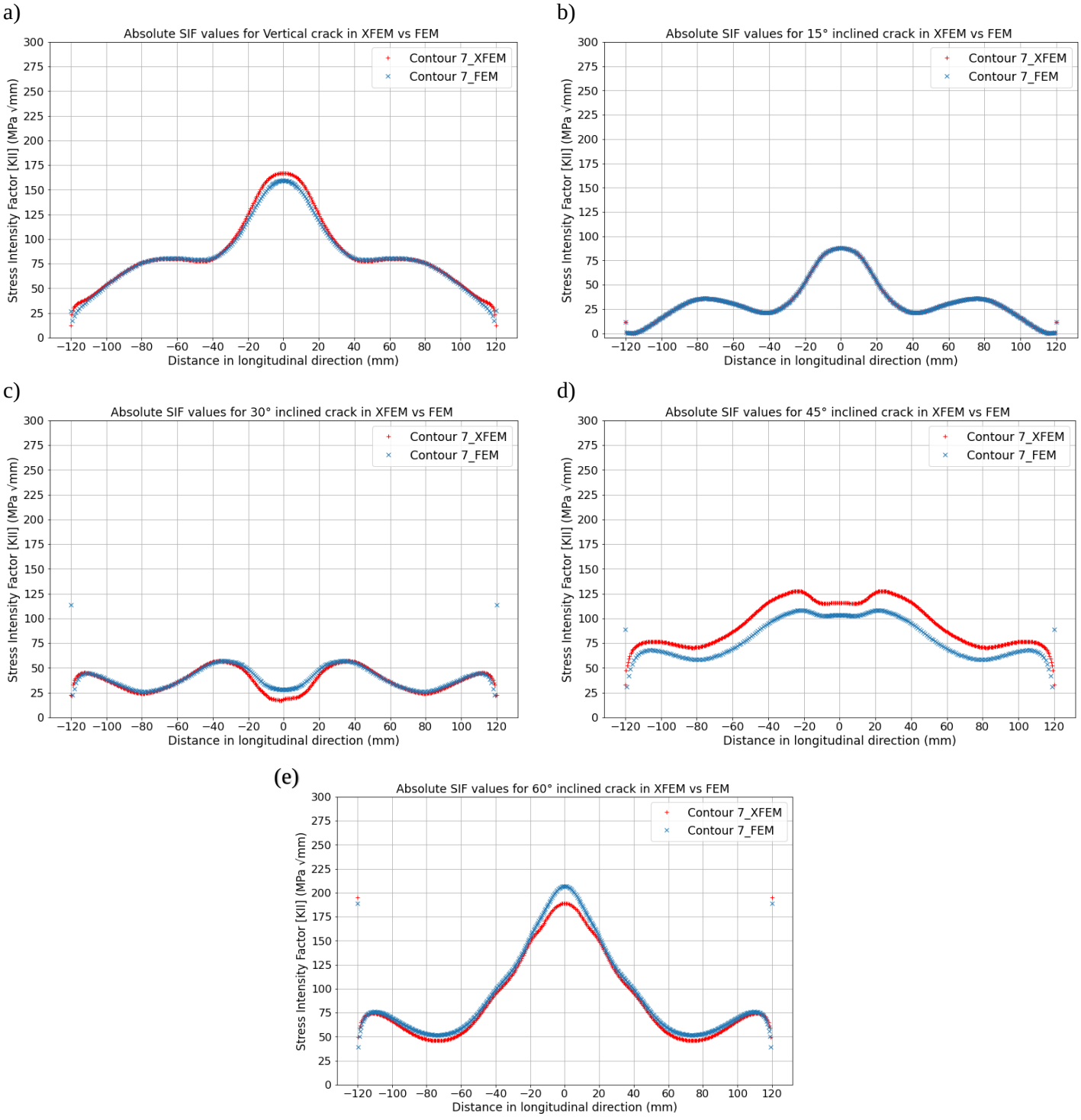

Figure 4.18: Absolute SIF values (K_{II}) for different crack inclinations considering only the last contour (XFEM vs FEM). (a) Vertical crack. (b) 15° crack. (c) 30° crack. (d) 45° crack. (e) 60° crack

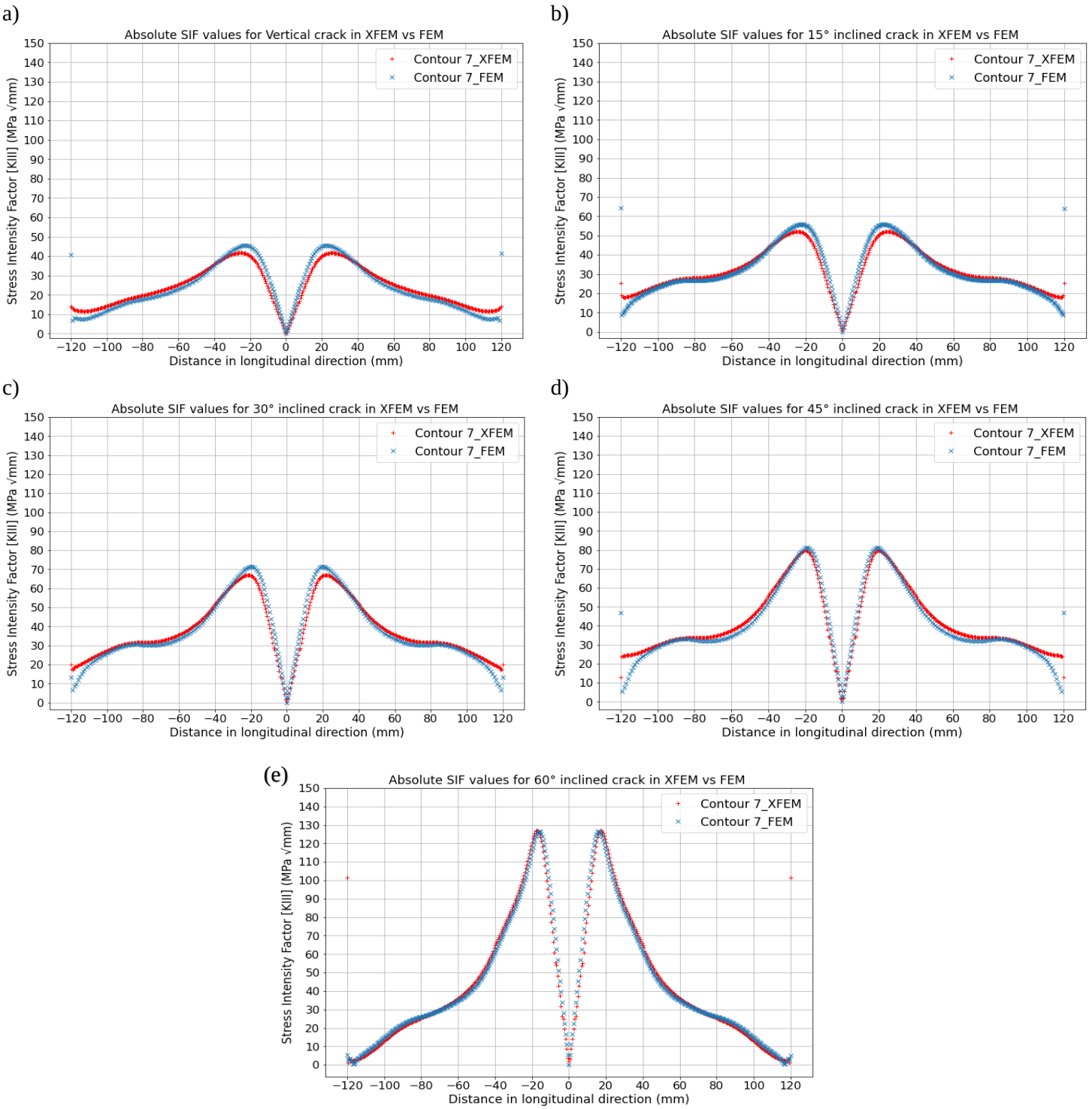

Figure 4.19: Absolute SIF values (K_{III}) for different crack inclinations considering only the last contour (XFEM vs FEM). (a) Vertical crack. (b) 15° crack. (c) 30° crack. (d) 45° crack. (e) 60° crack

From previous figures, it is obvious that there is a close match in the XFEM and FEM results. This proves that for stationary crack analysis, the FEM and XFEM give similar absolute values for SIF results in tension and compression. Hence the first step for validating the proposed methodology is satisfied and the method can be further used for propagating crack analysis.

4.4.4 Cyclic loading XFE model initial state validation

A comparison between the measured and FE calculated strain (improved FE model) at the aforementioned strain gauge positions is presented in Figures 4.19 and 4.20. The first FE model is also considered in this comparison. Note that the values from the improved FE-model here were altered in the sign after post-processing because the methodology used assumes that the applied compressive wheel load will be altered to a tension load with the same magnitude as mentioned before in 4.2. This is done to be able to make comparisons with the first model and experiment.

(a) (b)

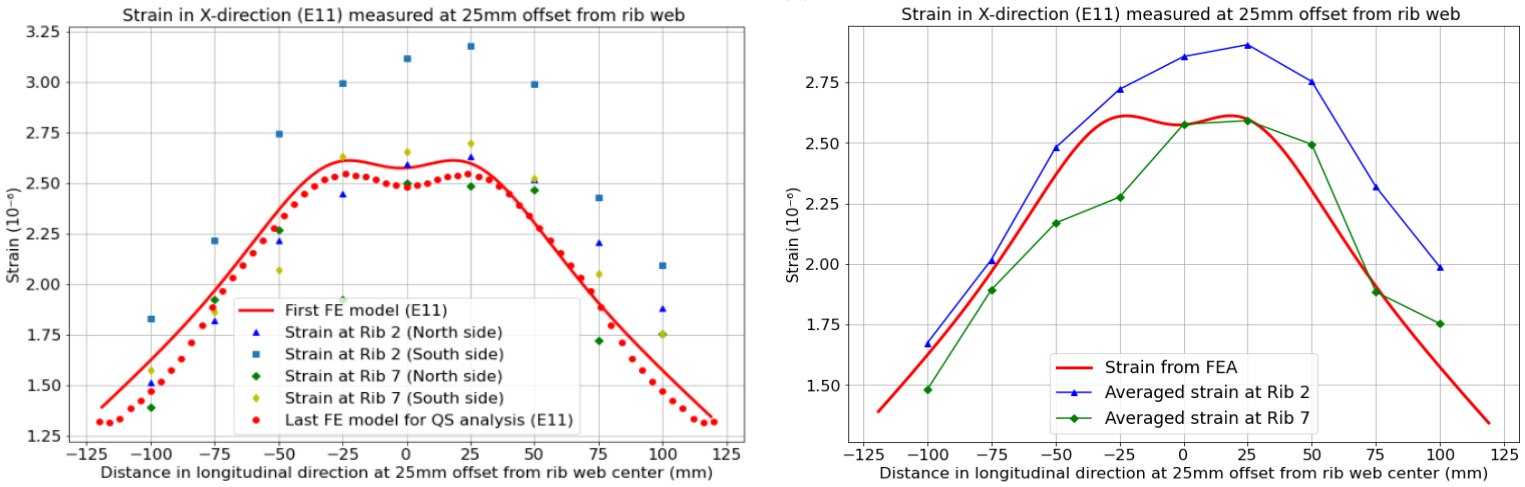

Figure 4.20: Strains in X-direction along a longitudinal path.
(a) Rib 2 & 7 (at N & S sides) measured strain vs FEA strains. (b) Averaged measured strains at rib 2 & 7 vs FEA strains

(a) (b)

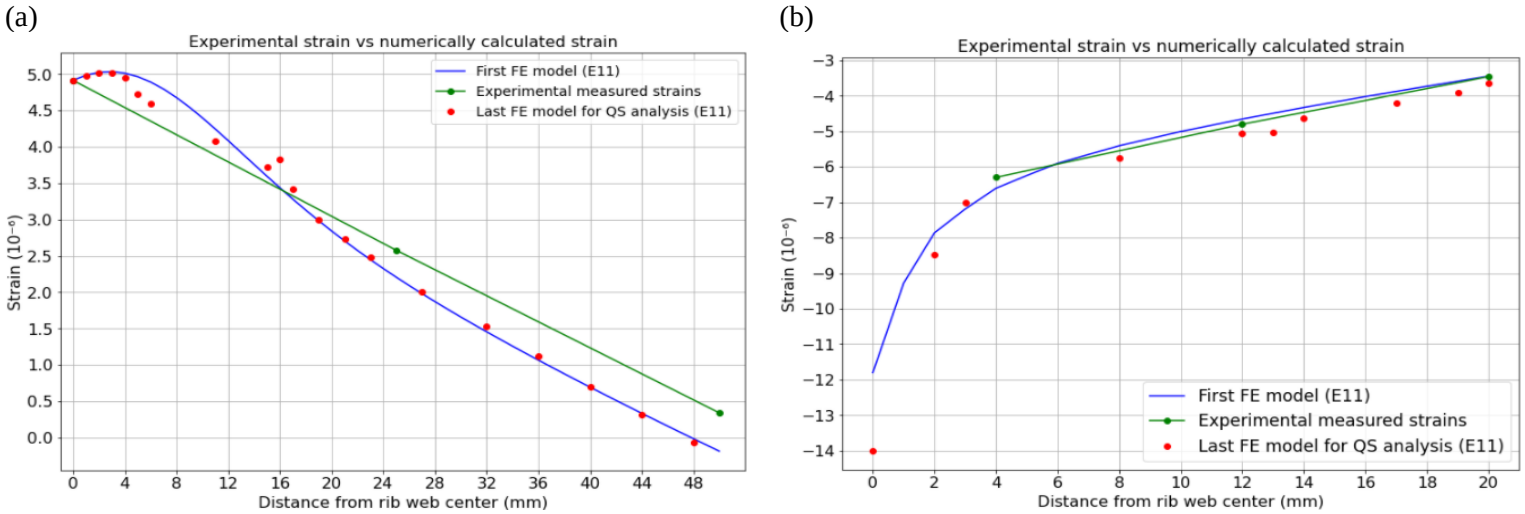

Figure 4.21: Strains in the X-direction along the transverse path. (a) Strain on deck plate top. (b) Strain at the deck plate bottom.

From Figure 4.20 and Figure 4.21, it is visible that good convergence exists between the first FE model and the improved FE model which is used for the cyclic loading analysis to make a propagating crack model. The average differences with the first FE model for the three paths considered are *3.2%, 3.3%,* and *3.5%* for paths one, two, and three, respectively. As for the differences with the experimentally measured strains, these are *4.5 %, 11%, and 6.7%* for the same three paths respectively. This showed that the different meshing strategy used in the improved model gives valid results for the stress distribution of the OSD detail.

4.4.5 Cyclic loading XFE model results and discussion

To obtain an initial prediction for the crack propagation direction in the OSD detail, the first propagating crack model which has the meshing strategy described in 4.3.6 and Table 4.1 is submitted. After running the model for some time it is then terminated and post-processed. From Figure 4.22 one can see the deformed shape of the sub-local part after the crack has opened. The undeformed shape of the STATUSXFEM output is shown as well. Although the predefined crack is inserted vertically in this model as mentioned before (see 4.3.5) when the crack starts to grow in the deck plate thickness direction the crack gets an inclination of almost *60°* as indicated in the figure below. This crack propagation direction is automatically predicted by the software without any user interference.

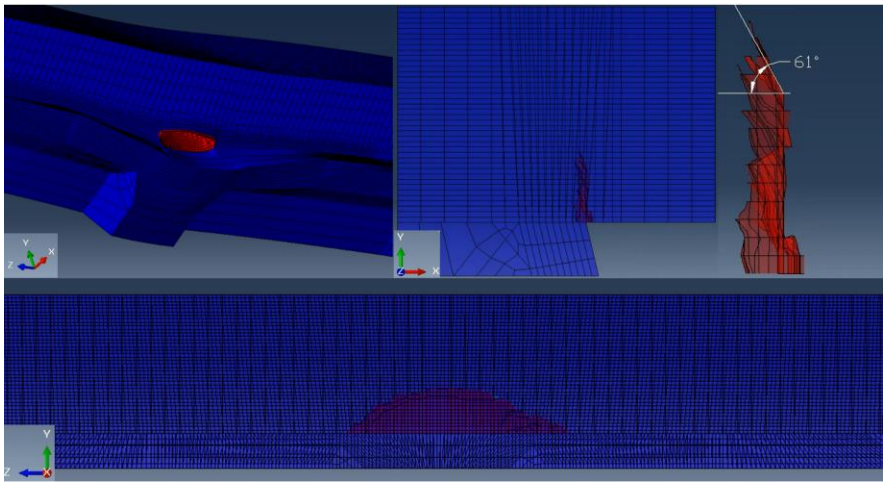

Figure 4.22: Different views of the propagating crack for the first cyclic loading model

It should be noted that the rib region in the sub-local part of the model is not selected in the propagating crack zone in this model. This model gave a good prediction for the initial crack propagation direction angle. This led to redefining the crack (see 4.3.5) and inserting it with an angle equal to *30°* with the vertical axis. The model meshing is adjusted to reduce the computational time as previously explained in 4.3.6. In addition to this, the whole sub-local part is now assigned the enriched element feature using the VCCT fracture criterion, including the rib web segment in the sub-local part.

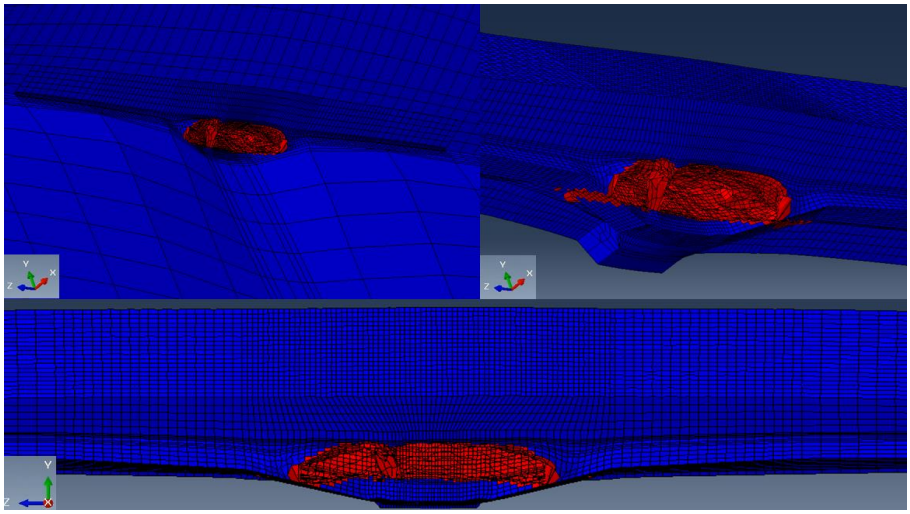

Figure 4.23: Different views of the propagating crack deformed shape in the improved cyclic loading model

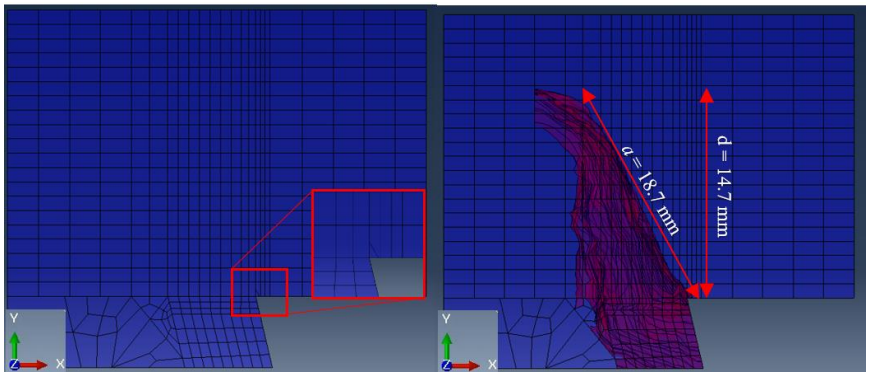

Figure 4.24: Undeformed shape of the cracked XFE model at the start and end of the analysis

In Figure 4.23 the deformed shape of the OSD detail is shown. This output belongs to the improved propagating crack model which is described in previous sub-sections (4.3.5and 4.3.6). It is visible that the crack propagated through two components. The first component is the deck plate thickness and the second one is the part of the rib web considered in the sub-local FE model part. This can be more clearly seen in Figure 4.24, where the undeformed shape of the crack at the start and the end of the analysis is shown.

In Figure 4.23 at the left side of the crossbeam web, there is a part of the crack which is visually not completely open while the element has lost its stiffness. Mechanically, this part can be treated as an opened region. When the displacement output result of the sub-local part is checked, it showed a smooth solution at the elements in this region. They have similar displacements as the detached elements in the propagating crack. This is shown in Figure 4.25, where more views of the displacement output are shown.

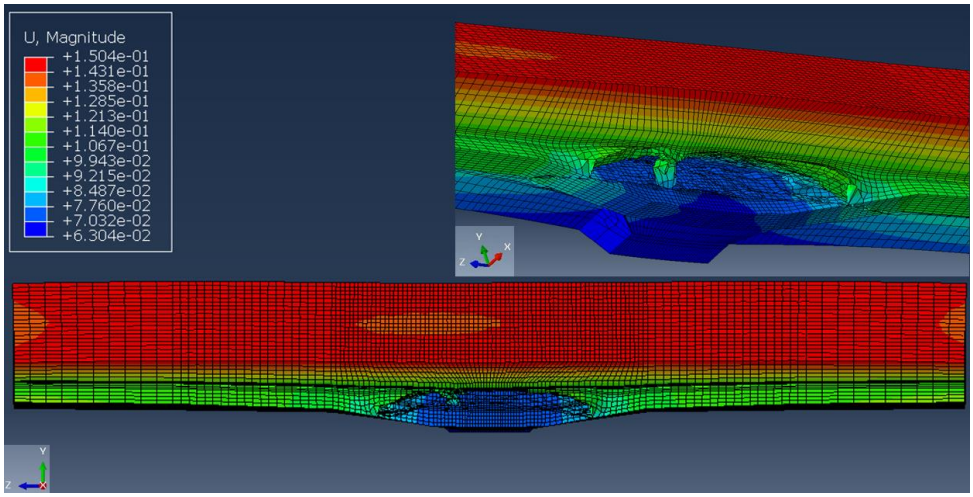

Figure 4.25: 3D and YZ view of the total displacement magnitude of the sub-local part.

Furthermore, like mentioned before in Figure 4.24 the undeformed shape of the crack in the XFE model is shown for two different moments of time where the crack sizes are different, at the beginning of the analysis, the initial predefined crack with its dimensions, which are given in Figure 4.8. When the analysis ended the crack dimensions measured are approximately; $a = 18.7\,mm,\ d = 14.7\,mm,$ and $2c = 102mm$ as in Figure 4.24. Where (a) and (d) are the inclined/actual and vertical crack depths, respectively.

Fatigue crack from the simulation compared to real cracks

In Figure 4.26 (a) different views from Abaqus® output (STATUSXFEM) have been presented. The semi-elliptical crack shape is visible here. However, for a closer look at the crack growth pattern through-thickness of the deck plate, Figure 4.26 (b) and (c) is shown and the crack propagation behaviour has been studied. In addition to that, the crack obtained from the automated crack propagation method using XFEM is shown here for the sake of comparison with a similar crack in different studies. Note that in Figure 4.24 the same crack is also shown with an indication of the vertical and inclined depth.

Following the angle predicted by the first XFE analysis shown in Figure 4.22, the initial predefined crack shown in Figure 4.8 is inserted with a *30°* angle. Figure 4.26 shows that the crack propagated with an angle equal to *28°*. The crack reached a vertical depth of *14.7 mm* (which is similar to the TOFD report from TU-Delft), at a vertical depth of around *7.9 mm* the crack propagation rate through the thickness slowed, and at a vertical crack depth equal to *13.1 mm* the crack started to change its propagation direction. The crack got arrested and propagated almost parallel to the deck plate surface with a slow propagation rate. This behaviour is also found in previous studies by different scholars on real full-scale OSD specimen testing [37]. It can be seen that the propagation angle numerically calculated by Abaqus® is close to the angles obtained from the experimental work indicated in Figure 4.26 (c).

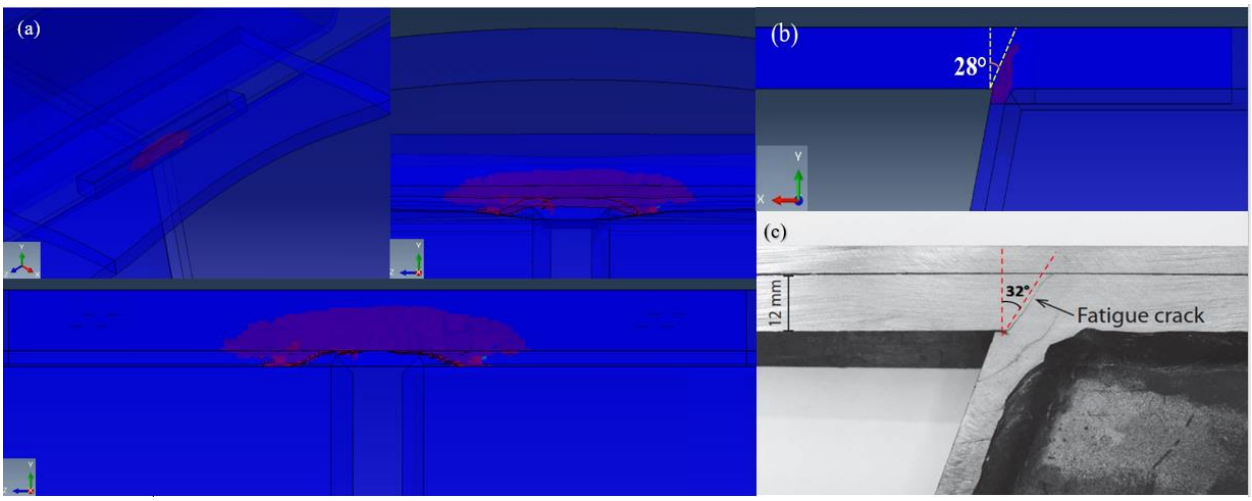

Figure 4.26: Semi-elliptical fatigue crack. (a) 3D and YZ deformed and undeformed view. (b) XY view of the fatigue crack. (c) 20 mm steel deck plate including 6 mm bonded steel reinforcement [38].

Although the deck plate thicknesses or the loading conditions are not the same, the fatigue crack shape and angle converge to the fatigue crack obtained from the XFE analysis carried out using XFEM in this thesis. Hence, it can be concluded that when the hypothesis of load sign change is considered and the same stress state as the experiment [37] is obtained, the near *30°* inclined crack will be obtained with a crack growth impedance as obtained from the XFE analyses. It should also be mentioned that the crack shape is not compared with the crack obtained from the TU-Delft experiment because the specimens were not cut.

Figure 4.27 (a) shows the crack geometry parameters (crack depth and length) plot over the loading history of the XFE analysis. Moreover, in Figure 4.27 (b) only the crack inclined and vertical depths are highlighted and shown. For more indication, a small subfigure showing a cut in the cross-section of the sub-local part at the middle of its length is provided. From Figure 4.27 (a) and (b) the complete crack propagation behaviour in both length and depth direction can be described. The crack first started to grow in both thickness and length direction. Due to the limited depth (*20* mm) compared to the part's length (*240 mm*) the crack can grow in, the crack grows more in the length direction than in the depth direction. It should be

emphasized that the given loading history here is indicated as a tool to see how the crack evolves to check the trend. It is out of the scope of this research to study the accurate loading cycle history.

The crack can be categorized into three different zones as in Figure 4.27 (b). The first phase is when the crack starts to propagate in the thickness direction of the *20 mm* deck plate, here the crack grows very fast through the thickness until it reaches a vertical depth of *7.9 mm* in less than *10%* of the loading time history. This corresponds to a crack length increase from *1 mm* to *38mm* within almost *15%* of the time. The crack depth then enters the second zone where the propagation speed becomes slower in the thickness direction since nearly *23%* of the time is needed for a relatively small increase in-depth direction. The crack depth in this zone increases from *7.9 mm* to *13.1 mm.* As for the crack length increase, the increase rate is fluctuating a bit between *10%* and *25%* of the loading history. In this period, the crack length increased to a length equal to *53 mm.* Returning to the crack depth increase, the crack started to slightly change propagation direction and got arrested when its depth exceeded *13.1 mm* as shown in Figure 4.27 (b). This marked the third and last zone of the crack propagation in the thickness direction as the vertical depth increase rate almost became constant while the inclined depth increased very slowly until it stopped as well. However, the crack length kept increasing with an approximately linear increase rate as it increased from *53 mm* to *102 mm* without considerable change in rate.

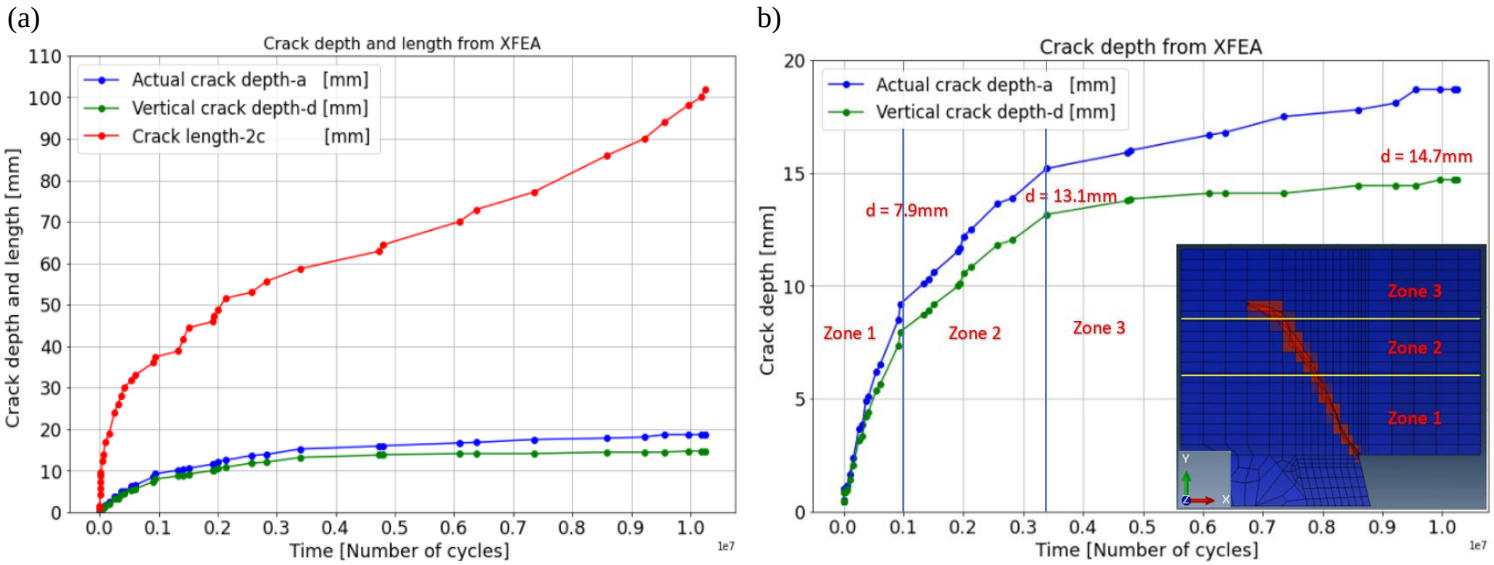

Figure 4.27: Fatigue crack depth and length vs time history of the XFEA.
(a) Inclined and vertical crack depth and crack length. (b) Inclined and vertical crack depth only (OSD cut).

An extra figure is added to show the crack from a different side and compare it with different experiment outputs. The details shown in Figure 4.28 (b) and (d) are from the experiment specimen mentioned before in 4.1 and 4.3.1 which is carried out by Wu et al. Figure 4.28 (a) shows a fatigue crack occurring and propagating through the rib web as well. It can be seen that after the crack has propagated a bit through the rib the crack also starts to propagate in the fillet weld between the rib web and deck plate as in Figure 4.28 (c). The crack cuts through the rib web thickness and occurs on the rib and weld surface. This is somehow analogous to the real test specimen (S2) as a crack occurred at the same place. Nevertheless, Figure 4.28 (d) showed a crack with a different shape than the simulation. The crack in the experiment propagated larger through the rib web and has a different propagation position.

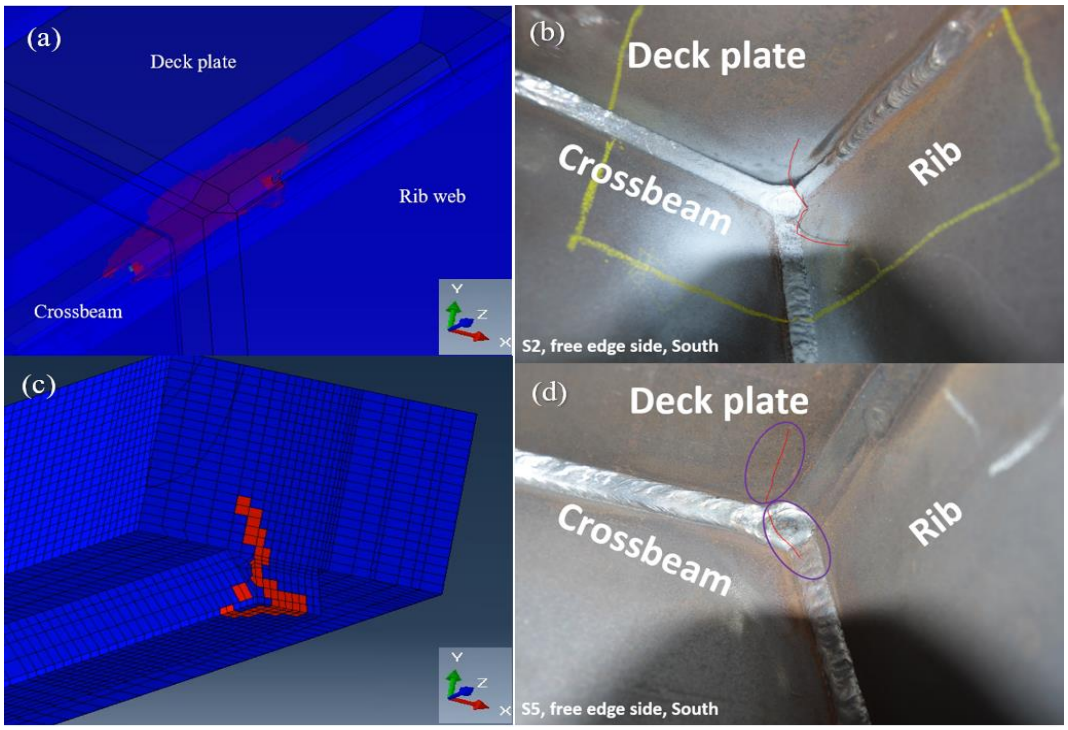

Figure 4.28: Fatigue crack propagation. (a) XFEA output (STATUSXFEM). (b) Experiment output (Wu et al).

Crack propagating normal to the maximum tangential stress direction

The figures attached in the next section are showing the uniaxial strain change (in x-direction) at the different strain gauge positions along the three paths defined in 4.4.1. The strain change is measured and plotted as a function of actual crack depth (a), vertical crack depth (d), crack length (2c), and time history using the number of load cycles. Hence, these various parameters augmentation's effects on how the strain changes are studied. Note that the time history consideration here is the number of cycles (loading history). It should be noted that the frequency for the loading considered is 1 Hz. Moreover, as stated before that the number of cycles or the fatigue life calculated by XFEM automated crack propagation analysis when using more elements through the thickness is much higher than in reality when more elements are present through the thickness. Hence, the fatigue life here is unreliable. However, the number of cycles shown here is used just as a tool to indicate the strain drop as a function of time as mentioned before.

Strain output from FE-model at path 1-gauge locations

In Figure 4.29 the strain change has been plotted for path 1 where the strain gauges were installed at the top of the deck plate along the longitudinal direction of the OSD segment. The behaviour of the strain change when considering the inclined crack depth (*a*) is almost the same as the strain behaviour when considering the vertical crack depth (*d*), this is explained by the fact that the vertical crack depth is a function of the inclined or actual crack length. This relation between the crack inclined and vertical depth holds till a loading history of less than two-thirds of the total crack propagation time in the model. Hence, the strain drop response is almost identical for the first two-thirds of the time in a qualitative way. The fact that the vertical and inclined crack depth differ qualitatively in the last third of the time is attributed to the change

of behaviour in the crack shape in the vertical direction as the crack starts to incline more and propagate parallel to the deck plate surface as mentioned before.

Furthermore, in Figure 4.29 (a) and (b) the strain drop trend can be resembled by a linear top line for the strain gauge locations close to the crack initiation zone (*-25 mm*, *0 mm*, and *+25 mm*). When moving away from the crack initiation zone (at strain gauges; *-50 mm* and *+50 mm*) the strain drops slightly in the beginning till the actual and vertical crack lengths reach *10 mm* and *8 mm*, respectively. After that, there is a steep slope in the strain drop till the crack reaches its largest length and the analysis is completed.

a)

b)

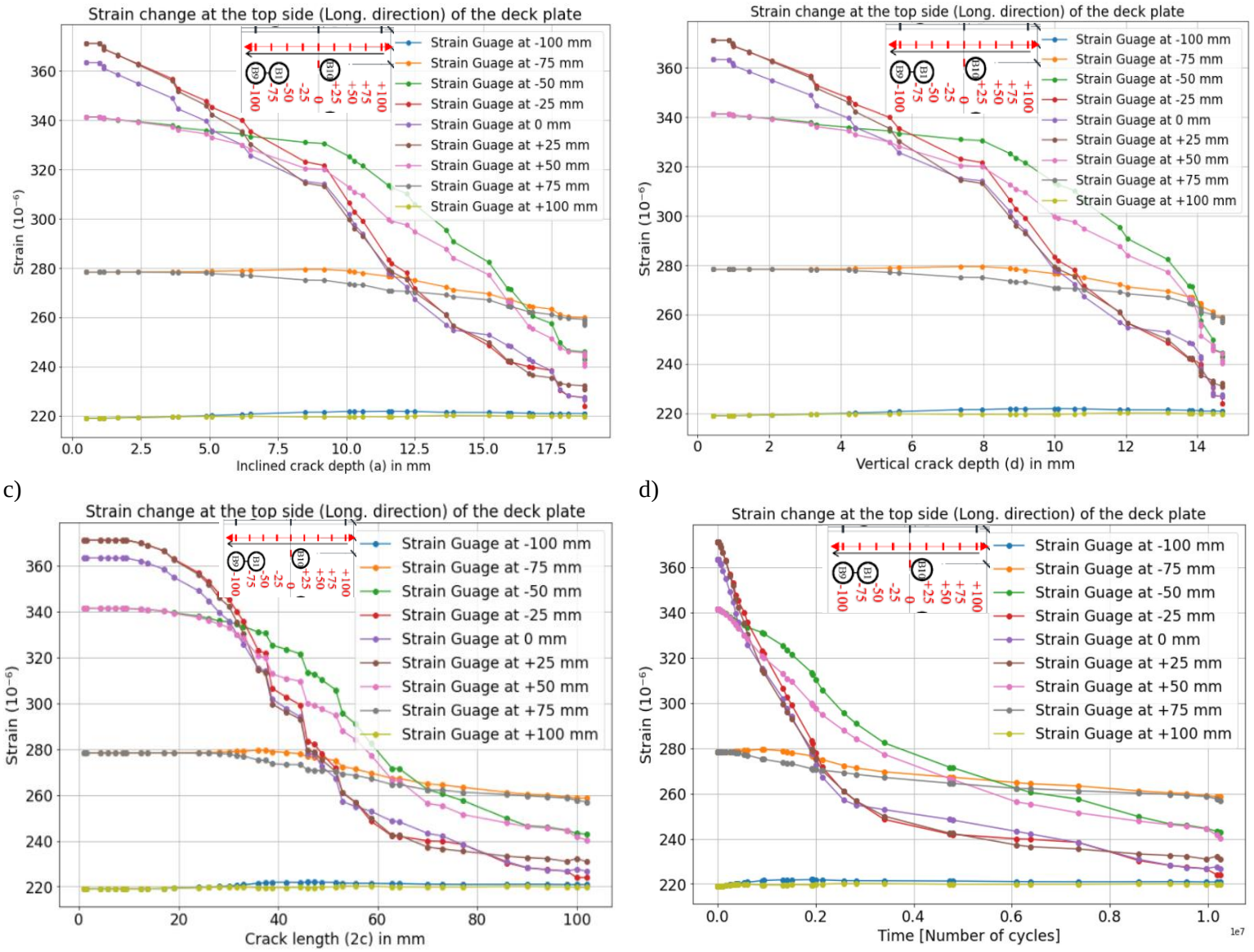

c)

d)

Figure 4.29: FEA strain drop at the top side (longitudinal path) of the deck plate vs;
(a) Actual crack depth [a]. (b) Vertical crack depth [d]. (c) Crack length [2c]. (d) Time [Number of cycles].

In Figure 4.29 (c) the strain change is studied with the crack length (*2c*) increase. For the strain gauge positions close to the crack initiation zone (*-25 mm*, *0 mm*, and *+25 mm*), until a crack length of around *15 mm*, there is no strain change and for the gauges, at *-50 mm* and *+50 mm* the strain is almost constant till a

crack length of *25 mm.* Then a strain decrease takes place. Although the strain values have some fluctuations, the overall strain decrease in this region can be approximated as a linear decrease, this linear behaviour continues till a crack length of *65 mm* for all before mentioned strain gauge locations. In the end, the decrease line slope reduces. Hence, the strain drops very slightly when the crack grows very large (*65 mm* to *102 mm*). Finally, the strain change is given as a function of loading history in Figure 4.29 (d). The strain decrease is relatively large at around a quarter of the total time taken for the crack to grow.

From subfigures (a), (b), (c) and (d) one can deduce that the strain dropped around *40%* and *30%* from its initial value throughout the fatigue crack depth and length total growth. These drop percentages are experienced for the locations corresponding to the set of strain gauges at the crack initiation zone (*-25 mm, 0 mm,* and *+25 mm*) and at a distance of *-50 mm* and *+50 mm* from the center of the detail of interest (crack initiation zone). Thus, a considerable loss of stiffness is experienced at these positions. The $\pm 75\ mm$ strain gauge positions are slightly affected by the fatigue crack growth as the strains are reduced by less than *10%,* while the strain positions coinciding with gauges at $\pm 100 mm$ from the center of the detail are almost constant through the whole fatigue crack growth occurrence. This is similar to reality since the further the measuring point gets from the peak strain area and crack initiation zone the lower the influence on the stress becomes. For more clarity about the strain change percentages, a figure showing the relative strain changes is added in appendix B [Figure 8.9].

Strain output from FE-model at path 2-gauge locations

The XFE calculated strains at the strain gauge locations of path 2 are analysed here. This is shown and explained in Figure 4.30. In all subfigures, when looking at the position of strain gauge located at *0 mm,* there is a noticeable phenomenon taking place. The strain range at that location experience a linear-like increase before the strain starts to drop and the detail fails. The explanation for this strain deviation is that when the cyclic load is applied on the deck plate the OSD detail first behaves elastically. When the crack occurs, the strains and stresses at this location keep increasing due to strain redistribution till the detail fails and strain drops quickly. The strain increases till an inclined and vertical crack depth become *13.75 mm* and *11.8 mm,* respectively. After that, the strain falls sharply when the crack depth increases. This shows that the detail cross-section here has lost a large portion of its stiffness leading to the loss of structural integrity. In the last *10%* and *5%* of the inclined and vertical crack depth growth, also the strain stabilizes and does not change till the analysis stops.

The strain also increases with the crack length increments. A non-linear increase is noticed in Figure 4.30 (c). Then the strain drops and remains constant for relatively many length increments. When reviewing the loading cycle/time history versus strain change behaviour, it seems that the strain increases rapidly at the beginning of the time, then decreased leading to losing the detail's integrity and the strain remained constant afterward with minimal change till the end.

Furthermore, the maximum strain increase ratio for the position of the strain gauge located at the connection center (*0 mm*) is *23%* approximately. This percentage converges with the relative strain increase which is around *24.5%* for gauge A5, measured from the experiment by Wu et al [37] (see Figure 4.31). The strain values and their differences are given in Table 4.2. In the table, the initial, maximum, and minimum strain values are given in addition to the variance ratios between the numerically calculated and the experimentally measured strains at both sides of the rib (Gauge A2 and A5). It is found that the numerically calculated strain is closest to that measured from gauge A5, although there is a relatively large difference in the dropped strain value. The initial and maximum values from XFEA are appropriately meeting that from the experiment (gauge A5) with differences of *7.75 %* and *10.95%,* respectively.

The strain change trend of the position of the strain gauge at *25 mm* from the rib web is almost identical for the actual and vertical crack depth, as well as the crack length. The strain decreases quickly in the beginning, then remains almost constant till the end. Eventually, there is roughly no strain change at the *50 mm* strain change position due to the same reasoning about the distance mentioned before.

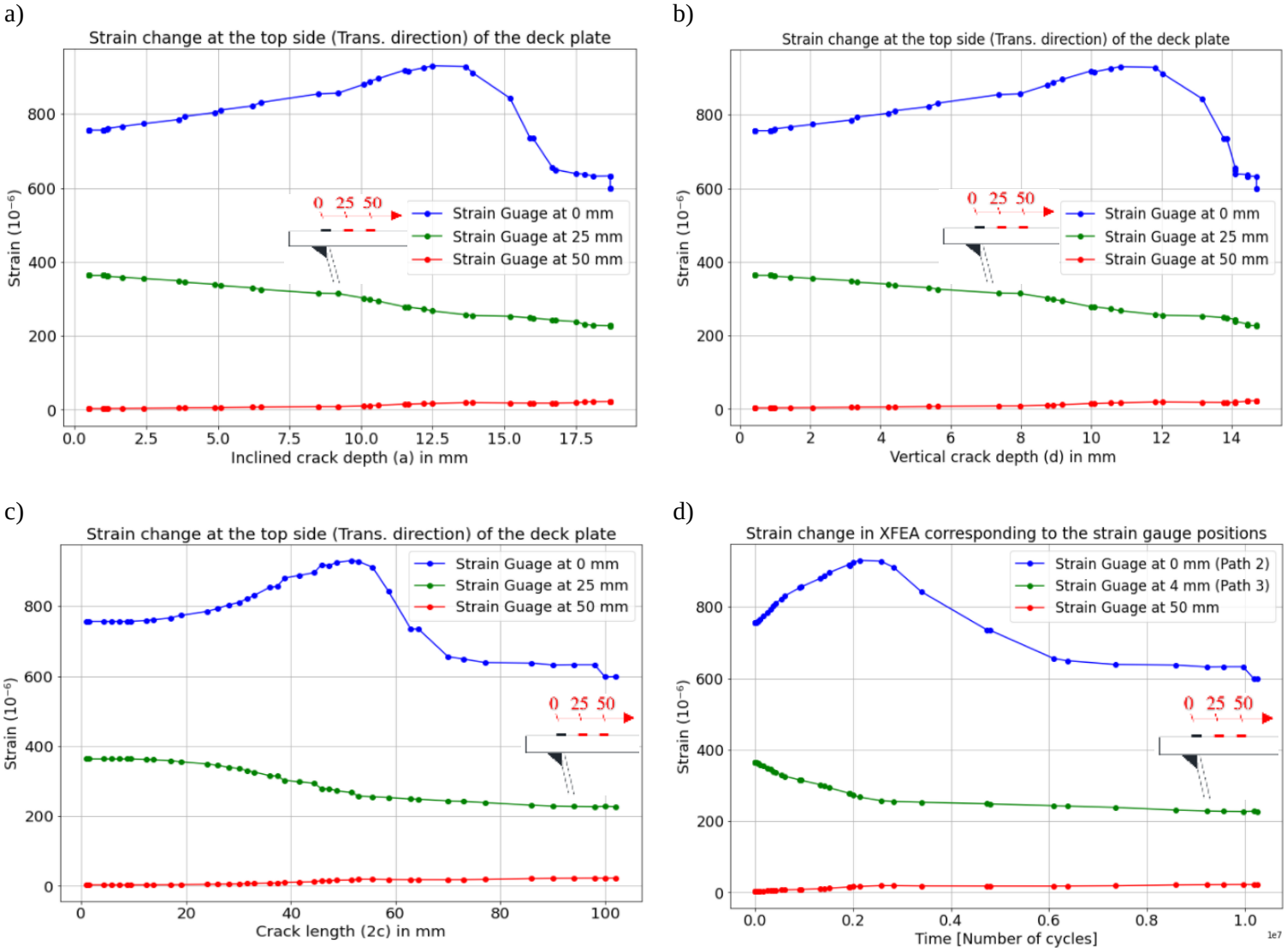

Figure 4.30: FEA strain drop at the top side (transverse path) of the deck plate. vs;
(a)Actual crack depth [a]. (b) Vertical crack depth [d]. (c) Crack length [2c]. (d) Time [Number of cycles].

Table 4.2: Strain values from XFEM and experiment and the difference ratios

Strain gauge location	**Initial Strain Value** $[\times 10^{-6}]$	**Maximum Strain** $[\times 10^{-6}]$	**Minimum Strain** $[\times 10^{-6}]$	$\Delta\varepsilon_i$ **(XFEM - Test)** [%]	$\Delta\varepsilon_{Max}$ **(XFEM -Test)** [%]	$\Delta\varepsilon_{Min}$ **(XFEM -Test)** [%]
Node at 0 mm	**756.4**	**935**	**600**	-	-	-
Gauge A2	645	1080	350	18.67% ↑	13.4 % ↓	71.4% ↑
Gauge A5	820	1050	480	7.75 % ↓	10.95 % ↓	25 % ↑
Node at 4 mm	**951**	**951**	**103**	-	-	-
Gauge C1	860	920	40	9.57 % ↑	3.37 % ↑	157.5 % ↑
Gauge C6	1030	1030	95	7.67 % ↓	7.67 % ↓	8.42 % ↑

a)

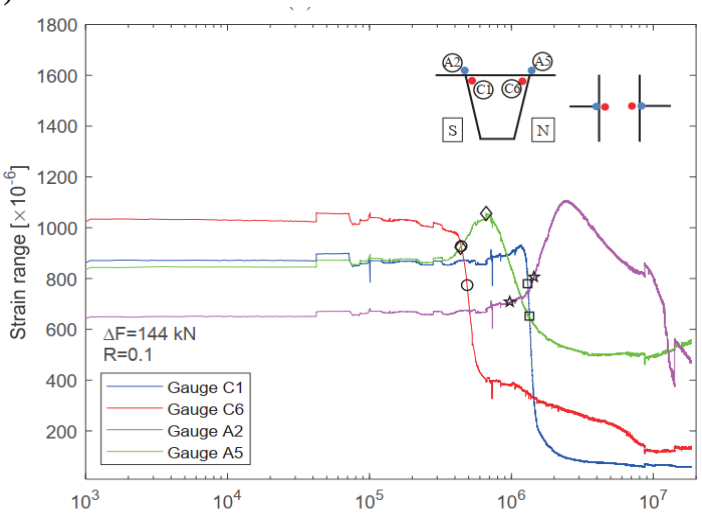

b)

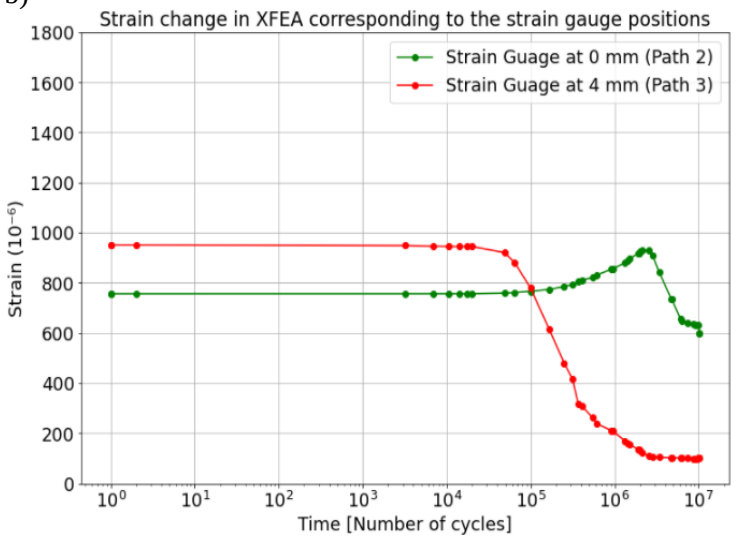

Figure 4.31: Strain change as a function of time history [number of cycles on log scale]. (a) Experimentally measured [37]*. (b) Numerically calculated.*

Strain output from FE-model at path 3-gauge locations

Path 3 measured dots are located at the bottom side of the deck plate with distances *4 mm*, *12 mm*, and *20 mm* from the weld root. For the location at *4 mm* strain gauge the strain reduced swiftly at a small actual and vertical crack depth as in Figure 4.32 (a) and (b). This indicated the reduction of the local structural solidity. The strain change is constant at the beginning of the crack length increase to a length of almost *12 mm* then the strain started to drop until a length of *58 mm*, then the strain change stopped till the end as in Figure 4.32 (c). When the strain change is studied with time, the plot showed a very sharp strain decrease (*90%* strain drop) within just *20%* of the time, after that the strain stabilized and remained constant till the analysis ceased. An elaboration to this behaviour is that the *4 mm* measured point from FE-model, lies in a singularity zone being close to the crack initiation point, so the stress and strain there drop very fast when the initial crack opens and starts to propagate. Moreover, the strain at the *4 mm* node is validated with the strain measured from the experiment. The *4 mm* node strain evolution with loading history is qualitatively similar to the strain measured from gauge C6 as in Figure 4.31. The relative strain change from XFEA is *10.8 %* which came very close to that of gauge C6 which has a value of *9.2 %*. Additionally, the maximum and minimum strain values approached the experiment strain values with difference percentages equal to *7.67 %* and *8.42 %*, respectively as given in Table 4.2.

The strain changes at *12 mm* and *20 mm* are more alike. For the change of strain when considering the crack depth increase, there is an approximately linear decrease of strain. The *12 mm* location has a higher decreasing slope than the location at *20 mm* distance. The relative strain change has been explicitly plotted and shown in Figure 8.11 in appendix B. Moreover, the strain dropped by around *77%* and 61% for the *12 mm* and *20 mm* locations, respectively. This happened at almost no more than a quarter of the crack propagation time. The strain values near the weld root not only drop faster but also decline more in

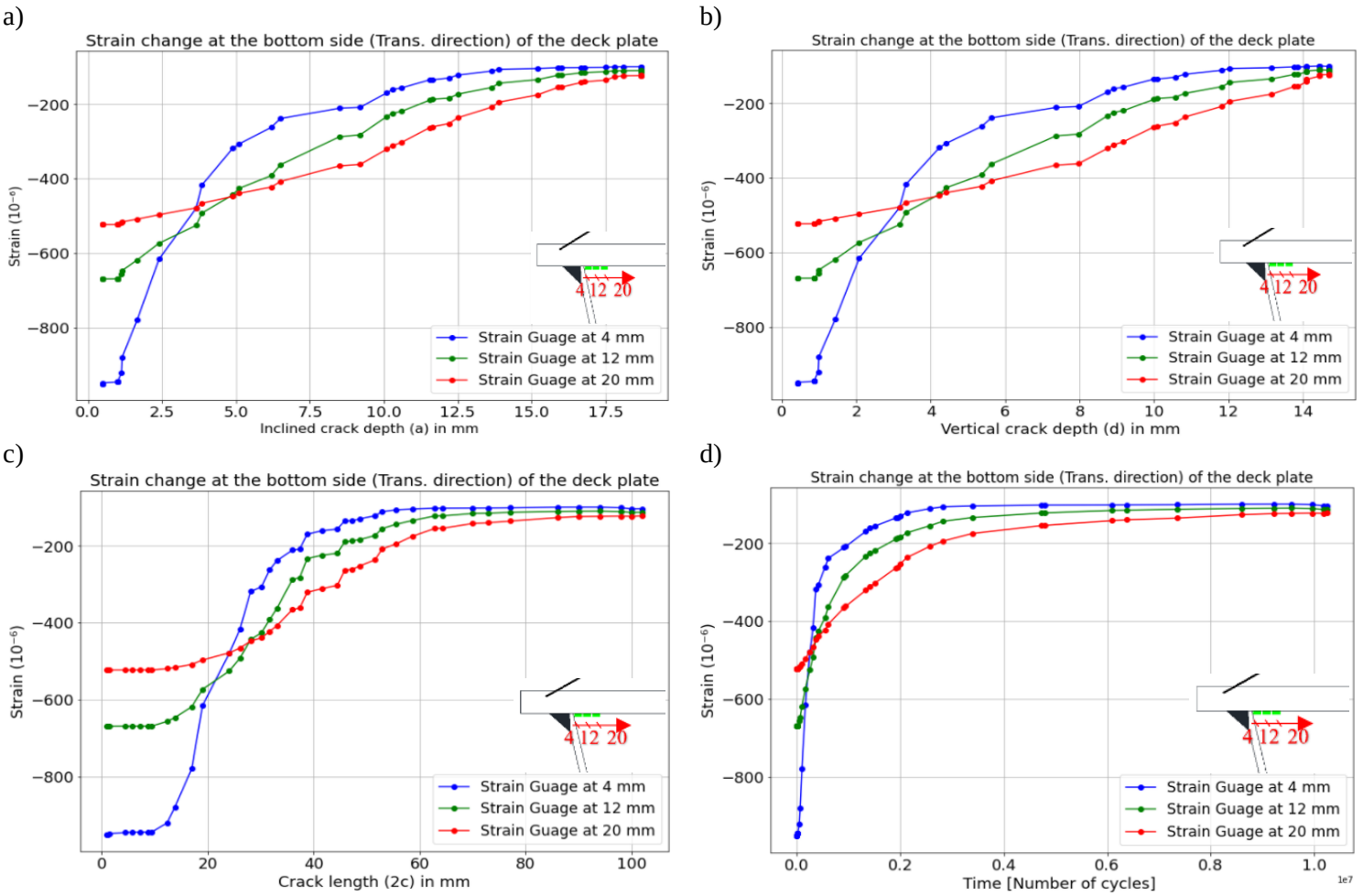

Figure 4.32: FEA strain drop at the bottom side (transverse path) of the deck plate vs;
(a) Actual crack depth [a]. (b) Vertical crack depth [d]. (c) Crack length [2c]. (d) Time [Number of cycles].

This in general shows that there is a reasonable similarity between the modelled propagating crack model and the real OSD segment. The differences in strain values can be attributed to multiple reasons. These reasons can be briefly summarized by indicating that in FE modelling, the material properties used are perfectly homogeneous which is not the case in reality. In addition, the precisely defined boundary conditions and applied load in the FE-model can also affect the strains. The strain gauges installed during the test are also sensitive and can influence the results if they slightly shift. This has most probably happened for gauges A2 and C1. To sum up, finite element modeling here considers a perfect environment when making a fatigue crack simulation. However, this is not identical to the real practical circumstances. Considering the complex stress states of the detail and the uneven strain measuring found in the experiments, it is recommended to carry out more study with different detail preparation, i.e. welding penetration, and welding residual stress included.

4.5 Conclusion

In this chapter, the fatigue crack growth behaviour in the OSD detail of interest was analysed and studied. This chapter includes the essence of this thesis as the main research question is tackled here. This was done by first validating the FE model's initial state by comparing the strain from static FEA with the strain gauge measurements from experiments. After that, the main methodology to model the fatigue crack under compression was divided into steps and was validated step by step.

First, the stress intensity factors from XFEM and conventional FEM stationary crack analysis were compared. Based on the conclusion of this comparison, the considered FE model was updated as the discontinuities were modelled as an enriched feature using XFEM cyclic loading analysis. Therefore, the initial state had to be first rechecked with the experiment strain measurements and the first FE-model strain readings. Thus, the propagation of the fatigue crack was modelled with more confidence. Finally, the model meshing strategy is improved to be to reduce computational cost. Eventually, after discussing the results, the following conclusions are drawn from the analysis of this chapter:

- The absolute SIFs values obtained from XFE and FE models are almost identical and this holds for the SIF values from all three fracture modes in compression and tension. Hence, more confidence is gained in modeling the propagating crack with the load-changing hypothesis.

- The highest loss of stiffness happened at the node at *4 mm* from the weld root as the strain there dropped by around *90%* in less than a fifth of the loading time. This is because the node is located in the vicinity of the crack initiation region. This node is validated with the experiment and the relative strain change is *10.8 %* and *9.2 %* for the XFEA and experiment, respectively.

- The first node in path 2 (*0 mm*) experiences a redistribution of stresses which led to different behaviour in the beginning as the strains first increased by almost *23%*. This relative change is comparable with that of the experiment where gauge A5 has around a *24.5%* increase ratio. Hence, the structural integrity of the detail reduces as the strain there dropped.

- The crack propagation angle and shape are neatly predicted by Abaqus® using the automated crack propagation analysis and the load sign change hypothesis. The crack has an average angle of *28°* which is validated with the literature. Besides, the crack has a semi-elliptical shape as expected.

- Regarding the propagating crack rate, the approach also showed promising results. The crack depth increase is classified into three stages. This rate is highest in zone 1, then became smaller in zone 2. Eventually, the increase rate almost came to an end in zone 3, as the crack is arrested in the depth direction and changed its angle. Further, the crack had a high length increase rate in the beginning, then the rate fluctuated for *10 %* of the loading history and finally keeps increasing with an approximately linear increase rate.

- The relation between the crack depth increase and the strain change can be concluded for the three paths as follows. An approximately linear relation between the crack depth increase and strain drop is found for the closest strain gauge locations on path 1. Moreover, the *0 mm* node on path 2 shows a linear strain increase as the crack depth increases till the element fails and strain quickly decreases. Finally, a fast non-linear strain decrease is experienced with the increase of crack depth at the *4 mm* node on path 3. All the relations mentioned hold till the crack depth increase stops.

- It can be concluded that the node at *0 mm* in path 2, is the most important location for the strain data correlated with the crack depth growth in all phases. The node can give a correct representation of the local detail integrity and how it is affected by the crack growth.

- The crack propagating through the closed rib web is noticed in the experiment done by Wu et al. However, the crack in the experiment is larger in the rib web, while this did not happen in XFEA due to the limited activated zone for crack propagation assigned to the XFE model.

5 Parameter analysis

In this chapter, the most important parameter for the OSD detail crack considered in this study has been selected and will be analysed. The parameter will then be changed and the crack behaviour in the model will be studied and examined for its sensitivity for the variation of this parameter. The results of this parametric study will be discussed and validated based on experiments from different literature.

5.1 Introduction

The crack propagation behaviour has been studied for the OSD with a *20 mm* thick deck plate. Hence, it is found necessary to study the crack characteristics for different OSD thicknesses. The weld root penetration was seen as a possible parameter to vary. However, after reviewing the literature it is found that partial weld penetration has little effect on the effective notch stress at the weld root [39]. Thus, little effect on the fatigue crack formation and propagation. In the end, it is decided to consider two thicknesses for the deck plate. The thicknesses studied are *16 mm* and *10 mm.*

5.2 Methodology

One parameter that is the deck plate thickness will be considered in this chapter for both values of *16 mm* and *10 mm* as mentioned before. The load applied on the deck plate will be adjusted in magnitude such that the hot spot stress remains the same. After that, cyclic loading analysis has been carried out for both models to make the crack propagate. The same hypothesis of changing the compression to tension load is used for these models to subject the crack initiation point to tension instead of compression. The two models' outputs and results are compared to experiments from previous studies which has the same deck plate thicknesses.

5.2.1 Load adjustment using SHSS

2D beam model

To adjust the applied load the structural hot spot stress will be calculated so that when the deck plate thickness changes, the corresponding HSS is kept similar, hence the same stresses for crack initiation. This is done first by a hand calculation using a 2D beam model to calculate the bending moments and after that, the load can be calculated. This 2D beam model was used by De Jong [1] to calculate the stresses at the deck plate detail and is shown in Figure 5.1.

As can be seen from Figure 5.1, the deck plate segment can be schematized as a fixed-fixed beam. Where the clamped ends represent the crossbeam to deck plate and close rib web welded connection. The bending moment at the fixations is calculated using the formula (5.1).

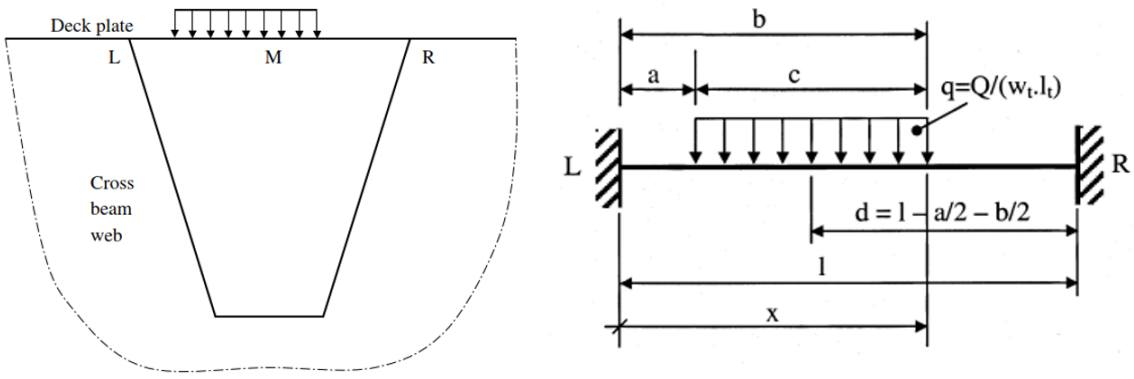

Figure 5.1: Mechanical beam model schematization by De Jong [1].

$$M_L = \frac{qc}{24l}\left(24\frac{d^3}{l} - 6\frac{bc^2}{l} + 3\frac{c^3}{l} + 4c^2 - 24d^2\right) \tag{5.1}$$

And q is the distributed line load when a unity length is considered and can be calculated using expression (5.2).

$$q = \frac{Q}{w_t \cdot l_t} \tag{5.2}$$

Where:

Q is the concentrated wheel load (N),

q is the uniformly distributed wheel load (N/mm),

w_t is the width of the tire footprint (mm),

l_t is the length of the tire footprint (mm),

l is the deck plate span between the closed rib webs, taken *300 mm* here.

The calculation of the load has been carried out using NEN-EN 1993-2 NB [14] and is presented in Appendix C. The loads obtained giving the same stresses are *92.158 kN* and *36 kN* for the *16 mm* and *10 mm* deck plate thicknesses, respectively.

3D FE model

The loads from the 2D beam schematization are verified by calculating the hot spot stresses using 3D finite element models. A static model is analysed for each thickness case with its corresponding load magnitude calculated previously. Static 3D FE models for the OSD with different deck plate thicknesses are analysed and the hot spot stresses are calculated for all cases and compared. The calculation is done using the linear stress extrapolation points at *0.4t* and *1.0t* (where *t* is the deck plate thickness) recommended by the IIW recommendations [11]. The structural hot spot stress for the welded detail was calculated using equation (5.3) from IIW [11]. This equation is also indicated in Table 2.1 for type "a" hot spots in 3D FEA. The full calculation of the hot spot stress has been provided in Appendix C.

$$\sigma_{hs} = 1.67\sigma_{0.4t} - 0.67\sigma_{1.0t} \tag{5.3}$$

The hot spot stress values obtained for the *20 mm*, *16 mm*, and *10 mm* are *227.4 MPa*, *228.1 MPa*, and *236.5 MPa*, respectively. This is also given in Table 5.1. The table also shows the corresponding load for each deck plate thickness considered. In addition to that the *20 mm* deck plate is considered as the reference case and the difference ratio in SHSS is calculated and given in the table for the two other cases. Hence, the ratios read *0.3 %* and *3.4 %* for the *16 mm* and *10 mm*, respectively and as given in Table 5.1. These differences are acceptable and the calculated load magnitudes are considered for the parametric analysis.

Table 5.1: SHSS and difference ratio calculation for various deck plate thicknesses

Deck plate thickness - t_{dp} [mm]	Load [kN]	SHSS - σ_{hs} [MPa]	SHSS difference ratio - $\Delta\sigma_{hs}$ [%]
20	144	227.4	-
16	92.16	228.1	0.3
10	36	235.4	3.4

The 3D finite element models considered for the stress HSS verification have almost the same models' description as the improved cyclic loading model in 4.3. These models are using tie constraints The only main difference is that the analyses here are static analyses made to calculate and check the hot spot stresses. More information about the cyclic loading models will be given later in this chapter.

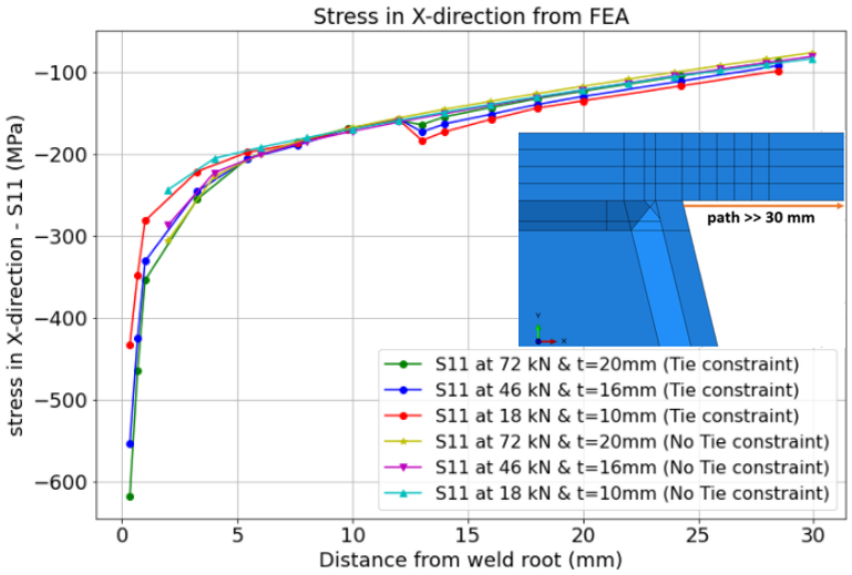

Figure 5.2: Stress in X-direction from FEA for different deck plate and loadings with and without using tie constraints

Figure 5.2 shows the stress in X-direction output from the different 3D FE models. The stresses are measured at distances from the rib web to the deck plate weld root. It can be seen that the stresses extracted from the static models when using three model parts are quite similar to the one using only two parts tied together without cutting a third sub-local part and tying it using tie constraints. However, there is one significant difference which is a sudden drop in the stress values measured from the models with tie constraints at the local region of the detail. This happens at the tie constraint connection surface between the two parts. On the other hand, the plots for the models with only two parts connected where a large local part is considered, show a smooth continuous stress field. This proves that the tie constraints cause a small discontinuity in the stress field, giving a bit erroneous values at the tied zone. These deviating values get closer to the correct values as the point measured moves away from the tied zone. Moreover, the average

differences were measured for the most deviating stress values read from after the tie constraint zone and are found to be *5%, 7%,* and *11%* for the *20 mm, 16 mm,* and *10 mm* deck plate thickness models, respectively. As a result, it can be concluded that the stress difference is acceptable and the stress values can be further considered for calculations.

Another point worth mentioning here is that in Figure 5.2 there is a difference in the first stress value which is almost at the weld root. The models where tie constraints are used give a higher value than the ones without tie constraints. This is due to the difference in element sizes used in both models at the local weld regions and has no relation with using tie constraints. Table 5.2 shows that the size of the local element at the weld root zone for the models using tie constraints is *0.3 mm.* This element size is smaller than that of the model without tie constraints at the local zone. This small element size leads to a high-stress peak compared to the stress from the other models. The smaller the element becomes at the weld root zone the more the singularity problem occurs and the higher the stress peak close to the root turns.

Table 5.2: Finite element mesh for parametric static analysis

FE models with deck plates of 10 mm, 16 mm, and 20 mm	**Global part**		**Local part**		**Sub-local part**	
	Element size	Interpolation scheme	Element size	Interpolation scheme	Element size	Interpolation scheme
Static analysis (Tie constraints)	15 mm to 50 mm	Linear (C3D8R)	8 mm	Quadratic (C3D20R)	0.3 mm to 4 mm	Linear (C3D8R) (C3D8)
Static analysis (No Tie constraints)	15 mm to 50 mm	Linear (C3D8R)	2 mm	Linear (C3D8R)	-	-

5.3 FE Models description

The static and cyclic loaded finite element models considered in this chapter have very similar characteristics to FE models considered in chapter 4 . All the models have the same geometry as the model cuts are the same as in 4.3.1. Only the deck plate thickness varies with the models (*16 mm* and *10 mm*), while all other geometry parameters remain constant. Moreover, the material properties are also linear elastic properties with Young's modulus and Poisson ratio as in Table 3.1. In addition to that, the boundary conditions are left the same as in 4.3.3. As for the applied loading, the loading magnitude changed with the deck plate thickness variation as illustrated in 5.2.1, while the loading amplitude and area whereover the load is applied remained the same as in the previous chapter.

5.3.1 Propagating crack for the varying deck plate thickness

Using the same approach as in the previous chapter which is XFEM in Abaqus® based on LEFM with the VCCT fracture criterion, the propagating cracks are defined for the *16 mm* and *10 mm* deck plate thickness XFE models. It is known that the automated crack propagation method used here calculates and predicts the crack shape and angle. In Abaqus®, the crack propagation angle is by default obtained as the direction normal to the maximum tangential stress. Hence, the initial predefined cracks in the two models were first inserted with a *30°* with the vertical axis. This is the angle obtained from the cyclic loaded XFE model in chapter 4 It was decided whether or not the initial inserted crack angle should be modified or kept the same after a preliminary analysis was run and the predicted crack angle was obtained. It was found that for the *16 mm* deck plate, there is no need to redefine the crack angle. On the other hand, the *10 mm* deck plate FE model predicted an almost vertical crack.

Figure 5.3 shows the predicted crack angle for the FE model with the *10 mm* deck plate thickness. It can be seen that the crack first started propagating with a *30°* angle at the weld root as this was the predefined angle. Then the software automatically predicted the angle and modified it in an automated way. Due to this predicted behaviour by the software, the initial predefined flaw was then rotated to be vertical instead of the *30°* angle with the vertical axis and the cyclic loading model is rerun to provide an accurate result.

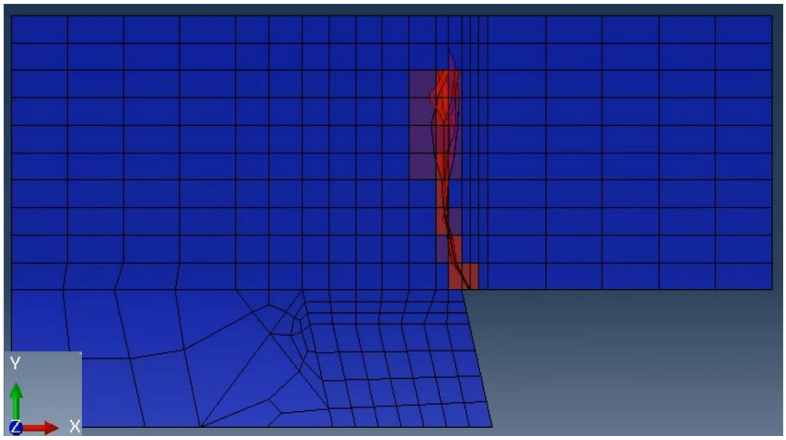

Figure 5.3: 10 mm deck plate predicted crack angle by Abaqus®

Furthermore, the method used is identical to the technique implemented in 4.3.5 for the Cyclic loading analysis. With the same material parameters equal to the parameters used by Maljaars et al. [8] ($C = 1 \cdot 10^{-13}, m = 3.0$) and the same initial crack size used by the final cyclic model in prvious chapter. Hence, the same subroutine is used without any changes.

5.3.2 Finite element mesh

The FE models of the two different deck plate thicknesses considered have almost identical meshing strategies and element sizes to that of the improved *20 mm* cyclic loading OSD model from chapter 4 shown in Figure 4.11. This holds for the meshing of all three parts of the models in the case of the static analysis as can be seen from Table 4.1 and Table 5.2. For the cyclic loading parametric models, slight mesh adjustments in the sub-local parts of these models took place. These slight modifications were done to handle the software limitation since sometimes single elements got intersected by two cracks forcing the analysis to terminate. As a result, the mesh has to be enhanced as shown in Figure 5.4.

The figure shows the mesh of the sub-local part for both *16 mm* and *10 mm* deck plate models. The *16 mm* case has identical meshing to the reference case. There is no need to adjust the mesh here. On the other hand, the mesh had to be adjusted when the deck thickness is reduced to *10 mm* as shown in Figure 5.4 (b). A single biased mesh through the thickness of the deck plate is used having an element size varying from *0.5 mm* to *2.5 mm.* Details about the mesh sizes used in the sub-local part are indicated in Table 5.3. Only the sub-local part is shown in the table because the other parts' meshing is identical to that of the parametric static analysis given in Table 5.2.

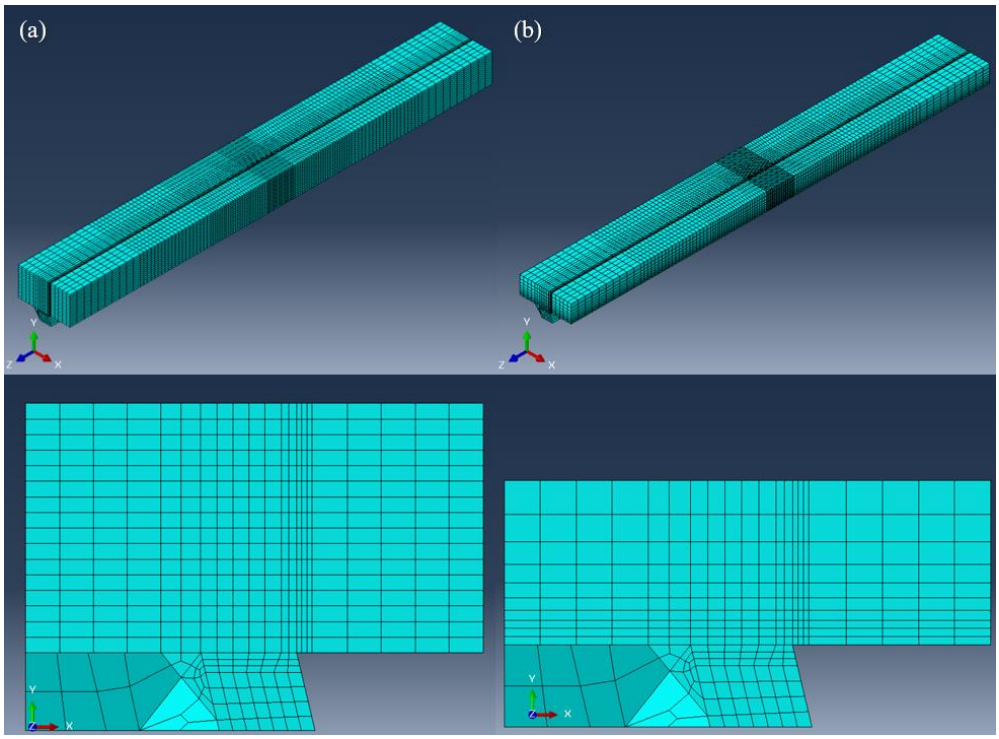

Figure 5.4: Finite element mesh for the sub-local part in parametric models. (a) 16 mm OSD. (b) 10 mm OSD

Table 5.3:Finite element mesh for parametric cyclic loading analysis

Cyclic loading analysis	**Sub-local part**	
	Element size	Interpolation scheme
16 mm deck plate model	0.3 mm to 4 mm & 1 mm element thickness	Linear (C3D8) & (C3D8R)
10 mm deck plate model	0.3 mm to 4 mm & From 0.5 mm to 2.5 mm element thickness	Linear (C3D8) & (C3D8R)

5.4 Results and discussion

The crack shapes and strain changes obtained from the XFE simulations for both deck plate thicknesses considered will be shown here. This numerical output will be compared to experimental tests output done by different researchers for quite some similar deck plate thickness cases.

5.4.1 Crack propagation in the 16 mm thick deck plate

The figure below shows different views of the deformed and undeformed shapes of the propagated crack in the deck plate and rib web. The figure indicates the crack length (*2c*) which is equal to *128 mm.* The crack propagated through the rib web component considered in the sub-local model part. However, the crack did not penetrate through the whole deck plate thickness as it has not reached the deck plate surface. In addition, there is a slight asymmetric crack growth in the length direction of the OSD.

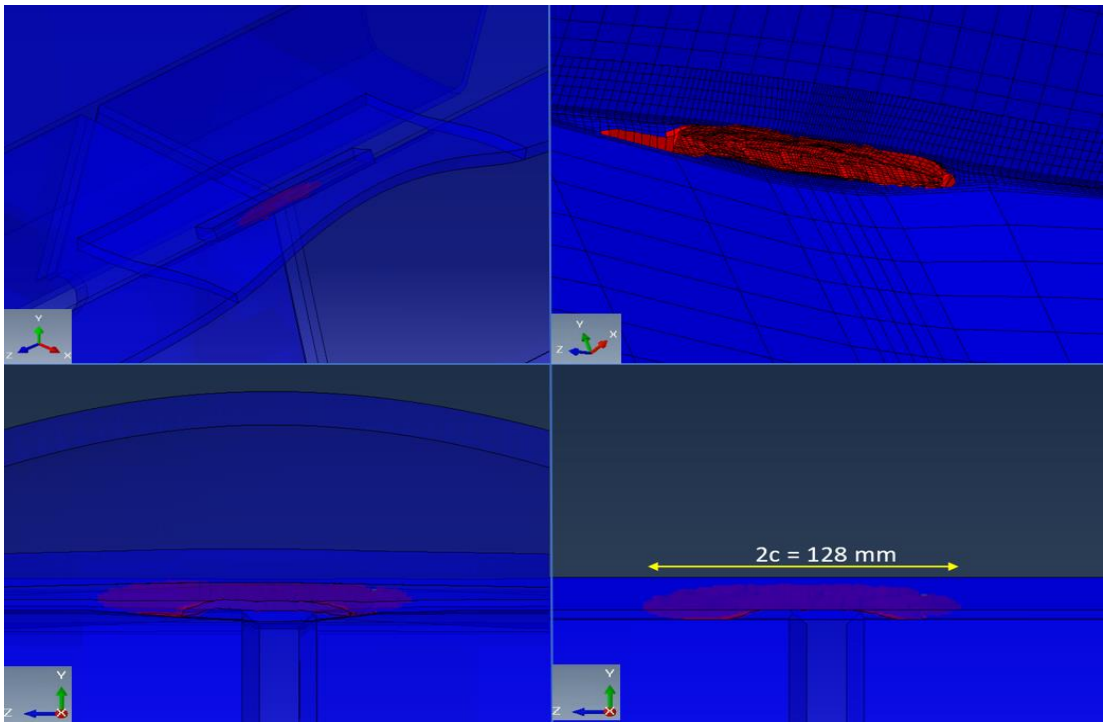

Figure 5.5: Different views of the deformed and undeformed 16 mm OSD

The crack propagation behaviour is similar to the *20 mm* OSD case, especially for the crack propagation in the thickness direction. The crack has an average propagation angle of *22°* as in Figure 5.6 (a). This came very close to the crack propagation angle obtained from the experiment by Harada et al [40] for the same OSD deck plate thickness of *16 mm* with *80 %* partial weld root penetration (see Figure 5.6 (b)). The angle is hardly *24°* and was measured at the center of the detail. The figure shows that the crack changed its propagation angle at the end, starting to propagate in a parallel direction to the deck plate surface.

The crack growth is more thoroughly studied by considering the crack depth and length increase during loading. This is shown in Figure 5.7, where the first figure shows the inclined (*a*) and vertical (*d*) crack depth increase, in addition to the crack length (*2c*) increase with time. The figure is corresponding to Figure 4.27 and it also shows that the crack depth increase behaviour in the case of a *16 mm* deck is similar to that of the *20 mm* OSD since the crack depth growth is categorized also into three zones. Figure 5.7 (b) shows that the crack depth has a high increasing rate from the initial crack size to a depth of *9.1 mm.*

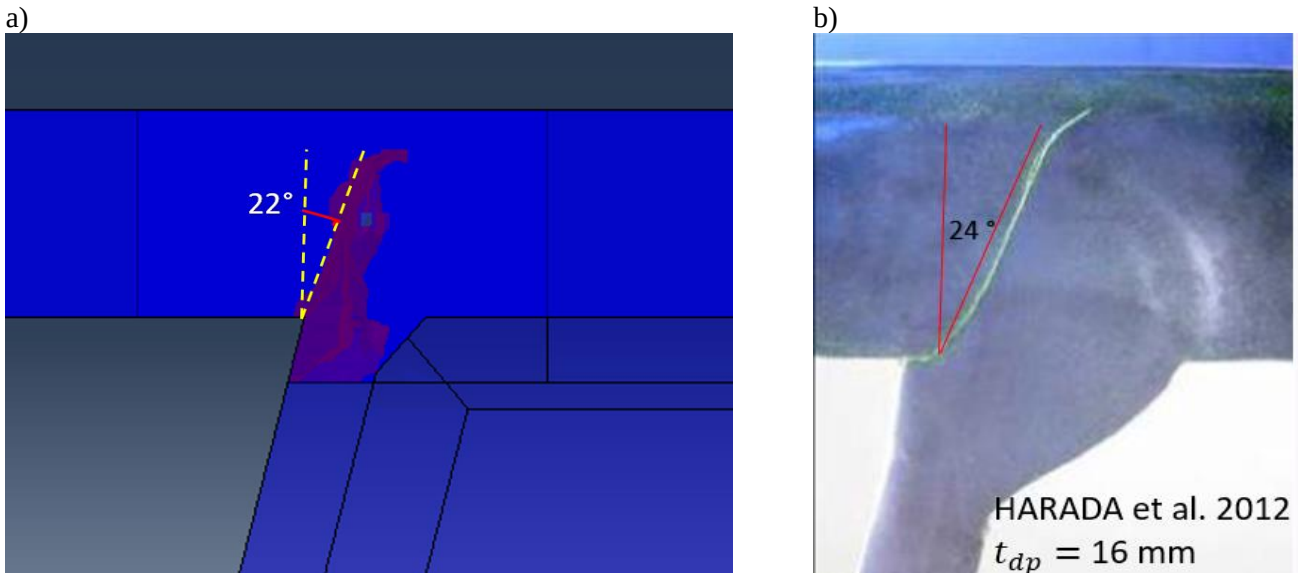

Figure 5.6: Fatigue crack in XFEA and experiment by Harada et al [40]

The increase rate then reduces significantly in a relatively short period till the depth becomes equal to *11.08 mm.* Finally, the depth increase almost stops as the crack gets arrested like in the *20 mm* deck case. The crack depth here also does not reach the deck plate surface. Moreover, the depth increase stops when reaching the value of *11.86 mm.* This value is almost three-fourths the thickness of the deck plate. This is also the case for the *20 mm* deck, as the crack there stopped at a *14.7 mm* depth.

The crack length got larger at a very high speed at the beginning till a *23 mm* length. After that the fracture length changed its increasing slope, having an almost linear increase with time. This nearly constant crack length growth rate remained valid till the end of the simulation and the length reached a value of *128 mm.*

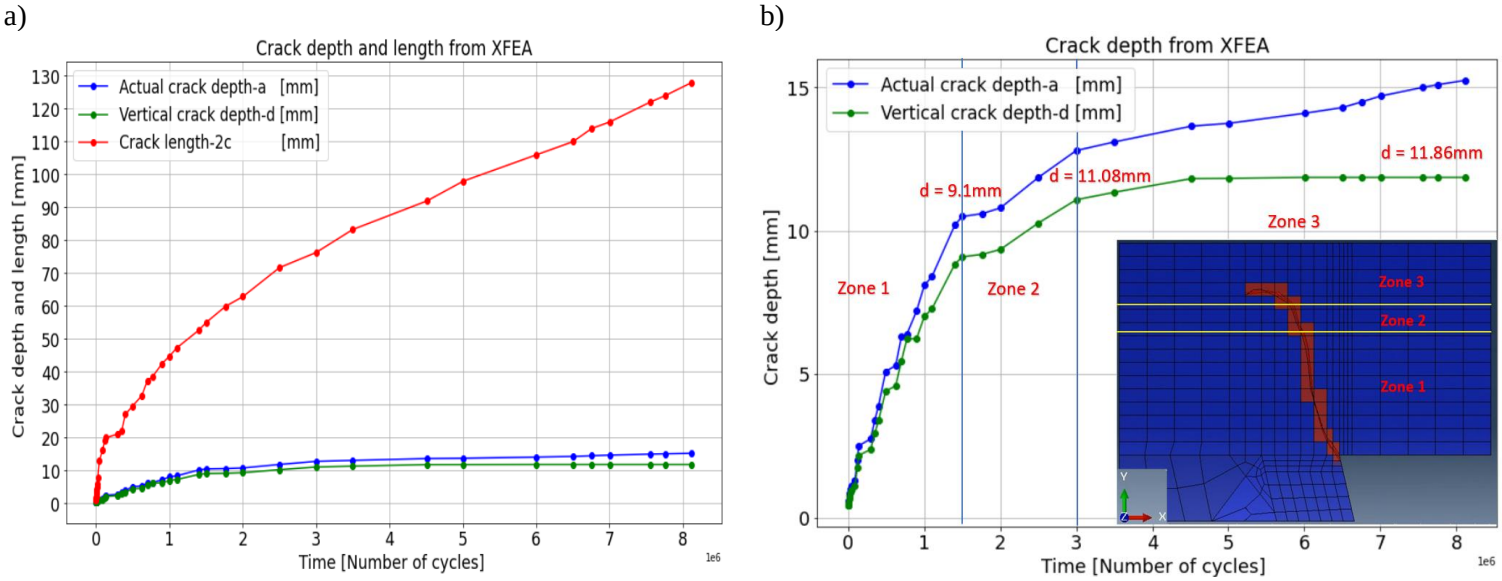

Figure 5.7: Fatigue crack depth and length vs time history of the XFEA (16 mm OSD).
(a) Inclined and vertical crack depth and crack length. (b) Inclined and vertical crack depth only (OSD cut).

5.4.2 Crack propagation in the 10 mm thick deck plate

The propagating crack when the considered deck plate thickness is *10 mm* is shown in Figure 5.8. This figure is analogous to Figure 5.5 which shows the same deformed and undeformed shapes but for the *16 mm* deck case. The crack in the below figure has a semi-elliptic shape which is cut from above. This cut is mainly due to the crack penetration through the deck plate. Unlike the reference case and the case of the *16 mm* deck, here the crack cuts through the total thickness of the deck plate as shown below in Figure 5.8. For a consistent notation, the lower and upper crack lengths have been given the same symbol with different subscripts as shown in the figure, where "c_b" and "c_t" stand for "c_{bottom}" and "c_{top}" respectively.

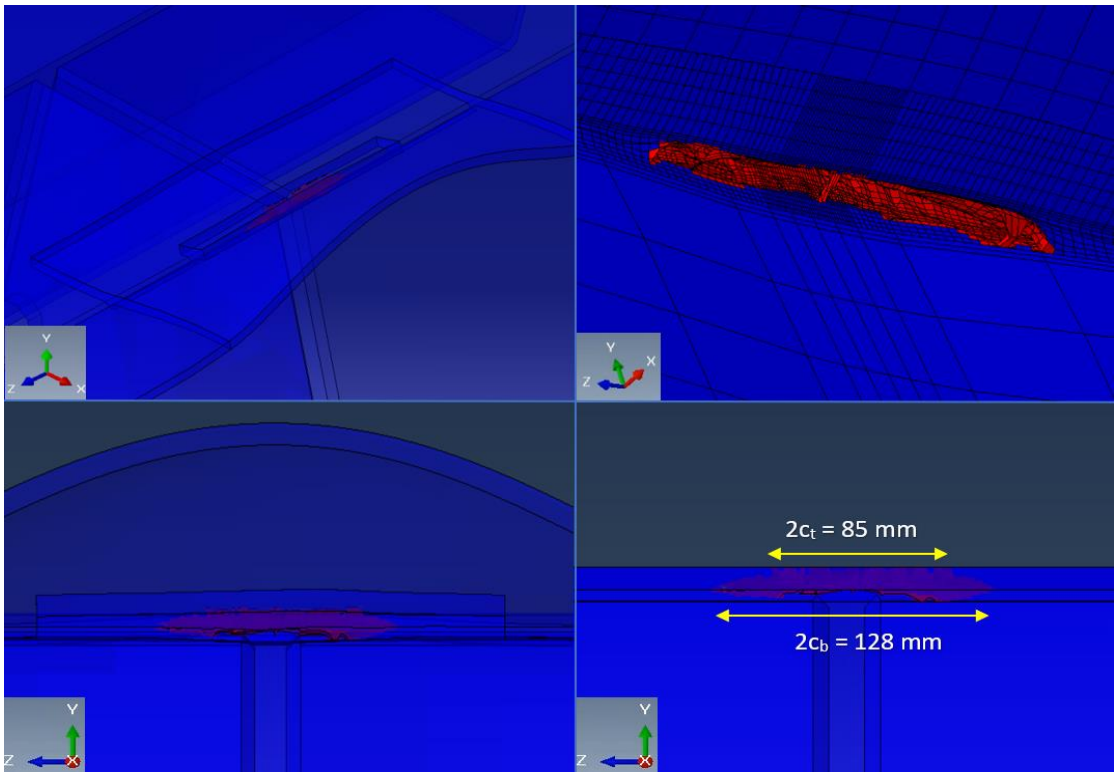

Figure 5.8: Different views of the deformed and undeformed 10 mm OSD

As can be seen from Figure 5.8, the crack has a different behaviour than for the reference and *16 mm* OSD cases. The crack here penetrates through the deck surface after a relatively short while from the crack growth initiation. This leads to that the crack depth parameter becomes fixed after the deck plate is fully penetrated. The crack propagation action has also been shown in Figure 5.9, where the lower and upper crack lengths are plot versus time. In addition, the crack depth is also plotted with its lengths to make a comparison between the depth and length, then it is shown explicitly in Figure 5.9 (b).

It has been found that unlike the reference and *16 mm* case, the crack here behaves dramatically different. The crack depth can be divided into two stages as in Figure 5.9 (b). It starts by propagating in the thickness with a high speed till its depth is almost equal to a third of the deck thickness (*3.2 mm*). Although the initial crack was inserted vertically in the model, the crack propagates with a *14°* angle in the first stage, then the angle changes and becomes nearly *0* ° when entering zone 2. The crack depth increase rate becomes a little bit less in this zone and preserves its slope with minimal fluctuations. This holds until the crack fully penetrates through the deck plate thickness.

Moreover, the crack length increase at the bottom and top of the deck plate is given in Figure 5.9 (a). The length is growing approximately linear at the lower surface of the deck with negligible variation in the increase rate. Furthermore, the crack reaches the deck plate surface and comes to be visible when the lower crack length becomes almost *60 mm*. At this moment the crack depth is *10 mm* at more locations and elements, which means that the crack is perceivable on the deck and has a length of *6 mm*. This takes place at around a third of the time. From the figure, it seems that the upper crack length propagation has a similar linear trend as that for its lower length. If the slight fluctuations are disregarded it can be deduced that both lower ($2c_b$) and upper ($2c_t$) crack lengths have similar propagation rates.

a)

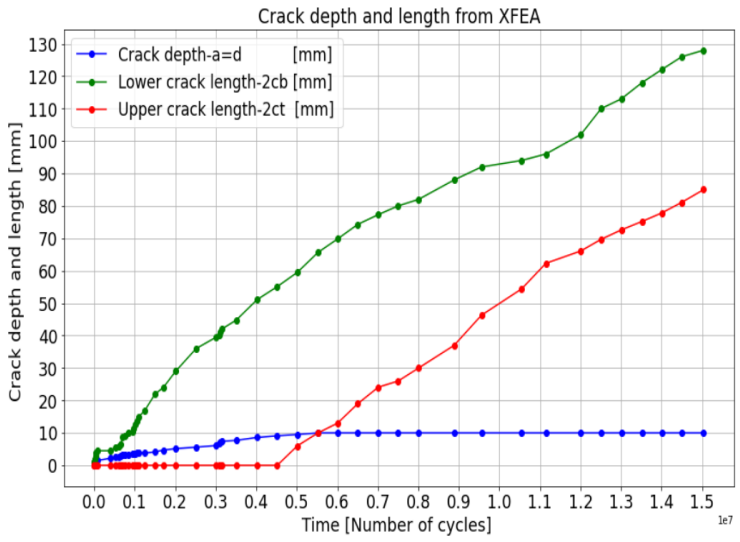

b)

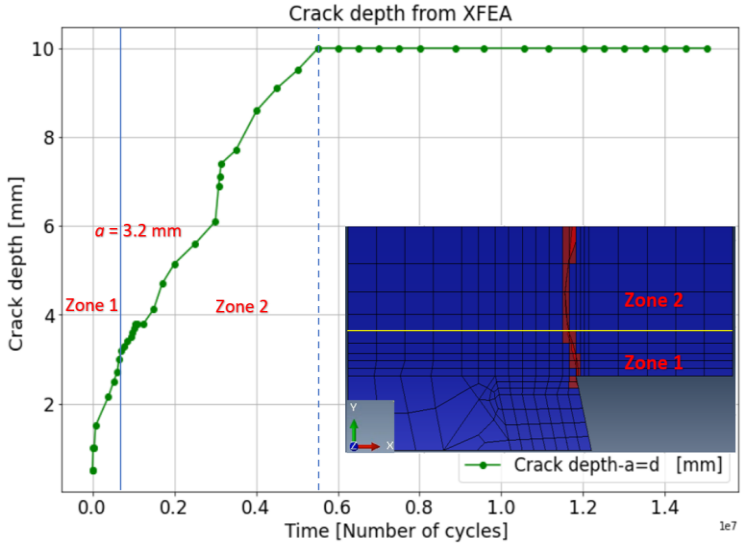

Figure 5.9: Fatigue crack depth and length vs time history of the XFEA (10 mm OSD). (a) Crack depth, lower, and upper crack length. (b) Crack depth only (OSD cut).

In Figure 5.10 the global crack growth phases are shown. As for the crack depth propagation zones, these zones can be sub-listed under phase 2 in Figure 5.10. It should also be mentioned that when studying and measuring the upper crack length, the occurrence of the crack on the top of the deck plate is not as smooth as in reality as the crack at some moments appeared as a set of discrete cracks which over time blended and increased in length to form one long crack with *85 mm* length as shown in Figure 5.11.

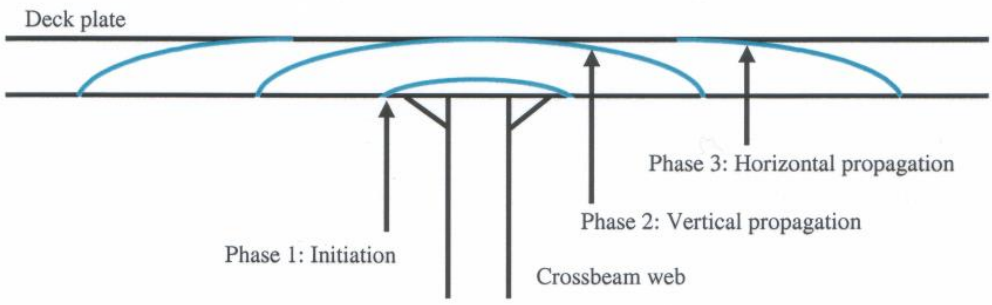

Figure 5.10: Crack propagation stages through the deck plate at the crossbeam [1]

In this figure, the crack shape at the top of the deck surface is qualitatively compared to the crack obtained in the experiment done by De Jong [1]. In the test carried out by De Jong, the rib was filled with polyurethane foam. The upper crack length obtained from the experiment was longer (*208 mm*) than the

one from the XFEM simulation. Both the cracks obtained from the simulation and the experiment have some curvature in the direction of the inner side of the rib. In practice, the investigated crack may be straighter than the ones obtained from the laboratory testing. This was explained by De Jong by mentioning that here the load position is fixed during the experiment and this leads to the rotation of the principal stress in the deck plate towards the crossbeam.

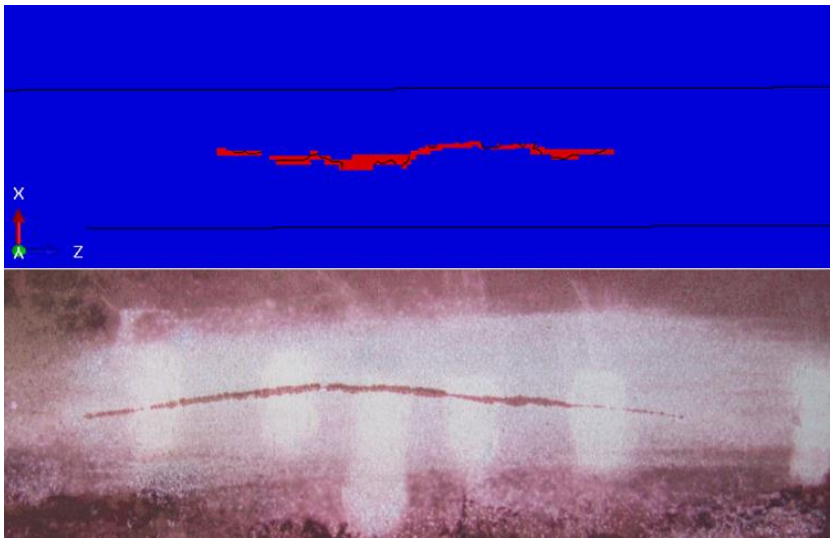

Figure 5.11: Fatigue crack from XFEA and De Jong's [1] *experiment.*

5.4.3 Evolution of strains in XFEA models

The uniaxial (X-direction) strain change due to the crack propagation has been studied here as in the previous chapter (4.4.5). Here only the most representing strain gauge locations are presented, while the rest can be found in appendix C. The strain adaptation is presented as a function of different crack parameters (crack depth and length). For some strain measurements, it is also important to show how the strain evolves with the loading/time history.

Strain ranges on the deck surface in the longitudinal path

Figure 5.12 and Figure 5.13 show the strain evolution for some nodes on path 1 for the *16 mm* and *10 mm* deck thicknesses, respectively. The strain drop behaviour for *0 mm* and ± 25 *mm* when the crack depth is increasing is approaching a linear decrease pattern. This holds until the crack gets arrested in the last zone and the crack depth growth stops. The crack is then arrested in the depth direction while the crack length continues to grow, leading to a strain decrease continuity as in Figure 5.12 (a) and (b) where the strain is reduced by an average of *50%* for the formerly mentioned nodes as in Figure 8.14 in appendix C. As for the ± 50 *mm* nodes, the strain at these nodes will get affected by the fracture when the crack starts to get larger in length. Hence, it can be seen that the strain will start to drop at a length of almost *35 mm* and a depth of approximately *6.2 mm.* Note that there is a difference in the decrease values of the strain of the -50 *mm* and $+50$ *mm* nodes, which is accredited to the asymmetric crack growth.

a)

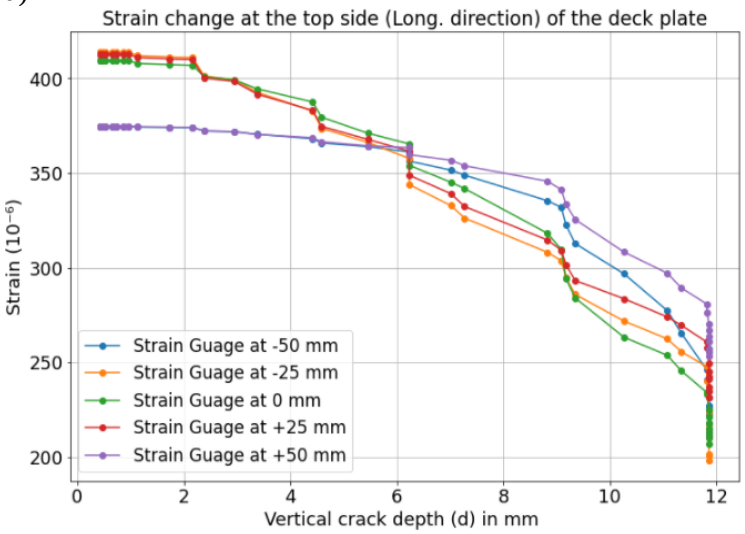

b)

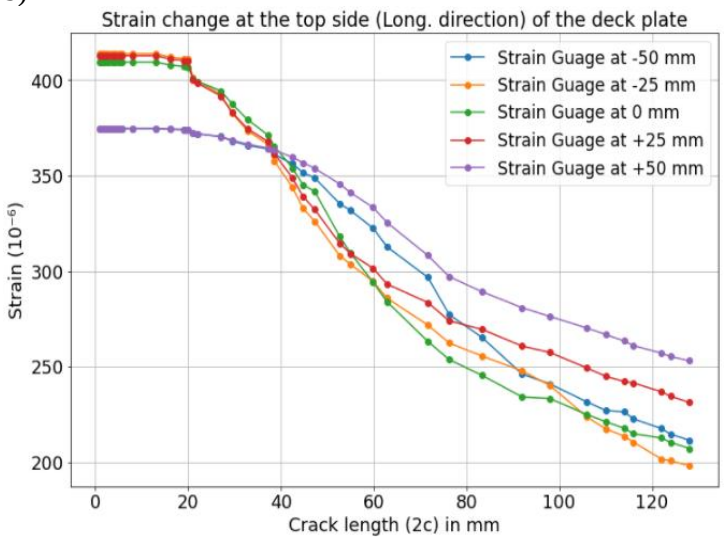

*Figure 5.12: FEA strain change at the top side (longitudinal path) of the **16 mm** deck plate vs; (a) Vertical crack depth [d]. (b) Crack length [2c].*

For the *10 mm* deck plate, first, the strain range at the same locations as in the *16 mm* deck case is presented in Figure 5.13 (a) where the strain range is plotted as a function of the crack depth. The initial strain value at *0 mm* and $\pm$*25 mm* for this case is close to that of the *16 mm.* Unlike the previous two cases, the strain remains almost constant for a larger crack depth in the beginning. Another noticeable difference is that the strain at $\pm$*25 mm* drops earlier than at the *0 mm* dot. However, in the end, the total reduction in strain is largest at the center node (*0 mm*) with a 45 % decrease of strain. Half of this strain decrease happened after the crack fully penetrated through the deck. It is also obvious from the figure that the strain reduces significantly when the crack reaches the deck plate surface. Note that the relative strain ranges for all dots are given in appendix C [Figure 8.19]. For the $\pm$*50 mm* positions, there is very little change in strain till the crack touched the deck plate. Thus, it is decided to leave this dot out in Figure 5.13 (b).

a)

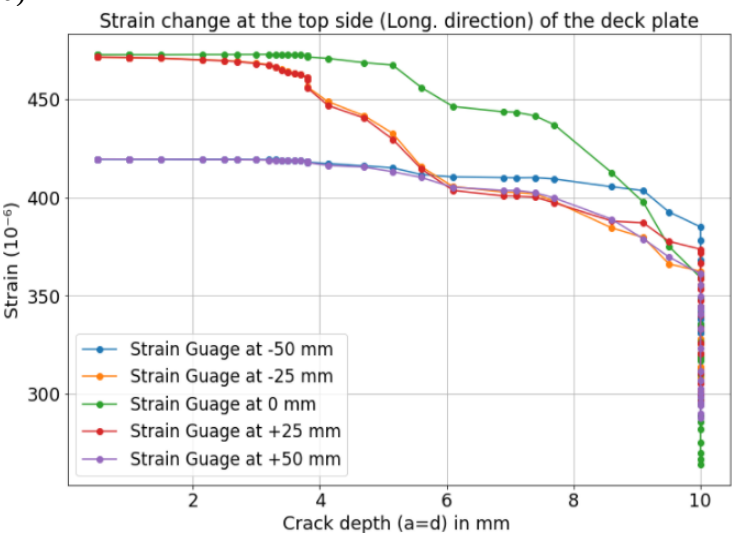

b)

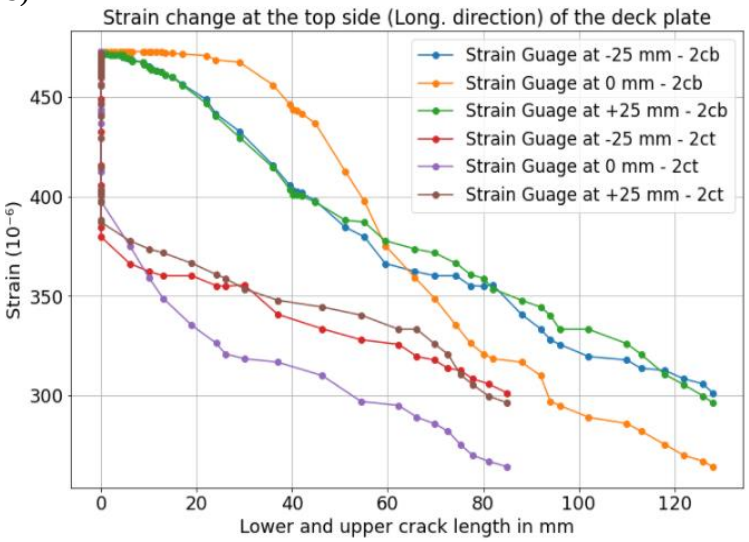

*Figure 5.13: FEA strain change at the top side (longitudinal path) of the **10 mm** deck plate vs; (a) Crack depth [d]. (b) Lower and upper crack length [$2c_b$ & $2c_t$].*

In Figure 5.13 (b), the strain range is plotted with the crack lengths. Both c_b and c_t are considered together in one plot to show the similarities in strain evolution with the crack growing at the top and bottom side of the deck plate. Similar to Figure 5.13 (a), the strain at *0 mm* drops at a larger crack length than that at ± 25 *mm.* This holds for both crack lengths. When the strain change is compared for both, crack lengths at the bottom and top of the deck plate, there is a similar trend in strain change as can be seen in the figure.

Strain ranges in the transverse paths

Figure 5.14 shows the results at the most representing strain gauge locations, while the remaining gauge results can be found in appendix C. In the figure, the strain range at each node is presented for the *16 mm* and *10 mm* decks simultaneously, to point out the differences between both cases. First of all, for both cases, the initial strain values are relatively close for all the measured nodes from both cases. When considering the strain adaptation to the different crack parameters and loading history, it can be seen that the stress/strain redistribution for the parametric models is quite higher than that of the *20 mm* deck plate [see Figure 5.14 (a), (c), and (e)]. This happens at the *0 mm* node where the strain increased by *43 %* and *59 %*, for *16 mm* and *10 mm*, respectively. Thereafter, the strain rapidly drops for the *16 mm* deck when the crack depth exceeds two-thirds of the deck thickness as in Figure 5.14 (a), while the crack becomes almost *72 mm* long [Figure 5.14 (c)]. Figure 5.14 (e) shows that this fall in strain starts at around the third of the crack growth time considered in the analysis. This shows that this node fails after the crack parameters and time have reached such values. Hence, the local strength of the detail is influenced.

On the other hand, from the same three sub-figures, the *10 mm* deck shows an unfamiliar strain behaviour for the last part of the strain change. The strain escalates at the beginning with the increase in loading time and crack's parameters increase having a close pattern to the *16 mm* OSD. Then the strain declines slightly after the crack reaches the deck surface with a crack length of around *66 mm* and it becomes visible from the top of the deck plate. Afterward, the strain redistributes again and increases after a relatively short period of decrease. This is dissimilar to the other two OSD cases where the strain fails once. A possible explanation for this is that when the crack starts to get visible at the deck surface above the cross-beam center location (*0 mm-node*) the strain decreases as that position is losing its stiffness, then when other cracks are forming on the deck surface, the strain at the center node starts to redistribute again. It has been mentioned before that the crack grew discretely at certain periods, leading to separate crack parts at the deck surface before these parts blend into one crack.

Like for the longitudinal path, the strain variation rate for the top crack length is similar to that of the lower crack length. Therefore, these figures are provided in Figure 8.21 (c) in appendix C. Moreover, it should also be mentioned that when selecting the *0 mm* node from the XFE models' output for these two cases, the change of strain shows high sensitivity corresponding to the position at the vicinity of the studied detail center. See Figure 8.22 in appendix C for more details.

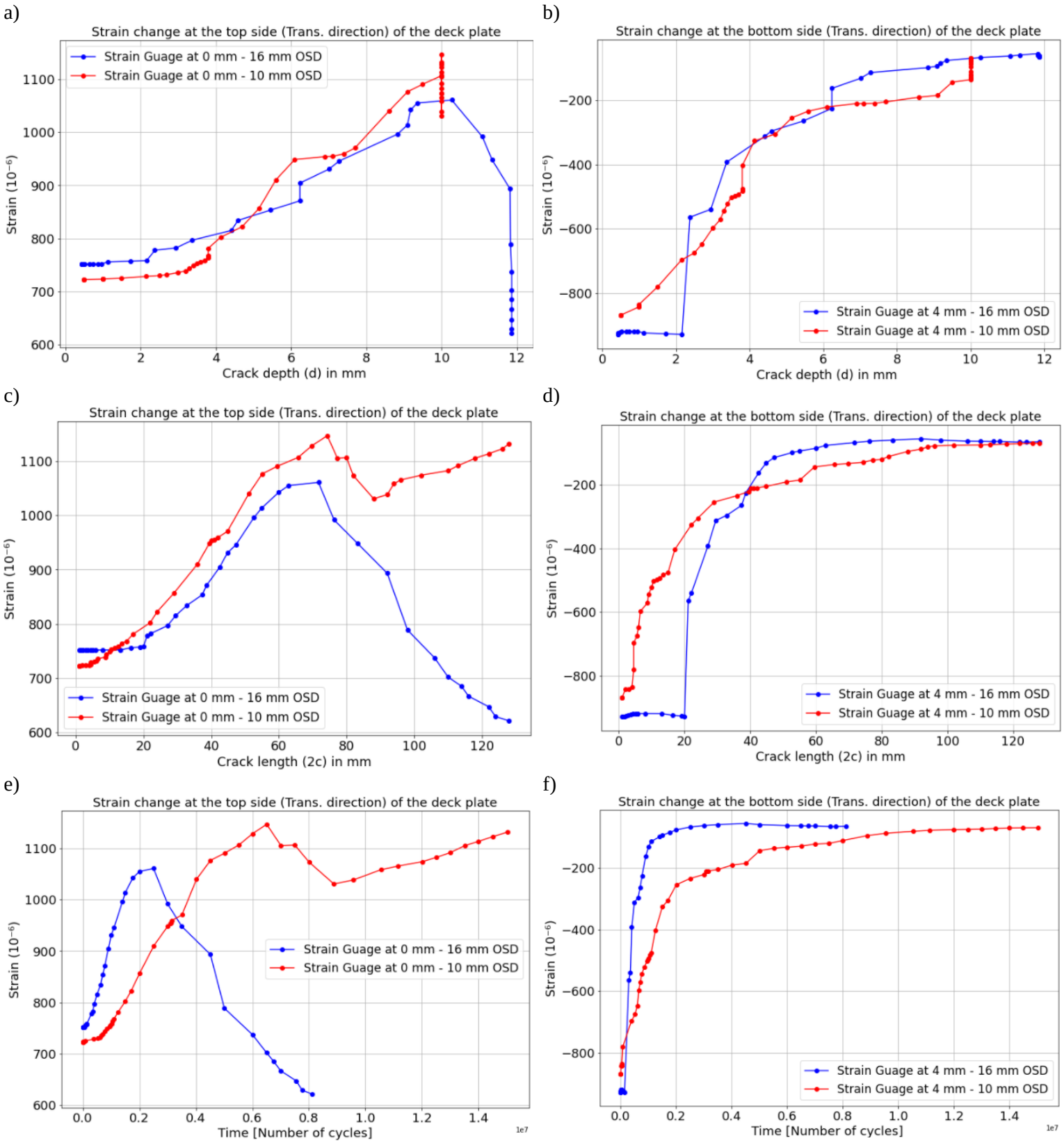

*Figure 5.14: FEA strain change at the top and bottom side of the deck plate (at 0mm & 4mm) for **16 mm** and **10 mm** OSD cases vs; (a) & (b) Crack depth. (c) & (d) Crack length. (e) & (f) Time [Number of cycles].*

Looking at the strain range at *4 mm* from the weld root shown in Figure 5.14 (b), (d), and (f), the strain reduction behaviour is close for both studied deck thicknesses. Figure 5.14 (b) and (d) show that the strain close to the local crack initiation point for the *10 mm* deck drops, in the beginning, faster than that of the *16 mm* deck. In a later stage when the crack depth and length reach around the third of their maximum reached value, the strain decrease rate alters and becomes higher for the *16 mm* instead of the *10 mm* deck. Finally, in both cases, the node lost almost all its stiffness as the strain decreased by *92 %* when the crack reached its maximum obtained depth and length. However, in the *10 mm* deck, the strain is still decreasing after the crack fully penetrated through the deck plate as shown in Figure 5.14 (b).

The *16 mm* deck showed a faster strain decline with loading cycles than the *10 mm* deck. This may not be accurate since the element size through the thickness is slightly changed for the *10 mm* deck model. Besides, it is concluded before that the change of element number through the thickness affects the number of cycles calculated, which is here referred to as the time aspect. From Figure 5.14 (e) and (f), the number of cycles calculated for the *10 mm* OSD model is larger than that for the *16 mm* one. An additional remark about the studied crack parameters with the strain range at this path is that, similar to the other two paths, the strain range as a function of the upper crack length has a convergent behaviour to that of the lower length. The plots considering this parameter and all the nodes on this path are also provided in Figure 8.23 and Figure 8.24 (c) in appendix C for more information.

5.5 Conclusion

In this chapter, a deck thickness parameter of the OSD has been studied for its effect on the fatigue crack propagation at the detail of interest. The deck plate thickness is varied because of its importance for OSD integrity. The deck plate thickness values of *16 mm* and *10 mm* are considered. The *20 mm* OSD case from the previous chapter is taken as a reference for the parameter analysis. The OSD is then modelled in Abaqus® for these two deck thicknesses, while the load applied on the deck plate is changed such that the hot spot stresses remain similar to the HSS in the reference model. Hence, the HSS at the crack initiation point is validated for the two static models. After that, the cyclic loading analyses are carried out for the parametric models by inserting an initial crack with the same size and angle as for the *20 mm* deck plate and using the same approach. The crack angle is changed only when the software predicted a different angle. The analyses' results were post-processed and compared to the crack growth from the *20 mm* OSD analysis and literature. Conclusions of the results are provided below;

- In general, the fatigue crack growth angle, shape, and rate in the case of the *16 mm* deck plate are close to that of the reference case (*20 mm*) as the crack also got arrested at around *75 %* of the deck thickness. In addition, the crack depth growth is divided into three phases as in the 20 mm thick deck plate, while only a small difference in the crack length growth behaviour is noticed.

- The method predicts vertical crack propagation when a *10 mm* deck is analysed. It is also showed that the crack penetrates through the deck plate thickness leading to a through-thickness crack. This crack shape is validated with the literature for the same deck thickness.

- The crack depth growth in the *10 mm* deck plate case is divided into two zones where the first zone is relatively small but has a fast crack depth enlargement, while in the second zone the crack slows down and keeps increasing till the deck plate surface is penetrated. Moreover, the crack growth rate in the length direction is almost constant.

- In general, the considered OSD cases have a common global crack growth behaviour where the crack initiates then increases in the thickness and length direction, then only grows in the length direction. The main difference lies in whether the crack will penetrate through the deck plate and affect the traffic safety more explicitly or will get arrested and not reach the deck surface.

- The strain change behaviour is comparable in all OSD cases including the *20 mm* case at most nodes of paths 1 and 3. The main difference is the thickness influence as the crack depth is different in each case. The node corresponding to the *0 mm* strain gauge has larger differences in the strain change behaviour, as the relative strain redistribution is increasing as the deck thickness decreases. Besides, the strain in the *10 mm* OSD increases again after it is redistributed and declined. This is most likely due to the discrete crack formation at the deck surface before merging into one crack.

6 Conclusions and Recommendations

In this chapter, the final conclusions are given and discussed. In addition, recommendations for further research are provided.

6.1 Conclusions

In this thesis, the main focus is to reliably predict fatigue crack propagation and estimate its influence on structural integrity. This challenge is tackled by considering the following steps to solve the problem.

Firstly, a simple CT case is considered and analyzed using XFEM within the LEFM framework. This is done to understand 9the method of propagating fatigue crack modeling provided in Abaqus®, gaining more confidence in using it, and understanding its limitations. The following is concluded from the CT analyses comparing it to the analytical prediction:

- The 3D fatigue cracks propagation simulation using strain energy release rate calculated from VCCT in Abaqus is sensitive to mesh sizes. The corresponding number of loading cycles extracted from direct cyclic step(s) may be overestimated when a refined mesh is applied and the crack front shape starts to change from a straight line through the thickness to curves.

- From the 3D analysis, considering a single loaded model with a single element through the thickness, the plane strain condition gives the best fit for the fatigue life.

Furthermore, the plane strain condition used to calculate the Paris' law parameters is used for the crack propagation analysis in the OSD model.

Secondly, an approach to model the OSD under tension-tension cyclic load proposed by [] is tested for which the absolute values of SIFs in stationary crack models are compared with the compressive load case. This answers a part of the first sub-research question which reads: "**What approach using XFEM can be used to simulate crack propagation?**". The second part of the subquestion is answered by the conclusion from the CT simulations since a **limitation** of this method was found as the fatigue life is overestimated by the through-thickness mesh refinement. This limitation is relevant for the OSD simulations as well. For the stationary crack analysis, the same absolute SIFs values are found in the two loading situations. Thus, the engineering approach is validated and can be further used to simulate the propagating crack in the studied detail. Consequently, sub-question 2: **How the stationary crack analysis simulated with XFEM and conventional FEM can support using this approach** is answered**.** The conclusions of the *20 mm* OSD crack simulations are given as follows.

- The crack propagation shape, angle, and rate are predicted and have a good agreement with experimental observation. The crack has a semi-elliptical shape and an average angle of *28°* to the vertical axis. In addition, the crack propagation rate in the depth direction consists of three zones, starting from a high rate, then smaller and very small. Finally, the crack arrest occurs.

- The strain evolution is validated for the two significant nodes having the same positions of the corresponding strain gauges in their experimental arrangement. The strain difference ratios at the node on the deck surface (*0 mm*) vary from *7.8 %* to *25 %* for the initial to minimum strain value, while the differences for the node at the lower deck side (*4 mm*) are from *7.7 %* to *8.4 %* for the same strain values.

- In the studied detail, the simulation shows that the crack propagates in the rib in addition to propagating in the thickness of the deck plate. Similar cracks are observed in the tested specimens. However, there are some differences found in the positions and sizes for the rib crack between the simulation and experimental investigation.

Since the considered methodology is validated for the *20 mm* OSD deck plate in predicting the crack behaviour, two deck plate thicknesses are studied to investigate the effect of the deck thickness on the crack behaviour and structural integrity. The conclusions obtained by simulating the OSDs with *16 mm* and *10 mm* thickness are given below.

- In the *16 mm* OSD deck plate, the crack shows similar behaviour as in the *20 mm* deck plate, as the crack is arrested at *75%* of the thickness and has an average angle of *22°*. The same conclusion was found in the literature. In addition, the crack depth growth for the *16 mm* deck plate can also be classified by the same three zones as in the *20 mm* deck case.

- For the *10 mm* OSD deck plate, the crack propagates vertically in the deck plate and the crack depth growth is divided into two zones. The crack depth has a high growth rate in zone 1 which reduces slightly when moving to zone 2 where the crack depth is almost 1/3 of the deck thickness. In this zone, the crack penetrates completely through the deck plate thickness leading to a surface crack that may affect traffic safety. The crack length increase rate is nearly constant throughout the total propagated length.

- A comparable strain evolution is obtained for all OSD deck plates including the *20 mm* deck. However, an inverse relationship between the deck plate thickness and the relative redistribution of strain is found. Moreover, the *10 mm* deck plate strain evolution on top of the deck (*0 mm*) is different after the crack propagates through the total thickness of the deck plate.

Considering the investigated cracks from the three studied OSD deck plates in this thesis. **The behaviour of the crack propagation for the detail with these different deck plate thicknesses** is interpreted. Thus, the third and final sub-research question is answered. It is demonstrated by these concluding remarks, that the method investigated has an acceptable level of accuracy for the investigated cracks. Hence, the crack behavior, as well as the local structural integrity, can be predicted. This finally leads to the answer to the main research question which is presented below.

How is the structural integrity affected by the propagation of fatigue cracks at the rib-to-deck plate welded connection at the crossbeam junction?

The structural integrity of the *16 mm* and *20 mm* thick steel decks is satisfactory because the crack is arrested, while the *10 mm* thick deck plate safety is not validated.

6.2 Recommendations

For the CT simulation the following recommendation can be provided;

- The unstable crack growth region at the end of the fatigue life can be accurately simulated using elastic-plastic fracture mechanics (EPFM) theory.

The following recommendations could be given for further studies based on the OSD XFEA results.

- Using a larger part for the activated crack zone can be better, since this may help to detect and study the macro crack shape when it propagates and transcend the sub-local part's boundaries.

- The use of finer mesh will certainly lead to more realistic and more accurate results.

- Fatigue crack propagation analysis with experimentally obtained material properties needs to be carried out using LEFM. Accurate SIFs along the crack should be guaranteed. The crack front needs to be propagated at all the calculated points using the fatigue propagation method, e.g. Paris' law.

- Taking the welding penetration rates and welding-induced residual stress into account for the crack propagation analysis.

7 References

[1] de Jong FBP. Renovation techniques for fatigue cracked orthotropic steel bridge decks. TU Delft, 2007. https://doi.org/resolver.tudelft.nl/uuid:239bdb2c-b59f-40d2-91b7-367139dbad13.

[2] Maljaars J, van Dooren F, Kolstein H. Fatigue assessment for deck plates in orthotropic bridge decks. Steel Constr 2012;5:93–100. https://doi.org/10.1002/stco.201210011.

[3] Xiao ZG, Yamada K, Ya S, Zhao XL. Stress analyses and fatigue evaluation of rib-to-deck joints in steel orthotropic decks. Int J Fatigue 2008;30:1387–97. https://doi.org/10.1016/j.ijfatigue.2007.10.008.

[4] Zhuang M, Miao C, Chen R. Analysis for Stress Characteristics and Structural Parameters Optimization in Orthotropic Steel Box Girders based on Fatigue Performance. KSCE J Civ Eng 2019;23:2598–607. https://doi.org/10.1007/s12205-019-1618-5.

[5] Robert Connor, John Fisher, Walter Gatti, Vellore Gopalaratnam, Brian Kozy, Brian Leshko, David L. McQuaid, Ronald Medlock, Dennis Mertz, Thomas Murphy, Duncan Paterson, Ove Sorensen JY. Manual for Design, Construction, and Maintenance of Orthotropic Steel Deck Bridges 2012:291.

[6] Zhang QH, Bu YZ, Li Q. Review on Fatigue Problems of Orthotropic Steel Bridge Deck. Zhongguo Gonglu Xuebao/China J Highw Transp 2017;30.

[7] De Jong FBP. Overview fatigue phenomenon in orthotropic bridge decks in the Netherlands. 2004 Orthotropic Bridg Conf 2004:489–512.

[8] Maljaars J, Bonet E, Pijpers RJM. Fatigue resistance of the deck plate in steel orthotropic deck structures. Eng Fract Mech 2018;201:214–28. https://doi.org/10.1016/j.engfracmech.2018.06.014.

[9] Anderson TL. FRACTURE MECHANICS Fundamentals and Applications. Fourth Edi. 1995.

[10] Correia JAF de O. an Integral Probabilistic Approach for 2014.

[11] Niemi E, Fricke W, Maddox SJ. Fatigue Analysis of Welded Components: Designer's Guide to the Structural Hot-Spot Stress Approach. 2006. https://doi.org/10.1533/9781845696665.

[12] A. Hobbacher. IIW document IIW-1823-07 FATIGUE DESIGN OF WELDED 2008.

[13] Eurocode V. NEN-EN 1993-1-9 2003;9.

[14] NEN-EN V, Delft TU. NEN-EN 1993-2 + C1 / NB 2020.

[15] Hellen T. How to undertake fracture mechanics analysis with finite elements. NAFEMS; 2001.

[16] J.R.Rice. "A Path Independent Integral and the Approximate Analysis of Strain Concentration by Notches and Cracks." J Appl Mech 1968;35:379.

[17] Shih CF, Asaro RJ. Elastic-plastic analysis of cracks on bimaterial interfaces: part I—small scale yielding 1988.

[18] Erdogan F, Sih GC. On the crack extension in plates under plane loading and transverse shear 1963.

[19] Paris PC, Gomez MP, Anderson WE. A rational analytical theory of fatigue the trend in engineering. U Washington, Seattle, Wa 1961;13.

[20] Schijve J. Fatigue of Structures and Materials. vol. 53. 2013. https://doi.org/10.1017/CBO9781107415324.004.

[21] Xin Haohui, Correia José A.F.O. VM. three-dimensional Fatigue Crack Propagation Simulation Using Extended Finite Element Methods for Steel Grades S355 and S690 Considering Mean Stress Effects. Engineering Structures. Eng Struct 2020;In press. https://doi.org/10.1016/j.engstruct.2020.111414.

[22] Nagy W. Fatigue Assessment of Orthotropic Steel Decks Based on Fracture Mechanics. Wim Nagy; 2017.

[23] ELBER W. Fatigue Crack Closure Under Cyclic Tension. Eng Fract Mech 1970;2:37–44. https://doi.org/10.1016/0013-7944(70)90028-7.

[24] Moës N, Dolbow J, Belytschko T. A finite element method for crack growth without remeshing. Int J Numer Methods Eng 1999;46:131–50. https://doi.org/10.1002/(SICI)1097-0207(19990910)46:1<131::AID-NME726>3.0.CO;2-J.

[25] Wang Y, Wang Z, Zheng Y. Analysis of Fatigue Crack Propagation of an Orthotropic Bridge Deck Based on the Extended Finite Element Method. Adv Civ Eng 2019;2019:80–90. https://doi.org/10.1155/2019/6319821.

[26] Systèmes D. Volume II: Analysis. ABAQUS 614 Anal User's Guid 2014;II.

[27] Xin H, Veljkovic M. Fatigue crack initiation prediction using phantom nodes-based extended finite element method for S355 and S690 steel grades. Eng Fract Mech 2019;214:164–76. https://doi.org/10.1016/j.engfracmech.2019.04.026.

[28] Benzeggagh M, Kenane M. MEASUREMENT OF MIXED-MODE DELAMINATION FRACTURE TOUGHNESS OF UNIDIRECTIONAL GLASS/EPOXY COMPOSITES WITH MIXED-MODE BENDING APPARATUS 1963;24:859–65.

[29] Wu EM, Reuter Jr. RC. Crack Extension in Fiberglass Reinforced Plastics. Spons by US Bur Nav Weapons, Rep No 275, Illinois Univ Urbana Dept Theor Appl Mech 1965:32.

[30] Reeder J, Song K, Chunchu P, Ambur D. Postbuckling and growth of delaminations in composite plates subjected to axial compression. 43rd AIAA/ASME/ASCE/AHS/ASC Struct. Struct. Dyn. Mater. Conf., 2002, p. 1746.

[31] Osher S, Sethian JA. Fronts propagating with curvature-dependent speed: Algorithms based on Hamilton-Jacobi formulations. J Comput Phys 1988;79:12–49. https://doi.org/10.1016/0021-9991(88)90002-2.

[32] ASTM E647−13. Standard Test Method for Measurement of Fatigue Crack Growth Rates. Am Soc Test Mater 2014;03:1–50.

[33] Bajpai A, Martin R, Faria H, Ibarboure E, Carlotti S. Epoxy based hybrid nanocomposites: Fracture mechanisms, tensile properties and electrical properties. Mater Today Proc 2020. https://doi.org/10.1016/j.matpr.2020.02.797.

[34] Standardization IO for. BS 7910:2005 Guide to methods for assessing the acceptability of flaws in

metallic structures 2005;3.

[35] Harris WJ. Metal Fatigue. N. E. Frost, K. J. Marsh and L. P. Pook. Clarendon Press, Oxford. 1974. Aeronaut J 1975;79:275–275. https://doi.org/10.1017/S000192400003548X.

[36] Pook L. Metal fatigue what it is, Why it matters. vol. 145. 2007.

[37] Wu W, Kolstein H, Veljković M, Pijpers R, Vorstenbosch-Krabbe J. 09.04: Fatigue behaviour of the closed rib to deck and crossbeam joint in a newly designed orthotropic bridge deck. Ce/Papers 2017;1:2378–87. https://doi.org/10.1002/cepa.285.

[38] Teixeira de Freitas S. Steel plate reinforcement of orthotropic bridge decks. TU Delft; 2012.

[39] Dung CV, Sasaki E, Tajima K, Suzuki T. Investigations on the effect of weld penetration on fatigue strength of rib-to-deck welded joints in orthotropic steel decks. Int J Steel Struct 2015;15:299–310. https://doi.org/10.1007/s13296-014-1103-4.

[40] Hideaki Harada, Takeshi Mori, Uchida Daisuke YK. Influence of the deck plate thickness and scallop on initiation and propagation behaviour of crack penetrating into steel deck plate at connection with transverse rib and through rib. Steel Constr Eng 2012. https://doi.org/https://doi.org/10.11273/jssc.19.73_65.

8 Appendix

(A) Fatigue Crack Propagation In CT

Stationary crack analysis

As mentioned in chapter 3 a comparison between the static models is done to validate that the SIF values in the static XFE model are similar to the SIF values in the FE model. Hence, the XFEM can be used for the propagating crack model. The SIF values are evaluated using the contour integral evaluation.

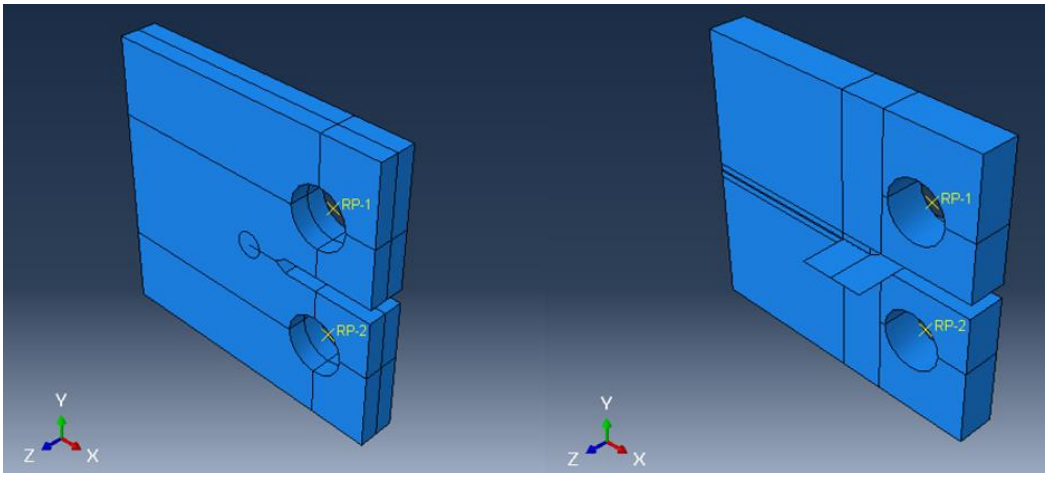

Figure 8.1: FE and XFE 3D-models (CT)

A 0.25 mm element size is used in both models in the local (crack front) region, while a 2 mm global mesh is used as can be seen in Figure 8.2.

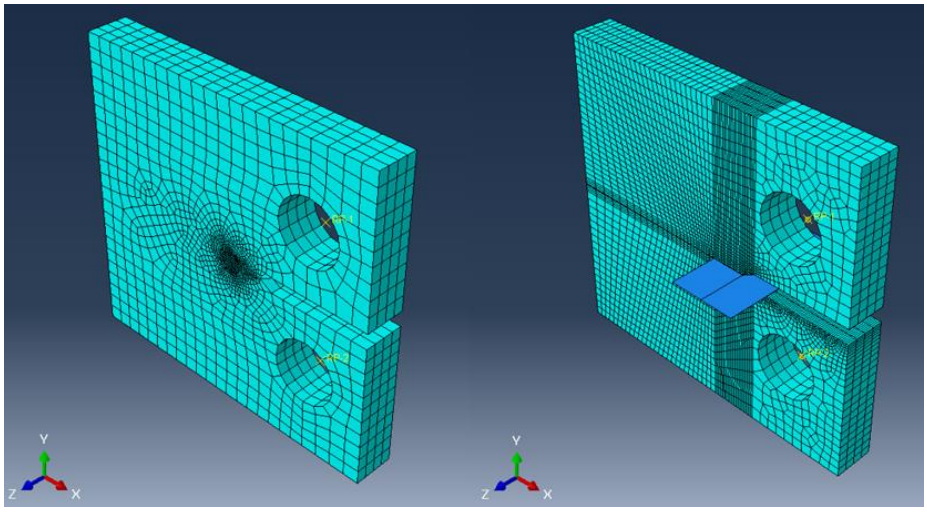

Figure 8.2: FE and XFE models' meshes

Table 8.1: SIF values for FE model

Contour number	1	2	3	4	5	Average
Finite element K_I ($MPa\sqrt{mm}$)						
-6-	418.5	603.3	610	611.9	613.1	571.36
-7-	431.5	623.5	630.6	632.6	633.9	590.42
-8-	445	642.1	649.7	651.9	653.2	608.38
-9-	431.5	623.6	630.7	632.6	633.9	590.46
-10-	418.5	603.3	610	611.9	613.1	571.36
	Total average					586.4

Table 8.2: SIF values for XFE model

Contour number	1	2	3	4	5	Average
Extended finite element K_I ($MPa\sqrt{mm}$)						
1	588.7	592.4	571.5	558.3	631	588.38
2	671.5	627	653.3	651.5	649.6	650.58
3	697.1	593.1	641.7	628.7	638.4	639.8
4	732.1	593.3	659.9	634.8	642.9	652.6
5	581.1	593.8	543.4	471.4	507.4	539.42
	Total average					614.2

Boundary conditions for CT

A short sensitivity analysis is carried out by comparing the results from two cases. The first case is applying boundaries at two reference points as in Figure 8.3 (a), while the second case is applying an extra boundary point at the center of the CT backside (RP-3) as in Figure 8.3 (b).

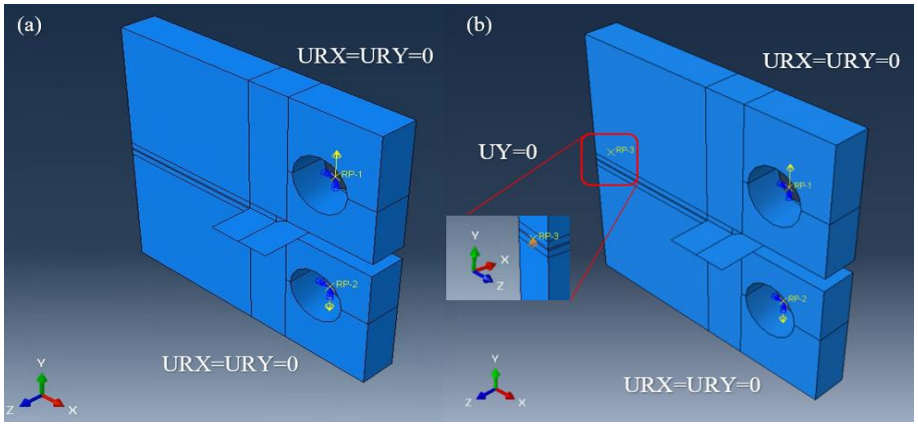

Figure 8.3: 3D double-loaded CT FE-model with different BCs. (a) Two boundary points. (b) Three boundary points

Table 8.3: Boundary conditions for CT in case of 2 boundary points

RP-1 (upper point)	RP-2 (lower point)	N (cycles)
URX=URY=0	URX=URY=0	39638
UX=UZ=0	UX=UZ=0	41427
UX=UZ=URX=URY=0	UX=UZ=URX=URY=0	41414
URX=0	URX=0	40868
UZ=URY=0	UZ=URY=0	40826
UZ=0	UZ=0	41092
UZ=URX=0	UZ=URX=0	40567
UZ=URX=URY=0	UZ=URX=URY=0	40569
UX=UZ=URX=0	UX=UZ=URX=0	41376
UX=UZ=URY=0	UX=UZ=URY=0	41419

Table 8.4: Boundary conditions for CT in case of 3 boundary points

RP-1 (upper point)	RP-2 (lower point)	RP-3 (Back pin)	N (cycles)
URX=URY=0	URX=URY=0	UY = 0	39783
URX=URY=0	URX=URY=0	UZ = 0	42010
URX=URY=0	URX=URY=0	URX=URY=0	42258
URX=URY=0	URX=URY=0	UY = URX = 0	40846
URX=URY=0	URX=URY=0	UY = URY = 0	40174
URX=URY=0	URX=URY=0	UY = URZ = 0	42542
URX=URY=0	URX=URY=0	UX = UY = 0	40876
URX=URY=0	URX=URY=0	UY = UZ = 0	40331
URX=URY=0	URX=URY=0	UY = URX = URY = 0	40334
URX=URY=0	URX=URY=0	UY = UZ = URX = URY =0	40515

Analytical fatigue life and crack propagation rate calculation for CT

Parameters input

```
a0, da, a, ai, astart,  amax = 12.5, 0, 0, 0.1, 5, 36.5
```

```
W, B, F,da1, C, m, nmax, E = 37.5, 6, 3600, 0.1, 5.21 *10e-14, 3, 100000000, 210000
```

Crack size calculation

```
def ac(a0, da, a, ai):
    atot = []
    while a < amax:
        da += ai
        a = a0 + da

        atot.append(a)
    atot.insert(0,a0)
    at=np.around(atot,1)
    return at
```

```
af = ac(a0, da, a, ai)
#print(af)
len(af)
a_step = [ai for i in range(len(af))]
#print(len(a_step))
```

Cycle Number calculation and cummulative number of cycles after each increment

```
def Nc(a0,W,B,F,da1,C,m,nmax):
    Nt = []

    for i in range(len(af)):
        N = ((B**m)*(W**(m/2))*((1-af[i]/W)**(1.5*m))*da1) / (((F**m)*C*(2+af[i]/W)**m) *
            ((0.886+4.64*(af[i]/W)-13.32*((af[i]/W)**2)+14.72*((af[i]/W)**3)-5.6*((af[i]/W)**4))**m))

        Nt.append(N)
        n = np.around(Nt, 2)


    return n

nf = Nc(a0, W, B, F, da1, C, m, nmax)


summ = 0

for j in range(len(nf)):
    summ = summ + nf[j]
    print(f"The total number of cycles after {j+1} load increments is {summ}")
    print(f"The number of cycles associated with increment {j+1} is {nf[j]}")
    if summ > nmax:
        break
```

```
nc = []
c = 0
for i in range(len(nf)):
    c += nf[i]
    nc.append(c)
ncf = np.around(nc, 2)

#len(nc)
ncf = [round(num, 2) for num in nc]
#print(ncf)
```

Stress intensity factor (SIF) calculation and cummulative SIF after each increment

```
def Kc(a0,W,B,F,C,m):
    Kt = []

    for i in range(len(af)):
        K = ((F*(2+af[i]/W)) * (0.886+4.64*(af[i]/W)-13.32*((af[i]/W)**2)+14.72*((af[i]/W)**3)-5.6*((af[i]/W)**4)))
        /(B*(W**0.5)*((1-af[i]/W)**1.5))

        Kt.append(K)
        Kr = np.around(Kt, 3)

    return Kr

KI = Kc(a0,W,B,F,C,m)

summ = 0
summn = 0

for j in range(len(nf)):
    summ = summ + KI[j]
    summn = summn + nf[j]
    #print(f"The total SIF after {j+1} load increments is {summ}")
    print(f"The SIF associated with increment {j+1} is {KI[j]}")
    if summn > nmax:
        break
```

```
dadN = []

for i in range(len(a_step)):
    DADN = a_step[i]/nf[i]
    dadN.append(DADN)

for i in range(len(dadN)):
    if dadN[i]== 0.01:
        print(i)
#print(dadN)
```

Fatigue MIXMODE subroutine (CT)

Plane strain and plane stress situations for both 2D and 3D XFE models of the CT were considered. Thus, all 4 subroutines are provided here.

1. **2D plane strain**

```
      SUBROUTINE UMIXMODEFATIGUE (DADN, GI_MAX, GII_MAX, GIII_MAX,
     1 GI_MIN, GII_MIN, GIII_MIN, TEMP, DTEMP, PREDEF, DPRED,
     2 NFIELD, NPROPS, PROPS, NSTATV, STATEV,
     3 NIARRAY, I_ARRAY, NRARRAY, R_ARRAY, NCARRAY, C_ARRAY, DA)

      INCLUDE 'ABA_PARAM.INC'

C
      DIMENSION PROPS(NPROPS),STATEV(NSTATV),PREDEF(NFIELD),
     1 DPRED(NFIELD),I_ARRAY(NIARRAY), R_ARRAY(NRARRAY),
     2 C_ARRAY(NCARRAY)
C
C     rC3=5.7757D-05
      rC=5.21D-13
      rm=3.0
      rE=210000
      rv=0.3
      rE2=rE/(1-0.3**2) !PLANE STRAIN
      ru=rE2/(2*(1+rv))
CCCCCCCCCCCCCCCCCCCCCCCCC
CCCCCCCCCCCCCCCCCCCCCCCCCCCCCCCCCCCCCCCCCCCCCCCCCCCCCCCCCCCC
CCCCCC
c     G1=K1**2/E2, G_2=K_2**2/E2, G_3=K_3**2/2u, u=E2/(2*(1+v))
      rKI_MAX=(GI_MAX*rE2)**0.5
      rKII_MAX=(GII_MAX*rE2)**0.5
CCCCCCCCCCCCCCCCCCCCCCCCC
      rKI_MIN=0
      rKII_MIN=0
CCCCCCCCCCCCCCCCCCCCCCCCCCCCCCCCCCCCCCCCCCCCCCCCCCCCCCCCCCCC
CCCCCC
      rKI_range=rKI_MAX-rKI_MIN
      rKII_range=rKII_MAX-rKII_MIN
CCCCCCCCCCCCCCCCCCCCCCCCCCCCCCCCCCCCCCCCCCCCCCCCCCCCCCCCCCCC
CCCCCC
      rK_eq=(rKI_range**2+rKII_range**2)**0.5
      DADN=rC*rK_eq**rm
C
      RETURN
      END
```

2. **2D plane stress**

```
      SUBROUTINE UMIXMODEFATIGUE (DADN, GI_MAX, GII_MAX, GIII_MAX,
     1 GI_MIN, GII_MIN, GIII_MIN, TEMP, DTEMP, PREDEF, DPRED,
     2 NFIELD, NPROPS, PROPS, NSTATV, STATEV,
     3 NIARRAY, I_ARRAY, NRARRAY, R_ARRAY, NCARRAY, C_ARRAY, DA)

      INCLUDE 'ABA_PARAM.INC'

C
      DIMENSION PROPS(NPROPS),STATEV(NSTATV),PREDEF(NFIELD),
     1 DPRED(NFIELD),I_ARRAY(NIARRAY), R_ARRAY(NRARRAY),
     2 C_ARRAY(NCARRAY)
C
C     rC3=5.7757D-05
      rC=5.21D-13
      rm=3.0
      rE=210000
      rv=0.3
      rE2=rE/(1-0.0**2) !PLANE STRESS
      ru=rE2/(2*(1+rv))
CCCCCCCCCCCCCCCCCCCCCCC
CCCCCCCCCCCCCCCCCCCCCCCCCCCCCCCCCCCCCCCCCCCCCCCCCCCCCCCCCCCCCCCCCCCCCCCCCC
CCCCCC
c     G1=K1**2/E2, G_2=K_2**2/E2, G_3=K_3**2/2u, u=E2/(2*(1+v))
      rKI_MAX=(GI_MAX*rE2)**0.5
      rKII_MAX=(GII_MAX*rE2)**0.5
CCCCCCCCCCCCCCCCCCCCCCCCC
      rKI_MIN=0
      rKII_MIN=0
CCCCCCCCCCCCCCCCCCCCCCCCCCCCCCCCCCCCCCCCCCCCCCCCCCCCCCCCCCCCCCCCCCCCCCCCCC
CCCCCC
      rKI_range=rKI_MAX-rKI_MIN
      rKII_range=rKII_MAX-rKII_MIN
CCCCCCCCCCCCCCCCCCCCCCCCCCCCCCCCCCCCCCCCCCCCCCCCCCCCCCCCCCCCCCCCCCCCCCCCCC
CCCCCC
      rK_eq=(rKI_range**2+rKII_range**2)**0.5
      DADN=rC*rK_eq**rm
C
      RETURN
      END
```

3. **3D plane strain**

```
      SUBROUTINE UMIXMODEFATIGUE (DADN, GI_MAX, GII_MAX, GIII_MAX,
     1 GI_MIN, GII_MIN, GIII_MIN, TEMP, DTEMP, PREDEF, DPRED,
     2 NFIELD, NPROPS, PROPS, NSTATV, STATEV,
     3 NIARRAY, I_ARRAY, NRARRAY, R_ARRAY, NCARRAY, C_ARRAY, DA)

      INCLUDE 'ABA_PARAM.INC'

C
      DIMENSION PROPS(NPROPS),STATEV(NSTATV),PREDEF(NFIELD),
     1 DPRED(NFIELD),I_ARRAY(NIARRAY), R_ARRAY(NRARRAY),
     2 C_ARRAY(NCARRAY)
C
C     rC3=5.7757D-05
      rC=5.21D-13
      rm=3.0
      rE=210000
      rv=0.3
      rE2=rE/(1-rv**2) !PLANE STRAIN
      ru=rE2/(2*(1+rv))
CCCCCCCCCCCCCCCCCCCCCCCCC
CCCCCCCCCCCCCCCCCCCCCCCCCCCCCCCCCCCCCCCCCCCCCCCCCCCCCCCCCCCCCCCCC
CCCCCC
c     G1=K1**2/E2, G_2=K_2**2/E2, G_3=K_3**2/2u, u=E2/(2*(1+v))
      rKI_MAX=(GI_MAX*rE2)**0.5
      rKII_MAX=(GII_MAX*rE2)**0.5
      rKIII_MAX=(GIII_MAX*2*ru)**0.5
CCCCCCCCCCCCCCCCCCCCCCCCC
      rKI_MIN=0
      rKII_MIN=0
      rKIII_MIN=0
CCCCCCCCCCCCCCCCCCCCCCCCCCCCCCCCCCCCCCCCCCCCCCCCCCCCCCCCCCCCCCCCCC
CCCCCC
      rKI_range=rKI_MAX-rKI_MIN
      rKII_range=rKII_MAX-rKII_MIN
      rKIII_range=rKIII_MAX-rKIII_MIN
CCCCCCCCCCCCCCCCCCCCCCCCCCCCCCCCCCCCCCCCCCCCCCCCCCCCCCCCCCCCCCCCCC
CCCCCC
      rK_eq=(rKI_range**2+rKII_range**2+(rKIII_range**2/(1-rv)))**0.5
      DADN=rC*rK_eq**rm
C
      RETURN
      END
```

4. **3D plane stress**

```
      SUBROUTINE UMIXMODEFATIGUE (DADN, GI_MAX, GII_MAX, GIII_MAX,
     1 GI_MIN, GII_MIN, GIII_MIN, TEMP, DTEMP, PREDEF, DPRED,
     2 NFIELD, NPROPS, PROPS, NSTATV, STATEV,
     3 NIARRAY, I_ARRAY, NRARRAY, R_ARRAY, NCARRAY, C_ARRAY, DA)

      INCLUDE 'ABA_PARAM.INC'

C
      DIMENSION PROPS(NPROPS),STATEV(NSTATV),PREDEF(NFIELD),
     1 DPRED(NFIELD),I_ARRAY(NIARRAY), R_ARRAY(NRARRAY),
     2 C_ARRAY(NCARRAY)
C
C     rC3=5.7757D-05
      rC=5.21D-13
      rm=3.0
      rE=210000
      rv=0.3
      rE2=rE/(1-00**2) !PLANE STRESS
      ru=rE2/(2*(1+rv))
CCCCCCCCCCCCCCCCCCCCCCCC
CCCCCCCCCCCCCCCCCCCCCCCCCCCCCCCCCCCCCCCCCCCCCCCCCCCCCCCCCCCCCCC
CCCCCC
c     G1=K1**2/E2, G_2=K_2**2/E2, G_3=K_3**2/2u, u=E2/(2*(1+v))
      rKI_MAX=(GI_MAX*rE2)**0.5
      rKII_MAX=(GII_MAX*rE2)**0.5
      rKIII_MAX=(GIII_MAX*2*ru)**0.5
CCCCCCCCCCCCCCCCCCCCCCCC
      rKI_MIN=0
      rKII_MIN=0
      rKIII_MIN=0
CCCCCCCCCCCCCCCCCCCCCCCCCCCCCCCCCCCCCCCCCCCCCCCCCCCCCCCCCCCCCCC
CCCCCC
      rKI_range=rKI_MAX-rKI_MIN
      rKII_range=rKII_MAX-rKII_MIN
      rKIII_range=rKIII_MAX-rKIII_MIN
CCCCCCCCCCCCCCCCCCCCCCCCCCCCCCCCCCCCCCCCCCCCCCCCCCCCCCCCCCCCCCC
CCCCCC
      rK_eq=(rKI_range**2+rKII_range**2+(rKIII_range**2/(1-rv)))**0.5
      DADN=rC*rK_eq**rm
C
      RETURN
      END
```

(B) Fatigue crack propagation in OSD

Fracture mode II (K_{II}), real values [MPa$\sqrt{mm}$]

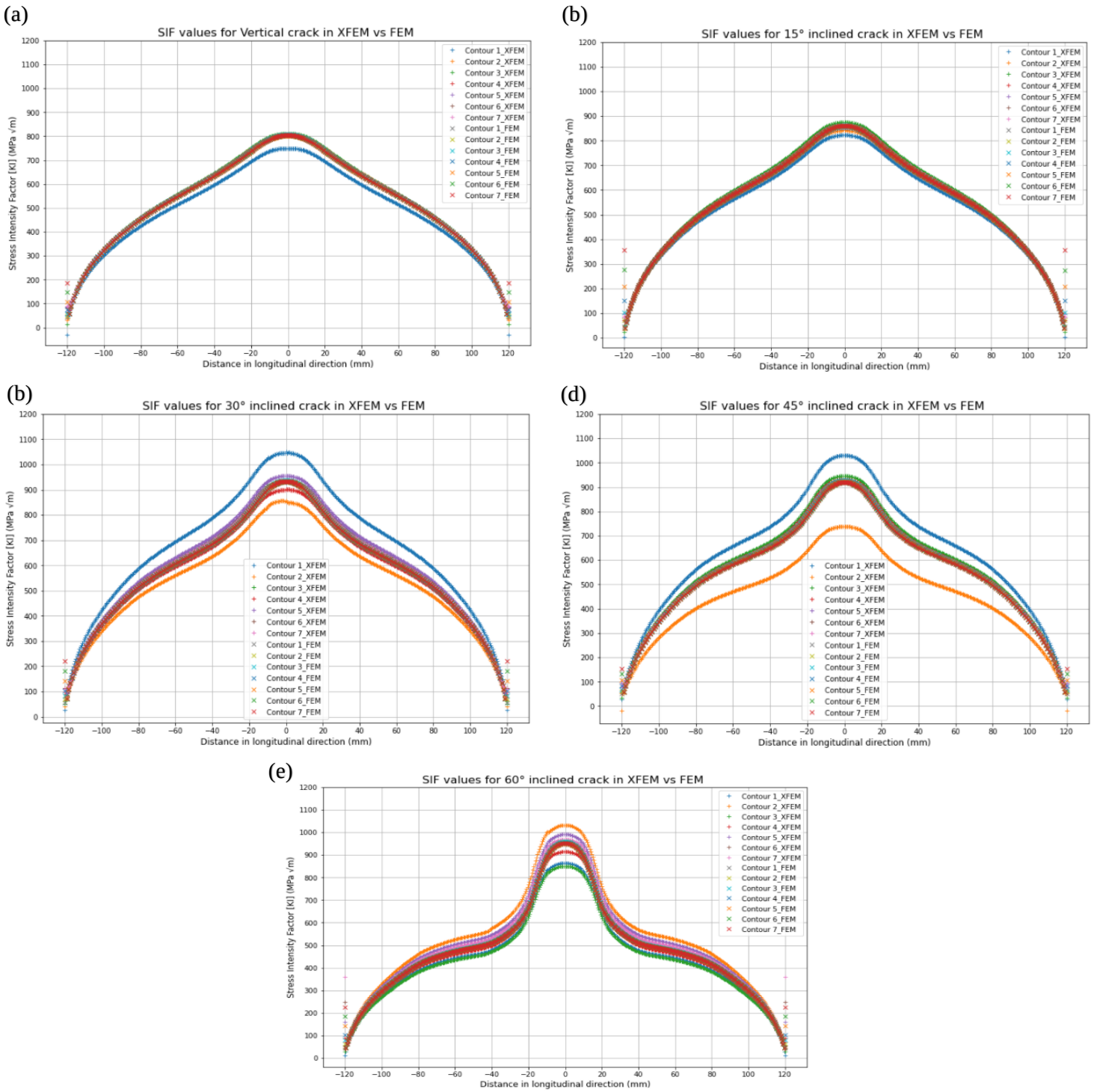

Figure 8.4: SIF values (K_I) for different crack inclinations considering all 7 contours (XFEM vs FEM). (a) Vertical crack. (b) 15° crack. (c) 30° crack. (d) 45° crack. (e) 60° crac

Fracture mode II (K_{II}), SIF absolute values [MPa$\sqrt{mm}$]

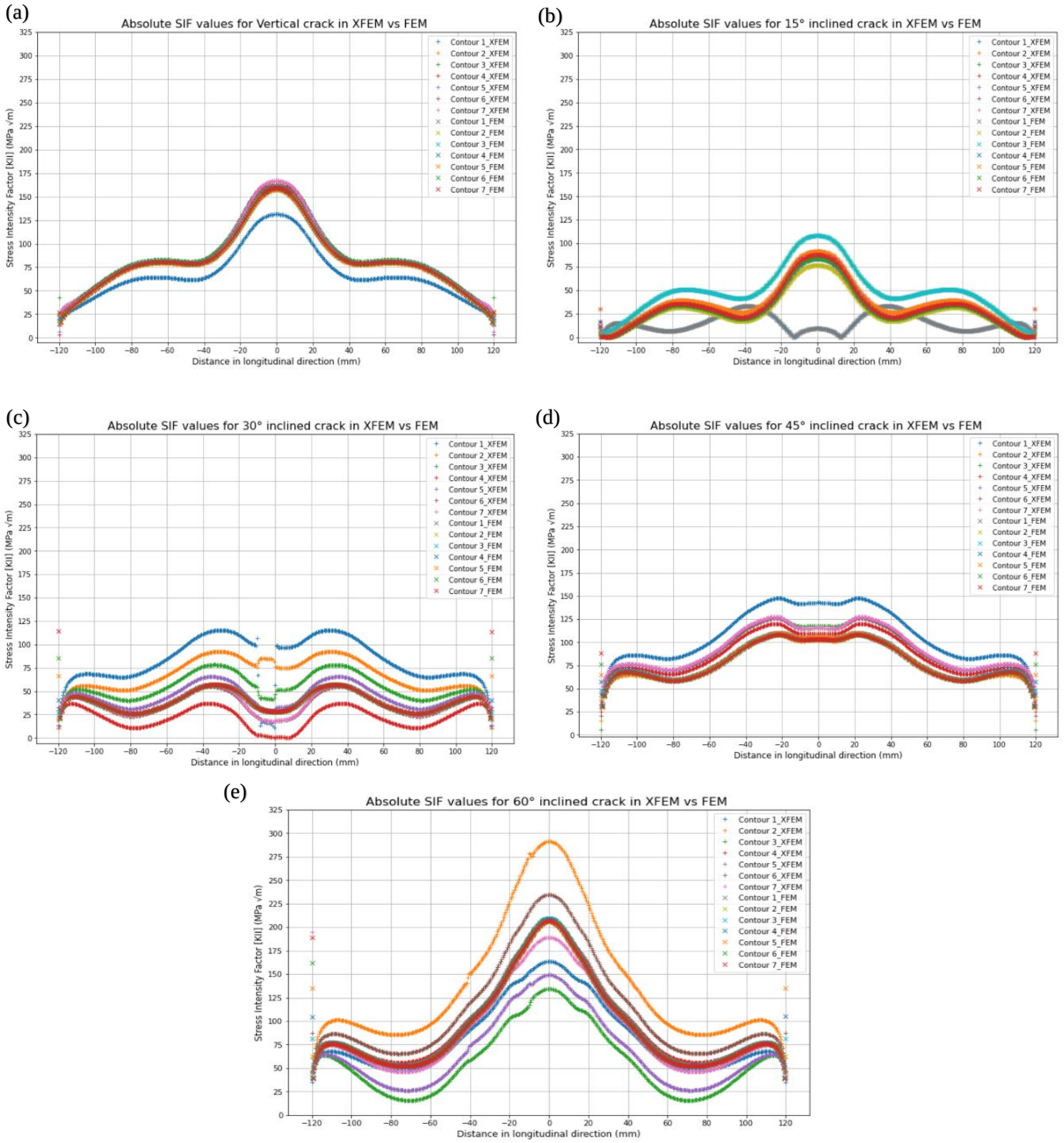

Figure 8.5: Absolute SIF values (K_{II}) for different crack inclinations considering all 7 contours (XFEM vs FEM). (a) Vertical crack. (b) 15° crack. (c) 30° crack. (d) 45° crack. (e) 60° crack

Fracture mode III (K_{III}), SIF absolute values [MPa$\sqrt{mm}$]

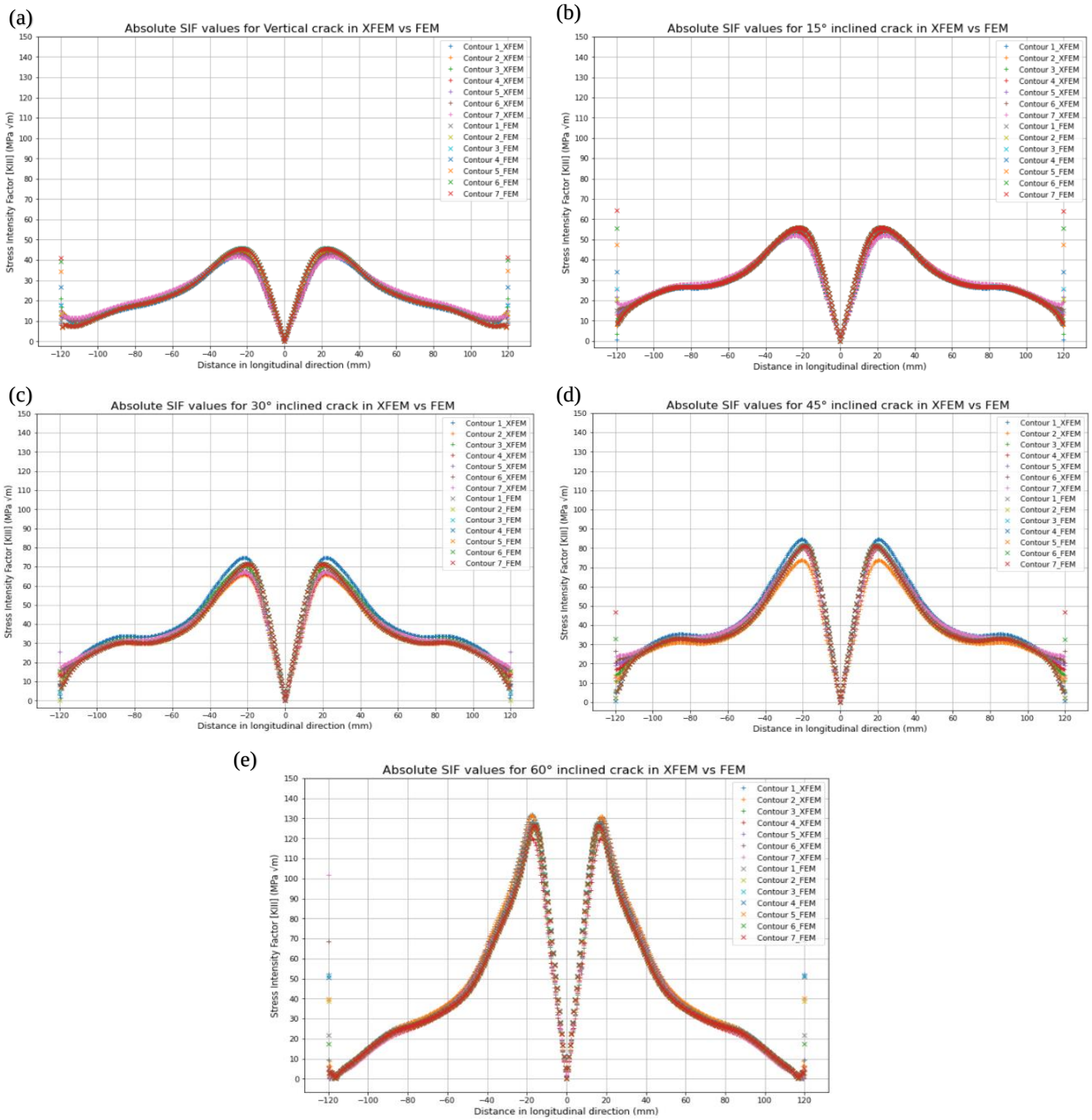

Figure 8.6: Absolute SIF values (K_{III}) for different crack inclinations considering all 7 contours (XFEM vs FEM). (a) Vertical crack. (b) 15° crack. (c) 30° crack. (d) 45° crack. (e) 60° crack

Fracture mode II (K_{II}), real values [MPa$\sqrt{mm}$]

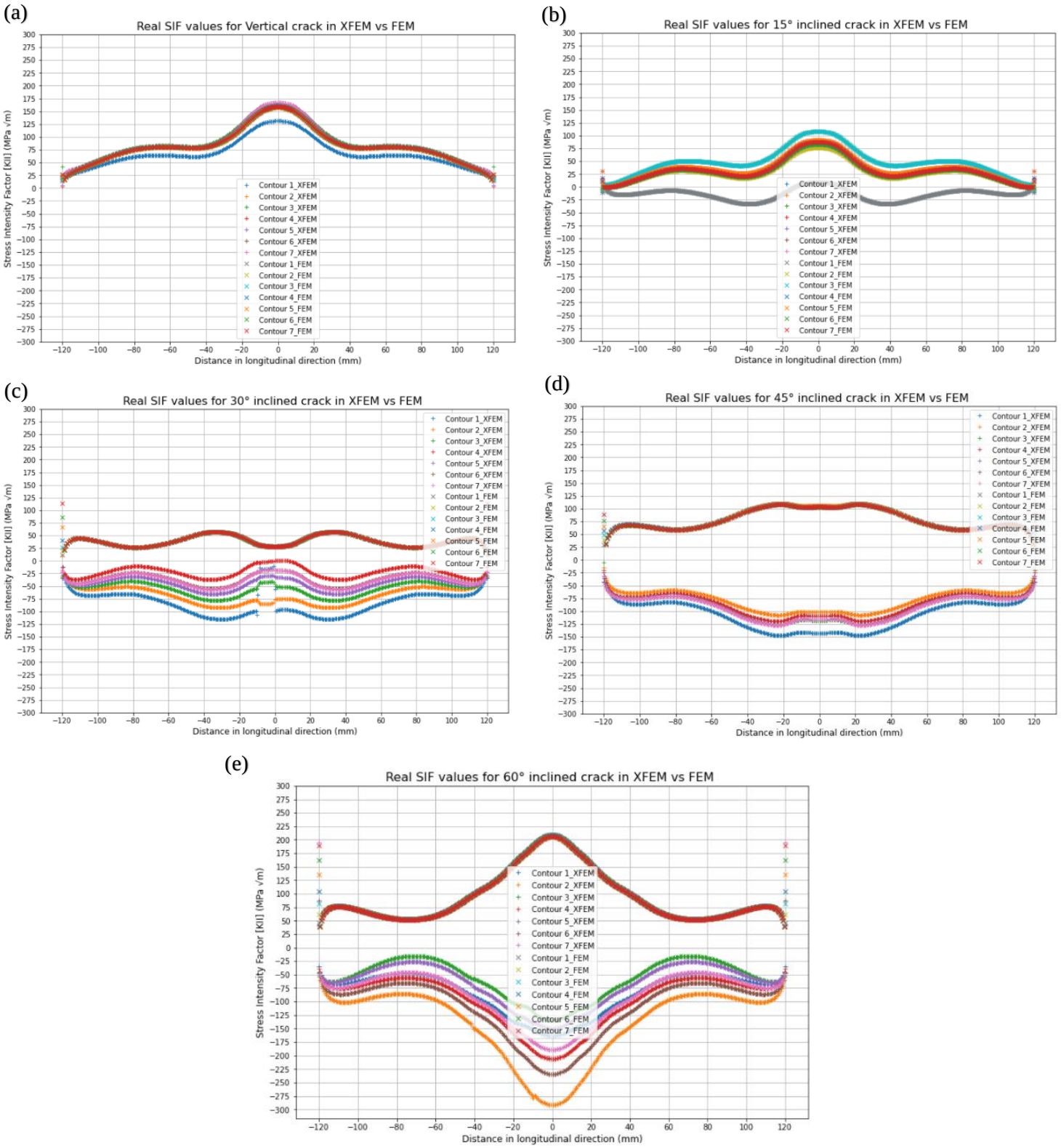

Figure 8.7: Real SIF values (K_{II}) for different crack inclinations considering all 7 contours (XFEM vs FEM). (a) Vertical crack. (b) 15° crack. (c) 30° crack. (d) 45° crack. (e) 60° crack

Fracture mode III (K_{III}), real values [MPa$\sqrt{mm}$]

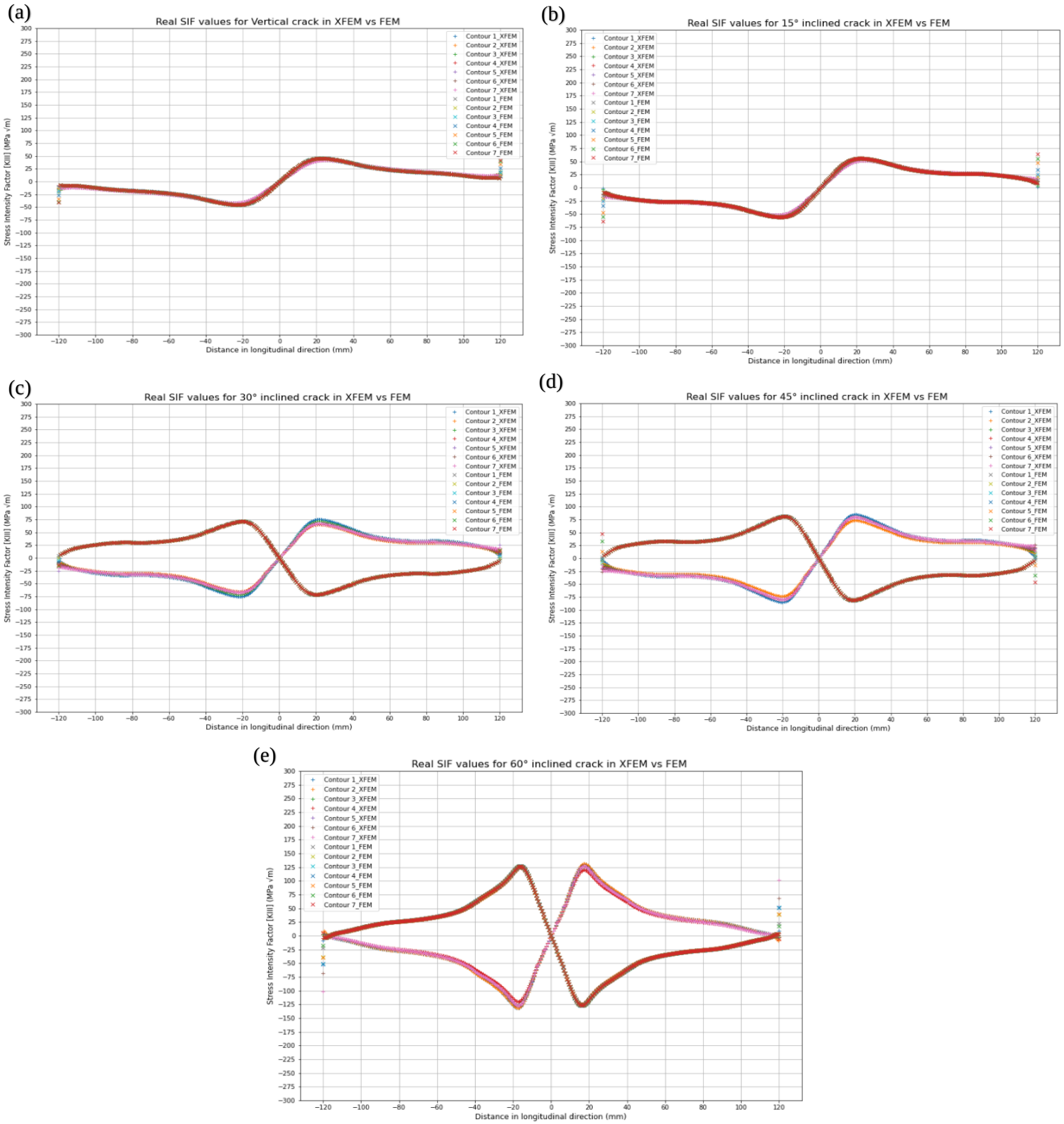

Figure 8.8: Real SIF values (K_{III}) for different crack inclinations considering all 7 contours (XFEM vs FEM). (a) Vertical crack. (b) 15° crack. (c) 30° crack. (d) 45° crack. (e) 60° crack

Fatigue MIXMODE subroutine (OSD)

```
      SUBROUTINE UMIXMODEFATIGUE (DADN, GI_MAX, GII_MAX, GIII_MAX,
     1 GI_MIN, GII_MIN, GIII_MIN, TEMP, DTEMP, PREDEF, DPRED,
     2 NFIELD, NPROPS, PROPS, NSTATV, STATEV,
     3 NIARRAY, I_ARRAY, NRARRAY, R_ARRAY, NCARRAY, C_ARRAY, DA)

      INCLUDE 'ABA_PARAM.INC'

C
      DIMENSION PROPS(NPROPS),STATEV(NSTATV),PREDEF(NFIELD),
     1 DPRED(NFIELD),I_ARRAY(NIARRAY), R_ARRAY(NRARRAY),
     2 C_ARRAY(NCARRAY)
C material data from_Fatigue resistance of the deck plate in steel orthotropic deck structures
C     rC3=9.623D-06
      rC=1.0D-13
      rm=3.0
      rE=210000
      rv=0.3
      rE2=rE/(1-rv**2) !PLANE STRAIN
      ru=rE2/(2*(1+rv))
CCCCCCCCCCCCCCCCCCCCCCCC
CCCCCCCCCCCCCCCCCCCCCCCCCCCCCCCCCCCCCCCCCCCCCCCCCCCCCCCCCCCCCCC
CCCCCC
c     G1=K1**2/E2, G_2=K_2**2/E2, G_3=K_3**2/2u, u=E2/(2*(1+v))
      rKI_MAX=(GI_MAX*rE2)**0.5
      rKII_MAX=(GII_MAX*rE2)**0.5
      rKIII_MAX=(GIII_MAX*2*ru)**0.5
CCCCCCCCCCCCCCCCCCCCCCCC
      rKI_MIN=0
      rKII_MIN=0
      rKIII_MIN=0
CCCCCCCCCCCCCCCCCCCCCCCCCCCCCCCCCCCCCCCCCCCCCCCCCCCCCCCCCCCCCCC
CCCCCC
      rKI_range=rKI_MAX-rKI_MIN
      rKII_range=rKII_MAX-rKII_MIN
      rKIII_range=rKIII_MAX-rKIII_MIN
CCCCCCCCCCCCCCCCCCCCCCCCCCCCCCCCCCCCCCCCCCCCCCCCCCCCCCCCCCCCCCC
CCCCCC
      rK_eq=(rKI_range**2+rKII_range**2+(rKIII_range**2/(1-rv)))**0.5
      rK_threshold=170
      if (rK_eq .GT. rK_threshold) then
      DADN=rC*rK_eq**rm
      else
      DADN=0*(rC*rK_eq**rm)
      endif
C
      RETURN
      END
```

Relative strain change at the gauge locations of path 1

a)

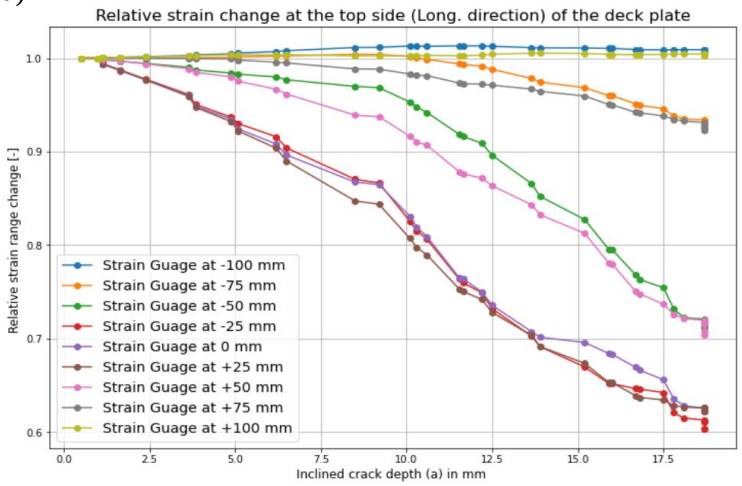

b)

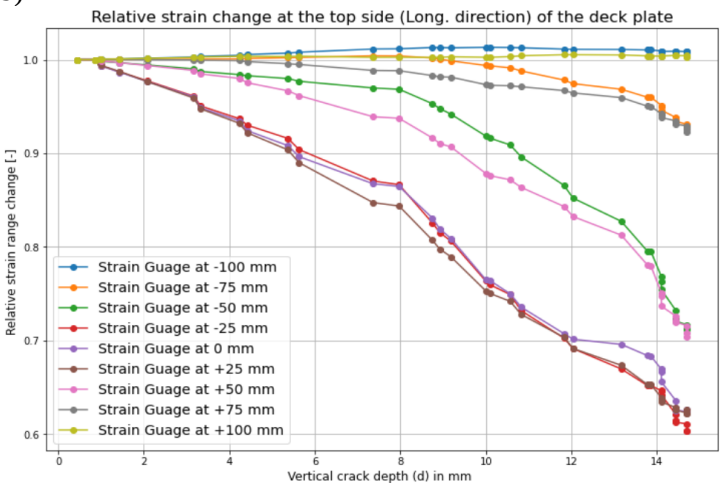

c)

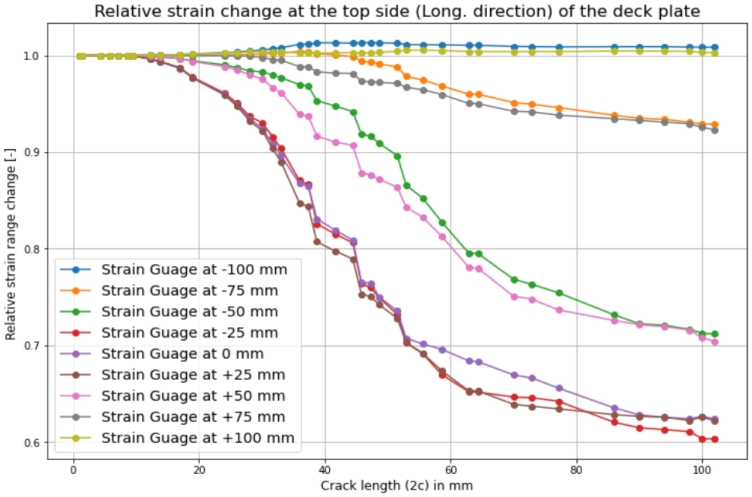

d)

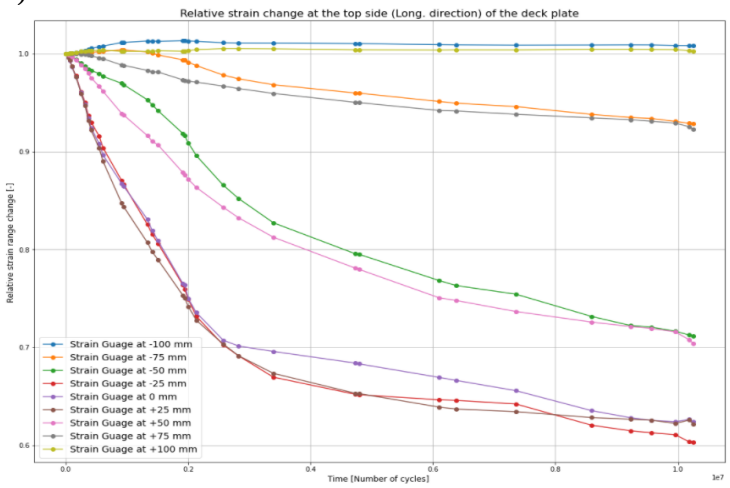

Figure 8.9: FEA relative strain drop at the top side (longitudinal direction) of the deck plate vs;
(a) Actual crack depth [a]. (b) Vertical crack depth [d]. (c) Crack length [2c]. (d) Time [Number of cycles].

Relative strain change at the gauge locations of path 2

a)

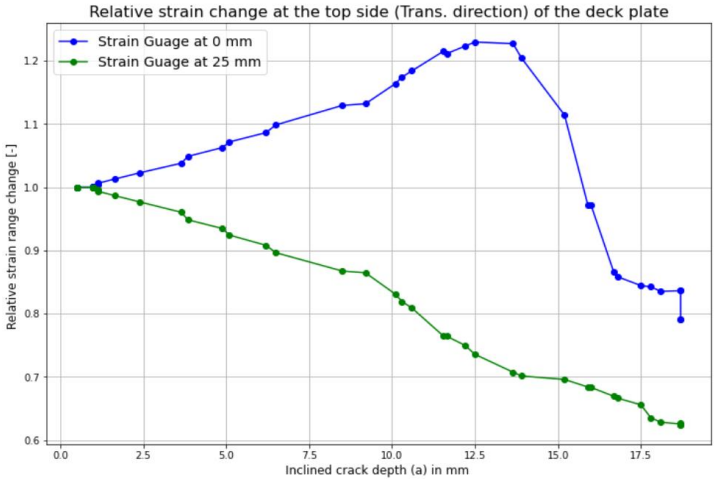

b)

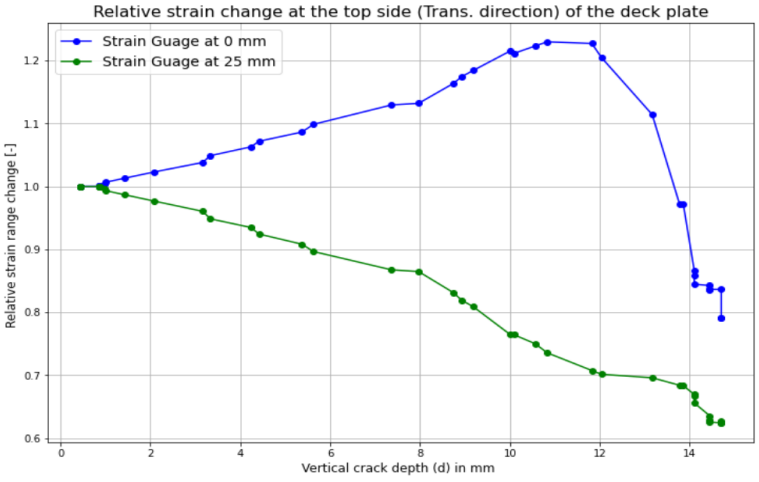

c)

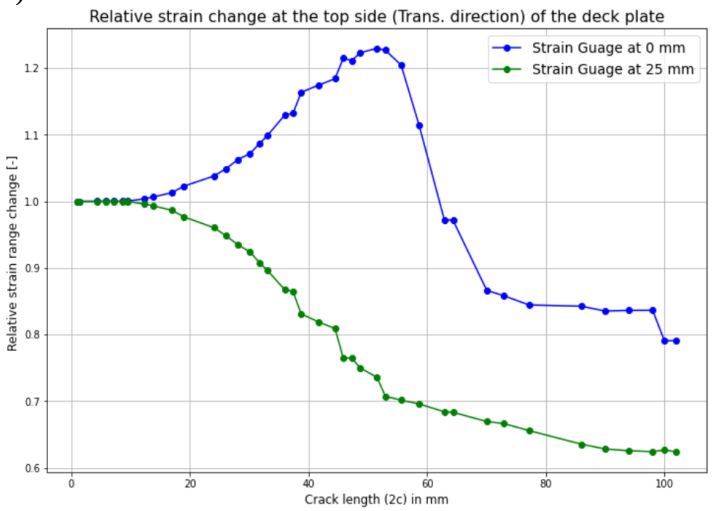

d)

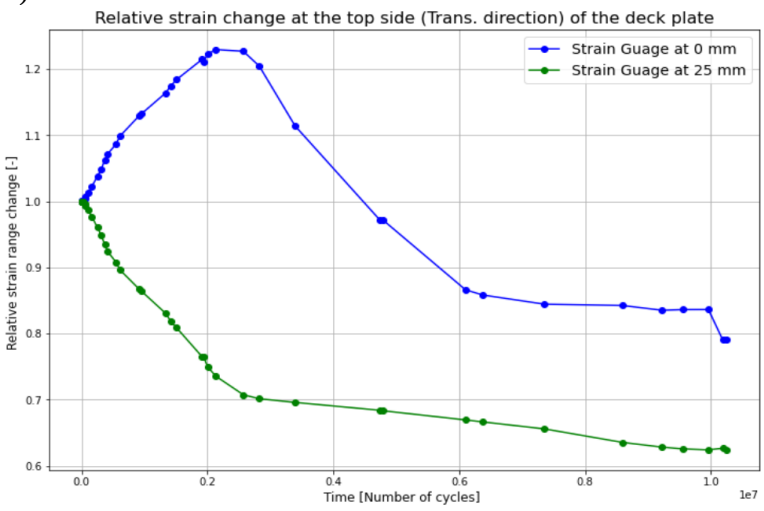

Figure 8.10: FEA relative strain drop at the top side (transverse direction) of the deck plate vs;
(a) Actual crack depth [a]. (b) Vertical crack depth [d]. (c) Crack length [2c]. (d) Time [Number of cycles].

Relative strain change at the gauge locations of path 2

a)

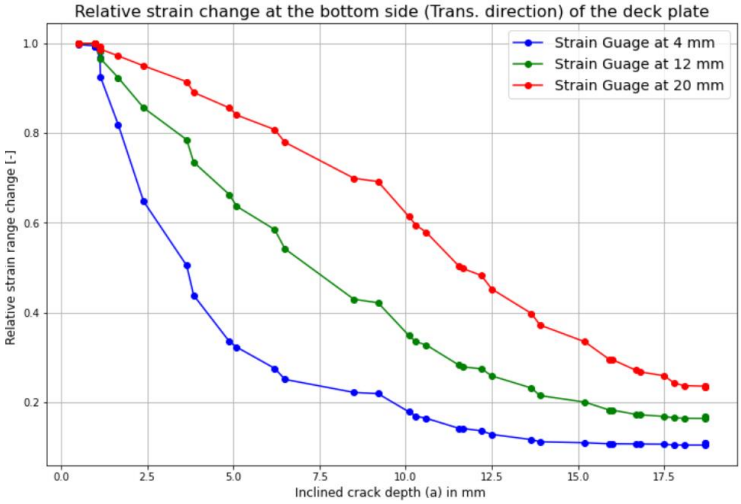

b)

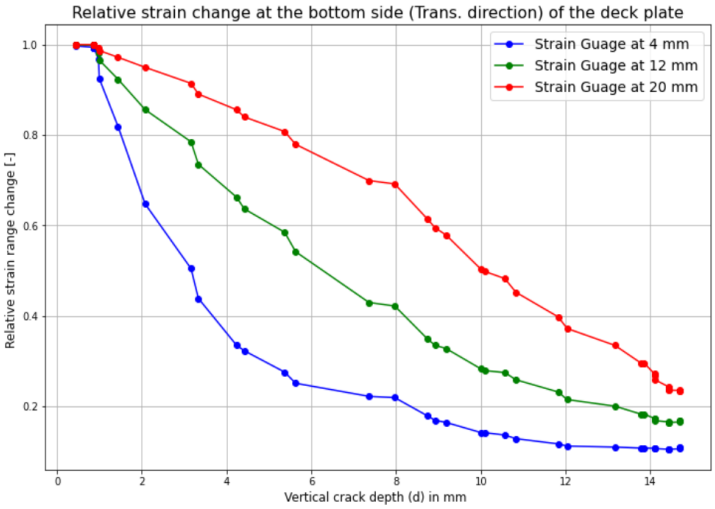

c)

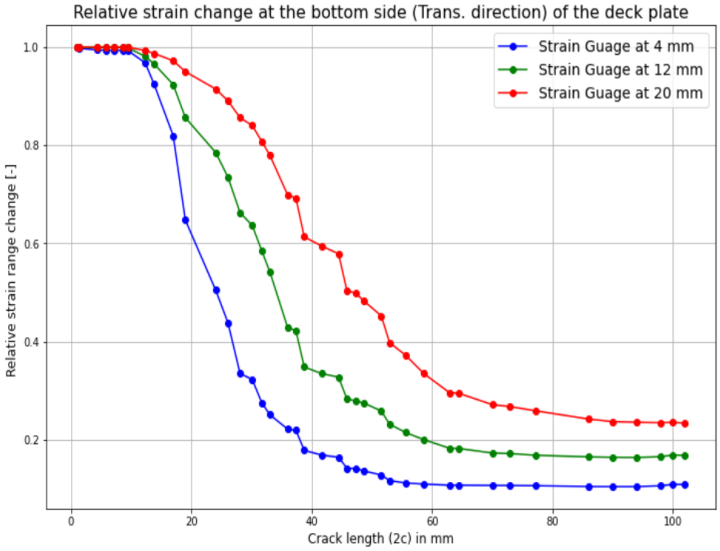

d)

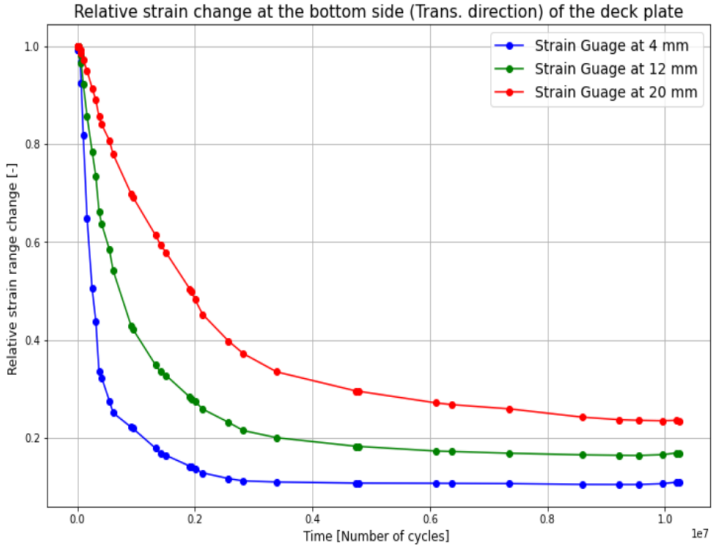

Figure 8.11: FEA relative strain drop at the bottom side (transverse direction) of the deck plate vs;
(a) Actual crack depth [a]. (b) Vertical crack depth [d]. (c) Crack length [2c]. (d) Time [Number of cycles].

(C) Fatigue crack propagation in OSD (Parametric analysis)

Hot spot stress calculation

2D beam model load calculation

First, the stresses were calculated for a load of *1 kN* based on the different thicknesses used. Then, the stress calculated for the *20 mm* deck plate case is linearly scaled to the experiment load value. From this stress value, the load values for the *16 mm* and *10 mm* thicknesses were obtained.

$$a = 60\ mm, b = 240\ mm, c = 180\ mm, d = 300 - 30 - 120 = 150\ mm$$

The effect of the load distribution is taken into account. Moreover, the distributed line load is calculated for a unit length (l_t *= 1 mm).*

$$q = \frac{1000}{(180 + 20) \cdot 1} = 5\ N/mm$$

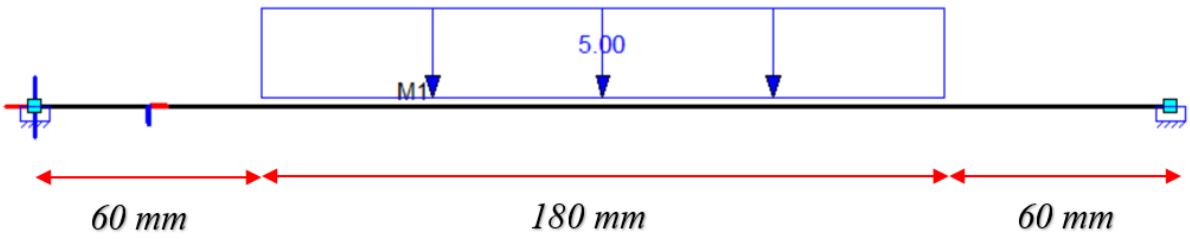

Figure 8.12: 2D beam model with 5N/mm distributed line load

$$M = \frac{5 \cdot 180}{23 \cdot 300} \cdot \left(24\frac{150^3}{300} - 6\frac{240 \cdot 180^2}{300} + 3\frac{180^3}{300} + 4 \cdot 180^2 - 24 \cdot 150^2 \right) = 29700\ N.mm$$

The stress concentration factor (SCF) for a deck plate without an asphalt layer is equal to the *1.11* value.

$$\Delta\sigma_{dp\_20mm} = \frac{1.11 \cdot 29700}{\frac{1}{6} \cdot 320 \cdot 20^2} = 1.545\ MPa$$

$$\Delta\sigma_{dp\_16mm} = \frac{1.11 \cdot 29700}{\frac{1}{6} \cdot 320 \cdot 16^2} = 2.415\ MPa$$

$$\Delta\sigma_{dp\_10mm} = \frac{1.11 \cdot 29700}{\frac{1}{6} \cdot 320 \cdot 10^2} = 6.181\ MPa$$

Linear scaling of the stress corresponding to *1 kN* gives;

$$\Delta\sigma_{dp_{20mm}} = 144 \cdot 1.545 = 222.523\ MPa$$

Calculating the load for the *16 mm* thick deck plate;

$$M_{16mm} = \frac{222.523 \cdot 320 \cdot 16^2}{6 \cdot 1.11} = 2737102.184\ N.mm$$

$$q_{10mm} = \frac{2737102.184 \cdot 24 \cdot 300}{180 \cdot \left(24\frac{150^3}{300} - 6\frac{240 \cdot 180^2}{300} + 3\frac{180^3}{300} + 4 \cdot 180^2 - 24 \cdot 150^2\right)} = 460.792\ N/mm$$

$$Q_{10mm} = 460.792 \cdot (180 + 20) \cdot 1 = 92158.323\ N = 92.158\ kN$$

Calculating the load for the *10 mm* thick deck plate;

$$M_{10mm} = \frac{222.523 \cdot 320 \cdot 10^2}{6 \cdot 1.11} = 1069180.541\ N.mm$$

$$q_{10mm} = \frac{1069180.541 \cdot 24 \cdot 300}{180 \cdot \left(24\frac{150^3}{300} - 6\frac{240 \cdot 180^2}{300} + 3\frac{180^3}{300} + 4 \cdot 180^2 - 24 \cdot 150^2\right)} \approx 180\ N/mm$$

$$Q_{10mm} = 180 \cdot (180 + 20) \cdot 1 = 36000\ N = 36\ kN$$

3D FEA model hot spot stress calculation

Location	20mm_72kN	16mm_46kN		10mm_18kN	
0.4t	7.8mm	5.44mm	7.8mm	3.26mm	5.44mm
	-193.345	-214.014	-196.946	-202.52	-202.52
	-178.434	-196.946	-181.136	-201.359	-190.354
	-195.273	-214.013	-196.946	-238.947	-201.359
	-174.753	-196.946	-181.136	-237.994	-193.003
Average	-185.45125	-205.47975	-189.041	-220.205	-196.809
Total average (Sigma_0.4t)	-185.45125		-197.26		-208.507
t	20mm		16mm		10mm
					-183.036
					-147.759
					-175.971
					-166.456
Sigma_t	-122.898		-151.234		-168.306
Sigma_hs	-227.361928		-228.098		-235.442
$\sigma_{hs} = 1.67\sigma_{0.4t} - 0.67\sigma_{1.0t}$					

Parametric models strain changes at all gauge locations

XFEA output of 16 mm OSD

All strains read from FEA at strain gauge locations on path 1 are given below.

a)

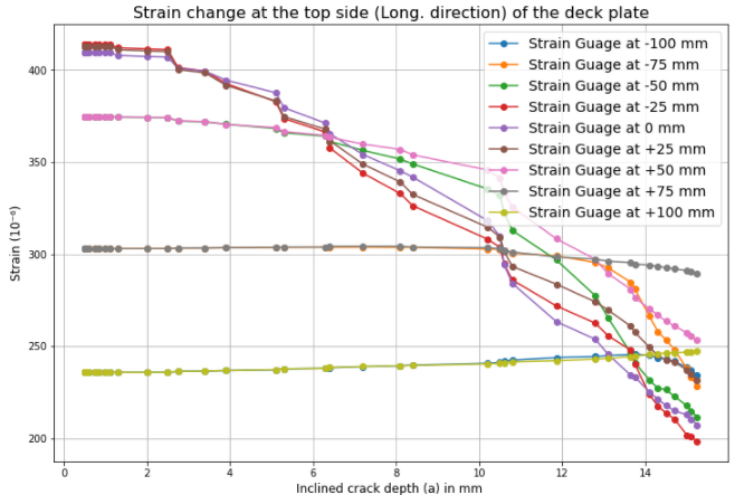

b)

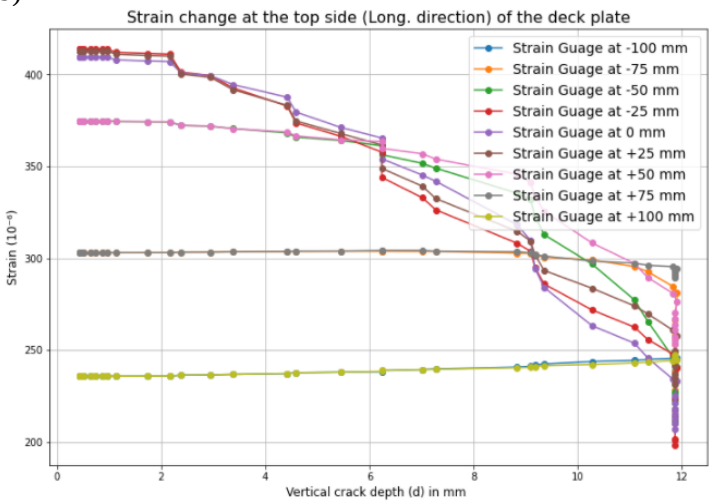

c)

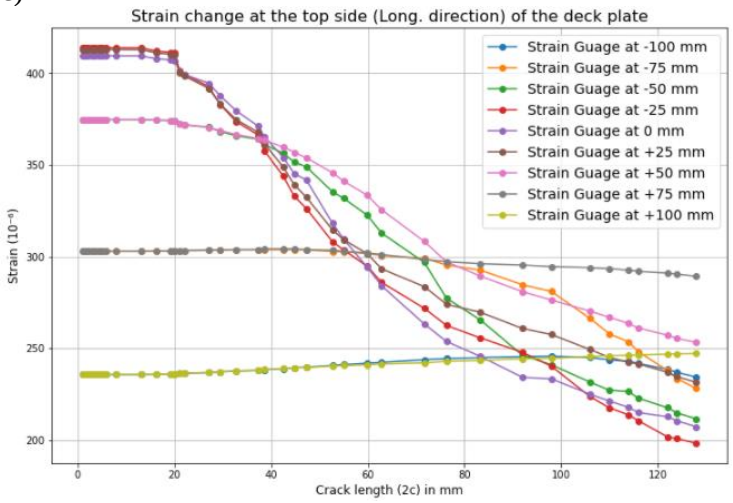

d)

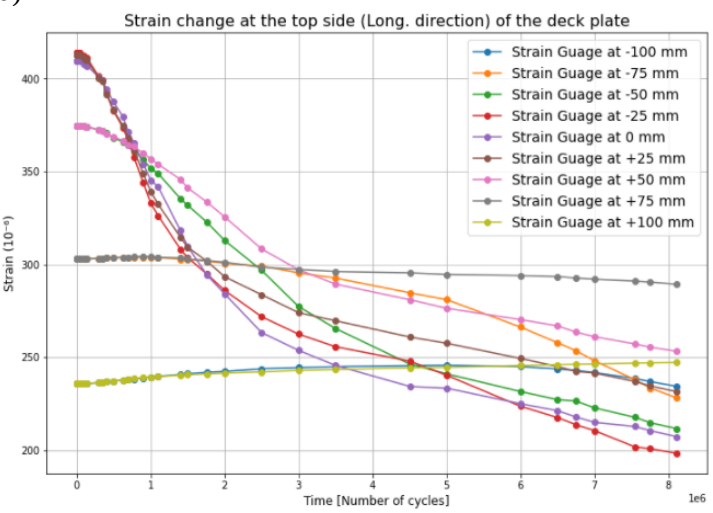

Figure 8.13: FEA strain drop at the top side (longitudinal path) of the deck plate vs;
(a) Actual crack depth [a]. (b) Vertical crack depth [d]. (c) Crack length [2c]. (d) Time [Number of cycles].

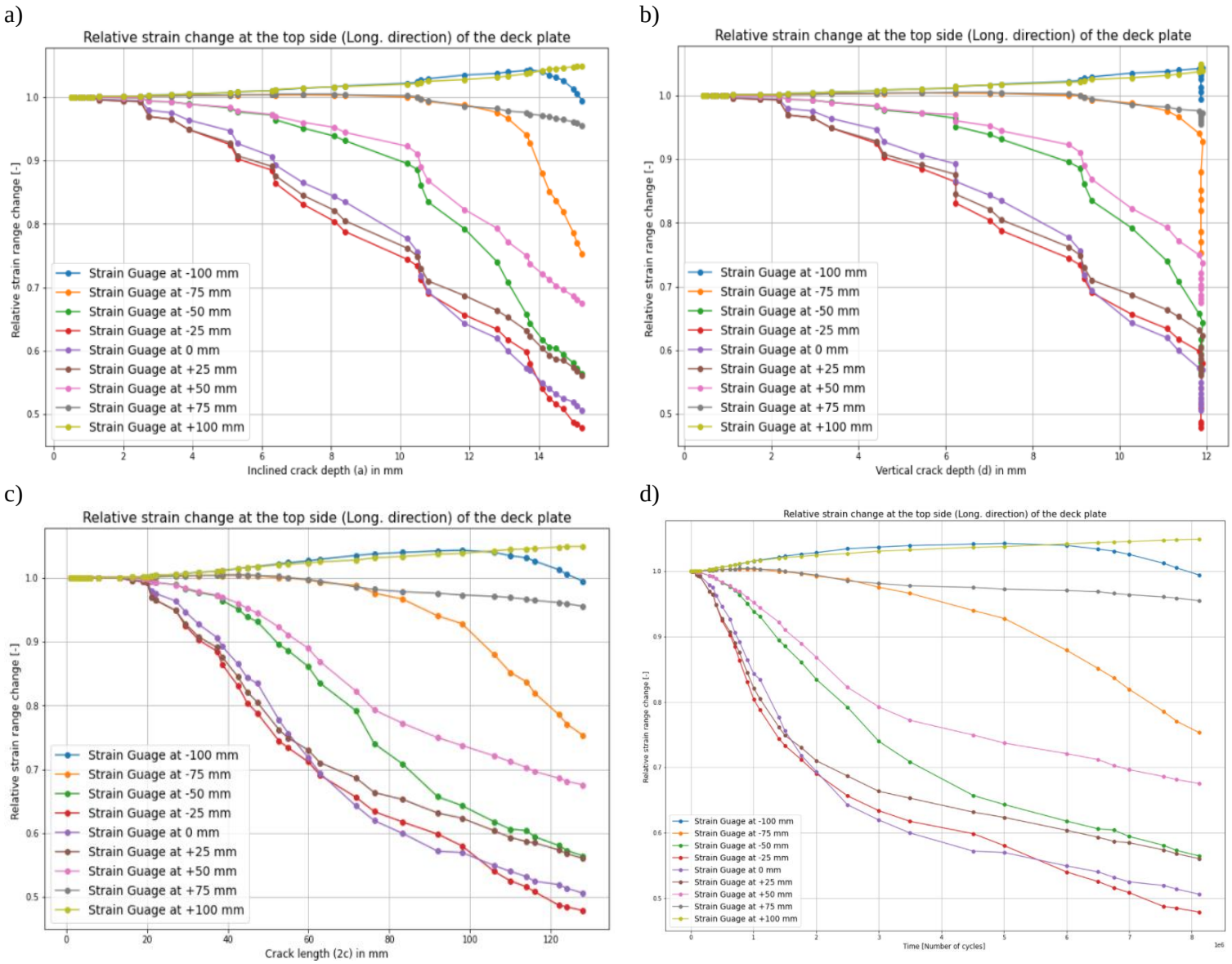

Figure 8.14: FEA relative strain drop at the top side (longitudinal path) of the deck plate vs;
(a) Actual crack depth [a]. (b) Vertical crack depth [d]. (c) Crack length [2c]. (d) Time [Number of cycles].

All strains read from FEA at strain gauge locations on path 2 are given below.

a)

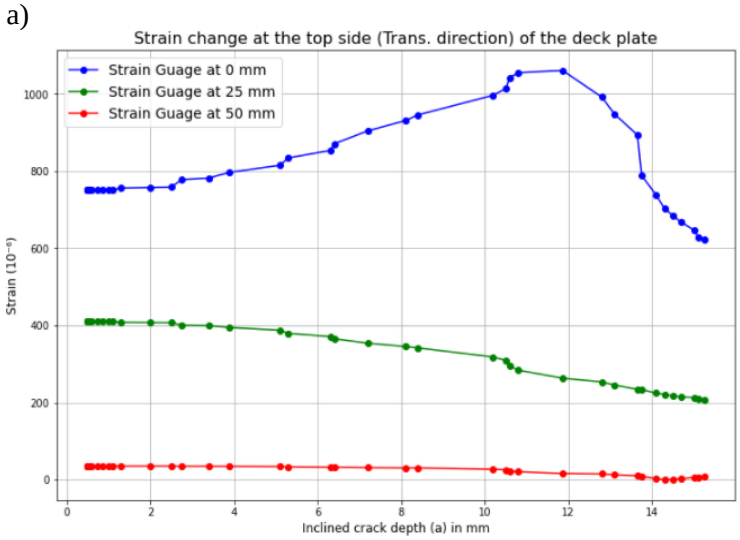

b)

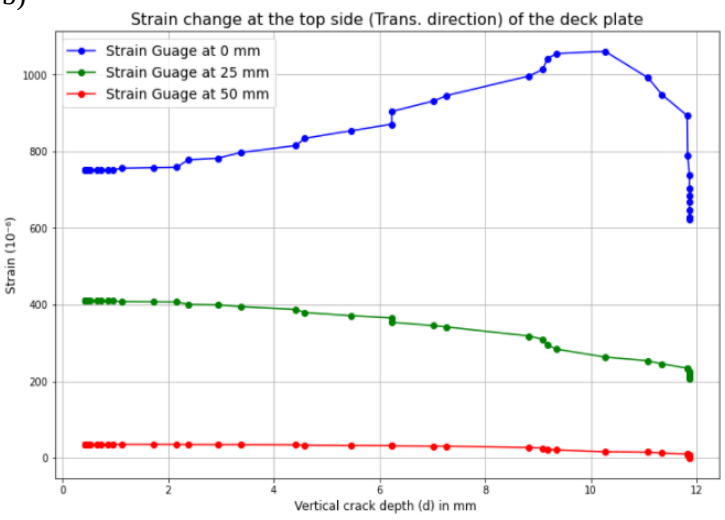

c)

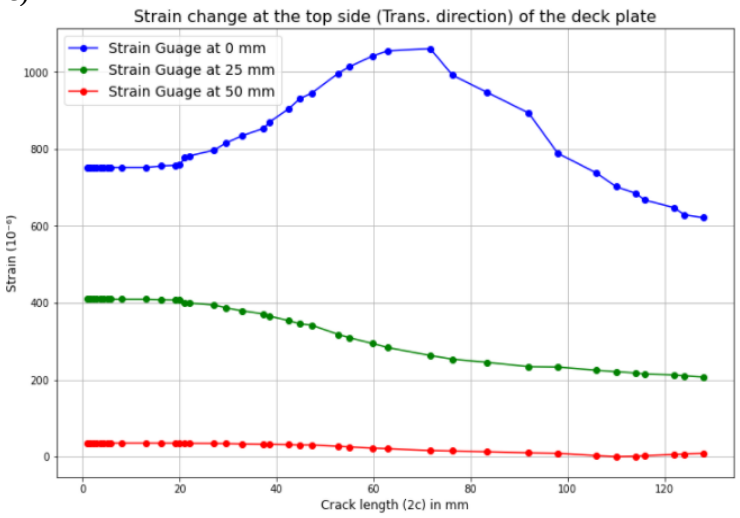

d)

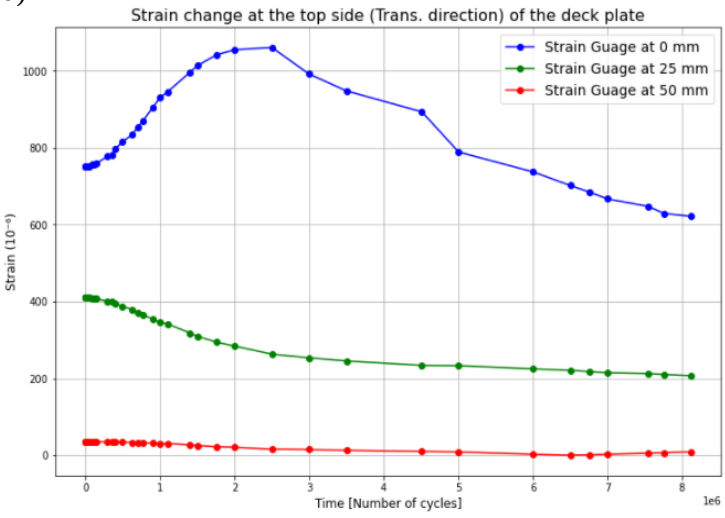

Figure 8.15: FEA strain drop at the top side (transverse path) of the deck plate. vs;
(a)Actual crack depth [a]. (b) Vertical crack depth [d]. (c) Crack length [2c]. (d) Time [Number of cycles].

a)

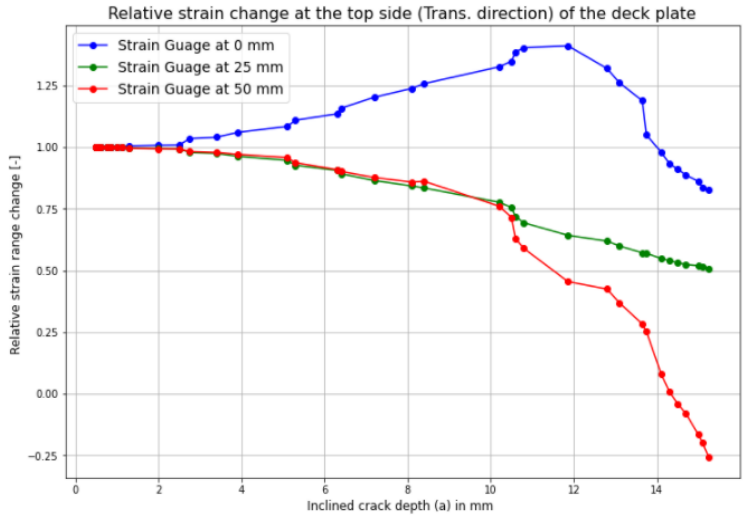

b)

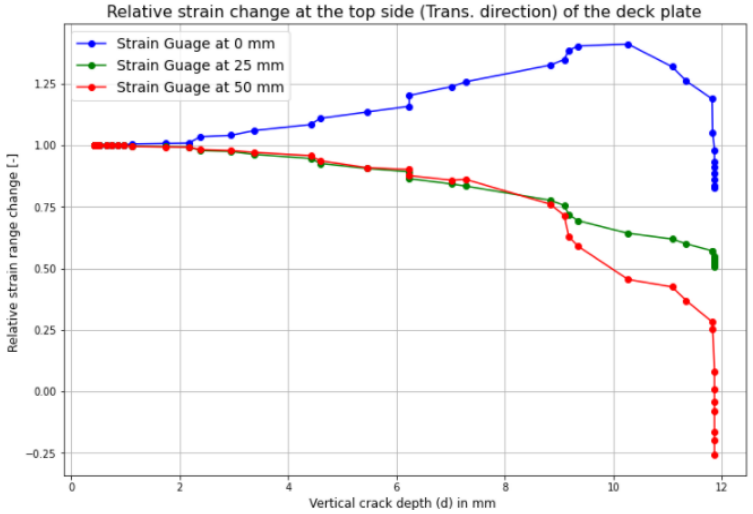

c)

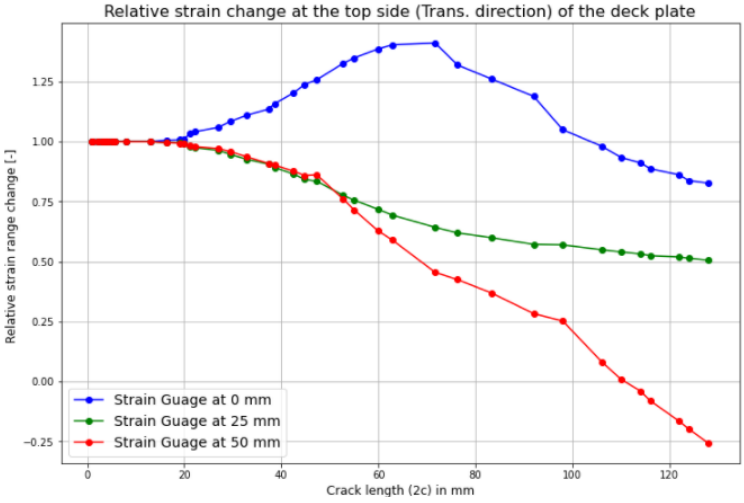

d)

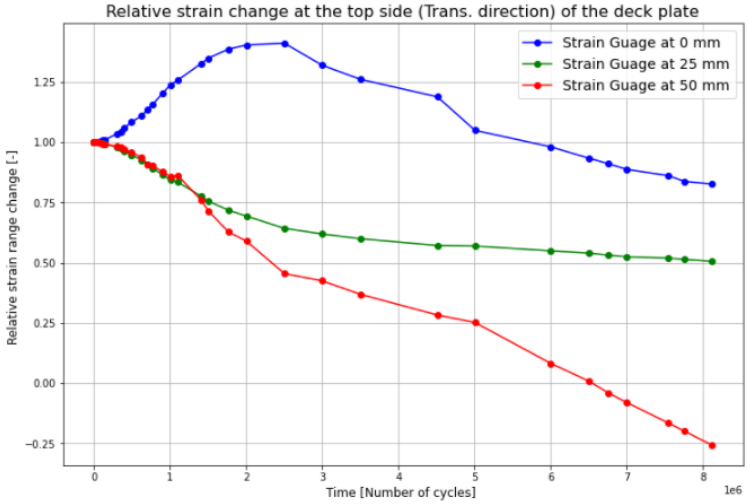

Figure 8.16: FEA relative strain drop at the top side (transverse path) of the deck plate vs;
(a) Actual crack depth [a]. (b) Vertical crack depth [d]. (c) Crack length [2c]. (d) Time [Number of cycles].

All strains read from FEA at strain gauge locations on path 3 are given below.

a)

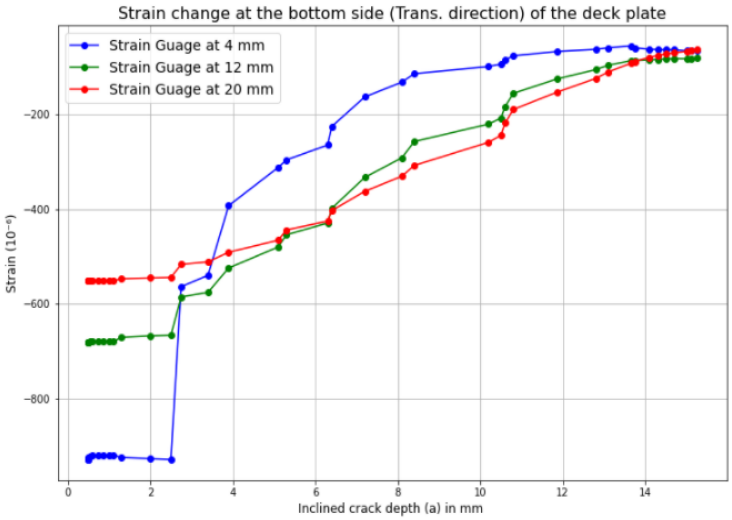

b)

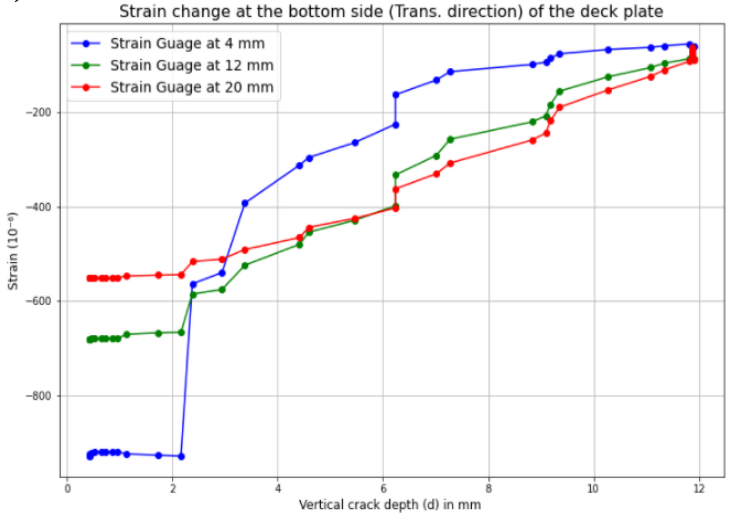

c)

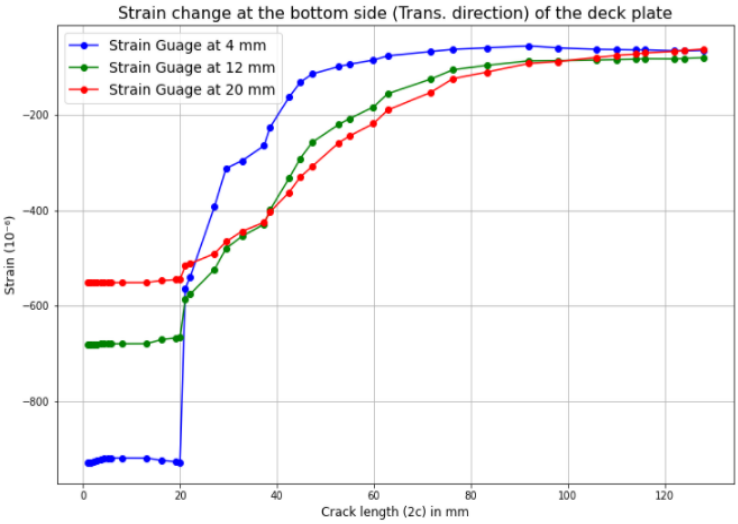

d)

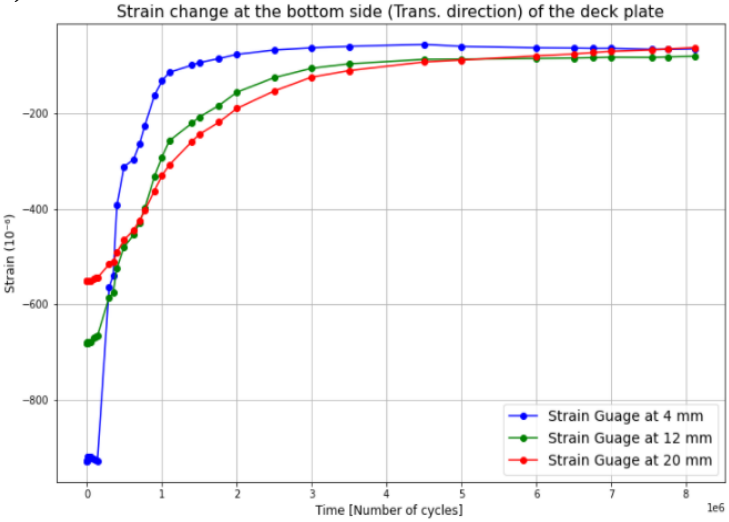

Figure 8.17: FEA strain drop at the bottom side (transverse path) of the deck plate vs;
(a) Actual crack depth [a]. (b) Vertical crack depth [d]. (c) Crack length [2c]. (d) Time [Number of cycles].

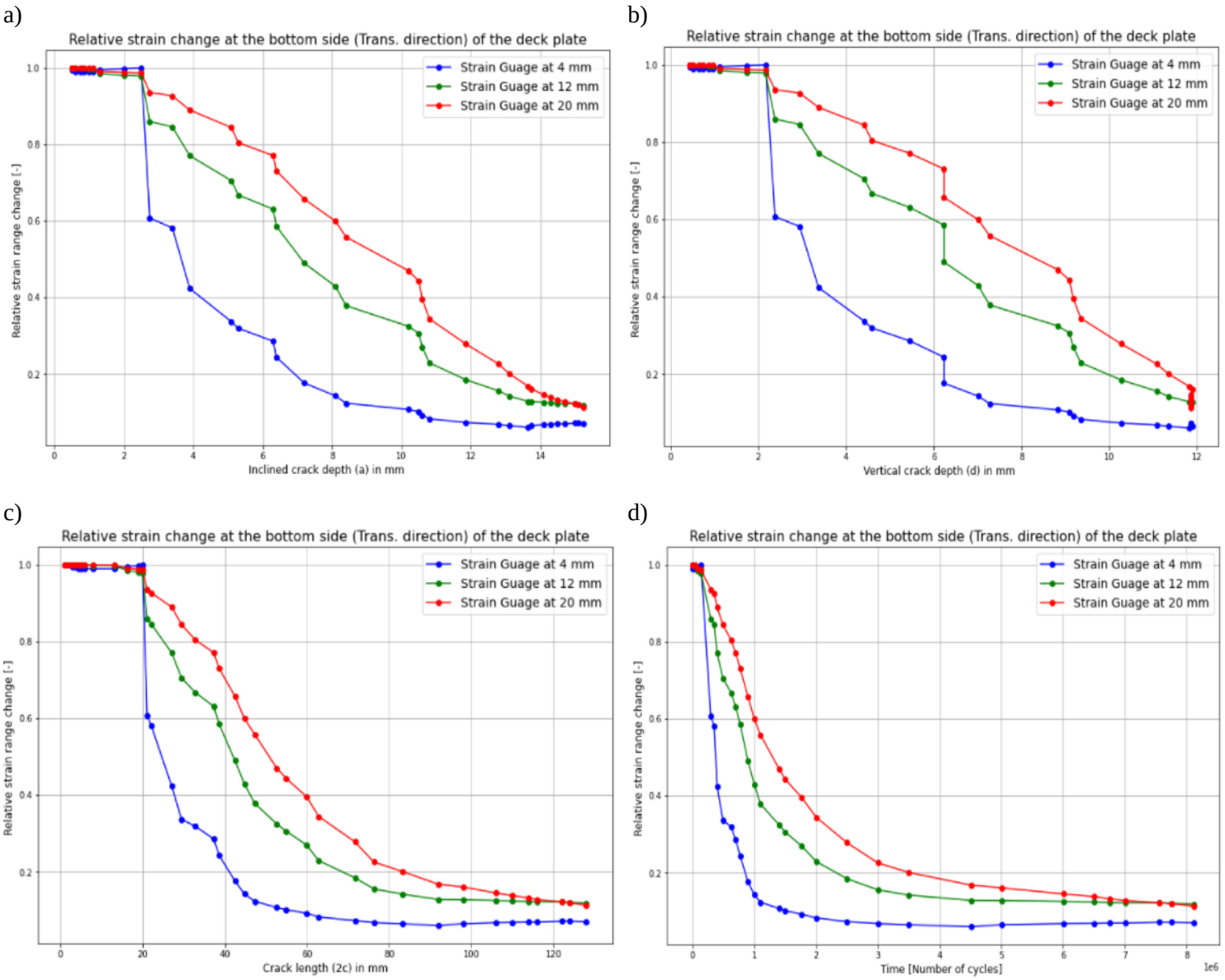

Figure 8.18: FEA relative strain drop at the bottom side (transverse path) of the deck plate vs;
(a) Actual crack depth [a]. (b) Vertical crack depth [d]. (c) Crack length [2c]. (d) Time [Number of cycles].

XFEA output of 10 mm OSD

All strains read from FEA at strain gauge locations on path 1 are given below.

a)

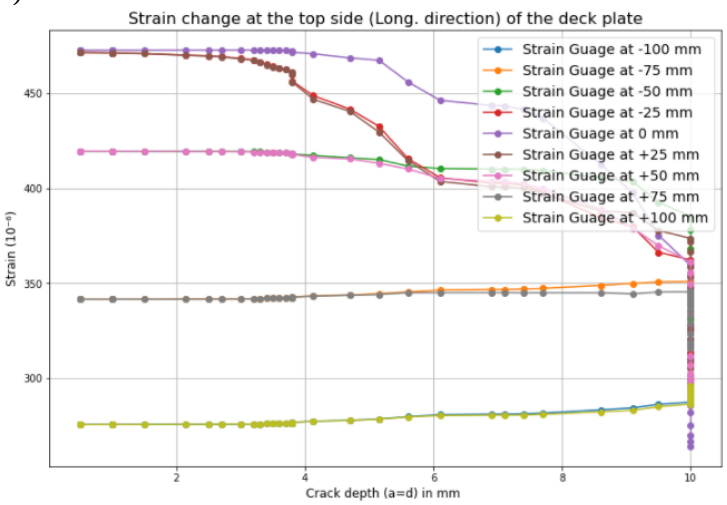

b)

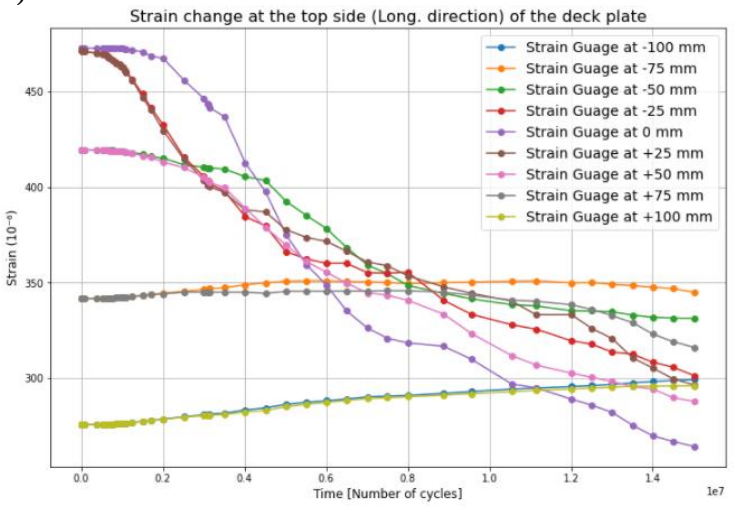

c)

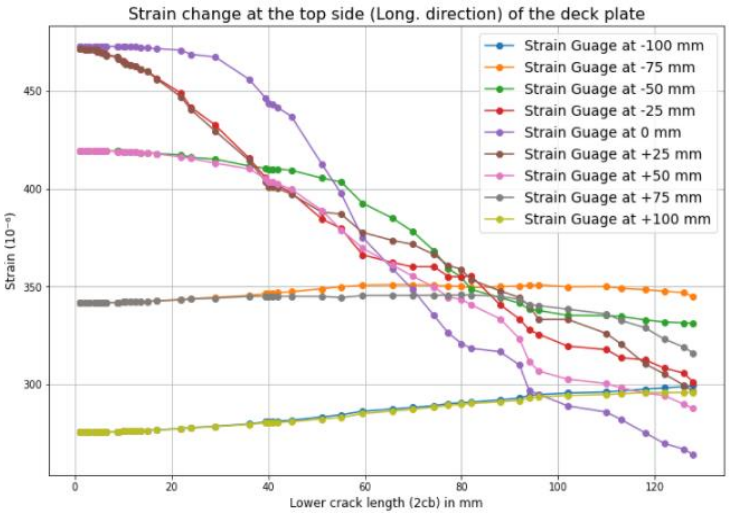

d)

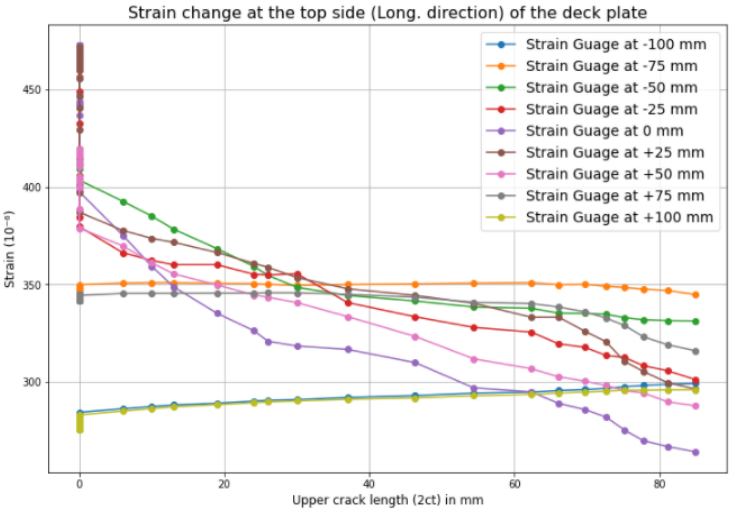

Figure 8.19: FEA strain drop at the top side (longitudinal path) of the deck plate vs;
(a) Crack depth [a=d]. (b) Time [Number of cycles]. (c) Lower crack length [$2c_b$]. (d) Upper crack length [$2c_t$].

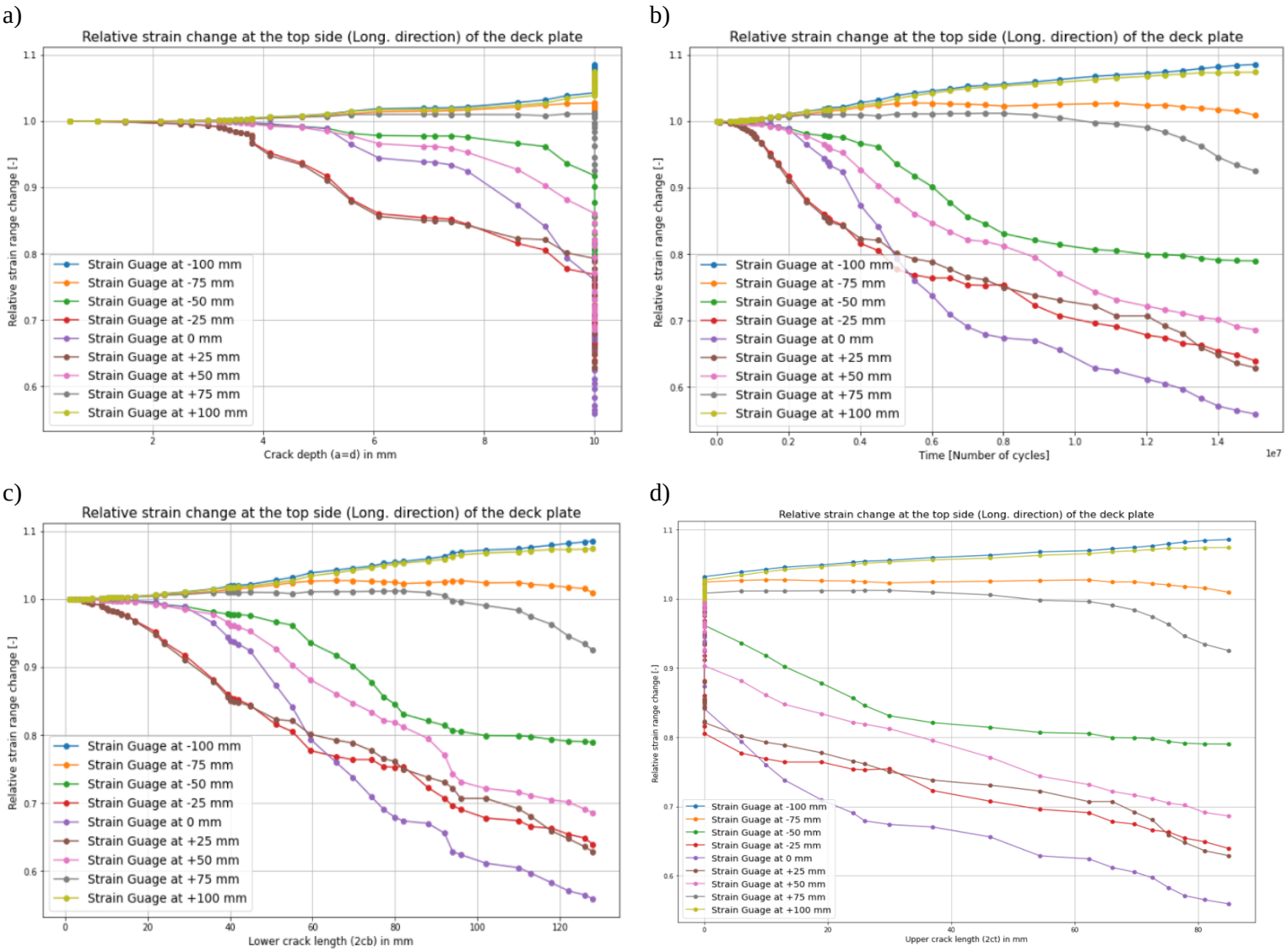

Figure 8.20: FEA relative strain drop at the top side (longitudinal path) of the deck plate vs;
(a) Crack depth [a=d]. (b) Time [Number of cycles]. (c) Lower crack length [$2c_b$]. (d) Upper crack length [$2c_t$].

All strains read from FEA at strain gauge locations on path 2 are given below.

a)

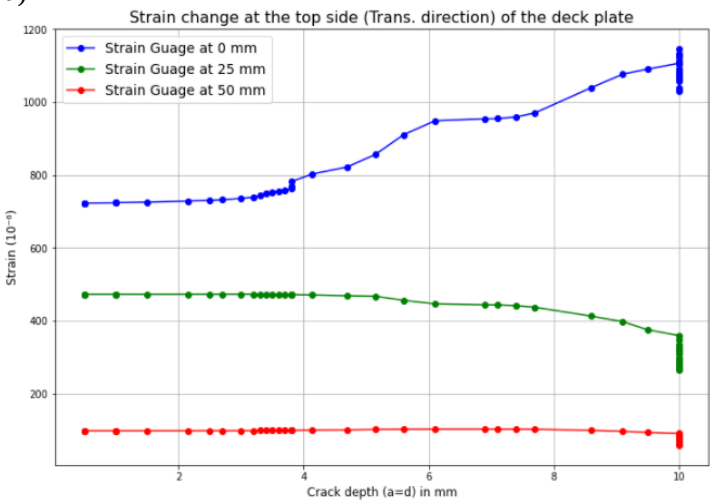

b)

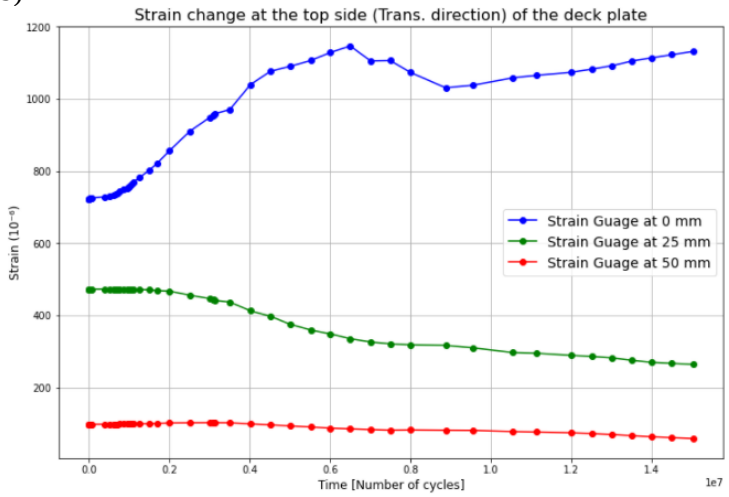

c)

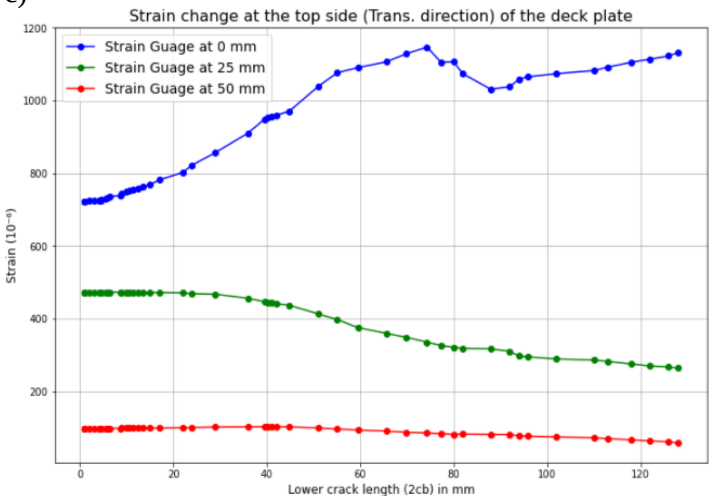

d)

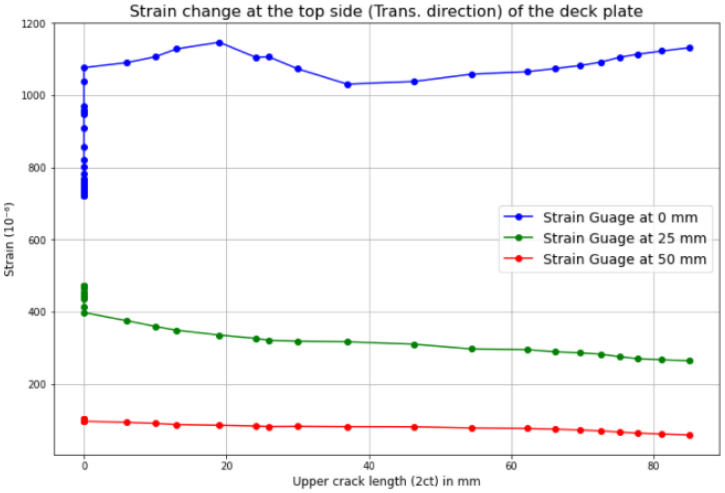

Figure 8.21: FEA strain drop at the top side (transverse path) of the deck plate. vs;
(a) Crack depth [a=d]. (b) Time [Number of cycles]. (c) Lower crack length [$2c_b$]. (d) Upper crack length [$2c_t$].

a)

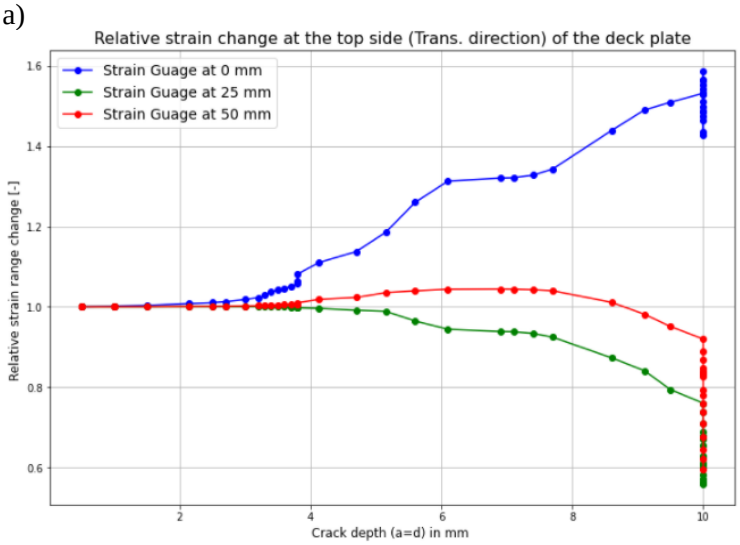

b)

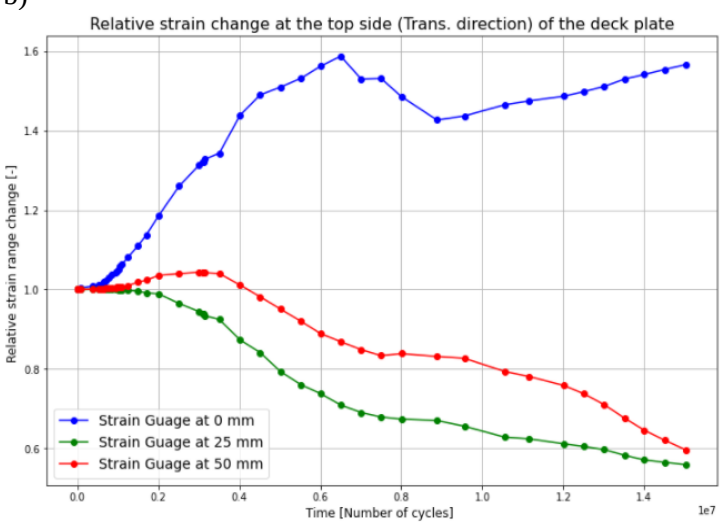

c)

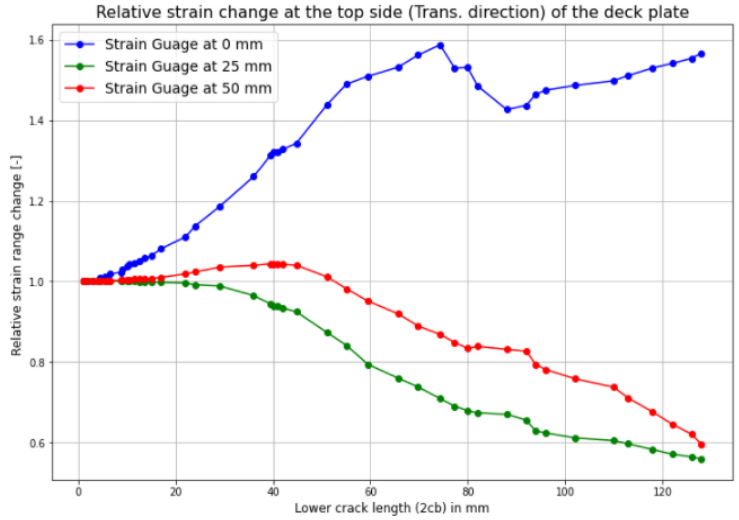

d)

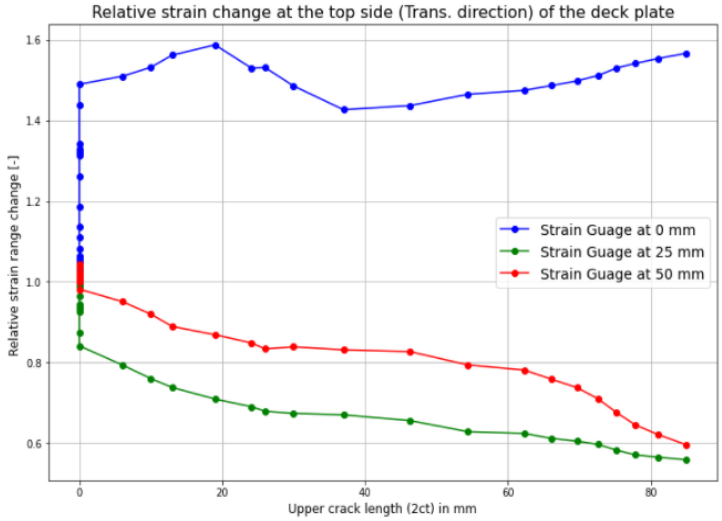

Figure 8.22: FEA relative strain drop at the top side (transverse path) of the deck plate vs;
(a) Crack depth [a=d]. (b) Time [Number of cycles]. (c) Lower crack length [$2c_b$]. (d) Upper crack length [$2c_t$].

All strains read from FEA at strain gauge locations on path 3 are given below.

a)

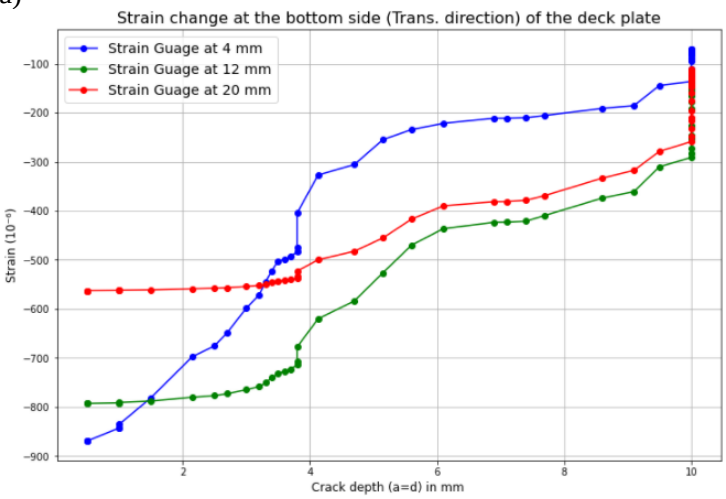

b)

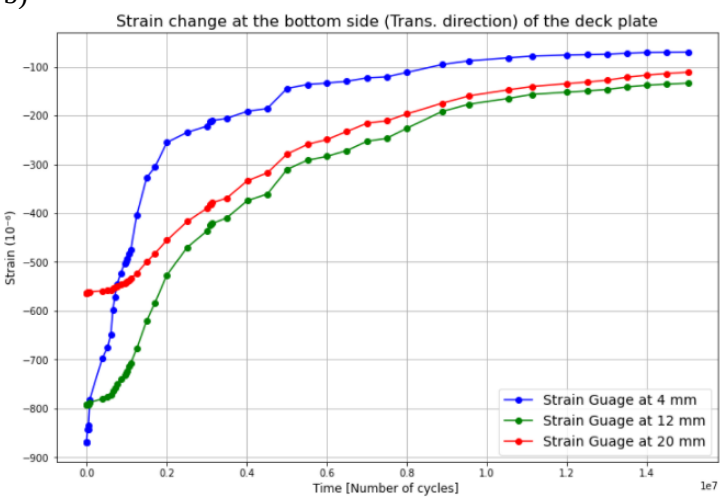

c)

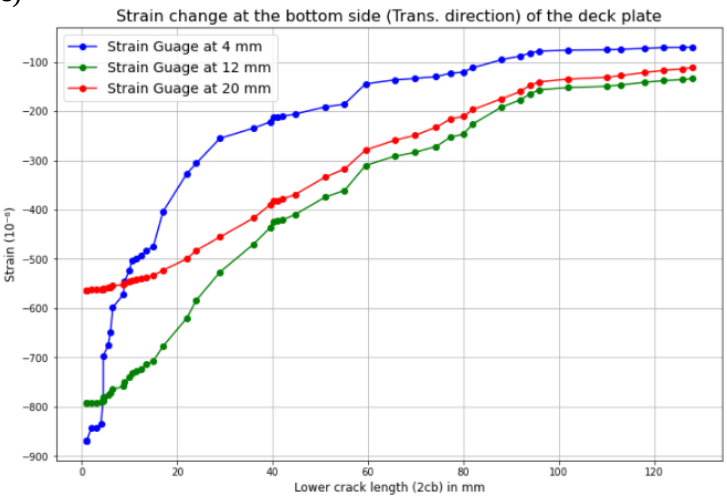

d)

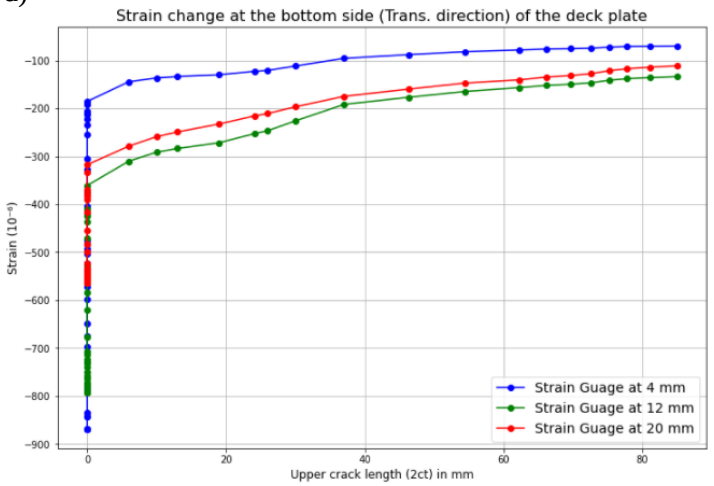

Figure 8.23: FEA strain drop at the bottom side (transverse path) of the deck plate vs;
(a) Crack depth [a=d]. (b) Time [Number of cycles]. (c) Lower crack length [$2c_b$]. (d) Upper crack length [$2c_t$].

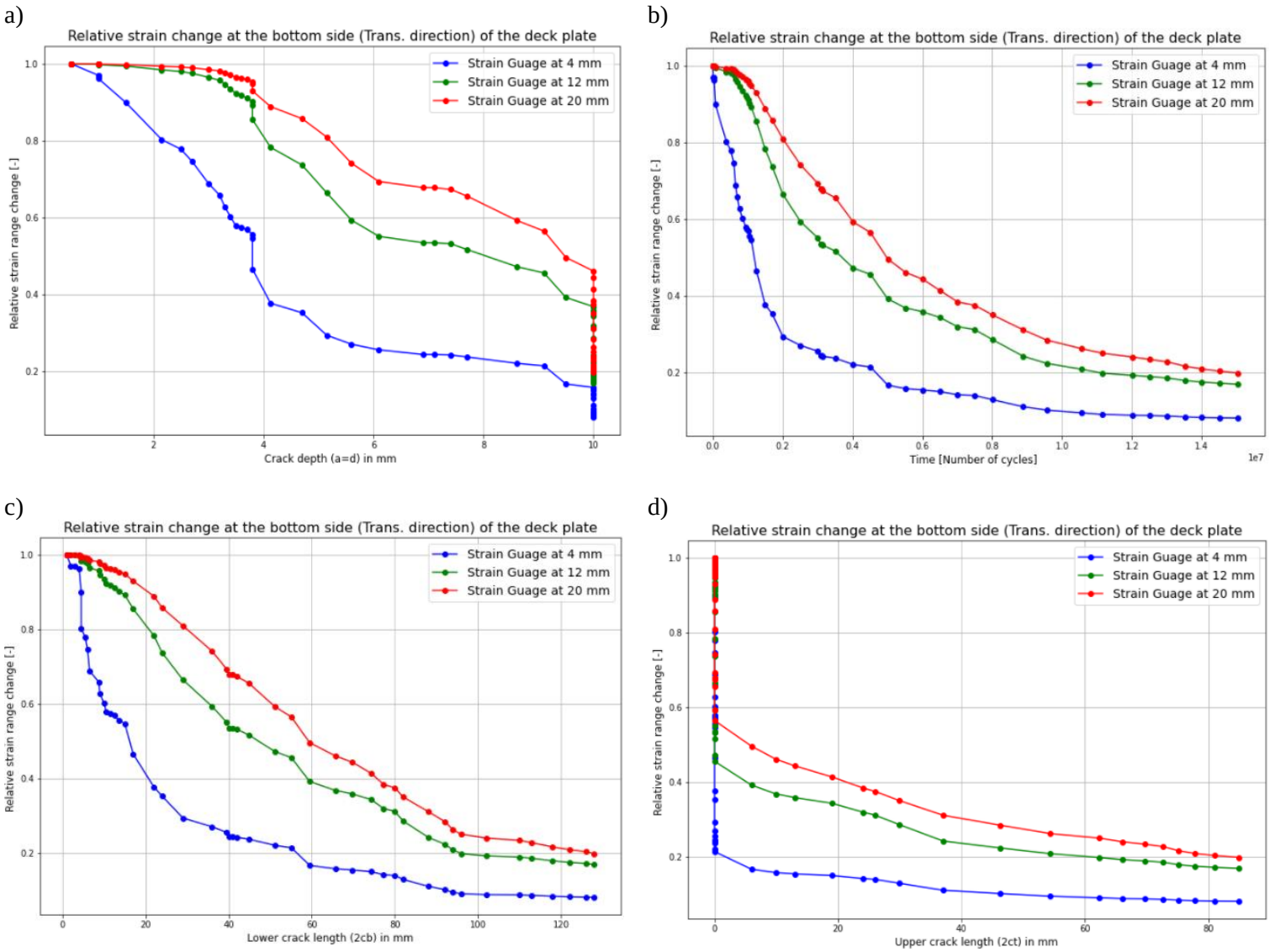

Figure 8.24: FEA relative strain drop at the bottom side (transverse path) of the deck plate vs;
(a) Crack depth [a=d]. (b) Time [Number of cycles]. (c) Lower crack length [$2c_b$]. (d) Upper crack length [$2c_t$].

Sensitivity of the output node

For the *16 mm* model the following nodes were considered.

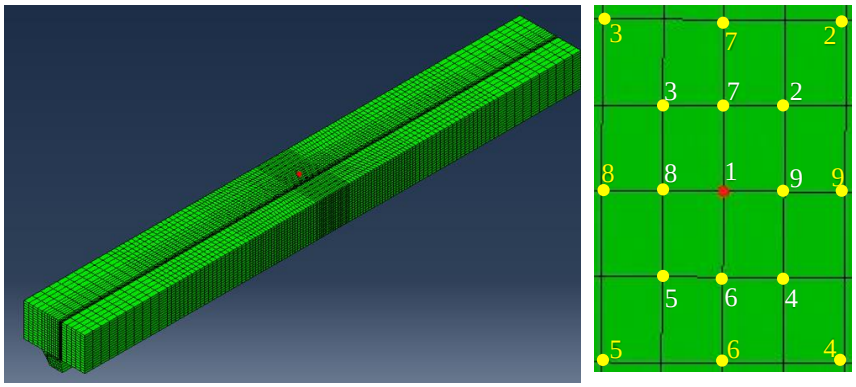

Figure 8.25: Finite element nodes considered for the sensitivity analysis (16 mm OSD)

The nodes were considered with one and two elements offset from the center node as shown in the figure. The element size is approximately *0.7 mm*. The maximum relative strain increase for all nodes is given by Table 8.5.

Table 8.5:Maximum relative strain change values for all chosen nodes (16 mm OSD)

Node	Max1	Max2	Max3	Max4	Max5	Max6	Max7	Max8	Max9
1-element offset	1.76	1.86	1.86	1.86	1.59	1.60	1.59	1.76	1.76
2-element offset	1.76	1.91	1.90	1.89	1.42	1.45	1.44	1.76	1.75

Node 5 is considered to have a two-element distance.

For the *10 mm* model the following nodes were considered.

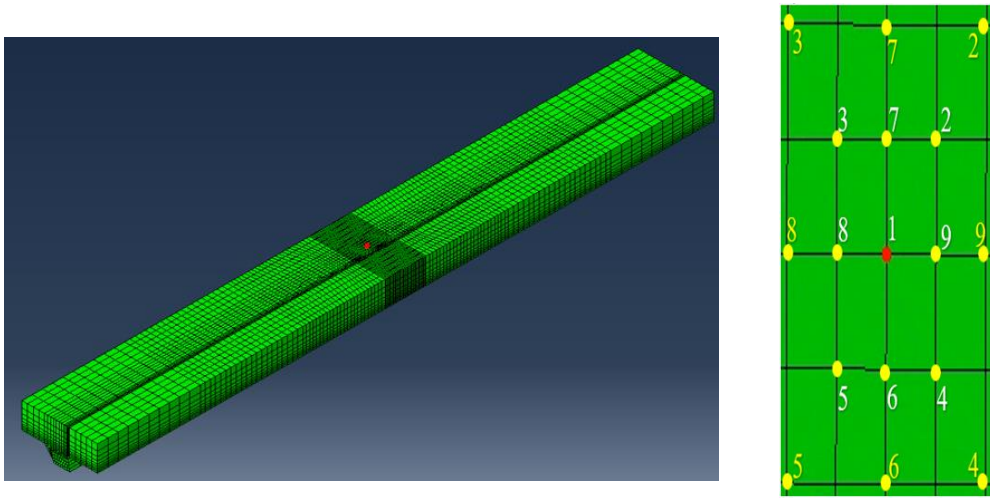

Figure 8.26: Finite element nodes considered for the sensitivity analysis (10 mm OSD)

The nodes were considered with one and two elements offset from the center node as shown in the figure. The element size is approximately $0.5 \times 1.0\ mm^2$. The maximum relative strain increase for all nodes is given by Table 8.6.

Table 8.6 Maximum relative strain change values for all chosen nodes (10 mm OSD)

Node	Max1	Max2	Max3	Max4	Max5	Max6	Max7	Max8	Max9
1-element offset	1.36	1.18	1.20	1.59	1.59	1.57	1.19	1.39	1.33
2-element offset	1.37	1.06	1.06	1.91	2.03	1.90	1.06	1.42	1.33

Node 5 is considered to have a one-element distance.